

SECURITY AND POLICY REVIEW WORKSHEET- Request for Public Release Clearance

(In Accordance With AFI 35-101, Chapter 15)

(Do not use this worksheet to request clearance of software source code or web pages.)

SUBMITTING ORGANIZATION (Office Symbol)

A. DOCUMENT TYPE (Documents must be complete including all figures, charts, photographs and text.)

<input type="checkbox"/> ABSTRACT	<input type="checkbox"/> JOURNAL ARTICLE	<input checked="" type="checkbox"/> THESIS	<input type="checkbox"/> DISSERTATION
<input type="checkbox"/> BROCHURES	<input type="checkbox"/> COURSE DESCRIPTION	<input type="checkbox"/> SPEECH	<input type="checkbox"/> OTHER
<input type="checkbox"/> CD-ROM	<input type="checkbox"/> PHOTO WITH CAPTIONS	<input type="checkbox"/> SUCCESS STORY	_____
<input type="checkbox"/> DISPLAY/EXHIBIT	<input type="checkbox"/> POSTER SESSION	<input type="checkbox"/> TECHNICAL PAPER	_____
<input type="checkbox"/> FACT SHEET	<input type="checkbox"/> PRESENTATION WITH TEXT	<input type="checkbox"/> TECHNICAL REPORT	_____

B. TITLE OF DOCUMENT

Laser Covariance Vibrometry for Unsymmetrical Mode Detection

NO. PAGES

221

C. AUTHOR(S) NAME AND DUTY TITLE

AFIT/GE/ENG/06-61

(Michael C. Kobold)

OFFICE SYMBOL

AFIT / ENG

D. COMPANY NAME (See instructions on last page)

Air Force Institute of Technology / ENG

INDICATE IF:

☐ CRDA ☐ OTHER ☐ N/A

E. FORUM (Public release clearance is not required for material presented in a closed meeting and which will not be made available to the general public on the Internet or in any print or electronic media)

DOCUMENT WILL BE <input type="checkbox"/> PRESENTED ORALLY	NAME OF CONFERENCE	LOCATION	DATE
DOCUMENT WILL BE <input checked="" type="checkbox"/> DISTRIBUTED IN PRINT	NAME OF PUBLICATION AFIT Thesis, AFRL/AFIT Library collection		SUBMITTAL DEADLINE

HAVE RELATED DOCUMENTS BEEN PREVIOUSLY CLEARED FOR PUBLIC RELEASE

☐ NO ☒ N/A ☐ YES AFIT CASE NUMBER

NOTE: If document will be released to a medium outside the Department of Defense, the following disclaimer must be added: The views expressed in this article are those of the author and do not reflect the official policy or position of the United States Air Force, Department of Defense, or the U.S. Government.

FOR AFIT/PA USE ONLY

SUBMIT TO: Air Force Institute of Technology
Public Affairs (AFIT/PA)
Building 642, Room 2401
2950 Hobson Way
Wright-Patterson AFB OH 45433-7129

FOR MORE INFORMATION

Phone: (937) 255-9354 DSN: 785-9354
FAX: (937) 255-2135 DSN: 785-2135
E-MAIL pa@afit.af.edu
WEB: <http://www.afit.mil/newsrm01.htm>

E. NATIONAL SECURITY AND TECHNOLOGY ISSUES

CHECK YES OR NO (Provide a brief explanation for all positive responses in the SYNOPSIS SECTION below.)

- ☐ YES ☒ NO DOES THE MATERIAL HAVE THE POTENTIAL TO BECOME AN ITEM OF NATIONAL OR INTERNATIONAL INTEREST
- ☐ YES ☒ NO DOES THE MATERIAL AFFECT NATIONAL SECURITY POLICY OR FOREIGN RELATIONS
- ☐ YES ☒ NO DOES THE MATERIAL CONCERN SUBJECTS OF POTENTIAL CONTROVERSY AMONG DOD COMPONENTS OR WITH OTHER FEDERAL AGENCIES
- ☐ YES ☒ NO DOES THE MATERIAL CONTAIN TECHNICAL DATA DEVELOPED UNDER CONTRACT OR INDEPENDENTLY DEVELOPED AND CONTROLLED BY THE INTERNATIONAL TRAFFIC IN ARMS REGULATIONS (ITAR) THAT MAY BE MILITARILY CRITICAL AND SUBJECT TO LIMITED DISTRIBUTION, BUT ON WHICH A DISTRIBUTION DETERMINATION HAS NOT BEEN MADE
- ☐ YES ☒ NO DOES THE MATERIAL CONTAIN INFORMATION ON NEW WEAPONS OR WEAPON SYSTEMS, SIGNIFICANT MODIFICATIONS OR IMPROVEMENTS TO EXISTING WEAPONS OR WEAPON SYSTEMS, EQUIPMENT OR TECHNIQUES
- ☐ YES ☒ NO DOES THE MATERIAL CONTAIN INFORMATION ON NATIONAL COMMAND AUTHORITIES, COMMAND, CONTROL, COMMUNICATIONS, COMPUTERS AND INTELLIGENCE, INFORMATION WARFARE, OR COMPUTER SECURITY
- ☐ YES ☒ NO DOES THE MATERIAL CONTAIN INFORMATION ON MILITARY ACTIVITIES OR APPLICATIONS IN SPACE, NUCLEAR WEAPONS, INCLUDING WEAPON-EFFECTS RESEARCH, CHEMICAL AND BIOLOGICAL WARFARE ISSUES, BIOLOGICAL AND TOXIN RESEARCH, HIGH-ENERGY LASERS AND PARTICLE BEAM TECHNOLOGY; ARMS CONTROL TREATY

F. SYNOPSIS (Provide a brief description of the system, process, or technology, including its state of development and whether the application is military, commercial, or dual-use). EXAMPLE: This is new concept of applying current development for high-powered lasers, specifically for military applications.

Classification diagnostics in this proof of concept simulation validate the data clustering capability of continuous wave modulation by the surface vibrations of a target for fundamental component modes. Laser vibrometry return provided cross – spectral covariance matrices that both validate the classification utility and provide recognition features for low frequency structural modes of vehicle skin. The finite element analysis of the structural vibration spectra related to the nonlinear contact used the control law methods of Dr. Winthrop's December 2004 AFIT Ph.D. dissertation. Analysis of the propagated optical field confirms the spectral reduction results reported in Flight Lieutenant Pepela's December 2003 AFIT thesis.

G. REFERENCES (Check all that apply)

- ☒ ALL REFERENCES ARE UNCLASSIFIED, UNLIMITED AND ARE AVAILABLE TO THE PUBLIC
- ☐ REFERENCE # ARE SUBJECT TO DISTRIBUTION LIMITATION. NO LIMITED INFORMATION FROM THESE REFERENCES IS INCLUDED IN THE DOCUMENT
- ☐ NO REFERENCES ARE INCLUDED IN THIS DOCUMENT

RELEASE AUTHORITY AND MANAGEMENT RESPONSIBILITY FOR JOINT EFFORTS

IS THIS INFORMATION CO-AUTHORED WITH SOMEONE FROM AN ORGANIZATION OUTSIDE OF AFIT.

☐ YES ☒ NO

DOES YOUR ORGANIZATION HAVE THE AUTHORITY TO RELEASE THE INFORMATION



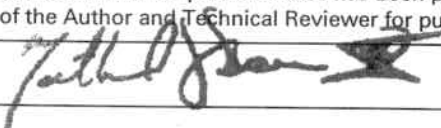
☐ YES ☒ NO

IF WORK IS SPONSORED BY ANOTHER ORGANIZATION, DO YOU HAVE THE AUTHORITY TO RELEASE ALL THE INFORMATION

☒ YES ☐ NO

IF NOT, WHAT ORGANIZATION SHOULD COORDINATE ON THE REQUEST APPROVAL

NOTE: If the organization is a DOD organization, AFIT/PA will coordinate release approval with that organization's PA office

I. AUTHOR/TECHNICAL REVIEW CERTIFICATION	
AUTHOR	
<i>I certify the information contained in the attached document is technically accurate and does not disclose classified, sensitive, or military</i>	
SIGNATURE 	DATE 06SEP06
AUTHOR(S) NAME (Print) Michael C. Kobold	TELEPHONE (937) 253-4770 (321) 591-3679
OFFICE SYMBOL/ORGANIZATION AFIT / ENG	E-MAIL ADDRESS michael.kobold@gd-ais.com, matadorsalsa@ieee.org
TECHNICAL REVIEWER CERTIFICATION (Faculty Advisor)	
<i>I certify the information contained in the attached document is technically accurate and does not disclose classified, sensitive, or military critical technology and does not violate proprietary rights or copyright restrictions. All security and technology issues listed above have been considered and any applicable Security Classification Guides have been reviewed.</i>	
SIGNATURE 	DATE 11 Sept 06
TECHNICAL REVIEWER'S NAME (Print) Stephen C. Cain	TELEPHONE (937) 255-3636
OFFICE SYMBOL/ORGANIZATION AFIT / ENG	E-MAIL ADDRESS Stephen.Cain@afit.edu
DEPARTMENT HEAD (or equivalent)/PROGRAM MANAGER CERTIFICATION	
<i>The attached material submitted for public release has been properly staffed and reviewed by this division/organization. I support the recommendation of the Author and Technical Reviewer for public release.</i>	
SIGNATURE 	DATE 15 Sep 06
NAME (Print) Nathaniel J. Davis IV	TELEPHONE 5-2024
OFFICE SYMBOL/ORGANIZATION AFIT/ENG	
AFIT PUBLIC AFFAIRS	
THE ATTACHED MATERIAL <input type="checkbox"/> IS <input type="checkbox"/> IS NOT CLEARED <input type="checkbox"/> CLEARED PENDING CHANGES (See page 1 for comments)	
SIGNATURE OF SECURITY AND POLICY REVIEW OFFICER	DATE
J. REMARKS (please reference the specific section)	



LASER COVARIANCE VIBROMETRY
FOR
UNSYMMETRICAL MODE DETECTION

THESIS

Michael Christopher Kobold, P.E., Civilian Contractor

AFIT/GE/ENG/06-61

DEPARTMENT OF THE AIR FORCE
AIR UNIVERSITY

AIR FORCE INSTITUTE OF TECHNOLOGY

Wright-Patterson Air Force Base, Ohio

APPROVED FOR PUBLIC RELEASE; DISTRIBUTION UNLIMITED.

The views expressed in this thesis are those of the author and do not reflect the official policy or position of the United States Air Force, Department of Defense, or the United States Government.

AFIT/GE/ENG/06-61

LASER COVARIANCE VIBROMETRY
FOR
UNSYMMETRICAL MODE DETECTION

THESIS

Presented to the Faculty
Department of Electrical and Computer Engineering
Graduate School of Engineering and Management
Air Force Institute of Technology
Air University
Air Education and Training Command
In Partial Fulfillment of the Requirements for the
Degree of Master of Science in Electrical Engineering

Michael Christopher Kobold, P.E., MS
Civilian Contractor


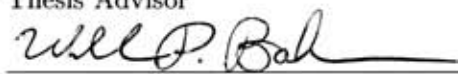
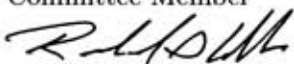
September 2006

APPROVED FOR PUBLIC RELEASE; DISTRIBUTION UNLIMITED.

Laser Covariance Vibrometry for Unsymmetrical Mode Detection

Michael Christopher Kobold, P.E., M.S. Physics, U of Michigan, Ann Arbor

Approved:

	<u>7 sep 06</u>
Dr. Stephen Cain	Date
Thesis Advisor	
	<u>7 Sep 06</u>
Dr. William Baker	Date
Committee Member	
	<u>7 Sep 06</u>
Dr. Richard G. Cobb	Date
Committee Member	

Abstract

Simulated cross – spectral covariance (CSC) from optical return from simulated surface vibration indicates CW phase modulation may be an appropriate phenomenology for adequate classification of vehicles by structural mode. The nonlinear structural to optical relationship is close to unity, avoiding nulls and high values; optical return contains sufficient spectral ID information necessary for data clustering. The FE model has contact between the homogeneous rolled armor (HRA) and vehicle hull, a simple multi - layer skin model typical of most vehicles. Most of the high frequency energy moved to lower frequencies. This nonlinearity segments contact vibration modes into two classes: symmetrical modes that do not vary with minor structural changes, and those that do. The fundamental mode symmetry created features that were insensitive to slight structural load path changes. Structural aging simulation affected spectral and CSC fine structure generated by non-symmetrical modes. Structural vibration spectral analysis related to the nonlinear contact uses methods from Maj Winthrop’s December 2004 AFIT PhD dissertation. Analysis of the propagated optical field confirms the spectral reduction results of Fl Lt Pepela’s December 2003 AFIT thesis.

Acknowledgements

For the guidance of Professor Cain, the generous resources support from AFRL/SNAT, GD-AIS, and Branch Chief Matt Dierking, AFRL/SNJM laser vibrometry project manager, I am indebted. AFRL/SNAT Technical Leader Rob Williams directed my use of these CSC techniques for other venues over the past year, which has been a great help. The initial thesis work and all of my course work were generously funded by the Dayton Area Graduate Studies Institute (www.dagsi.org). I appreciate the efforts of my committee, thesis advisor Electrical Engineering Professor Stephen Cain, Professor Richard Cobb for insight into the laser vibrometry systems, modal analysis, and control issues, and Dr. William Baker whose assistance with the nonlinear differential equations was essential in uncovering the structural response features represented by seemingly simple systems. I appreciate the assistance of Aerospace Engineering Professor Robert Canfield who fielded most of my structural questions and Dr. Palazotto for assistance in validation of the preliminary MathCad stress analyses that were the basis for several FE modelling assumptions. I appreciate the persistence of former TACOM customer Roberto P. Garcia (Army) for information on HRA and his contact at GD Land Systems, Steve Meinsche, and for their insight into the target vehicle. I am appreciative of access to several exterior resources including my introduction to imaging at www.ultrasound.med.umich.edu, Brian Fowlkes, Paul Carson, and discussion about applications of this method to medical imaging, my introduction to USAF radar systems at Northrop Grumman (NGC) where Bob Halstead and his team, Brian Lima, Lou Fiori, and Ron Higgins brought me in to see the workings of large radar system programs. Other NGC personnel including John Patterson and Bob James were instrumental in growing my experience in aircraft vehicle systems. From that structures group, NGC sent me through their Radar Systems Certification program that led to my involvement with remote sensing and return to working with lasers. My uncle's fascination with technology and experience with test equipment at Eton in Florida drove me on; Reno Kobold had a keen grasp of radar and avionics systems. I am grateful for the support of General Dynamics - AIS

Reconnaissance and Surveillance Systems managers Dave Doty, Mark Axtell, Dave Gross, Jim Schmitz, and Alex Bennet in allowing me to schedule classes around the work schedule and resources to perform the work. Dr. Frank Baxley who hired me to work at SNJT for Dr. Richard Sanderson and Dr. John McCalmont whose guidance provided experience on their IR equipment and imaging systems, and the experience of many physics and optical engineering discussions in that lab, was a great welcome boost. Ted Rose of The MacNeal Group, Mary Baker, Ph.D. of SDRC, Milford, OH, and Bob Coppolino, Ph.D. of The Measurement Group, provided insight into the best model to use for the work, PSD issues, and the model characterization issues involved with random response versus spectral analysis of direct transient results. Professor Lieutenant Colonel Matthew Goda's direction on the effects of turbulence for laser vibrometry was very helpful. Finally, MAC assistance from the Ph.D. recipient for "the" MAC dissertation, Professor Randall J. Allemang of Cincinnati, a collaborator with Professor Canfield at AFIT, is greatly appreciated.

Michael Christopher Kobold, P.E.

Table of Contents

	Page
Abstract	iv
Acknowledgements	v
List of Figures	xi
List of Tables	xiv
List of Symbols	xv
List of Abbreviations	xvii
I. Introduction and Applications	1
1.1 Research Summary	4
1.2 Historical Developments and Classical Laser Vibrometry	9
1.3 Modal Analysis in the vehicle industry	11
1.3.1 Structural Modes	11
1.3.2 Physical Model for the FE model	12
1.3.3 Low frequency structural modes can be good ID features	12
1.4 Organization of the thesis	13
II. Simulation Description	15
2.1 Signal Processing Objectives	15
2.1.1 Structural v. optical $\Gamma_{cross-spectral}$, CSC, Coh	15
2.1.2 Spatial and spectral structural coherence	16
2.2 Structural Model	18
2.2.1 Structural Statistical Stationarity	19
2.2.2 Structural Vibration Transfer Functions	23
2.2.3 Vehicle properties affected by nonlinearities	25
2.2.4 Nonlinearities Summary: which apply, which are active	26
2.2.5 Following load deflection curves: Nyquist is not enough	27
2.2.6 Anti – Symmetric Modes	29
2.2.7 Symmetric is not the antonym of un – symmetrical	30
2.3 General Laser Optics	34
2.3.1 Existing Laser Doppler of military vehicles	34
2.3.2 Non – random laser vib. & adaptive classifiers	35

	Page
2.3.3 Test Equipment Specifications	36
2.3.4 Quadratic phase, Matlab modulation diagnostics	37
2.3.5 Limits of Resolution	39
2.3.6 Surface Roughness effects, speckle generation . .	39
2.3.7 Speckle noise – Considerations for CW lab use .	40
2.3.8 Target Grid Aliases Quadratic Phase Wrapping	42
2.3.9 Optical mixing, noise and resolution	42
2.3.10 Phase modulation retrieval: Reference Mixing .	43
2.4 Optical Physical Model Overview	47
III. Chapter 3: Structural Vibration Modulated Laser Beam Response	49
3.1 Non – Diffraction Beam Modulation Optics	49
3.1.1 Cross – Spectral Covariance (CSC)	49
3.1.2 CSC matrix form, structural coherence, & ρ_{corr}	52
3.2 Coherent return, phase modulation mode shape	55
3.2.1 Source of the Paraxial Approximation	56
3.2.2 Using the Paraxial Wave Equation	57
3.2.3 Plane Wave Modulation, time averaged result .	58
3.2.4 Paraxial to target, time averaged modulation . .	60
3.3 Stationarity: ‘Image’ SNR drives time history length . .	62
IV. Theoretical and Simulated Results	64
4.1 Theory Result: Plane Wave spectral reduction	64
4.1.1 Plane wave assumptions and preliminary details	66
4.1.2 Derivation of the plane wave solutions	67
4.1.3 Slow Sine Sweep spectral elimination	72
4.1.4 Multi – modal small deflection spectral reduction	76
4.1.5 Plane wave illumination spectral elimination . .	79
4.2 Physical and optical model assumptions	82
4.2.1 Overview of the simulation assumptions	82
4.2.2 Structural assumptions	83
4.2.3 Optical assumptions	83
4.3 Results: Mathematical preliminaries	84
4.3.1 Simple systems that model structural contact .	84
4.3.2 Single DOF Contact Nonlinear response	86
4.3.3 Two DOF system eigenvalues: Contact changes antisymmetric response	90
4.4 Results: Finite Element Analysis	92
4.4.1 Structural FEA study B : Time History Response	93

	Page
4.4.2 FEA Time History Response: Contact Response	94
4.5 Simulation results: Structural and optical response . . .	97
4.5.1 Time History Response of Optical Imaging Return	97
4.5.2 Normal Mode Frequencies	99
4.6 Frequency Response: Optically Imaged Radiant Flux . .	103
4.6.1 Imaging Laser Vibrometry Time Response . . .	104
4.7 Results: Trade Studies, vertices from a baseline analysis	117
4.7.1 Study A: Random Response, Contact Stiffness .	117
4.7.2 Study B: Load path variation (mount vibration)	135
4.7.3 Bolt Area Configurations used in the Ensemble	137
4.7.4 Imaging versus Non – imaging CSC calculations	138
V. Conclusions: target & spectral ID, industrial use	146
5.1 Considerations for Target ID	150
5.2 Considerations for Spectral Estimation	151
5.3 Considerations for Structural Design	152
5.4 Considerations for Industrial Laser Vibrometry	156
5.4.1 CW laser covariance vibrometry	157
5.4.2 Non – stationarity of nonlinear dynamics	158
5.5 Concluding Remarks	159
Appendix A. Physical Vibration model	161
A.1 Structural Loading	161
A.2 Structural Nonlinearities	163
A.2.1 Zienkiewicz’ closed form energy transfer proof .	163
A.3 Modal Analysis	164
A.3.1 Field nonlinearities, in general	164
A.3.2 Driving mass structure definition	166
A.3.3 Wandering modes of nonlinear structures	168
A.3.4 Damping Distributes the Driving PSD	170
A.4 Nonlinearities Summary	172
A.4.1 Nonlinearities affecting FEA and CW results . .	173
A.4.2 Why use Bolt Area Variations for an Ensemble?	174
Appendix B. Finite Element Model	176
B.1 FE modelling for surface displacement and speed output	176
B.2 Physical Model	176
B.2.1 Symmetric Boundary Conditions	177
B.2.2 Physical Model for the FE model	180

	Page
B.2.3 Fixity	187
B.2.4 FE Model Element Summary	187
B.2.5 Contact Gap Element Validation	190
B.2.6 Contact nonlinear: static (per time step) solution	192
B.2.7 Transient Model Validation	192
B.3 Frequency Response: Vibrating Plate Contact Response	194
B.3.1 Fourier Transforms of Direct Transient Time His- tories	194
B.3.2 Trade Study B, ensemble ΔA_{shear}	195
Appendix C. MathCad Vibration Frequency and Deflection Estimates	203
C.1 Closed form plate frequency calculations	203
C.1.1 Input Parameters	203
C.1.2 Modal frequencies, HRA welded to hull (t=4") .	204
C.1.3 Normal mode frequencies, Hull-only (t = 3") . .	204
C.1.4 Normal mode frequencies, HRA – only (t=1") .	205
Appendix D. Closed form nonlinear contact response, Single DOF . .	206
D.1 Single DOF (SDOF) calculations	206
Appendix E. Closed form MathCad 2 DOF nonlinear contact	208
E.1 Two DOF DE's and solutions	208
Appendix F. Closed form 2 DOF nonlinear contact eigenvalues	213
F.1 Damped 2 DOF sprung mass system Eigenvalue solutions	213
F.1.1 Stiffnesses for stable systems	214
F.1.2 Dimensionless formulation	214
F.1.3 Analysis of the 2 DOF SEVP DE	218
F.1.4 Synthesis of the 2 DOF SEVP DE	218
F.1.5 Physical nonlinear 2 DOF solution Synthesis . .	219
F.1.6 Energy balance, Lyapunov function	220
F.1.7 One DOF Lyapunov Function: Solution envelope	221
Bibliography	222
Index	229

List of Figures

Figure		Page
1.	Laser Vibrometry Applications – Target ID	3
2.	Optical Signal Processing Model	8
3.	Unsymmetrical, symmetrical, antisymmetric, & symmetric modes	31
4.	Fresnel versus Fraunhofer approximations	38
5.	Mixing $\lambda = 10\mu m$ return return to target at 1 and 10 %	44
6.	Mixing $\lambda = 10\mu m$ return to target at 1,000 & 10,000 %	45
7.	Change in Phase = 2 u	68
8.	Plane Wave Solution targets	69
9.	Sine Swept: Panel $\Phi_e(mode)$ versus beam return	75
10.	Multi – Modal One Dimensional Plane Wave Solution	80
11.	The arctangent model of contact stiffness	88
12.	Nonlinear orbit for Low closed gap stiffness	89
13.	Real eigenvalue parts subdue antisymmetric mode	105
14.	Full 0.2 sec time history FEA direct transient response (SOL 129)	106
15.	FEA deformation v. Φ_e images for t = 1.74 ms v. 15.98 ms . .	107
16.	Bolt Area Variation Time History by time step (non – uniform Δt)	108
17.	Bolt Area Variation Time History on a uniform time scale . . .	109
18.	Long time history, “Image SNR’s”	110
19.	“Image SNR” Spectrum	111
20.	Structural Normal Modes	112
21.	First normal mode, soft and hard contact	113
22.	Second normal mode, soft and hard contact	114
23.	Third normal mode, soft and hard contact	115
24.	Imaging versus Non – Imaging $\Phi_e(t)$	116

Figure		Page
25.	Study A: FEA Impulse responses $FRF_w(f; k_{contact}) \forall k_{gap}$	119
26.	Study A: Non – imaging $\Phi_e(f; k_{contact})$ random response $\forall k_{gap}$.	121
27.	Study A $ CSC_{structural} $: 30 random load ensemble, with/without gravity	124
28.	Study A $ CSC_{optical} $: Comparison across different $k_{contact}$	125
29.	Study A $\angle CSC_{structural}$: Ensemble over 30 random loads	126
30.	Study A $ CSC_{structural} $: Ensemble over 32 locations	127
31.	Study A $\angle CSC_{structural}$: Ensemble over 32 locations	128
32.	Study A $ CSC(\Phi_e) $ Image: random load Ensemble	129
33.	Study A $\angle CSC(\Phi_e)$ direct Random load Fourier response Ensemble	130
34.	Study A $ CSC(f_\Phi, f_{str}) $ Ensemble over 30 random loads	132
35.	Study A diag $ CSC(f_\Phi, f_{str}) $ plotted: Ensemble over 30 random loads	134
36.	Study B: Structural FRF by Bolt Shear Area Variation	136
37.	Study B ensemble averaged imaging $\Phi_e(x, y)$ spectra	139
38.	Study B $ CSC_{structural} $, bolt variations model sensing variation	140
39.	Study B $\angle CSC_{structural}$, bolt variations model sensing variation	141
40.	SNR(t) for all bolt configurations	142
41.	Optical CSC Magnitude image, 27 bolt configurations	143
42.	Optical CSC Phase image, 27 bolt configurations	144
43.	Structural vibration model schematic	165
44.	One DOF over – simplified physical model for contact	181
45.	The physical model for the FE model	182
46.	FEA Mirror Symmetry on plate edge	183
47.	Hull to system frame loading	184
48.	HRA and Hull system, the quarter panel model, alone	185
49.	Gravity Load at 45 degrees, side is slanted	197
50.	Application of Symmetry and Antisymmetric BC's	197

Figure		Page
51.	Quarter Model's portion of the full deformation shape	198
52.	Plan View of FE model, constraints, and loads	198
53.	Plot of applied load in time and its effective PSD.	199
54.	Direct Transient Structural FEA response with SS BC's	200
55.	Short Time Step history	201
56.	Long Time Step history	202
57.	Double Eigenvalues on the zero radical delineate mode change regions	215

List of Tables

Table		Page
1.	Nonlinear System Frequency Response Effects	25
2.	Vehicle system properties effected by nonlinearities	26
3.	Assumptions of the Optical Physical Model	47
4.	Assumptions listed by Analysis Regimes	82
5.	Assumptions of the structural physical model	83
6.	Assumptions of the optical simulation results	84
7.	Normal modes undergoing transient excitation	102
8.	Baseline FEA configuration	117
9.	Nonlinearities Affecting FEA – CW	173

List of Symbols

Symbol		Page
Φ_e	Radiant flux of irradiance (E) or exitance (M)	3
P_d	Probability of Detection	5
P_{fa}	Probability of False Alarm	5
$\gamma_{xy}^2(f)$	Structural coherence function	16
$H(f)$	Structural transfer function for cross – spectral PSD . . .	16
c	Speed of sound, shock propagation speed	16
$G_{xy}(f)$	Structural cross – spectrum (PSD), $f > 0$ (one – sided) . .	17
$G_{xx}(f)$	Structural source PSD	17
$G_r(f)$	Reference “auto – spectrum”	18
$T_{stationarity}$	Load path stationarity period	19
Q	Oscillator quality	24
(m,n)	Structural mode, m half cycles in x, and n in y	31
w	Structural out – of – plane deflection	31
D_{op}	Diameter of the optic aperture or effective pupil	39
λ_o	Laser mean (center) wavelength	39
f_{length}	Effective optic focal length	39
f_{min}^{mesh}	Minimum FE model surface mesh spatial frequency	39
CSC	Cross – Spectral out-of-plane spatial covariance	50
$C(f_u, f_v)$	Cross – Spectral out-of-plane spatial covariance	50
M	Number of spectral vectors (stochastic samples)	52
N	Number of frequency bins	52
$[S_{MR}]_{row++}$	Permutation of rows: “row++”	53
Coh	Coherence function (structural vibration)	54
F_o	Phase front radius of curvature	57
W_o	Gaussian profile spot size at e^{-1} reduction	57

Symbol		Page
E	Electric Field in Volts / meter or Newtons per Coulomb .	58
E_e	Irradiance, Watts per m^2	59
c	The speed of light	59
E_{mod}	Electric field modulated by the target	60
E_{mode}^{multi}	Multi – mode average Electric Field	60
M	$M = \frac{2a}{\lambda_{x.high}}$ highest low strain energy x mode considered .	70
N	$N = \frac{2b}{\lambda_{y.high}}$ highest low strain energy y mode considered .	70
S	The Poynting vector, in Watts	71
$\Delta\phi$	Optical change in phase from deflection	71
ϕ_n	Modal participation factor, $w_{m,n}(x, y) = (\Delta z)_{m,n}(x, y)/2$.	72
ϕ	Uniform MPF $\phi = \frac{w_{max}}{N}$; $\sum_{n=1}^N \frac{w_n^{max}}{N} \sin \frac{\pi y}{b/n} = \phi \sum_{n=1}^N \sin \frac{\pi y}{b/n}$.	76
Γ	Spectral Frequency Response (Structural Eng., DSP) . . .	138
$E_{ijkl}(t)$	Relaxation Tensor	171
σ_{ij}	Stress, in MPa or psi	171
B	Bulk Modulus, $B = \frac{E}{3(1-2\nu)}$	177
kN/mm	Structural stiffness units, kilo Newton per mm	191
λ_i	Eigenvalues	217
Λ	Matrix with eigenvalues along the diagonal	217
Γ_i	Eigenvectors	217
Σ	Matrix whose columns are the eigenvectors	217

List of Abbreviations

Abbreviation		Page
TACOM	Tank Automotive Command, 11 Mile Rd., Warren, MI . . .	v
CW	Continuous Wave	1
CSC	Cross Spectral Covariance	1
ATR	Automated Target Recognition	1
MAC	Modal Acceptance Criterion	2
CMIF	Complex Modal Indicator Function	2
FDAC	Frequency Domain Acceptance Criterion	2
OEM's	Original Equipment Manufacturer	2
SAIC	Science Applications International Corporation	4
COTS	Commercial Off the Shelf	4
LIDAR	Light Detection And Ranging	4
MPF's	Modal participation factors	5
MSC	MacNeal – Schwendler Corporation	8
NASTRAN	NASA structural analysis software completed in 1967 . . .	8
FEA	Finite Element Analysis	8
DPLM	Dual Pulse Laser Modulated	9
PSD	Power Spectral Density	9
DE's	Differential Equations	9
STM	Scanning Tunnelling Microscopy	10
iid	Independent identically distributed	16
MPF's	Modal Participation Factors	18
FWHP	Full Width at Half Power	24
DOF	Degree Of Freedom	25
PDF	Power spectral Density Function	27
LADAR	Laser Radar, Detection and Ranging	29

Abbreviation		Page
HRA	Homogeneous Rolled Armor	32
H – F	Huygens – Fresnel	34
MTI	Moving target indicator	34
TDOA	Time difference of arrival	34
AV's	Aerial Vehicles (includes unmanned)	35
DoD	Department of Defense	36
PRF	Pulse Repetition Frequency	36
PRR	Pulse Repetition Rate	36
IPP	Inter – Pulse Period	36
CTF	Coherent transfer function	39
OTF	Optical Transfer Function	39
ANSI	American National Standard Institute	39
ROC	Receiver Operating Curve	48
FDAC	Frequency Domain Acceptance Criterion	50
TDOA	Time Difference Of Arrival	52
W – K	Wiener-Khinchin	52
BC's	Boundary Conditions	55
SDOF	Single DOF	85
LTI	Linear time invariant (system)	86
isL	(Stability) In the sense of Lyapunov	88
SEVP	Special Eigenvalue Problem	99
FWHH	Full width at half height	146
OSU	The Ohio State University	152
HBM	Harmonic Balance Method	152
SHM	Simple Harmonic Motion	166
dB	deci Bell	170
AETC	Acoustic & RADAR signal processing company	174
BC's	Boundary Conditions	176

Abbreviation		Page
FOV	Field of view	180
SS	Simply supported (rotations released)	185
NAFEMS	A British Standards Non – profit Organization	189
EVP	Eigenvalue Problem	216
SEVP	Special Eigenvalue Problem	216

LASER COVARIANCE VIBROMETRY FOR UNSYMMETRICAL MODE DETECTION

I. Introduction and Applications

In order to show the utility of continuous wave (CW) phase modulation as a foundation for laser vibrometry for structural mode spectral identification, this work studied several response characteristics. First, the spectra of the optical CW return adequately demonstrate the structural spectra for variations on the structure. Secondly, simplistic closed form models of structural plate contact show that symmetrical modal frequencies do not vary. Thirdly, simulated optical returns from nonlinear contact structural models of typical vehicle skin show similar frequency behavior, thus indicating which structural modes upon which to base laser structural vibrometry. Some bands in the cross spectral covariance are stationary with respect to modest variations in the structural model. The cross spectral covariance (CSC) of detected spectra are sufficiently diagonal for spectral ID, yet when “corrupted” by transient response have coupling features directly related to “nonlinear” normal mode frequencies of the structure. Finally, the simulated cross – CSC from optically received return off of surface vibration, provides necessary (but not sufficient itself) indication that phase modulated CW laser vibrometry is an appropriate phenomenology for adequate classification of vehicles by structural mode.

This multi – disciplinary thesis combines modal analysis practices in the structural engineering fields with signal and image processing in optical engineering.

Features used in automated target recognition (ATR) often include cross – section, polarization, and shape. We propose using only the (normal mode) modal

frequencies for ATR. Laser shape dimensioning methods¹ for mechanical design circa 1985 with accelerometers and lasers help validate separate structural ‘normal modes’ that are the basis eigenvectors of the structural vibration response for a given vehicle. A dozen values such as the modal acceptance criterion (MAC) [2] and other MAC’s [3] compare the measured modes to the simulated modes. In the commercial equipment industry these comparisons provide metrics that validate the usefulness of the dynamic response of simulation Finite Element models, the FE models. Along with these eigenvector MAC’s there are a few MAC’s that compare only the response spectra rather than mode shapes. These frequency based MAC’s include the complex modal indicator function (CMIF) [23] a set of singular value decomposition response functions and the frequency domain acceptance criterion (FDAC) [57] which compares input versus output spectra or response spectra at sensed by the lasers scanning different locations.

The laser signal processing industry has been using a CSC that provides a measure of information about the system similar to that provided by the FDAC but using the same spectra, the output signal, on both the abscissa and ordinate of the image of the matrix. The CSC also has historical bases in the 1970’s, albeit in a different manner. Strong features in these matrices include the frequencies at magnitude and phase changes due to resonances or near resonances as seen in experimental versus FEA results for the FDAC (which is misleadingly similar to the FRAC), and the SCC [4, 68]. Such results (not shown) were validation metrics for this work.

These and other signal processing methods, applied to received laser modulation from vibrating vehicle surfaces as shown in Figure 1, provide alternative methods for target ID. CW phenomenology also provides for description of individual pulse return in classical laser vibrometry systems. This thesis emphasizes structural mode identification rather than matching sensed nonlinear response to the driving load PSD since an objective of original equipment manufacturers (OEM’s) is to remove

¹These laser dimensioning and mode shape measurement systems pre – date laser vibrometry systems.

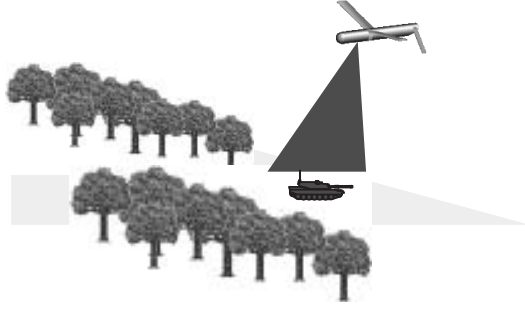


Figure 1: One application of Laser Vibrometry is improvement in Target Identification. Structural identification, part of this task, seeks to identify spectral response. Laser Vibrometry can identify characteristic vibration modes on a structure.

that phenomenology. Identification of structural modes due to loads far below one ‘g’ is a phenomenology that is here to stay for the foreseeable future.

This CW laser vibrometry simulation uses a nonlinear contact vibration that models actual vehicle skin rather than typical laboratory structural specimens.² The laser illumination return, upon mixing with the coherent reference beam of appropriate power, images the phase modulation. A simple sigmoid study discussed on page 5 determines a modest level of classification adequacy provided structural and optical spectra are comparable. As demonstrated in subsections 4.6.1 and 104 on pages and 4.7.4 and 138, the spatial integration of the irradiance over the detector area provides a radiant flux (Φ_e) with frequency domain response that sufficiently matches that of the vehicle for target ID.³

The next step after the “FEA modulated” Fresnel image propagation simulations of this thesis is to perform experiments on vehicles directly. Except for a few locations⁴ multi – layer skin nonlinear contact response is dominant for vehicle surface vibration effect. The lossy nonlinear radiation – absorption process is not usually

²Additional advantages of the system (structural FEA - optical Matlab signal processing) include provisions for expedient minor modifications to simulate comparisons in detected return.

³ $\Phi_e(x_i, y_i; t; f) = \int_{\Delta x_i} \int_{\Delta y_i} [E_e \text{ or } M_e] dx dy$ uses inbound irradiance E_e or outbound exitance M_e .

⁴Regions of most direct sound absorption include the acoustic radiation to absorption in the usually triangular single layer patches on the engine hood, similar patches of non – multi – layer skin on the decklid absorbing trunk noise, and small cross section welded features.

beneficial for spectral ID of the source excitation, a process ignored in the structural mode ID method suggested by this thesis.

A preliminary validation of the concept used the collection of vehicle dimensioning data with an SAIC commercial off the shelf (COTS) LIDAR⁵ with the scanner turned off [64]. This January 2006 collection at WPAFB showed 10 to 30 Hz modulation, the maximum of this limited⁶ system but sufficient to show that vehicle skin panel vibration provides adequate laser modulation for classification.

This thesis uses simulated vibration results from a structural Finite Element model using MSC/NASTRAN to generate nonlinear (contact) armor plate surface deflections input to a set of Matlab beam propagation, modulation, image back – propagation, and radiant flux summation scripts. Such armor is conveniently rectangular, serving as a general structure for a laser vibrometry target ID study. The result is a set of responses for several different design variables that simulate the laser vibrometry return from multiple vibrating layers of vehicle skin clattering in contact, including both imaging and non – imaging (spatially integrated) return. The simulation used both random excitation and physical impulse loads comprising trade study A (random) and B, respectively.

1.1 Research Summary

In an effort to add to the repertoire of systems for identification of vehicle structures through their vibration signatures, this work studies the interaction of laser illumination with simulations of vehicle skin vibration. The objective of this study is to quantify the relationship between the actual vehicle surface vibration characteristics and those reported via remote sensing systems. With the choice of structural mode identification through spectral ID the vehicle need not be idling but should have some excitation approaching 0.001 ‘g’ loading which could be a wind

⁵On April 18, 2006 Science Applications International Corporation (SAIC) acquired Geo-Spatial Technologies, Inc. (GSTI), a Springfield, Va., and Seattle, Wa., firm who was the vendor in January running this WPAFB Area B collection with their Commercial Off the Shelf (COTS) Light Detection And Ranging (LIDAR) dimensioning system.

⁶The detected z deflection measurement varied over only three quantization levels.

noise that excites panel vibration on a micron level. This interferometric analysis can detect deflections that are a fraction of the operating laser center wavelength which can be less than 1 micron. This study (“the work”) seeks to model vibration of target vehicles to estimate surface vibration structural modes.

Much of the historical laser vibrometry work for target ID involves normal mode shape analysis that measures out – of – plane (normal) surface speed. Many studies catalog the existence of characteristic modes or resonances or to try to match the excitation source PSD assuming the structural model is linear, which is often not the case.

This work investigates the inter – relationship of the ‘normal modes,’ which on the surface appear individually as standing waves, whose assumed linear combination comprise the dynamic response of the vehicle skin to any structural vibration energy source. The modal participation factors (MPF’s) for this combination may be complex, having both amplitude and phase. It is these phase relationships that the CSC matrices measure. OEM noise and vibration engineers can already easily identify vehicle models from one another by the frequency values of the first couple of normal modes. Remote spectral ID using features in optical spectra and their CSC matrices is an extension of this ID capability.

Selection of a classification system upon successful implementation of a laser vibrometry target ID system is out of the scope of this thesis. However, there is evidence of the ability of such a system to provide adequate performance. A simple sigmoid multi – hypothesis neural spectral ID classification [43] using 6 actual laser Doppler modal frequency measurements from a 1998 Redstone Arsenal test for NATO [54] showed Probability of Detection (P_d) of 80 to 85 % and Probability of False Alarm (P_{fa}) of 10 to 15 %.⁷ These moderately adequate results are public unclassified data that show the capacity of a laser vibrometry system to provide adequate improvement

⁷These criteria assume an adequate choice of resonance quality (Q), number of spectral samples, and tight priors using the FEA result versus experiment frequency differences for the modes in the Pininfarina chassis [48] as the Gaussian spectral error variance for random seeding [43].

for vehicle classification based on running, idling, or even wind noise generation of micron level vibrations.

While traditional Hilbert transform analyses [55, 500] and Geological analysis tools [79, 11022-11023] do provide information on spectral variances, a full CSC provides relationships that can lead to time dependence of the modes from their inverse Fourier transform relationships (which is beyond the scope of this thesis). CSC analysis provides information on its own that indicates spectral signatures for particular structures. The typical laboratory vibrating plate is useful due to its spectral correlation to closed form and numerical solutions given in Roark [92], but they are not typical of most of the exterior skin for nearly any target vehicles. This work analyzes a simple two layer model of vehicle skin, the armor bolted on a tank. Typical commercial and personal vehicles have skin with a nonlinear contact effect of multi – layer stack – ups. The two layer model used here is the simplest form of vehicle skin inter – layer contact.

While listening devices that detect sound – induced window pane vibrations are a well known technology, vibrations on the surface of a vehicle are often correlate poorly with sources. First, there are many sources, secondary sources, and load paths for sound and vibration energy that end up in the surface vibrations of target vehicles. Secondly, the largest generation mechanisms for vehicle vibrations, road noise and engine operation, are wide band sources whose lower frequencies are preferentially “absorbed” into vehicle structural modes. Third, there are numerous nonlinear structural vibration energy conduits, including the radiation and re – absorption of acoustic energy, motor and other mounts whose passive forms are also quite nonlinear. For example, fasteners not only dampen the structure but provide clamp – up nonlinear load transfers. Also, nonlinear materials such as plastics and simple metal internal hardware are now so thin that they routinely operate in the large deflection mode, contributing to nonlinearity. The main focus of this thesis is on the particular dynamic response from another aspect of common commercial vehicles, multi – layer

body in white⁸ construction. Therefore, except for limited cases, target identification using the “listening device” vibrometry methods is not considered.

Four major elements comprise the work. 1) A two DOF model of nonlinear contact as a crude model for skin layer contact, albeit lumped into one contact at the same instant in time, serves as a check on the full three dimensional physical vibration simulation. 2) A set of 3 – D Finite Element models provide estimates of the spectra by simulation of the time domain response of a grid of points over the surface of the outer skin, in this case M1A1 armor bolted to the hull. The geometrically nonlinear contact between the armor and the hull is a mature use of nonlinear FEA, yet provides insight to general vehicle acoustic transmission based on two different trade studies in this work. 3) Third, several Matlab translators for MSC/NASTRAN Finite Element models and analysis results produce a set of deflection grids in time for the optical image propagation scripts, integrating the system. This system integration allows for the use of OEM FE models, and structural changes to these models, for characterization of the vibrometry return.⁹ 4) Finally, a Matlab simulation models detection at 4 km of a 10 micron¹⁰ optical Gaussian beam at shining on the FEA resultant deflections over time.

Calculations of the change in phase at different locations over time result in both imaged and non – imaging spatially integrated power at the simulated detector. As shown in Figure 2, the return from the assumed specular exitance mixes with a

⁸The ‘body – in – white’ is the welded stamped metal – only shell for the entire vehicle that often has white coating (just as bare aircraft have green primer over the Aluminum skeleton and shell). This is an improvement over the old body and chassis structures. The outer skin is almost always composed of many layers that terminate at different boundaries having been extruded for different purposes. Evidence is easy to see in an automobile being prepared for body work. Repair never pushes skin out from the inside but uses a crude screw mechanism to grab the skin to pull it into place. The inner surface of the outermost skin is usually not accessible without excessive destruction of the vehicle. This an example of the multi – layer skin that makes lab specimen response less easy to correlate to actual vehicle skin dynamics.

⁹OEM’s retain FE models for all the vehicles licensed for sale for legal and regulatory purposes. With OEM cooperation these models can help determine vibrometry signatures to complete an evolving catalog for target ID.

¹⁰ $\lambda = 10\mu m$ is kept conveniently “long” to mitigate aliasing and phase wrapping issues. It is physically realizable. But the results are essentially the same as physical imaging systems with smaller wavelengths.

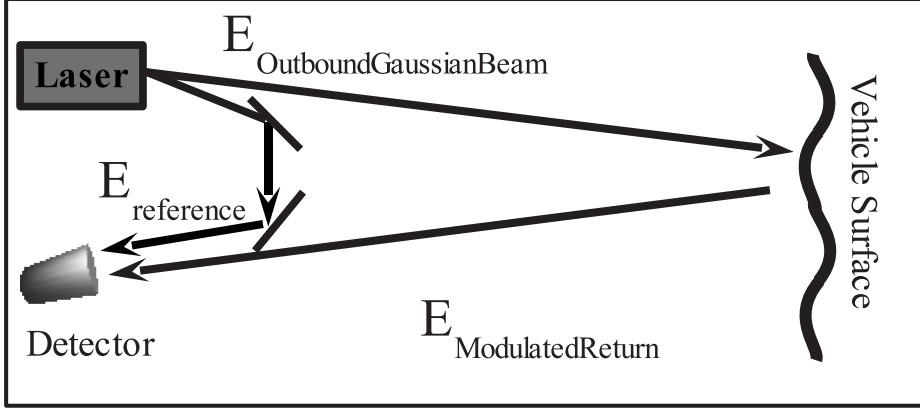


Figure 2: Coherent short duration CW or Pulse Sampling irradiance undergoes a spatially harmonic phase modulation as a function of beam profile location due to target vehicle surface skin structural vibration.

coherent part of the original beam to allow detection of the phase change at the target. The simulation assumes the optical system is photon limited so this speckle noise is the main noise component effect in the ability to sense the phase modulation. The speckle noise is a random phase in space and time that represents the surface roughness. Results show that the remote sensing spectra adequately match the structural vibration, including non – imaging spatially integrated power.

This thesis compares the sensed return from a simple plate vibration (hull only) with a simple two layer plate contact vibration response (HRA). Contact nonlinearity is only one of the myriad other common nonlinearities that are a basic part of ordinary vehicle body – in – white construction. But for simplicity it is the only specific nonlinearity featured in this thesis. Contact plate structures are more prevalent in existing target vehicles and they behave differently enough from single layer specimens to affect the vibrometry results. The integration of MSC NASTRAN finite element analysis (FEA) nonlinear contact deflection results into a system of Matlab image propagation scripts in this work provides a foundation for optical sensing analysis of commercial vehicles.

Using classical CW this thesis simulates laser vibrometry that detects structural vibration modes. This work builds onto spatial reduction / elimination / averaging

observations for large spot sizes at the target for target ID laser vibrometry seen in laboratory experiments in a prior thesis in the AFIT Aerospace Engineering department.¹¹ This thesis also provides characterization of methods that are less sensitive to laser vibrometry mounting vibration (page 157) than the commercial dual pulse laser modulated (DPLM) surface speed detection systems [43, 54]. Use of a CW system can provide a groundwork for structural normal mode ID and target ID in general cases by sensing the structural surface skin power spectral density (PSD) of vehicles like a tank or red force pick up truck which is driven by an idling engine PSD. The classification problem is often merely binary:

Hypothesis 1: The target is a Red force¹² vehicle.

Hypothesis 2: The target is a Blue force vehicle.

1.2 Historical Developments and Classical Laser Vibrometry

One of the first examples of Optical Vibrometry is the citing of lightning photography in Lord Rayleigh’s investigation [80, 110] of poles in solutions of acoustic differential equations (DE’s): “Availing himself of Foucault’s method for rendering visible minute optical differences, Töpler succeeded in observing spherical sonorous waves originating in small electric sparks, and their reflection from a plane wall [82]. Subsequently photographic records of similar phenomena have been obtained by Mach [49, 765].” Reports of holographic vibration analysis appear in 1965 [63]. Goodman describes this technique that “. . . may be regarded as a generalization of the multiple – exposure interferometry method to the case of a continuous time exposure of a vibrating object.” [32, 257]

Classical Vibrometry has been used in industry for indications of machine failure (currently termed “health monitoring”). Changes in motor or journal bearings PSD’s

¹¹Spectral elimination / reduction (phase averaging) is discussed in the referenced abstract, pages 1-1, **3-1**, shown in Figure 4.4, discussed in section 4.2.3 on page 4-3, and in the recommendations in the conclusion of [58], pages 6-1 ff.

¹²In general, the ‘Red’ force is the opposing force. The ‘Blue’ forces are our troops.

can indicate imminent breakdown. Before 1980 the typical vibration sensing devices were not unlike miniature seismological devices, microphones with massive inner coils to measure base changes in inertia such as those produced by the BM Manufacturing Company [56, 1843]. In the late 1980's lasers were being used in 'speckle photogrammetry' mode [78] because the speckle due to coherence effects stays mapped with the surface as it moves. Changes in speckle were related to changes in strain.¹³ At the same time (in the middle 1980's) Gerd Binnig and Heinrich Rohrer won the 1986 Nobel Prize in physics for piezoelectric STM [19]. Although the STM piezoelectric crystals were mainly microscope probe tip control mechanisms, piezoelectric technology grew until encompassing both transducer and sensing element technologies (vibration and acoustical). A speculative conclusion could be that attention on this new STM technology may have postponed the extension of laser speckle photogrammetry into analysis of vibration. Systems were already set up in research labs for this purpose at that time “. . . Numerous [heterodyning speckle interferometric] systems have been set up for measurement of displacement, vibration, and strain that are practical and can be applied to routine engineering measurements.” [78, 514, 515]. Massive breakthroughs in STM and other technologies filled the literature and appeared to have subdued this laser speckle interferometry work in favor of the exciting new piezo crystal based nanometer technologies emergent in the late 1980's.

We can assume that a CW laser vibrometry detection mechanism, the change in phase due to vibration deflection shapes, is due to the same mathematical order as the piston term in the expansion of atmospheric turbulence effect on laser beam propagation. *Vibration amplitude may be random but the resonance frequencies are not.* Piston, the change in phase randomly distributed across a large spot size beam

¹³A similar effect, that surface roughness generates speckle, provides a requirement for the Matlab image propagation to add noise to the simulation. This noise generates a closed form spatially “harmonic” image prior to “propagating” the image to the detector such that it displays properly. The speckle seen reflected from shining a laser pointer on any reasonably smooth surface is equivalent. Moving the surface (a shiny text book cover will do) causes the speckle to move. From this simple conference room experiment we can see how straining the surface similarly produces a strained version of the speckle.

profile (cross – section), is an air turbulence effect ignored in this work that will affect both the sensed vibration phase change and the phase noise.

1.3 *Modal Analysis in the vehicle industry*

Structural aspects of target vehicles vibrate in ways that can defeat some forms of laser vibrometry. Understanding of structural modal response can improve laser vibrometry methods. Use of CW as a basis for single pulse or laser Doppler phenomenology can enhance historic (small spot size) mode shape scanning methods. Section 1.3 investigates some vehicle skin vibration basics. It is by no means complete and issues raised receive some elaboration in subsequent chapters as necessary.

1.3.1 Structural Modes. Vibrating surfaces of vehicles have characteristic “Normal Modes” that are a useful identification feature to distinguish models and vehicle types from each other [43,81,83]. Convertibles typically have the lowest fundamental mode frequencies, f_o , of nearly any common vehicle.¹⁴ A major goal in commercial vehicle structural design is to maintain mode separation to reduce the transfer of strain energy from mode to mode. Coupling between modes can lead to more problems than the common transfer of vibration energy down to lower frequency modes – some resonances may become problematically high. Sometimes mass ‘dampers’ are used to absorb energy at certain modes.¹⁵ Some modes are stiffened to move the energy at the prior frequency to a more desired location.¹⁶ Details like these are useful vibrometry identification features of a particular vehicle.

The armored target vehicle under investigation for this thesis will usually have a fairly flat panel facing some direction that is nearly in line with part of an airborne sensor’s flight path. The modes for the un – reinforced rectangular armor panel are

¹⁴Suspension frequencies are often in the 17 to 28 Hz range.

¹⁵Mass “dampers” were used, for example, in some early 1985 GM front wheel drive vehicle exhaust systems to reduce exhaust resonance.

¹⁶Many convertible Corvettes have very high rockers to stiffen the fundamental mode by creating deep beam webs on both sides of the vehicles, thereby increasing a very low f_o often still well below $f_{suspension}$.

a superposition of vibration modes that are sinusoidal in space and time as shown in the FEA results (Figures 21 and 23 through on pages 113ff) and basic structural texts [69, 81].

1.3.2 Physical Model for the FE model. The physical model of the structural component used for the FE model begins with work on an overly lumped mass model.¹⁷ The overall system is geometric nonlinear (contact) as described in the over – simplified sketch in Figure 43 on page 165. This is the model for the mathematical single and two DOF results in Chapter IV. Overall characteristics of the physical model include a large armor plate attached to the slanted side front or side fender area of an armored vehicle. A one inch (1) Homogenous Rolled Armor (HRA) plate is bolted onto a hull.¹⁸ FE model particulars such as “in plane rotations are released at joints” are listed in the FE modelling Appendix B. Page 184 compares the ‘normal mode’ analyses (SOL 103) and some aspects of the nonlinear contact transient analyses (SOL 129) to “hand” calculations using Roark’s formulas [92] for a typical FE model validation.

1.3.3 Low frequency structural modes can be good ID features. Structural vibration analysis techniques in the domain below 400 Hz usually operate on nearly discrete modal frequency responses such the mode lists provided by undamped normal modes analyses which are similar to those used in industry [48]. Compared to these nearly discrete low frequency structural vibration analyses, many signal processing techniques use PSD’s that are continuous in nature. Signal processing PSD analysis techniques can apply to vibrational PSD’s at ‘moderate’ frequencies (greater than 400 Hz). Thankfully, the PSD of lightly damped structures are still nearly discrete towards the entire low end below 400 Hz. This is due to the smaller density of modes

¹⁷This closed form model is intentionally overly simplified to investigate the response characteristics as discussed in many OEM FEA check lists; always perform a very simple analysis of the problem.

¹⁸Values such as $t_{HRA} = 1$ inch do not represent actual structure but are meant to be general, useful values from which vehicle designers and sensors engineers can extrapolate actual response.

at low frequencies.¹⁹ These fundamental frequencies provide a floor at about 20 Hz for vehicle suspensions to over 100 Hz for other structures. Above this floor is where mode coupling can occur. The nonlinear nature of structural systems which allows vibration strain energy to move from high energy modes down to low energy modes appears in the results discussed in item 1 on page 146 and in the damping relations on page 163. However, the impact nature of combustion and clattering parts²⁰ in the engine causes the initial piston engine PSD under consideration to contain sufficient low frequency energy to excite the lower structural modes before nonlinear transfer effects.

1.4 Organization of the thesis

Chapter one (this chapter) outlines the scope of laser vibrometry applied to target ID related and its relation to spectral ID. This introduction describes how existing public NATO laser Doppler data on several military vehicles shows a simple classifier provides adequate target ID based on structural vibration measured by Doppler return for low frequency structural modes in this albeit small sample size study. This is the framework to investigate the CW return from structural modes as a basis for interferometry based structural mode ID on common multi – layer vehicle skin.

Chapter two describes the signal processing model including issues of stationarity and coherence. A description of the structural model defines the terms used to describe the particular forms of multi – layer mode shape symmetry that show up as features in the spectral response. A description of the optical system describes the simulation specifications for modulation and reference imaging to provide the spatially integrated non-imaging classification feature information that is the main objective of this work.

¹⁹Considering that as the main response resonance frequencies decrease, the structural wavelengths for particular resonances increase to approach fundamental wavelengths which are approximately integer ratios of the major dimensions of the vehicle. Hence the mode density is low.

²⁰There are clattering albeit lubricated components (thus undergoing impact on the oil fluid) that ring all modes like the Fourier transform of a sharp delta – like spike impulse.

Chapter three describes optical processing issues. This chapter delineates the image propagation algorithms used for the work.

Chapter four displays the results for all studies. First a theoretical calculation shows a mechanism for spectral reduction seen in a recent prior thesis [58]. Secondly, single and double DOF closed form nonlinear damped oscillators, building on a recent AFIT dissertation [90], model the dynamics of the physical contact and how that affects the structural vibration modes. The modal frequencies either increase or stay constant with contact stiffness depending on their symmetry class (as defined in Chapter two). The results of this section are seen in the contact stiffness study. Thirdly, the results of linear normal modes analysis include displays (Figures 21 and 23 through on pages 113ff) and a list (Table 7 on page 102) of the vibration mode frequencies and mode shapes that random and transient loads excite in the system. Finally, the result from the FEA transient nonlinear contact structural analyses are split into two trade studies. Trade study A uses a set of 30 random loads on the variation of structural contact stiffness. The dynamics and optical results from this study follow the findings of the closed form nonlinear damped oscillators. Trade study B rings the modes with a 3.6 ms impact that provides clear results without the signal averaging required for random response for vehicles with vibration sources of all types. The symmetrical modes show up sharply in trade study B cross spectral covariance (CSC) plots, and do not change frequency with slight load path modifications (trade study A). Non – symmetrical center frequencies were sensitive to minor structural changes.

Chapter five provides a conclusion of the results. This includes a list of considerations for target ID, spectral estimation, structural design, and industrial laser vibrometry use.

II. Simulation Description

The description of the basic coherent interferometric style of remote sensing of vehicle vibration combines theory from structural analysis as well as optical engineering.

2.1 *Signal Processing Objectives*

The signal processing in this work is multi – faceted. The modal analysis of the structure is quite involved yet necessary in order to understand the remote sensing of ordinary vehicle skin vibrations. Modal signal processing in this work does not measure the mode shapes as is customary, but rather involves analysis of the signal and spectra of the direct time integrated contact nonlinear transient finite element analysis (FEA) results and the spectra of the simulated detected returned irradiance. The structural temporal signals distribute spatially over the structure with time delays that vary with frequency, as measured by the structural coherence and sensed by the Cross – Spectral Covariance (CSC) of the detected return irradiance. The laser beam illuminating the target is described by ‘input parameters’ that describe the Gaussian profile beam. The vibration phase modulates this beam producing an exitance that is no longer Gaussian in profile. This modulated signal, spatially and temporally determined by the Matlab simulation, is propagated by more simulation code to the detector where it is mixed (referenced), segmented into detector cells, and sensed in a logarithmic fashion in order to display the phase modulation. All non – imaging metrics used in this work are spatial averages.

2.1.1 Structural v. optical $\Gamma_{cross-spectral}$, CSC, Coh. There are some additional advantages and some disadvantages in using cross – spectral analyses. A look at the rationale for use of structural cross correlation and relationships to cross – spectral analysis in theory and practice provides supporting evidence for use of cross spectral techniques to analyze vibration response. These methods also provide the rationale for calculation of the structural coherence and related MAC values [2].

“the cross – spectrum between the input $x(t)$ and the output $y(t)$, analogous to the cross – correlation function¹ . . . is $G_{xy}(f) = H(f)G_{xx}(f) = |H| \cdot G_{xx}(f)e^{-j2\pi fd/c}$ Hence **the time delay, $\tau_1 = \frac{d}{c}$ appears in the cross – spectrum as a linear phase shift** given from [the magnitude and phase of $G_{xy}(f) = |G_{xy}|e^{-j\theta_{xy}(f)}$] by $\theta_{xy}(f) = 2\pi f\tau_1 = 2\pi f\frac{d}{c}$. **The important advantage of a cross – spectrum analysis over cross – correlation analysis is that the propagation need not be non – dispersive to obtain meaningful results.** Specifically, for a fixed distance d , the propagation velocity c is given as a function of frequency by $c(f) = \frac{2\pi fd}{\theta_{xy}(f)}$ where $\theta_{xy}(f)$ is in radians and is not necessarily a linear function of frequency.

“Correlation analysis has definite advantages over spectral analysis procedures for path identification problems [text refers to a multipath single source problem figure] . . . However, for the source identification problem [the text then refers to a multi – source independent path problem figure] spectral techniques are now [1993] used almost exclusively. Specifically, the analogy to the correlated output (power) relationship [the relation for $G_{xy}(f)$ above] is the coherent output (power) relationship given by $G_{xy}(f) = \gamma_{xy}^2(f)G_{yy}(f)$

“By using the coherence functions $[\gamma_{ij}]$ rather than correlation coefficient functions, the contribution of an input $x(t)$ to the measured output $y(t)$ is expressed as a function of frequency rather than in overall terms only. . . Finally, spectral density functions provide a convenient vehicle to directly estimate properties of single – input physical systems from input/output data which readily extend to multiple – input systems.” [18, 67] Emphasis added.

2.1.2 Spatial and spectral structural coherence. Bendat and Piersol’s text is a structural random vibration text. Their definition of the coherence function [18, 54], $\gamma_{xy}^2(f)$, shown in Equation 1 is what we will refer to as the “structural coherence.” The other variables are defined in the quotation from the same reference on page 15 where $H(f)$ is the transfer function providing the one – sided² output power spectral

¹Bendat and Piersol [18, Eq. 3.71, p. 64] refer to their structural correlation relationship: $R_{xy}(\tau) = \lim_{T \rightarrow \infty} \frac{1}{T} \int_0^T x(t)[|H| \cdot x(t - \frac{d}{c} + \tau) + n(t + \tau)]dt = |H| \cdot R_{xx}(\tau - \frac{d}{c})$ where they use $y(t) = |H| \cdot x(t - \frac{d}{c}) + n(t)$ with a “shock” propagation speed c , propagation distance d , and a simple case where $H(f) = H$ (constant), the noise, n , is independent identically distributed (iid), and the structural medium is non – dispersive.

²This vibration and noise group uses ‘S’ for the two – sided PSD and ‘G’ for the one-sided form that only uses positive frequency.

density (PSD) or “cross – spectrum” $G_{xy}(f)$ for a given input PSD $G_{xx}(f)$. These PSD’s are the Fourier transforms of their respective autocorrelation functions and cross correlation function R_{xx} , R_{yy} , and R_{xy} [18, 50] via the Wiener - Khintchine theorem.

$$\gamma_{xy}^2(f) = \frac{|G_{xy}(f)|^2}{G_{xx}(f)G_{yy}(f)} \quad 0 \leq \gamma_{xy}^2(f) \leq 1 \quad (1)$$

The “cross – spectrum phase” $\theta_{xy}(f)$ defined in the same quotation is a major behind – the – scenes factor in our CSC calculation, a source of variation in the phase of the CSC. Their calculation [18, 95 ff], using a Schwartz inequality method and Fourier transform relationships including cross – spectral phase, results in Equation 2. They also support the observation that the CSC is unity on the diagonal; the spectral variances are all unity for the FEA results and the image propagation simulation accomplished in this thesis.

$$|S_{xy}(f)|^2 \leq S_{xx}(f)S_{yy}(f)|G_{xy}(f)|^2 \leq G_{xx}(f)G_{yy}(f) \quad (2)$$

Although these structural engineers use a γ symbol for the “coherence function,” it more closely resembles the square of the spatial quasi – monochromatic complex coherence factor of statistical optics, $\mu_{12} = \frac{G_{12}(\nu)}{\sqrt{G_{11}(\nu)G_{22}(\nu)}}$ rather than the complex degree of coherence $\gamma_{12}(\tau) = \frac{\Gamma_{12}(\tau)}{\sqrt{\Gamma_{11}(0)\Gamma_{22}(0)}}$ [33, 183,202]. $\Gamma_{12}(\tau)$ is the statistical optics symbol for correlation.

The inequality relationships in Equation 2 are proven for structural vibration stochastics [18, 55,56] where S and G are the two – sided and one – sided cross – spectral density functions respectively. These inequality relationships appear in many domains of engineering including statistical optics, image processing (spatial spectra), and acoustics. Equation 2 indicates the rationale for the limits on the domain of Equation 1.

In an indirect manner, the optical CSC relates to structural measurements called the *cross – acceptance function*, $j_{ik}^2(f)$, shown in Equation 3 where α and β are the locations along the structure [18, 128]. $G_r(f)$ is a reference “auto – spectrum” and L is the length of a beam – like structure.³ In this work the mode shape functions $\phi_k(\nu)$ are the normal mode ‘vectors’ shown in Figures on page and listed in Table on page each with its own characteristic frequency.

$$j_{ik}^2(f) = \frac{1}{L^2 G_r(f)} \int_0^L \int_0^L \phi_i(\alpha) \phi_k(\beta) G_{p_\alpha, p_\beta}(\alpha, \beta, f) d\alpha d\beta \quad (3)$$

While this is a relationship between the spectral response and locations over the continuous structure, those locations respond with various phase lags for all the various modes. The combined set of “acceptances” indicate the response for a given frequency f over the entire structure. This has an indirect effect on the cross – spectral response in that some modes are subdued due to non – acceptance.

2.2 Structural Model

Particular combinations of structural vibration modes are the primary feature meant for detection in this study⁴. The surface vibration is essentially a linear combination of the normal modes. The detected feature that allows for identification of model or vehicle type is a set of modal participation factors (MPF’s) that form the

³The FRAC and SCC [3] are FRF forms of this cross spectral relationship for particular combinations of spectra. The FRAC used in validation of this work is the same as Prof. Randall Allemang’s Synthesis Correlation Coefficient [4] except that input and output spectra are the comparison axes of measured spectra versus the simulated FE model spectra used for most SCC calculations. Parts of these “MAC’s” are similar to the cross – acceptance function of Equation 3.

⁴Modal analysis for target ID is much like spectrometry in this regard. It uses the identification of only the frequencies where there are substantial resonances such as hydrogen having strong ‘Balmer series’ lines at 384, 388, 397, 410, 434, 486, 656.27, and 656.29 nanometers (representing frequencies from 781 down to 457 Tera – Hertz). If we ignore the ‘fine structure’ within even the closely spaced lines, target ID using spectral (modal) ID is much like spectrometry. We can match a vehicle based on the lowest mode frequencies in Hz. For ‘vehicle B’ using laser Doppler on a small spot on a military vehicle in a NATO study, $f_{vehicle} = [8, 28, 34, 40, 56, 68, 76, 86, 88, 116]$ [54]. The applicability of spectral ID to target ID is seen by the identification of these Hydrogen lines red shifted by three degree Kelvin (lower in frequency than the list provided above) even though all the frequencies were different (all with the same shift).

MSC NASTRAN FEA MPF vector, $\vec{\Phi}_i$. These vectors usually model only the modes below 400 Hz. There are usually only about a dozen modes not truncated from the analysis.⁵ These spectral features will move over time; the hundreds – fold DOF $\vec{\Phi}_i$ vector changes (hyper –) “direction” often. Therefore the $\Phi_i \equiv \vec{\Phi}_i$ are a stochastic classification features of this analysis. The modal frequencies (f_i from the eigenvalues $\omega_i^2 = 4\pi^2 f_i^2$) are pseudo – constant deterministic descriptions of the harmonic time evolutions that these random amplitudes ride upon. Φ_i variation is necessarily a result of static indeterminacy of most vehicle structures.⁶ NASTRAN estimates Φ_i results for each mode ‘i’ from linear and nonlinear frequency response analysis [76]. $[\Phi_i] = [\Phi_1 \dots \Phi_i \dots \Phi_m]$ represents a discrete PSD matrix with energy at each of a number of specific frequencies segmented into the different vectors comprising the matrix according to their ‘participation’ at particular modes ‘i’ as described in [48]. While this work does not use the FEA modal participation factors Φ_i directly, they are an integral part of the results and application of the method.

2.2.1 Structural Statistical Stationarity. It is static indeterminacy that creates the unknowable nature of the load path in most non – truss structures. Truss systems are often present in high load structures that are built for a particular function since they are statically determinate. The static indeterminacy of the skin and internal structures in the majority of vehicles is what drives the stationarity period in this CW laser vibrometry detection of structures $T_{stationarity}$ is the length of time that the load path remains sufficiently similar for “locally” stationary spectral ID. A model of this

⁵The physical model is an assumed perfectly manufactured $1 \times \frac{1}{2}$ m, 3 inch thick armor plate on an inch thick armored vehicle hull (details are in subsection B.2.2 on page 180). For this FE model the number of DOF’s is approximately $5 \times 2 \times 286 \approx 3,000$ which is the same number of modes the FEA could generate if automatic truncation to the lower frequency modes did not occur. An automated version of the Lanczos eigenvalue decomposition method in MSC/NASTRAN used in this work selected the first (lowest) 10 modes in the ‘normal modes’ SOL 103 solutions. The nonlinear solution has no mode number restriction since SOL 129 is a direct transient response that integrates time solutions to the 3k DOF DE’s; it effectively uses all the modes, being a non – modal solution sequence (direct versus modal). We have seen that only the first few modal frequencies are enough for ID [43].

⁶Truss structures (landing gear are an example) have sufficient static determinacy to avoid these forms of vibration energy (PSD or PDF) modal frequency fluctuations.

type of statistical variation is the ensemble set for Trade Study B. However, the FEA must be actively manipulated to accomplish this model of physical behavior. Minor fluctuations in physical systems will not appear in the results of the FE model; the FEA will choose a particular hyper – dimensional load path for a particular FE model.

FEA will effectively keep the same load paths⁷ for each analysis because most solution sets decompose the same matrices although they may use different forward solutions by combination of BC’s and other processing. However, the nonlinear analyses actually change the structure of the mesh to the deformed shape at each time step and within each time step. Therefore, nonlinear models represent some minor static indeterminacy, but only for a substantial change in the input loading and BC’s.

What this means is complicated but important for simulation of remotely sensed vibration fields. Unlike linear models, we cannot say that the FEA chose only one load path, or that this FEA load path may or may not be seen in test. Whereas statically indeterminate structures, which the FE model happens to represent exactly, *will* change their load path during each test. Structures in general have the same tendency. There is no standard method to determine the load path changes from time step to time step. Luckily, the HRA plate system FE model is so simple that except for the four attachment bolts there is essentially little opportunity for substantial load path change ignoring the inter – plate contact. Direct transient response analysis deter-

⁷Running the same FE model another time should produce “precisely” the same FEA result. For nonlinear runs seemingly negligible changes in the model can change the time step at which the adaptive system modifies the time step increment value. The ‘movie’ for this thesis is an example of a subtle version of this situation. The images of radiant flux on the detector (Figure 15 on page 107) are from the propagation of the phase modulation from the NASTRAN SOL 129 output of z displacements of the HRA nodes only. A separate NASTRAN run, different only in its selection of all nodes as output for displacement for PATRAN, was aligned in only about half of the time steps, the rest being at most 18 ms apart, hence the name almostSynch01.wmv for this MPEG ‘movie’ which compares the wire frame deformed shapes to the optical detected return. The results were negligibly different when later time steps coalesced; the nonlinear load increment system (not the solution iteration at a given load increment) does integrate in minuscule error within each time step, as does the Newmark – Beta time integration along the time line. There is also a slight error stack – up from load increments. Each load increment iterates the solution and has a Newton’s method iteration convergence before adding some more of the load. A check of the punch file values showed these results for different runs were negligibly different. These negligible error accumulations notwithstanding, the point discussed in the referencing text above stands; running the NASTRAN FEA many times does *not* make an ensemble of detections.

mined that normal modes show up in a slightly modified form in the FEA simulated time history results.

The math shown in the one and two DOF models in subsection 4.3 on page 84 describes how this change occurs. The remote sensing features of interest, the component fundamental modes, do appear to be fully intact in the nonlinear structural model response. Their effect becomes clear after signal decomposition, taking the DFT of the responses for each pixel. This indicates that integrated radiant flux signals sense that these modes participate in the total return. The DFT (Matlab's `fft` function) of the integrated irradiance provides this result, adequately matching structural vibration (described in subsection B.3.1 on page 194) and in the results in Chapter IV). Static indeterminacy that would drive load path changes in a physical measurement does not remove the features of interest in this HRA – hull component system model. variations in FE model load paths create this static indeterminacy for the ensemble of collections in Trade Study B.

Trade study B in this thesis uses 27 bolt configurations⁸ as an ensemble of these FE models to simulate load path variation due to static indeterminacy. For this work these are not fully random variations, but rather a practical set of all combinations of baseline and bolts that are 10% thicker combined with baseline and more configurations that are 15% thicker. Using combinations of all three configurations creates an approximate ensemble with an adequately uniform distribution. The plot showing the spectral response of the SOL 129 displacement results in Figure 36 on page 136 (Fourier transform of the nonlinear direct transient time history results) shows that this pseudo – random ensemble is adequate for use calculating the Cross – Spectral Covariance.

The mechanisms for movement (change) of resonant frequencies due to structural nonlinearities [46] driving change in the components of the modal participation

⁸Three of the thirty sample FE models produced time step variations so far different from the others that they were discarded. The automated FEA time step ‘bi – section’ created time step variations that might have affected the splining operations necessary for spectral estimates with the Matlab `fft` function.

factor matrix of vectors ($[\Phi]$) are partially considered in this analysis. Wandering resonance frequencies are a known result of many nonlinear systems as shown in separate numerical perturbation analysis results [15]. Similar results using ‘control laws’ as the nonlinearities in the structure in closed form [90] for this slapping skin feature (contact between structural surface skin and stiffeners) are found in Appendices D through F. Extension of these ‘control law’ methods to laser vibrometry in these Appendices shows that for appropriately high contact stiffness (as stiff as the underlying base system structure) the nonlinear solution is asymptotically stable and high contact stiffnesses push the antisymmetric modes much higher in frequency while the frequencies of the symmetric modes in this two mode system are uniformly constant. Restriction to two DOF and therefore two modes is sufficient for plate – hull contact due to the loading and geometry. A physical plate will have more modes, an infinite number, but only the lower modes have most of the strain energy. An FE model of a plate will have the number of modes equal to the number of active DOF’s, the number of vectors Φ_i in the matrix $[\Phi]$.

Assume that after impact transients the vibration strain energies for each Φ_i are constant in time, statistically stationary. Assumptions of stochastic stationarity require research subsequent to this thesis to determine the period of stationarity, $T_{stationary}$, the time after which change in the PSD might be noticeable. The FEA results show that the transient responses for the HRA plate system drive the energy to the lowest fundamental component modes, as expected. This is most of the change in $[\Phi]$ we expect to see from contact nonlinearity. The increase in antisymmetric modal frequencies is a direct effect of nonlinear contact as shown in the closed form 2 DOF solutions. These dynamics results also show up in the Fresnel propagated CW optical images and non – imaging full aperture flux.

A primary assumption of trade study B is that $T_{stationary}$ is constant over the entire analysis duration of a fifth of a second, 0.2 s. FEA nonlinear simulation results show that this limited stationarity assumption is valid soon after the transient (Trade Study B) from a structural point of view, but the optical response takes longer to

reach steady state. Input engine PSD's (not used in this work) are not stationary and will have separate $T_{engine}^{stationarity}$ and $T_{response}^{stationarity}$ values. As described in the analytical discussion and deduced from the impact response in trade study B, different engine PSD's still drive the low frequency surface standing wave structural modes since higher frequency modes are "damped out" and driven to lower frequencies through many different physical mechanisms.

Target ID algorithms usually need large $T_{stationarity}$, the response duration that is sufficiently stationary before structurally coherent secondary sources mix with the initial steady state structural response. Algorithms need to detect, recognize / classify within the minimum of all $T_i^{stationarity}$ for a sufficiently complete limited set of useful low frequency modes, 'i.' While this is not a problem with the response to the random load time histories (the more academic random response trade study A), this is an issue for the more practical nonlinear transient response (trade study B) to a structural impulse or impact.

A preliminary suggestion to maintain stationarity is to choose vibration auto – correlation above a certain threshold.⁹ A method to determine the proper value for the vibration autocorrelation is necessary but is out of the scope of this thesis. In this work we assume a full stationarity within the selected response time range selected by inspection of the most stationarity sensitive feature, the image SNR,¹⁰ over time.

2.2.2 Structural Vibration Transfer Functions. The ID phenomenology investigated in this work, CW sensing of structural modes, is not limited to stationary vehicles. The terrain will 'ring the modes' just as Trade Study B results show and identification of the frequency location of a few of the lowest frequency modes is sufficient for target ID [43]. The ATR phenomenology proposed is classical spectral ID in the form of the CSC matrices similar to MAC's used in the modal analysis industry.

⁹For this work assume $\Gamma_{vibration}(t, \tau) = 1$, perfect temporal auto – correlation.

¹⁰Equation 44 on page 98 describes the 'image' SNR plotted in Figures 18 and 19 on pages 110ff.

A common signal processing assumption is that the driving frequency is a major component of the output Power Spectral Density (PSD). This assumption does not directly apply to full structural vehicle systems in general and this signal processing model in particular. Three major reasons show that high frequency vibrations drive low frequency modes due to piston or turbine engines, thus breaking the typical linear transfer function model. This physical minimum energy tendency and the efforts of OEM's to remove noise transmission are reasons to promote identification of structural modes over use of an engine PSD for a classification feature.

First, from a linear system transfer function point of view, piston engines and even turbine engines have signal components that are not harmonic. This is true of piston engines due to their reciprocating components and controlled explosive nature and less intuitively, turbine engine combustion as well; these impacts effectively excite all vibration modes (all available frequencies). Secondly, linear damping ¹¹ spreads out any input PSD, lowering the oscillator 'quality',¹² and thereby increasing the response in the outlier frequencies. By this mechanism, damping systems such as the motor mounts drive both higher and lower frequency modes more than an undamped engine input PSD.

Finally, nonlinearities throughout all the vehicle systems absorb modal energy of a given PSD and return it with different PSD's. Appendix A provides an incomplete list of a couple dozen nonlinear vibration mechanisms found in most all commercial vehicles, and a list of references on the subject. There are many more physical mechanisms by which an input PSD gets modified by nonlinear systems, including complications related to acoustic radiation, transmission, and re – absorption. Table 1 provides a list of different effects these nonlinearities produce.

¹¹Linear damping is actually more rare in nature than generally thought, but assuming damping is linear is adequate for many approximations.

¹²Oscillator quality $Q = \frac{1}{2\gamma} = \frac{\omega_o}{|\Delta\omega|}$ [81, 75] or for EE's $Q = \frac{\omega_o L}{R} = \frac{1}{\omega_o RC}$ where $\Delta\omega = \omega_2 - \omega_1$ is the full width at half power (FWHP) bandwidth.

Table 1: Nonlinear System Frequency Response Effects

1.1	Generation of subharmonics $n_i\omega_o$ above and below $\omega_o, n, i \in \mathcal{Z}^+$
1.2	Movement of response frequencies, including the fundamental frequency, as a function of time.
1.3	Eventual attraction of Vibration strain energy to modes of low potential energy.

Single degree of freedom (DOF) and two DOF nonlinear oscillators have frequency responses due to resonant and damped frequencies ω_o and ω_1 as described below and in subsection 4.3.3 on page 90. The effect of these systems is summarized in a December 2004 AFIT dissertation that provides methods for closed form nonlinear solutions [90]. Course notes at different universities provide insight in to the mechanism for fluctuation in the values of the modal frequencies [6, 15]. Tracking of these frequencies as they move during changes in a structures design is an engineering task named ‘mode tracking.’¹³ There are several theories that address these issues but the methods chosen in this work are basic.

2.2.3 Vehicle properties affected by nonlinearities. Mathematical closed form models allow unique simplifications. Table 2 lists physical structural model characteristics not used in the closed form solutions.

“Transfer Function” definitions the signal processing community would ordinarily expect to see are difficult to find in the literature for full vehicle systems or components. Not only are the shock and vibration response PSD’s working on nearly discrete transfer functions [81, 167], $H_{component}(f) \approx H_{high}(f > 200Hz) + \sum_i^{f < 200Hz} \Phi_i \delta(f - f_i)$,

¹³Mode tracking applies to CW target ID due to the variation in vehicle response within the same model; it is highly likely that one of the first couple dozen modes will ‘cross’ during typical variations. Classical identification of the mode requires viewing of the mode shape, physical pattern matching, which is the main objective of most MAC values. The modal analysis field started in the 1940’s to analyze wing flutter issues. A public example is available in the case study of a computer disk drive manufactured in Ann Arbor in the 1980’s [8, Ch. 35]. Since lower modes have sparsely packed frequencies the spectral ID methods suggested for CW target ID become susceptible to a mode tracking requirement if the ATR algorithm uses too many modes in an attempt to reduce false alarm too far. The laser Doppler identified modes of the military vehicles measured at Redstone Arsenal for NATO [54] were adequately sparse such that mode tracking was not an issue for a simple sigmoid classifier [43].

Table 2: Vehicle system properties effected by nonlinearities

2.1	Modal mass, assumed constant, actually varies a bit.
2.2	Modal stiffness, assumed constant, actually varies a bit.
2.3	Follower forces track differently, they are not statistically stationary.

but with the dimensionality on the order of millions of DOF, the system is highly coupled in space and time. The effect on PSD transfer due to the uneven absorption of strain energy in modes within the input PSD, and mode wander due to nonlinearities, combined with the millions of DOF’s in the system, combine to make transfer functions for vehicles nearly unique, with a much smaller variation within the model.¹⁴ These $H_{component}(f)$ functions, where they have been estimated, are not readily available. From a business point of view, noise and vibration control is a competitive part of vehicle manufacturing, marketing, and litigation. Therefore, much vehicle structural engineering knowledge is proprietary.

2.2.4 Nonlinearities Summary: which apply, which are active. The meaning of “nonlinear” is often not straightforward. This subsection is a short version of Appendix A where the nonlinearities are tabulated and discussed in detail in order to explain some many of the structural assumptions used in this CW simulation. Some signal processing and air turbulence nonlinearity descriptions appear in Sections 2.2 and 2.3. It is far from accurate but sufficient to assume the vibration load PSD applied just beneath the surface on a stiffener or frame is similar to the continuous engine PSD source. Nonlinear system effects which cause modal frequencies to vary efficiently change the PSD. Other nonlinearities are common, including contact slapping of skin on a stiffener between fasteners. Nonlinear FEA vibration analysis includes assumptions that the plate slapping contact has negligible frictional hysteresis and ignores Hertzian impact damping [41, p 20, Sec 2.1.1].

¹⁴While ‘fingerprinting’ a particular vehicle via structural mode spectral ID appears feasible, classification to vehicle model class with ATR, given that OEM engineers can ID a vehicle from the modal frequency list of the first 10 modes, is also available with current technology [43, 54].

Structural nonlinear effects have many forms including material, geometric,¹⁵ large deflection, large strain, follower forces, Joint Friction (structural damping), nonlinear damping, and active or semi – active control. The latter come from the ubiquitous “new” motor mounts (circa 1990) with internal hydraulics, orifices, and check valves. For the effect of simplicity we apply the engine PSD (or power spectral density function, PDF) rather than the skin PSD. Yet, these types of nonlinearities listed above will still effect the response even at locations proximate to the loading mechanisms¹⁶ Appendix A has a discussion of nonlinearities including a list of pertinent nonlinearities affecting system and vibrometry response.

2.2.5 Following load deflection curves: Nyquist is not enough. CSC analysis and convergence of the spectral estimate in general required relatively high frequency resolution, much higher than sampling at the Nyquist rate. This thesis works on two main sets of data. Trade Study A uses a 0.2 second (s) duration pseudo – burst random load time history while Trade Study B uses a 0.2 s duration time history for a 3.6 millisecond (ms) Gaussian shaped time pulse (1.0 FWHH). Trade Study A uses nearly the entire 0.2 s time histories with little waste since nearly the entire 0.2 s is sufficiently stationary. But while the impact load efficiently rings all the modes (no averaging is necessary for the spectra to take form) only two thirds of the Trade study 0.2 s shock response is used in an attempt to avoid using non – stationarity time regions of the damped nonlinear shock response. The sampling frequency for both trade studies, even with NASTRAN’s adaptive time integration step size going up to 200 ms in regions of minor deflection change, was adequate for the vibration modes of interest ranging up to 400 Hz ($T_{400Hz} = 2.5ms$). The splines of the time history data used

¹⁵Geometric nonlinearities include arc length member shortening versus first order perpendicular deflection where the length in the un – deformed direction is only affected by axial loads. A ‘linear’ cantilever stretches more than a nonlinear cantilever due primarily to the geometric assumption of using $\sin \theta \approx \theta$. Basic cantilever deflections being normal to the beam, the beam length in 3 dimensional space is increased by the deflection, which is not a physical reality. But for small deflections, ‘linear’ analysis, this is a negligible effect as long as stresses due to the stretching are ignored (such microscopic axial strain can lead to stress values well over yield).

¹⁶This effect is on the physical model. One type of loading mechanism for the FEA is the large mass method (Figure 46) for driving input for frequency response solution sequences.

the finest sampling (0.2 ms) in order to fulfill DFT uniform time step requirements. Such sampling leads to computer memory problems and subsequent matrix partition coding in an attempt to get spectra with minimal leakage and variance error. Since validation including comparison to the normal modes solutions shows that the proper modes did appear in the transient data, this error appears to be small.

Because the structural FEA must follow the load deflection curve tightly, the time steps are necessarily much smaller than the frequency resolution of the first few modes requires. So the ‘short’ runs at 0.1 second are too short to allow sufficient N – point DFT’s to produce a good spectral estimate with the equipment available today. More increases in the length of the time history data would be useful (which would require more computer resources). The interest in low frequencies (108 Hz) drives the necessity of running the DFT up past $N = 64k$ points for $n = 200$ time step points. As a rough estimate the minimum sampling period for 108 Hz would be $\frac{1}{2 \cdot 108 \text{ Hz}} = 0.00463 \text{ sec} \approx 4.6 \text{ ms}$. But our transient analysis already drives us down to 0.2 ms time steps, thus increasing CPU memory load on the DFT while providing a minimum length of signal. This challenging balance is especially problematic for the strobe method¹⁷ for target classification improvement.

In order to use methods like the Matlab DFT command `fft(signal, number of points)`, the input must be splined data.¹⁸ This DFT requires a uniform time step. The splined data must have the minimum time step in order to pick up the response without substantial FEA error. One could argue that a coarse spline should be sufficient at frequencies below 500 Hz. Considerations of modest isolated error stack up shows use of finer splines is a prudent consideration especially since static nonlinear FEA load increments and time integration do produce a minor cumulative error in the system. Minor errors can accumulate when allowed to interact with one

¹⁷Cyclic averaging [60, 893] and Synchronous Averaging signal enhancement [65, 32] are essentially similar to strobe photography, all methods that might improve classification for this application.

¹⁸Since the DFT transform is a discrete time transform the input is necessarily uniform time step data. Since the splines are more refined than the shortest FEA time step, in combination with the DFT they act like low pass filters.

another (as in a tolerance stack – up). So a frequency bin size at $N = 64k$ for the calculated Nyquist threshold sampling is period is insufficient. The added restriction that the DFT only works efficiently for orders of 2 leaves us to “optimize” the spectra ‘modulo’ 2^p . To estimate the frequency resolution for the resulting DFT using the Fourier scaling property, divide the frequency bin value by the time step size and the number of DFT points, $f_{axis}(f_{bin}) = \frac{f_{bin}(1:\frac{f_{b,max}}{2})}{\Delta t \cdot N}$ where $f_{bin} = f_b$ is the discrete frequency bin number.¹⁹ Subsection B.2.6 on page 192 discusses load increments, iterations, and other aspects of following the (potentially millions of) DOF’s load deflection curves in greater detail.

2.2.6 Anti – Symmetric Modes. Dual Pulse Laser Modulation Vibrometry (DPLM) systems have been susceptible to phase front modulation averaging for large spot sizes, “spatial elimination” or “spatial reduction.” When vibration spatial frequencies (structural wavelengths) are smaller than the spot size, more than one ‘Chladni zone’ can be contained within the spot size. If so, phases of inboard vibration Chladni zones²⁰ can cancel with phases of outboard vibration Chladni zones from an offset location after propagation to the detector. The advent in the future of imaging LADAR may solve this issue. However, non – imaging systems may still be preferable due to cost, mass, and simplicity. Current non – CW narrow beam laser vibrometry systems are sensitive to detection PSD features at particular locations on the vehicle surface but are not able to make the same identification with a wide beam due to phase cancellation.

A symmetric mode is one that has an even number of half wavelengths in x and y, so the contact of the plates has a strong affect on the ‘antisymmetric’ modes. Symmetric modes are mostly unaffected by contact except that compression of the HRA to the hull is more stiff than expansion of the HRA away from the hull. Since this compression is symmetric due to an odd number of half wavelengths along the target

¹⁹For the moment, an unsupported command in Matlab circumvents the necessity of this calculation by automatically transferring the system into a valid spectrum by sensing input sampling.

²⁰Reference Chladni footnotes on pages 184 and 90.

plate, these modes shapes are not affected as much by the nonlinearity of contact. These symmetric modes of vibration are not the ‘symmetrical’ version of the ‘unsymmetrical’ modes described subsection 2.2.7 on page 30, they are merely symmetric in deflection about the $x = 0$ and $y = 0$ axes. So we use ‘antisymmetric’ for an odd number of half antinodes about $x = 0$ and $y = 0$ planes as we use ‘unsymmetrical’ for the concept that penetration into the hull is resisted, the HRA and hull vibrate against each other, unsynchronized (usually by approximately π radians). If there was no contact with the hull, if the HRA was synchronous with the hull at zero phase, an ‘antisymmetric’ mode would be symmetrical about the $z = 0$ axis. This symmetry directly affects laser vibrometry.

2.2.7 Symmetric is not the antonym of un – symmetrical. In order to describe certain physical characteristics of the nonlinear contact vibration responses the terms unsymmetrical and antisymmetric have particular meaning for this work, as shown in the upper panes of Figure 3. In general, throughout this thesis, the term unsymmetrical indicates modes that are not symmetrical about the plane of contact, the $z = 0$ plane. These modes are preferentially excited by the nonlinear contact of the plates since the ‘symmetrical’ (not ‘symmetric’) modes are lower in energy (with lower mode frequencies) than they otherwise would be. The HRA armor in symmetrical modes vibrates with the hull. The unsymmetrical modes vibrate against the hull, in a mirror symmetry about the $z = 0$ plane, as shown in the upper panes of Figure 3.

However, thinking in another dimension, so to speak, the quantity of antinodes in the x and y directions within the plane of the plate is another feature that plates in contact tend to change. Figure 3 shows a comparison of unsymmetrical versus antisymmetric modes in the manner these terms are used in this work. Upper panes a and b assume the mode shapes are symmetric in y to determine that pane b is symmetrical. Antisymmetry merely indicates the existence of nodes of negligible movement inside the plate whereas unsymmetrical indicates there is contact between the HRA and hull.

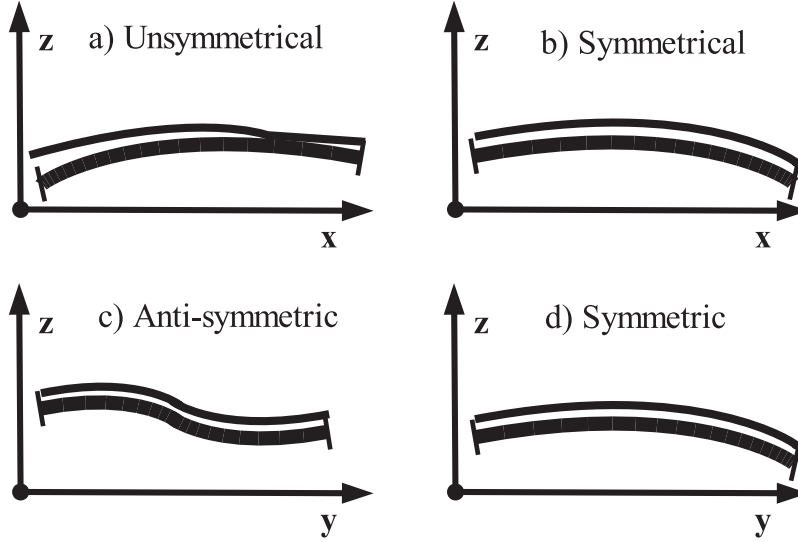


Figure 3: These four plots show slices through the vibrating HRA – hull system at a particular point in time. The HRA is thinner than the hull.

Before analyzing the nonlinear differential equation results for the simplified two DOF model, which shows symmetrical mode frequencies remain constant with increasing gap stiffness,²¹ we can see a different reason why the geometry and physics “favors” the symmetric and symmetrical modes; they are the lower energy modes.

As a gedanken experiment, with one corner of a $L_x \times L_y$ plate, at the origin, set the number of antinodes in the y direction to one so that the deflection shape has one half of a wavelength and is described by a cosine function thusly, $w(y) = w_o \sin(\frac{2\pi ny}{2L_y})$, which we describe as a ‘symmetric’ mode shape for the purposes of this thesis. ‘m’ and ‘n’ describe the 2 – D mode number, (m,n). ‘w’ is the vertical deflection. If there are half waves without mirror symmetry the mode is ‘antisymmetric.’ For example in a system with $w(x) = w_o \cos(\frac{2\pi mx}{2L_x})$ has ‘m’ anti – symmetric anti – nodes. In this

²¹The 2 DOF nonlinear lumped mass model is where the symmetrical and unsymmetrical terms most easily describe the motion of the 2 point model of the hull and HRA plates as if both plates were point masses at $x = 0, y = 0$ and m_{HRA} at $z = \frac{t_{HRA}}{2}$ with m_{hull} at $z = \frac{-t_{hull}}{2}$ where t is the usual structural engineering symbol for thickness. The analogy to plates would include both symmetries discussed above. The high school physics experiments with two masses on springs shows the symmetric and symmetrical (expansion of both springs in unison) as well as antisymmetric and unsymmetrical (‘antisymmetric’ vibration of the masses together and apart without a change in center of mass) one dimensional mode shapes which is the genesis of these symmetry terms.

case the right hand side is inbound while the left hand side is outbound, which is our spatial model of the equivalent antisymmetric mode for one object. If the mode is also unsymmetrical in that dimension the contact fluctuates cyclically, providing a form of stiffening. The contact occurs on both sides alternately and we essentially have an effective two object antisymmetric system π out of phase with each other, a small rotation angularly stopped oscillator.

For unsymmetrical and symmetric modes, while the $x > 0$ side of the homogeneous rolled armor (HRA) is in contact with the hull, the compression produces a moment in the negative y direction resisting the antisymmetric mode. Similarly the $x < 0$ contact produces a moment in positive y . These fluctuating contact induced moments effectively drive the frequency of these antisymmetric modes higher. In part because these modes would have higher energy for the same displacement, they absorb less vibration energy; all other stiffnesses being equal, their deflections will be very small compared to the fundamental modes.

From an optics point of view, if the fundamental modes are of the right size to show up in the detection system (but more susceptible to counterproductive phase wrapping), the higher frequency antisymmetric modes will have less effect on the sensed phase modulations. However, in the case that the fundamental mode amplitudes are so large that they encompass hundreds of cycles and the higher frequency antisymmetric modes start to have deflections approaching a substantial percentage of a wavelength, then a remote sensing system not tuned to fundamental modes will start preferentially picking up those higher frequency modes. This is a form of system nonlinearity related to source vibration amplitude that we assume to be inactive for this work. When the antisymmetric modes have deflections at the size of the optical wavelength, their phase modulated return power should become a large percentage compared to the fundamental mode (which is reasonably capable of being phase unwrapped), but not equal since their effect at the perimeters is smaller. This work assumes small deflections and thus the largest amplitudes are assumed to produce far less than 2π of phase modulation for the purposes of simulation.

Therefore, a CW detection system can tend to preferentially detect some unsymmetrical modes (that cannot penetrate the hull) while retaining the major preference for symmetric modes (that do not produce unmatched moments from contact with the hull). In Figure 36 on page 136 the former is at 220 Hz while the latter symmetrical mode is at 108 Hz.

Phase modulated optical signals (the imaging and non – imaging ‘return’) provide detection features to distinguish between different structures, different models, and different vehicle types. The target structures include tanks, pick up trucks, or other vehicles. Their surface skin vibrations are a major function of the skin stiffness, structural stiffness, and the boundary conditions, as driven by an idling engine PSD. Other vibration sources such as firing of ordinance, pothole impact events, and random terrain loads, or even wind and surrounding noise, are necessary for full characterization of targets in all encounters. Serendipitously, all of these loads usually behave like low power typical random loads with interspersed strong impulses.²² The impact load generated to ‘ring all modes’ in this thesis in trade study B is equivalent to a pothole load. It can represent part of the excitation due to combustion in even a jet engine, and is sufficient to model a typical impact vibration mode test used in the industry. For any of these loading methods, partly due to nonlinear mechanisms of strain energy transfers through the structure, it is mostly the low frequency structural modes that receive the majority of the strain energy. To a lesser extent the broad frequency band of a piston engine PSD driving the structure acts the same way. Even in this work we find the result that the PSD at the source changes as it transfers through the structure as the structural part of this thesis shows.²³

²²Terrain loads are used at the Tank Automotive Command, 11 Mile Road, Warren, Michigan (TACOM) Roberto.P.Garcia@us.army.mil and his contact at GD Land Systems, Steve Meinsche (meinsche@gdls.com).

²³Figure 53 on page 53 shows the PSD for the 2.6 millisecond impulse is far from flat. However, as the discussion in subsection 2.2.1 on page 21 shows, the contact nonlinearity modelled for this one vehicle component (HRA – hull contact for one armor plate) acting alone drives high frequency input energy into lower frequency modes. The hundreds of nonlinear components throughout the vehicle create more harmonics that end up shunting energy into the lower frequency modes.

2.3 General Laser Optics

Simulation of this CW system to measure phase modulation from the target surface is a basis to investigate vibrometry methods. CW is not as susceptible to large spot size spectral reduction (except for metal strips) as dual pulse systems and it is also less sensitive to laser mounting vibration. But CW use will incur a susceptibility to air piston turbulence (see page 51). CW methods require optical processing of the return with a coherent mixing beam that affects the theoretical limits of resolution. This simulation work paints the target with a typical laser beam using the paraxial approximation to the Huygens – Fresnel (H – F) integral [9, 72]. The back – propagation to the detector uses Fresnel diffraction via Fourier transforms in Matlab [21, 426]. While this method is commonplace for closed form imaging [45], Matlab image propagation simulations with Gaussian wavefronts require care with an interaction between spatial grid aliasing and phase wrapping to avoid cycle skipping.²⁴

2.3.1 Existing Laser Doppler of military vehicles. This work analyzes a coherent sensing for direct target ID and as a basis of the double pulse MTI type and Doppler classical laser vibrometry, to understand the phenomenology of each pulse. The existing systems at AFRL SNJ to research vehicle surface deflection detection is a Dual Pulse Laser Modulation (DPLM) system to gauge the speed of vibration of a plate structure, the speed normal to the plate surface. This is a moving target indicator (MTI) and time difference of arrival (TDOA) technique used for laser vibrometry to detect harmonic surface motion. Some research uses CW Doppler for vibration ID. For example, an AFRL spectrogram approach²⁵ using YALO CW system that provided NATO data [54] determined military vehicle structural vibrations. These experiments already studied target classification using actual Doppler data due to vibration through atmosphere including rain. The previous AFIT thesis that measured

²⁴A one – dimensional form of this effect appears in a plot in the reference text [31, p 22 Fig 1.18].

²⁵Extraction of the modulation uses a local oscillator (LO) mix similar to the reference beam simulated for this thesis. The NATO study measures the vibrational frequency using Doppler shifts in the Tera – Hertz range [54, 43,44]. The signal modulation in this thesis is a form of FM, specifically it is PM by the target.

spectral reduction used a laser Doppler System [58]. Unfortunately for use in small aerial vehicles (AV's) and other applications, these are necessarily small spot size systems that require sophisticated tracking systems²⁶ and a very stable base, whereas a CW system can merely paint the entire vehicle (cover the vehicle with a spot size just larger than the vehicle)²⁷ and is less susceptible to mount vibration (page 157). Although the Doppler frequency shift available is in an easy to detect 100 MHz range for some laser systems,²⁸ this work investigates methods in order to form a base of understanding of the interaction between the phase modulation systems involved for large spot size system. Starting from 'first principles' helps avoid missing some of the necessary physics. The mechanical engineering mathematical considerations for the vibrations at the surface, considering their source, are often similar to the mathematical considerations of the laser propagation and signal processing involved in detecting these vibrations; both modal analysis and remote sensing work using spectral estimation,²⁹ assuming stationarity, sufficient frequency (spectral) resolution, control of aliasing, and sufficient sample size.

2.3.2 Non – random laser vib. & adaptive classifiers. ASCII text values for surface vibrations from simulation using MSC NASTRAN are the input for the Matlab scripts to determine single pulse laser modulation (CW) response. Modal response analysis compares cross – correlation “signatures” that relate to various structural vibration modes. FEA provides adequate simulation of low frequency (FRF(f) for

²⁶“There will always be a need for a good target tracking system along with narrow beam LADAR to make sure that the laser beam hits the same spot of the vehicle during the measurement interval. However, this is very difficult and if a moving target is being tracked, the beam will move . . .” [54, 17] We remove the “same spot” constraint by using large spot size CW.

²⁷Such large spot coverage would have clutter in the pipe, the area of transmission and imaging. This method assumes techniques to process such clutter rejection are adequate in enough cases to warrant its use.

²⁸For a $3\mu\text{m}$ laser the classical Doppler shift [88, 505-506], $\gamma = 1$ is $\omega = \gamma\omega'(1 + \beta \cos \theta')$ $\approx \omega'(1 + \beta \cos \theta')$, for observer angle $\theta' = 0$ (head – on velocity), with a Mach one speed, we get $\beta = \frac{V}{c} = \frac{334\text{m/s}}{3 \times 10^8\text{m/s}} \approx 10^{-6}$ so laser frequency $\nu_{\lambda=3\mu\text{m}} = \frac{3 \times 10^8\text{m/s}}{3 \times 10^{-6}\text{m}} = 10^{14}$ Hz gives Doppler shifts near 100 MHz.

²⁹Spectral estimation includes many techniques including filtering, windows, and parametric (ARMA) [48, 54] and MUSIC and ESPRIT [86] as opposed to the preliminary investigations use unbiased but inconsistent spectral estimates, Periodograms, as we do here.

$f < 500$ Hz) structural mode detection. A major focus of this thesis is the low frequency modes. The vehicle “noise and vibration” field usually assumes most of the energy from most types of impulse or other forcing PSD’s end up in these low frequency modes upon reaching ‘steady state.’ Idling engines drive much of their energy into these modes, the largest displacement modes of the vehicle structure such as hood and fender full panel diaphragm modes.

Laser vibrometry can give some indication of the quantitative nature of energy transfer from input engine PSD’s to “output” vibrational PSD’s that are detected, in this case, by CW laser vibrometry. While direct acoustic excitation of a truck hood may provide a large engine PSD component to the detected surface, we assume that the vehicle engineers or defense contractors have done their job handling noise and vibration. We expect the engine PSD energy has been appropriately dampened (dissipated) and spread to surrounding ‘normal modes’, mostly those below 400 Hz. We seek to identify the structure based merely on its characteristic low structural mode frequencies. The long term intent of studying FEA for laser vibrometry is that FE models used in industry and in the defense industry for structural vibration certification can provide the Department of Defense (DoD) reference information that indicates the nature of laser modulation from the surface of targets driven by various input PSD states.

2.3.3 Test Equipment Specifications. The original equipment used at AFR-L/SN per the Dierking Report [28] was a DPLM system, the “Multifunction Ladar Integration and Demonstration” Coherent Technologies system. The specifications for this system include power of 0.5 to 2.5 W, PRF or PRR of 1 to 1.2 kHz, IPP of 40 to 1000 μsec , pulse widths of 7 to 12 ns, operating at 2.091 μm , operated in the doublet mode selection. The AFIT work of Flight Lt. Pepela used a Doppler laser.

For the calculations in this work we use the same nominal laser power of 1 Watt as the DPLM system provided during the AFRL / SNJ experiments. The radiometry calculations derive from the use of Fresnel diffraction (propagation) of the

beam [27, 38,56]. The return from the target is from reflection and thus the typical signal loss radiometry applies to the return. The optical sensing of vibrations on the assumed specular surfaces undergoes a phase change of twice the deflection in wavelengths (not including the reflection phase change) as shown in Figure 7. The reference beam profile is equivalent in power to the Gaussian laser beam travelling twice the distance L. The ‘sensing’ beam propagates L meters in a Gaussian profile via the H – F integral using the paraxial approximations and then reflects back to the detector after modulation. The detector system mixes the sensed image with a percentage of the reference beam. The reference factor (A Matlab simulation variable) is a parameter that causes the factored reference beam to have the same power over the detector array as the return.

2.3.4 Quadratic phase, Matlab modulation diagnostics. Test images in the Matlab code show the illuminating quadratic phase beam and its modulation of simple diagnostic vibration mode shapes (Figures 5 through 6 on pages 44 through 45). Further analysis and section plots of these data provided validation through the use of optical response relations like Equation 6. Modulation of this laser beam at the target by the vibrating surface is a function of location but the assumed turbulence free propagation is space invariant. Since the Amplitude Spread Function [33, 298] is space invariant, the “4 – dimensional Fourier transform linear systems approach” is appropriate for analysis of a partially coherent version of this system [33, 313]. However, the small bandwidth and very large coherence time and coherence lengths allow use of Fourier transform methods for propagation with Fresnel diffraction. The Fresnel approximation in Equation 5 assumes a “quadratic phase” in the aperture where r_{ao} is the distance from a point in the aperture plane (x_a, y_a) to a point in the simulated observation plane (x_o, y_o) . ‘z’ is the normal distance between the planes. $k = 2\pi/\bar{\lambda}_{laser}$ is the wave number for the laser at its center wavelength, $\bar{\lambda} = \lambda_o$.

$$r_{ao} = \sqrt{z^2 + (x_o - x_a)^2 + (y_o - y_a)^2} = z \sqrt{1 + \left(\frac{x_o - x_a}{z}\right)^2 + \left(\frac{y_o - y_a}{z}\right)^2} \quad (4)$$

$$r_{ao} \simeq z \left[1 + \frac{1}{2} \left(\frac{x_o - x_a}{z}\right)^2 + \frac{1}{2} \left(\frac{y_o - y_a}{z}\right)^2 \right] \quad (5)$$

$$h(r_a, r_o) \simeq \frac{e^{jkz}}{j\lambda_o z} \exp \left[j \frac{k}{2z} [(x_o - x_a)^2 + (y_o - y_a)^2] \right] \quad (6)$$

This impulse response or weighting function in Equation 6 has a phase that is a circle or ellipse in the cross – sectional phase, a spherical wavefront [32, 59 ff]. Therefore, the “observed field strength . . . can be found from a Fourier transform of the product of the aperture distribution . . . with a quadratic phase function $e^{j\frac{k}{2z}[x_a^2 + y_a^2]}$ ” [32, 61]. This assumption compares to the “stronger” Fraunhofer approximation where the phase is “flat” in the aperture because we are even further from the source using even smaller angles, $z \gg k[x_a^2 + y_a^2]_{max}/2$.



Figure 4: (a) The Fresnel approximation of quadratic phase assumes a spherical wave at the aperture whereas (b) the “more stringent” Fraunhofer criterion assumes a constant phase at the aperture, a more distant and / or smaller image.

Assuming far field remote sensing, the written analysis will use the Fresnel approximation. However, a Matlab image propagation function coded for this work actually assumes a more stringent Fraunhofer condition at the aperture; simulation of detector optics drives this limit due to the focusing property of the camera lens. Estimates of phase front modulation using simple low order symmetric test ‘vibrations’ are thereby straightforward to identify in this work’s Matlab simulation.

2.3.5 Limits of Resolution. The optical model used for the CW simulation in this work is well within coherent transfer function (CTF) considerations, which is appropriate due to the coherent nature of this system. This CTF calculation appears just before the beam mixing subsection 2.3.10 on page 43. Nevertheless, a more basic check using a crude estimate for an optical transfer function (OTF), a triangle function centered on the spatial frequency origin, provides an estimate of image sampling for this CW laser vibrometry system. Setting the image spatial sampling frequency, $f_{sampling}^{spatial}$, to twice the estimated spatial cutoff frequency, $f_{cutoff}^{spatial}$ sets the minimum FE model mesh density for useful simulation. D_{op} is the diameter of the optic. λ_o is the mean (center) wavelength of the laser. f_{length} is the effective optical focal length.

$$f_{sampling}^{spatial} = \frac{D_{op}}{\lambda_o z} \geq 2f_{cutoff}^{spatial} = \frac{2D_{op}}{\lambda_o f_{length}} \quad (7)$$

Since $\lambda_o = 10\mu m$, $D_{op} = 40mm$, and $z = 4km$, then $f_{min}^{mesh} = \frac{1}{50cm} = 2m^{-1}$ is the minimum FE Model surface mesh spatial frequency (density). The target grid has 250 elements per 50 cm, a cell pitch of 2 mm. The minimum spatial frequency used for the target grid (the Matlab simulation for this work) is $f_{min}^{FEmodel} = \frac{1}{50cm/250} = 500m^{-1}$ which is appropriately greater than the required spatial frequency, f_{min}^{mesh} .

2.3.6 Surface Roughness effects, speckle generation. The major signal noise in this laser vibrometry system is speckle for which characterization related to surface roughness is well understood [45]. Modification of the main Matlab script using surface roughness of one micrometer introduces intricate interference patterns including azimuthal symmetry of dark fringes.³⁰ While information on paint surface roughness is difficult to come by, metal finishing surface roughness is a very mature field. The American national standard surface texture ANSI B46.1-1985 governs definitions of surface roughness as described in the Mechanical Engineer's reference book, the *Ma-*

³⁰Use of long wavelengths in the simulation mitigates the phase wrapping producing these fringes. In measurement systems the target is continuous so the interaction of phase wrapping with aliasing is overcome.

chinery's Handbook [53, 667], and in [14, 13-75], by James A. Broadston (author of the ANSI standards).

The surface roughness definition industry is replete with drawing symbols for various tool mark residues, average roughnesses, and different methods to measure and define different types of surface roughness. A few tables show ‘average’ values (customary mean values) of roughness [14, Table 13.5.3] and “Preferred series Roughness Average Values, (R_a)” [53, Table 1, p. 676]. The latter reference has many sketches detailing the terminology of sampling length, maximum waviness, cutoff, et cetera as well as Fig. 5 page 672 which shows the range of average roughness for 30 machinery finishing practices. These tables show that a surface roughness of one micron (40 micro inch) is a listed surface roughness for bare steel, but 0.80 microns is ‘preferred.’

So while the roughnesses that can produce intricate coherent image effects are very smooth, they are common machine tolerances as well. The Matlab scripts in this work used a 0.05 micron finish since the maximum deflection was within $w_{max} = 78.8\mu m$. The representation in the code is as a ‘roughness’ coefficient of the speckle noise representing 0.063 % of the maximum deflection easily modified for trade studies. Use of a Gaussian distribution of random phase with respect to incoming intensity is a common practice [38, 313]. The number of speckles (of intensity) produced by such a phase relationship is usually considered to be a negative binomial distribution of the pixel cell intensity, which simplifies to a Poisson distribution in the case of uniform intensity profile or averaged assumptions in non – imaging (total) intensity partition law calculations [29, 138]. Since this simulation builds the phase directly, not a speckle count, the Matlab simulation uses random phase to build images of the speckle noise.

2.3.7 Speckle noise – Considerations for CW lab use. Image processing in this work necessarily considers speckle noise, which is a multiplicative noise. Such a phase noise system is better imaged by using the log of the irradiance ($\ln(E_e(t))$),

where the irradiance $E_e(t)$ is the spatially integrated radiant flux). Since this noise represents the surface roughness, it appears in the argument of a harmonic, equivalently in the imaginary exponent of an Euler representation of an analytic signal. This phase noise is additive with the vibration signal but multiplicative with the phase modulation of the signal. This nature of the noise has a few features that require attention for laboratory use of CW.³¹

An investigation into logarithmic transformation of image irradiance ($E_e(x, y; t)$ in W/cm^2) with speckle noise [12] derives methods that transform the necessarily multiplicative speckle noise into an additive noise by taking the logarithm of the image irradiance.³² Referring to a previous paper [47] an observation on signal to noise ratio (SNR) matches that found in our simulation. The obvious result and sanity check is that the SNR is one (1.0) for multiplicative noise since $|e^{i(\phi_{signal} + \phi_{noise})}| = |U_{signal}U_{noise}/U_{signal}| = 1$. Additionally, “They showed that the spatial frequency power spectrum of the noise intensity is independent of the object, except for a multiplicative factor equal to the total [image] power in the object, which means that the speckle noise in this case is multiplicative signal – dependent noise, and that the signal – to – noise ratio in the image is equal to unity.” [12] Their main result is that the log of the noise approaches a Gaussian distribution faster than the multiplicative (direct) irradiance noise.³³

Since the simulation in this work assigns a speckle, such distribution is not an issue. However, the output images, “logarithmically transformed” (to use Arsenault’s term), image the deformation shape much better than other methods. The extent of the improvement is so large as to make measurement of a per – pixel SNR for these CW methods irrelevant. Additionally, “. . . the response of the human visual system

³¹While Coherent Imaging (CW in this form) is an old field of optical engineering, this ‘new’ use, apparently regressive compared to the expectations for DPLM, requires a visit to coherent imaging issues passed over in favor of DPLM.

³²These algorithms for modification of photographic images are applicable to pixel by pixel application as accomplished with Matlab in current digital technology.

³³Their convergence is based on (photographic paper) grain count whereas present technology would use a pixel count statistical measure of the (surface roughness) noise. [12]

is approximately linear in log intensity, . . .” [12, 1160]. Therefore, use of the log of the irradiance is appropriate for this simulation.

2.3.8 Target Grid Aliases Quadratic Phase Wrapping. Phase comparison images can help in understanding of the modification of the phase due to the deformed shape of the vibrating surface. These images compare the phase alone, “quadratic phase,” versus modulated phase of the Gaussian beam wavefront in a flat plane normal to the direction of propagation. The modulated Gaussian profile irradiance results in rectangular grid patterns of circles of phase wrapping, which are due to the non-linearly increasing aliasing – an effect of quadratic phase (phase squared grows at an increasing rate). This ever increasing phase change interacts with the target grid spatial aliasing to make the images numerically intractable for computation of the modes they represent. While some form of stochastic pattern recognition should work, such classification techniques are out of the scope of this thesis. This simulation avoids these issues by using a $\lambda_o = 10\mu m$ laser.

2.3.9 Optical mixing, noise and resolution. In the physical optical model the Gaussian beam incident on the target radiates back to the detector where, as shown in Figure 2 on page 8, the irradiance from the target mixes with a scaled portion of the original laser assumed to still be coherent with the irradiation incident on the detector. The coherence assumption is the result of derivations, calculations, and assumptions based on medical technology results in an SNR improvement paper [20]. The range of mixing proportions for a scale on the reference beam that adequately enhances the phase information from the vibration modulated assumed specular coherent image return from the target is large, two orders of magnitude.

Reduction in reference beam radiant flux Φ_{ref} represents losses due to propagation over $2L$ (8 km in this case). The phase of the detected electric field $E(x, y; t)$ includes representation of most of the phase modulation at the target. Assume some optical system is available that does reduce the mixing to this level without drasti-

cally affect the cross – sectional mutual coherence of the reference beam.³⁴ Once the power of the returned and reference beams are matched, mixing effectiveness depends on the joint coherence of the two beams. In order to maintain coherence with the reference beam to the return over the 8 km round trip path, the coherence time must be $\tau_{coh} = \frac{8 \times 10^3 m}{3 \times 10^8 m/s} = \frac{8}{3} \times 10^{-5} \approx 26.7 \mu s$.

2.3.10 Phase modulation retrieval: Reference Mixing. The Matlab simulation model starts out with mixing beam integrated radiant flux, $\Phi_{mix}(x, y)$, and the radiant flux return from the target that creates the image, $\Phi_{modulated}(x, y); t$, matched to the same value of power.³⁵ Since the main objective of this work is to identify structural vibration modes, identification of shapes is key. The images in Figures 5 through 6 show that mixing ratios, $[\overline{\Phi}_{mix}/\overline{\Phi}_{modulated}]$, from 0.01 to 100.0 provide adequate pattern matching conditions while ratios between 0.1 and 10.0 provide essentially the same maximum classification capability from images of a higher order mode (normal mode frequency above 400 Hz) with simply supported edge vibrations (a full structural cycle along the short edge and half a cycle on the long edge). It is the registration of the test mode shape (1×2 here) that is important, more important than magnitudes since modal analysis needs to match shapes first. Without proper shape representation the imaged return would be invalid. A higher frequency mode is more difficult to classify from a poorly mixed image. Therefore, this is a conservative measure of mixing range considering the more important modes for this work to detect are the lowest frequency modes.³⁶

While the phase does become additive enough for spectral ID after taking the logarithm, it is far easier to prove the *field* phase separates in an additive manner. For example, assume a laser has an initial electric field of $A_L e^{j\psi_2}$ with a phase pro-

³⁴Avoid transmission through anything acting like a moving ground glass diffuser [33, 151].

³⁵Typical values of radiant flux return range from tens to hundreds of milliWatts shown in the Matlab script logs for each different Matlab image propagation configuration result.

³⁶These fundamental component and other low frequency modes are more important because they contain more strain energy (producing more deflection) and they are less susceptible to spectral reduction than higher frequency modes.

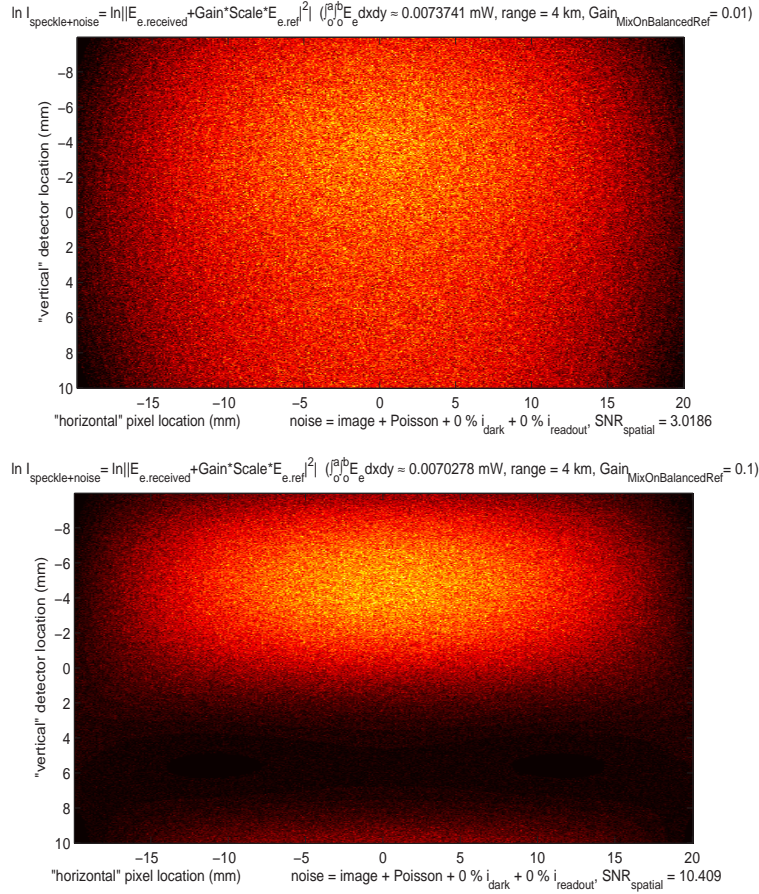


Figure 5: Target return mixes with a mutually coherent portion of irradiance. After the Matlab script matches the radiant flux over the detector of the target image and the beam split reference beam, the reference beam receives a further irradiance gain of 1 % (upper, barely resolved) 10 % (lower pane).

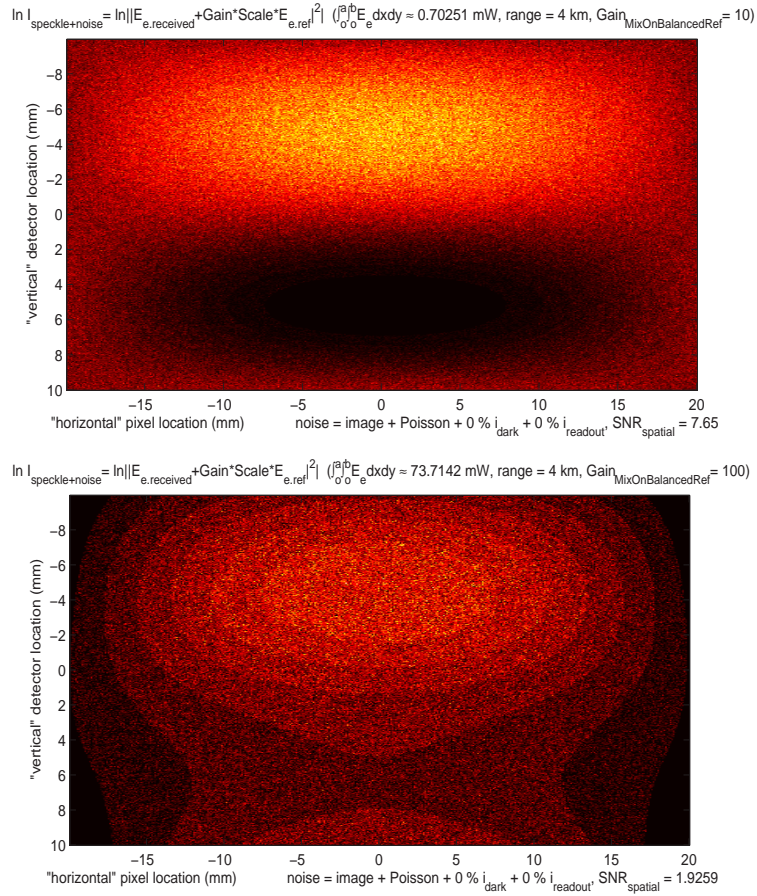


Figure 6: Target return mixes with a mutually coherent portion of irradiance. After the Matlab script matches the radiant flux over the detector of the target image and the beam split reference beam, the reference beam receives a further irradiance gain of 1,000 % (upper pane) 10,000 % (lower, barely resolved).

file of $\psi_2(x, y)$ just before the target at range L . The target vibration deflection, $w(x, y)$, produces a phase change at one point of $\psi_1(x, y)$ assuming full stationarity. The beam wave vector, \mathbf{k} is in this case approximately parallel to the plate vertical z deflection, $w(x, y)$, which is a linear superposition of vibration modes, $w(x, y) = \sum_{m=1}^M \sum_{n=1}^N w_{m,n}(x, y)$. The resulting phase is $\psi_1(x, y) = j \frac{2\pi}{\lambda} 2w(x, y)$. The laser beam field $A_L e^{j\psi_2}$ is incident normal to a target with vibration $\frac{\psi_1^{max}}{2} e^{j\mathbf{k}_r \cdot \mathbf{r}} e^{j2\pi f_{m,n} t} e^{\frac{-t}{T_{stationarity}}}$ as described in Equation 17 on page 58. Indices ‘m’ and ‘n’ are the number of spatial half cycles in the x and y directions, respectively, for a particular mode defined as mode (m, n) . The time fluctuation provides identification of structural modes by their frequencies $f_{m,n}$, but to see the effect of proper laser image mixing we drop the time modulation and assume temporal stationarity in order to see the effect of the mode shapes, $\psi_1^{m,n}(x, y; f_{m,n})$. Since the phase change is twice the vibration amplitude, the resulting modulated image is a propagated form of the field just after the target, $A_m e^{j(\psi_1 + \psi_2)}$. Scaled in amplitude to match the Gaussian beam propagated by a distance of $2L$, $A_{ref} \approx \frac{A_L}{2L}$, the reference beam will have the same field value (in V/m) as the imaged field from the target. Even though the laser beam does not change in time, a more difficult task is to match the negative of its phase front, ψ_2 , with an approximation $\psi_2'(x, y) \approx -\psi_2(x, y)$ for the reference beam.

Since the reference beam $A_{ref} e^{j(\psi_2')} \approx A_{ref} e^{j(-\psi_2)}$ is assumed to match the detected image $A_{det} \approx \frac{A_L}{2L} e^{j(\psi_1 + \psi_2)}$, the sensed field $E_{det} \approx A_{det} e^{j(\psi_1 + \psi_2)} + A_{ref} e^{j(\psi_2')}$ becomes $E_{det} = A_{det} e^{j(\psi_1 + \psi_2) + \psi_2'} \approx A_{det} e^{j\psi_1}$. The logarithm of the resulting detected referenced field $\ln(E_{referenced}) \approx \psi_1 + \ln(A_{det})$ is a field modulated spatially with essentially the same pattern as the vibration pattern on the target. The logarithm of the intensity is more complicated. The rationale for analyzing the phase of the field is that the simulation provided the field for use in model checks and validation plots not reproduced herein. Field phase is easy for simulation but other available methods are necessary to extract phase from the intensity sensed by actual fielded detector.

Table 3: Assumptions of the Optical Physical Model

Item	Description
3.1	Long wavelength, $\lambda_{sim} = 10\mu m$, in lieu of smaller λ_{laser} reproduces essentially the same physics.
3.2	Large range (4 km) smoothes out the Gaussian phase front yet provides essentially the same physics.
3.3	Reduced displacements, below half λ_{sim} . Small deflection avoids phase wrapping from vibration.
3.4	Assumption that the target is a poor emitter (and, therefore, a near – perfect reflector).

2.4 Optical Physical Model Overview

While similar issues are nuisances for physical systems, the simulation must avoid a particularly tantalizing and pernicious combination of phase wrapping and aliasing. Several modifications to the physical model keep the Matlab optics simulation within the realm of useful coherent imaging.³⁷

These assumptions reduce the combined effect of phase wrapping and aliasing in the Matlab simulation output which would produce non – analytical images.³⁸ This is a simulation effect due to target grid sampling that a good CW system in the field can deal with. Phase wrapped aliased images with cycle skipping (a two – dimensional form of similar communications issues [31, 22]) still appear to model the target deflections. The development of pattern recognition algorithms for Automated Target Recognition (ATR) for these patterns would be challenging. These patterns have a nonlinear relationship between the quadratic phase (the phase change is a quadratic function of the vibration amplitude due to beam profile) and the Matlab simulation grid sampling related aliasing. There may be a data processing system of pattern matching that can use these rectangular grids of phase wrapping circles [42]

³⁷The imaging simulation is necessary for non – imaging results to ensure propagation and mixing effects are properly allocated. The non – imaging results are spatially integrated across the detector surface after propagation and mixing as would be the case with an actual non – imaging sensor.

³⁸Non – analytical in this sense means the images that appear to model the target can have enough aliasing in the nonlinear phase wrapping (Gaussian \Rightarrow quadratic phase) that unwrapping of phase is impossible because of nonlinear loss of information (cycle skipping).

in the resulting images. However, the assumptions of Table 3 allow for results that are accessible in a straightforward analytical appraisal.

This work uses a reflectivity of one, a perfect reflector. If a physical system has reflectivity in a manner that defeats a particular structural mode (a potential countermeasure to CW) the system would have to perform its eigenvector match (probably with Principle Component Analysis, Karhunen – Louve theory) on more spectral peaks analyzing wider bandwidth. Yet adequate clustering of the data with only a few modes is reasonable. Corrupting one mode (effectively all that a countermeasure paint could provide) would be a negligible effect on classification performance. An overly simple sigmoid classifier [43], developed to show system performance bounds, worked well on actual laser Doppler data [54]. Even with one corrupt mode the system still lies in the upper left quadrant of the receiver operating characteristic (ROC) curve, P_d over 80 % with P_{fa} under 15 % (see page 5).

The return³⁹ in the Matlab simulations for this work assumes total reflectivity. Since results use reflectivity of one (1.0) the user may need to adjust methods for their own situation if absolute flux values are important. This simulation is mildly anti – conservative in this regard. Considerations of signal to noise ratios after referencing (mixing return with the reference beam), propagation, and detection of the beams are not a part of this work. Error due to mode mismatch from the current and future use of the Matlab code appears negligible as seen in subsection 2.3.10 on page 43.⁴⁰ Therefore, this work serves as a basis for modal detection of vehicle surface skin vibration modes characteristic to their vehicle type under the stated ideal laser imaging conditions.

³⁹The term ‘return’ represents the returning irradiance, $E_e(W/cm^2)$, the radiant flux in Watts, $\Phi_e(t) = \int E_e(x, y; t) dx dy$, or the modulated electric field E in V/m or Newtons per Coulomb.

⁴⁰The Matlab scripts use slightly modified versions of Fresnel propagation scripts [24].

III. Chapter 3: Structural Vibration Modulated Laser Beam Response

The object / target modulation of the illuminating laser beam creates an return image that no longer has a Gaussian profile. Therefore numerical propagation back to the detector cannot use the laser beam parameter method used in this chapter to determine the phase front at the target. Equation 22 shows numerical diffraction is necessary because the object is no longer Gaussian in profile. This is the final result of optics analysis in the middle of this Chapter. A plane wave solution¹ shows a theoretical basis for the spectral reduction measured in an earlier AFIT laser Doppler vibrometry thesis [58]. The end result is not just a description of the detected vibration by laser probed optical return, but an analysis of the dynamics of the signal and how fluctuations in the optical energy (radiant flux, $\Phi_e(t)$) indicate vibration modes that modulated the reflection. Since most optical analysis methods assume stationarity, this chapter has a short stationarity study including analysis modifications to attain sufficiently stationary signals. The structural modal analysis industry has been analyzing nonstationary signals for decades [87]. A quick look at structural modal analysis methods (of the stationary kind) and how they relate to some optical spectral analysis techniques provides the integrating influence that wraps the optical results in the regime of target detection, recognition, and ID with an eye toward the introduction of these CW methods for vehicle classification.

3.1 *Non – Diffraction Beam Modulation Optics*

Several considerations of the phase modulated return from the laser beam irradiated target are not *directly* related to the propagation of the beam.

3.1.1 Cross – Spectral Covariance (CSC). The CSC plots show a pattern that relates to the phase relationship between spectral bands. This familiar pattern

¹This plane wave solution portion was submitted to Applied Optics in March 2006 as a separate paper.

seen in other structural modal analysis matrices such as the frequency domain acceptance criterion (FDAC) has a major structure segmented by phase changes at resonances or spectral peaks. References [2, 3, 23, 59, 60] describe some historical significance in the modal analysis industry of CSC type calculations, how they relate to other modal acceptance criteria such as the FDAC [57]. The auto – FDAC is similar to the ‘structural’ CSC used in this work. The history provides insight into why laser vibrometry started mostly using point location tracked spotting.

Spectral covariance provides a measure of temporal correlation between frequency components (u or v) rather than the power at any one frequency. The Cross – Spectral out-of-plane spatial covariance, $CSC \equiv C(f_u, f_v)$ in Equation 8, provides a measure of the coupling in time between vibration modes through the phase relationship effect of at least two mechanisms, (1) nonlinear contact mode effects and (2) multipath acoustics and load path loops. In the relations derived in this Chapter continuous spectral quantities $F(u) = F[k]$ and $F(v) = F[k]$ represent the discrete response spectra of either the structural vibration ($F[k] = \sum_{j=1}^N \Delta z(x, y; t) (e^{-2\pi i/N})^{(j-1)(k-1)}$) or optical return ($F[k] = \sum_{j=1}^N \Phi_e(t) (e^{-2\pi i/N})^{(j-1)(k-1)}$). These discrete forms are the language of the discrete Matlab ‘fft’ formulation used in this simulation.² These CSC’s compare phase relationships of particular response bands with other bands ‘cross – spectrally.’ $E[...]$ is the ensemble average over either random load instances or load paths for trade study A or trade study B respectively. Multipath generated covariance should be related to vibration strain energy path lengths through all vehicle components into the vehicle skin for major sources such as engine vibration.

$$C(u, v) = \frac{E \left[\left(F(u) - E[F(u)] \right) \left(F(v) - E[F(v)] \right)^* \right]}{\sqrt{E \left[\left(F(u) - E[F(u)] \right) \left(F(u) - E[F(u)] \right)^* \right] E \left[\left(F(v) - E[F(v)] \right) \left(F(v) - E[F(v)] \right)^* \right]}} \quad (8)$$

²The cross-CSC in Equation 46 on page 133 uses both spectra to investigate the phase relationship between object (vibration) and image (optical radiant flux $\Phi_e(t)$) shown in Figure 34 on page 132.

The cross covariance calculation in Equation 8 can use the ensemble averages of equivalent surface normal speed data (derived from laser return by the vendors' software [28, 54]) or the deflection data from MSC/NASTRAN FEA results as done in this simulation. Temporal correlation of this vibration field data is related to measurement of the frequency modulation (FM) and in this case, Phase Modulation (PM) for laser vibrometry. This paper will discuss methods for remote determination of the vibration field on the vehicle. Considering the mode shapes these vibrations excite, the spatial phase relationships provide a superimposed slant to the radiated wavefront akin to electronic steering in radar or acoustic arrays. So the full effect includes more than first order phase modulation, piston. Therefore, the optical phenomenology for the microscopic model for a particular point on the target, purely piston phase change, is more complicated for non – imaging return.

Piston is often affected by the speed of travel of the supporting platform of the proposed target ID system (an aircraft pod, for example). So while CW would remove the time of flight sensitivity of DPLM systems, there is a platform sensitivity related to the integration time required for sensing low frequency structural vibration. There are methods to remove superfluous phase readings from piston related phase changes including speckle registration, polling structural nodes (locations not vibrating for particular frequencies), and comparison of one band of response to others that represent negligible structural response. There is another method to mitigate piston effects on the CW return. While piston will affect DPLM systems and point based (imaging) CW, a *non – imaging* CW system integrates over the spatial difference across the image, the mode shapes. Most phase modulation methods are adversely effected by piston, to the extent that low order modes are the target signature of choice where CW has less mode shape distortion.³ **It is the change in mode shape in time that provides the dynamics response measurements for CW, thus reducing**

³Another piston effect is spatial variation of phase which, if within the Greenwood frequency [70] might act as a sampling screen. There are some potential solutions to spatial piston for non – imaging CW vibrometry sensing

expected piston temporal distortion effects. Modal frequency error is neither a direct nor linear function of mode shape error.

3.1.2 CSC matrix form, structural coherence, &mathcal{E} \rho_{corr}. Correlation function analysis is similar to CSC analysis in its relationship to the processing of Fourier Transforms of the data to arrive at a time delay, as used in many time difference of arrival (TDOA) analyses. Gutjahr and Holmes used relationships similar to the Wiener – Khinchin (W – K) theorem⁴ to transform ensembles of acoustic spectra and their cross – covariances into TDOA data for location of thunder as a validation of radar data on the location of lightning as it travelled through the clouds of New Mexico [34], [35], and [37]. Dr. Charles B. Moore [51] recently sent archived papers from Charles R. Holmes [37] on the subject to AFRL / SNAT. The correlation used for TDOA is on the time side of the Fourier dual space and by W – K is the transform of the power spectra. Their CSC matrices indicate the error in the TDOA distance estimates.

The correlation coefficient, quite a different quantity, is more similar to the CSC in form except that it uses statistics of the time histories themselves rather than the spectra. The correlation function provides more insight to the structural vibration aspects of the target.

The CSC used in this thesis is built from matrices of M spectral vectors, the spectral dynamic or spectral optical return energy response for N frequency bins. The M vectors for each separate configuration form the ensemble⁵ for the statistics. In the case of trade study B the configurations are variations of the bolt cross – sectional

⁴The Wiener – Khinchin theorem, Eq. 9, indicates power spectra and correlations are Fourier duals.

$$\begin{aligned}\Gamma(t_2 - t_1) &= \Gamma(\tau) = \int_{-\infty}^{\infty} G_U(\nu) e^{-j2\pi\nu\tau} d\nu \\ C_U(t_2 - t_1) &= \Gamma_U(t_2 - t_1) - \bar{u}(t_2)\bar{u}(t_1)\end{aligned}\tag{9}$$

⁵The reason for 30 random load time histories for each structure in trade study A and the nearly 30 for trade study B is the statistical guideline indicating that a sample of 30 approaches a statistical ensemble. Compare to Central Limit theorem guideline results. The omitted 3 “bad” trade study B response sets were merely too difficult to spline before Fourier transform calculations.

areas that changed the load paths in the structure. The mean removed form of these spectral ensembles, $S_{MR}(f_q)$, are the input for the averaging operations using the Expectation operator ($E[\]$) shown in Equation 10 and in other presentations [42]. The CSC in Equation 10 compares phase information from different bands (f_u versus f_v) of the same spectrum.

$$CSC(f_u, f_v) = \frac{E[S_{MR}^T(f_u)S_{MR}^*(f_v)]}{\sqrt{E[S_{MR}^T(f_u)S_{MR}^*(f_u)]E[S_{MR}^T(f_v)S_{MR}^*(f_v)]}} \quad (10)$$

The covariance of one frequency band with another indicates an un – calibrated nonlinear degree of structural coherence [26, 10] between these bands of vibration energy. The optical CSC senses and estimates the structural CSC and to some extent can see more of the relationships between different bands of energy due to the phase modulation birth of the optical signal.

With a representation of a permutation operation as either $[S_{MR}]_{row \rightarrow +1}$ or $[S_{MR}]_{row++}$ the parallel full matrix form of the CSC takes shape [42]. This permutation shifts the rows up while putting the top one on bottom. Transposed, this permuted matrix is a system of M column spectral vectors of length N where the spectra are shifted in a permutation to the left until just before arriving at the original form of matrices of mean removed spectral vectors S_{MR} . This permutation in the denominator a recipe for parallel calculation of the CSC in matrix form for Matlab provides Equation 11.

$$[CSC(f_u, f_v)] = \frac{[S_{MR}]^T \times [S_{MR}]^*}{\sqrt{[S_{MR}^{\odot 2}]_{row++}^T \times [S_{MR}^{\odot 2}]^*}} \quad (11)$$

The parallel CSC defined in Equation 11 is similar to what some texts call the ‘correlation coefficient’ $\rho(\tau) = \frac{C_{xy}(\tau)}{\sigma_x \sigma_y}$ [18, 49] which compares the structural covariance $C_{xy}(\tau)$ of the response at time lag τ to the input and output standard deviations (σ_x and σ_y), thus normalizing this correlation coefficient. However, that those correlation coefficients use the time histories and covariances of the time lag whereas the

CSC is a weighted ensemble average of the cross spectra, a function of frequencies. The CSC is normalized by division by the spectral variances because it is the phase relationship that is of interest; the phase relationship is the feature we intend to use for classification.

A bridge from CSC analysis to structural concepts provides an understanding of how comparison of CSC matrices helps indicate structural features. In this case a relationship between system outputs, y , and system inputs, x , is with the ‘scalar’ or ‘ordinary coherence’ (Coh) calculated in the vibration industry [5, 701]. This reference has a description that provides insight into phenomenon involving structural coherence and its relationship to structural response that is very useful.

“. . . The coherence function [structural response ‘Coh’] can be thought to describe the division of output power into coherent and incoherent parts with respect to the input.

When coherence is zero, the output is caused totally by sources other than the measured input. In general, then, the coherence can be a measure of the degree of noise contamination in a measurement. Thus with more averaging, the estimate of coherence may contain less variance, therefore giving a better estimate of the noise energy in a measured signal. This is not the case, though, if the low coherence is due to bias errors such as nonlinearities, multiple inputs, or leakage.

The coherence function indicates the degree of causality in a frequency – response function. If the coherence is equal to 1 at any specific frequency, the system is said to have perfect causality at the frequency. In other words, the measured response power is caused totally by the measured input power (or by sources that are coherent with the measured input power). A coherence value less than unity at any frequency indicates that the measured response power is greater than that due to the measured input. This is due to some extraneous noise also contributing to the output power. It should be emphasized, however, that a low coherence value does not necessarily imply poor estimates of the frequency – response function, but simply means that more averaging is needed for a reliable result.

Two special cases of low coherence are worth particular mention. The first situation occurs when a leakage bias error occurs in one or both of the input and output measurements. This causes the coherence in the area of the peaks of the frequency response to be less than unity. This error can be reduced by the use of weighting functions or by cyclic averaging. The second [low structural coherence] situation occurs when a significant

propagation delay time occurs between input and output as may be the case with acoustic measurements. If a propagation delay of length t is compared to a sample function length of T , a low estimate of coherence will be estimated as a function of the ratio t/T [30]. This propagation delay causes a bias error in the frequency response and should be removed prior to computation if possible.” [5, 701 ff]

This scalar coherence ratio Allemang and Brown discussed above uses time history inputs x and outputs y . There are similarities in the input datum for a CSC of the structural spectra. There are structural delays in vibration energy propagation from one part of a structure to another which would not be present at steady state except in nonlinear systems that delay bands of response (like typical vehicles). This delay can happen when the energy finds a structural path to follow that other frequency bands cannot similarly follow, where there are differences in the mechanical impedance at different frequencies.⁶ Even if the load path is the ‘long way around’ that portion of energy that bleeds through will suffer a delay that can show up in this ‘ordinary coherence’ ratio and may well be the issue with low values of CSC seen at interesting bands.

3.2 *Coherent return, phase modulation mode shape*

This second attempt at a more concise closed form solution considers rectangular structures without any free – free edge boundary conditions (BC’s). It does not provide as much insight or as simple a result as a function of Bessel functions. This section shows the need to use a simulation (Matlab) to perform the propagation. The resulting formula provides more insight into the modulation issues than a display of numerical simulation results would provide.

⁶Dispersive effects, where the speed of sound differs at different wavelengths and directions (wave vectors), $\vec{c} = \frac{d\omega}{dk} \frac{\vec{k}}{k}$, comprise a subset of this difference in mechanical impedance, Z . Here Z is a function of which component the calculation is for, with directionality being more of an issue of transmission through complicated stamped solids. The speed of sound, c , changes from component to component and has a complicated complex formulation inside joints. The extent to which Z is a function of frequency indicates a nonlinear nature of a particular component, fastener, or interface.

3.2.1 Source of the Paraxial Approximation. In order to have a background for the full closed form paraxial solution for the detected phase modulated optical return described in subsection 3.2.3 on page 57, a brief foray into beam parameters follows. This description is incomplete. The resulting relations culminating in Equation 22 are the theoretical basis for laser vibrometry target ID at moderate range.

The Paraxial approximation is a small angle approximation described both in general by Goodman [33] pages 178 ff, and with a description of Gaussian beam profiles [9, 69 ff]. The subscripted variables in Equation 12, R_o , x_o , and z_o represent the location vector, offset, and relative on – axis range of the system.

$$|R - R_o|_{paraxial}^2 = |z - z_o|^2 + \frac{|x - x_o|^2}{2|z - z_o|^2} \quad (12)$$

Solutions to the wave equations for Gaussian coherent laser beams using this paraxial approximation in Equation 13 are solutions to the paraxial wave equation.

$$U_o(r, z) = V(r, z)e^{ikz}\frac{1}{r}\frac{\partial}{\partial r}\left(r\frac{\partial V(x, y)}{\partial r}\right) + 2ik\frac{\partial V(x, y)}{\partial z} = 0 \quad (13)$$

We can arrive at the paraxial approximation of the temporal correlation through an equivalent but slightly different development of the “small angle approximation” and then apply it [33, 178 ff] for an analytical propagation of the beam profile to the target. ρ represents the distance of ‘pinholes’ through which the separate paths of optical radiation travel to the optical axis, the off axis radius. ξ and η represent the locations in the object profile related to x and y, the profile locations at the detector. ‘ z_2 ’ is the detector range.

$$r_2 - r_1 \cong \frac{1}{2z_2} [\rho_2^2 - \rho_1^2 - 2x\Delta\xi - 2y\Delta\eta] \quad (14)$$

With the paraxial approximation, $\vec{k} \bullet \vec{r}$ is no longer merely a product of sinusoids (surface vibration). This is part of the reason for numerical propagation (diffraction).

3.2.2 Using the Paraxial Wave Equation. The solution $V(r, z)$ to the paraxial wave equation $V(r, z) = A(z) \exp[-\alpha kr^2/p(z)]$ combined with the Boundary Conditions $A(0) = a_o$ and $p(0) = 1$ lead to the Input Beam Parameter Relations, using the phase front radius of curvature $F_o = 100$ m and the Gaussian profile spot size (at $\frac{1}{e}$ of the initial width) [9, 67], $W_o = 5.0 \times 10^{-2}$ m.

$$p(z) = 1 + i\alpha z = 1 - \frac{z}{F_o} + i \frac{2z}{kW_o^2} \quad (15)$$

$$U_o(r, z) = \frac{1}{1 + i\alpha z} e^{ikz + \frac{ik}{2z} \frac{i\alpha z}{1 + i\alpha z} r^2} \quad (16)$$

A Greens function solution of the Huygens – Fresnel integral for Gaussian beam profile propagation arrives at the same solution as Equation 16 [9, 71]. But this only gets us to the target using conventional (input) beam parameters. Diffraction of the modulated form of this illumination will give the final result in Equation 22 (the relation that shows the requirement for numerical simulation). Equation 16 describes the beam irradiance profile as it propagates from the laser to the vibrating surface under study. A surface reflection change in phase, ϕ_r , is applied uniformly with negligible variation along the surface.⁷ The mean phase value depends on the similarly formulated ‘range phase’ $e^{ikz} \Big|_{z=R} = e^{i\frac{2\pi R}{\lambda}}$. A simple plane wave solution and further simplifications clarify qualitative aspects of the propagated mixed phase measurement imaging results the Matlab scripts simulate.

⁷The phase change appears as δ_t in [21, 755 ff], a section on complex reflection and transmission coefficients for stratified conducting media (metallic films).

3.2.3 Plane Wave Modulation, time averaged result. Vibration modulates the phase of the laser beam. The field necessary for calculations is the vector Electric Field, E , in N/coul or V/m. Assuming the derivation for paraxial field $V(r,z)$ and its cross – sectional profile $U(r,z)$ applies to \vec{E} (the “field”), we can modulate the field with vibration modes of the structure where $w_{m,n}(x,y)$ represents plate deflection normal to the surface for mode related to the modes (m,n). These modes are the eigenvectors of a ‘Normal Modes’ FEA. The eigenvalues of these eigenvectors provide the frequencies related to these modes, $\lambda_i = \sqrt{2\pi f_{structural}}$ where in this case $f_{str} = f_{m,n}$ for mode (m,n) of a rectangular plate. Almost all lower modal frequencies $f_{m,n}$ are easily distinct for most actual imperfect plates. However, single layer perfectly square plates share some frequencies in cases where it turns out the non – imaging system could not distinguish their return related to the vibration equation of motion in Equation 17, $f_{n,m} = f_{m,n} \Leftrightarrow \lambda_{m,n} = \lambda_{n,m} = 2a/m = 2b/n$ for a particular mode m,n. Here the maximum deflection amplitude is w_{max} for m spatial half cycles in the x direction and n in y for this $a \times b$ size plate. Assume we are within the period of stationarity, $T_{stationarity}$, so that the last term is unity.

$$w_{m,n}(x,y;t) = w_{max} \sin\left(\frac{\pi x}{a/m}\right) \sin\left(\frac{\pi y}{b/n}\right) \cos(2\pi f_{m,n}t) e^{-\frac{t}{T_{stationarity}}} \quad (17)$$

Since $\Phi_e(t)$ and E are nonlinear in time, this time averaging calculation is not just pedagogic, it is useful for future laboratory diagnostics, average power metrics. The time averaging integration pulls the modulation into the argument of a Bessel’s function via Equation 19 [10, 580]. The time average of the result of the spatial

modulation generated Bessel's function⁸ is a simple calculation compared to the instantaneous spatial averages accomplished in Section 4.1.

$$J_o(\xi) = \frac{1}{2\pi} \int_0^{2\pi} e^{i\xi \cos \theta} d\theta \quad (19)$$

Assuming not much time has passed (light damping), the vibration modulation of the electric field becomes a series of Bessel's functions of the first kind of order zero. Using Equation 17 the time averaged irradiance E_e at a particular point in Equation 20 is a harmonic function of both spatial dimensions for the return from this rectangular plate.

$$\overline{E_e(x, y)} = \frac{1}{T} \oint_T E_{amplitude}(x, y) \exp\left[i2w_{m,n}(x, y; t) \frac{2\pi}{\lambda}\right] dt \quad (20)$$

In structural vibration equations c is the speed of sound. However, in the following relations ' c ' represents the speed of light and ϵ_o is the permittivity of free space. Subsequent calculations change from exitance to electric field, omitting this product of constants.

$$\overline{E_e(x, y)} = \frac{c\epsilon_o}{2} e^{-j\frac{4\pi}{\lambda}R} \int_0^a \int_0^b \prod_{m=1}^M \prod_{n=1}^N J_o\left(\frac{4\pi}{\lambda} w_{max} \sin \frac{\pi x}{a/m} \sin \frac{\pi y}{b/n}\right) dx dy \quad (21)$$

Taking the plane wave results from Equation 21 for use with the paraxial approximation of the field at the target, the next subsection shows explicitly the reason numerical integration and propagation is necessary for the post modulated field. These

⁸Abramowitz has a more detailed definition [1, 360, #9.1.20] using an analytical carrier function shown in Equation 18 for all orders of Bessel's functions. If a particular calculation of the spatial integration does not factor out the harmonics as in Equation 30 this half cycle integration is necessary.

$$J_n(\xi) = \frac{i^{-n}}{\pi} \int_0^\pi e^{i\xi \cos \theta} \cos(n\theta) d\theta \quad (18)$$

approximations in subsection 3.2.4 based on Equation 21 are also used in a plane wave result in Section 4.1 to show two theoretical mechanisms for spectral reduction in laser vibrometry from strips of metal (bars or beams) that are free on two opposing edges.

3.2.4 Paraxial to target, time averaged modulation. With the assumption of modal stationarity and paraxial illumination, the time averaged fully modulated electric field, E_{mod} , just after reflection sums to the detected field shown in Equation 22. $m = \mu$ and $n = \eta$ are the maximum mode numbers for x and y that have meaningful deflection ($w_{max} \equiv (\Delta z)_{max}$). These numbers are bound to be small, if not zero for some structures. This equation also uses laser beam input parameters defined earlier for Equation 15 describing the beam profile in the x – y plane at the target ($z = L$).

$$\overline{E_{mod}} \approx \frac{\tilde{E} e^{ikL + \frac{ik}{2L} \frac{i\alpha L}{1+i\alpha L} (x^2+y^2) - i\phi_r}}{ab(1+i\alpha L)} \int_0^a \int_0^b \prod_{m,n=0}^{\mu,\eta} J_0\left(2kw_{max} \sin \frac{\pi x}{a/m} \sin \frac{\pi y}{b/n}\right) dx dy \quad (22)$$

Factoring the phase into separate terms ($e^{\alpha+\beta} = e^\alpha e^\beta$) Equation 22 describes the modulated field, E_{mod} , just after reflection.

If we allow modal coupling an expansion of the Bessel's function helps show the behavior of the time averaged field E_{mode}^{multi} spatially integrated at the detector. The first order correction to the Bessel's function is smaller than a cosine correction, $J_0(\xi) = 1 - \frac{\xi^2}{2^2(1!)^2} + \frac{\xi^4}{2^4(2!)^2} - \frac{\xi^6}{2^6(3!)^2} + \dots$ [71, 534, #4]. So to second order the integrand product is different from zero by a correction amount of almost $\xi^2/4$ as shown in Equation 23 where the range phase front e^{ikL} and the arbitrary phase $e^{-i\phi_r}$ are set to unity leaving the quadratic phase front in the coefficient. α was defined in the right hand side of Equation 15 on page 57.

The **multi – modal** time average field displays another spectral reduction form:

$$\overline{E_{mode}^{multi}(x, y)} \approx \frac{\tilde{E} e^{\frac{ik}{2L} \frac{i\alpha L}{1+i\alpha L} (x^2+y^2)}}{ab(1+i\alpha L)} \int_0^a \int_0^b \prod_{m,n=0}^{\mu,\eta} \left(1 - \frac{\left(2kw_{m,n}^{max} \sin \frac{\pi x}{a/m} \sin \frac{\pi y}{b/n} \right)^2}{4} \right) dx dy \quad (23)$$

$$\begin{aligned} \int_0^a \int_0^b \left(1 - \frac{\left(\beta \sin(\xi) \sin(\gamma) \right)^2}{4} \right) d\xi d\gamma &> \int_0^a \int_0^b \left(1 - \frac{\left(\beta \sin(\xi) \sin(\gamma) \right)^2}{4} \right) \dots \\ &\times \left(1 - \frac{\left(\beta \sin(2\xi) \sin(\gamma) \right)^2}{4} \right) \dots \left(1 - \frac{\left(\beta \sin(m\xi) \sin(n\gamma) \right)^2}{4} \right) \left(1 - \frac{\left(\beta \sin([m+1]\xi) \sin([n]\gamma) \right)^2}{4} \right) \dots \\ &\times \left(1 - \frac{\left(\beta \sin([m+1]\xi) \sin([n+1]\gamma) \right)^2}{4} \right) \dots \left(1 - \frac{\left(\beta \sin(\mu\xi) \sin(\eta\gamma) \right)^2}{4} \right) d\xi d\gamma \end{aligned} \quad (24)$$

The spectral reduction in Equation 23, where “large spot size” assumes illumination of the entire target, appears in the product terms within the integrand shown in Equation 24. At higher levels of approximation of the Bessel’s function (more factors left in the integrand) the difference from unity becomes small as the exponent and divisor increase geometrically (2, 4, 6, ...). Remaining at this second order estimate, the integration of more terms (including more modes, m,n) reduces the return, but the terms have less of an effect, as shown in Equation 24 because $\sin^2(r\theta)$ approaches a comb function in the limit of high coefficient r. In the uniform MPF $\phi_i = \phi_j \forall i, j$ assumption, instead of calculating participation factors we assume an equi – modal participation but set a modal cut off, N, the highest mode used. Combining this ‘discrete’ form of uniform modal participation distribution allows the estimation of a qualitative time averaged spectral reduction result. The fundamental mode $(\beta \sin(m\xi) \sin(n\gamma) \equiv 2w_{m,n}^{max} \sin \frac{\pi x}{a/m} \sin \frac{\pi y}{b/n} \text{ where } m = n = 1)$ provides the largest contribution. Each additional mode included has a reduced time averaged impact while the total return continues to reduce error (more slowly) with these added terms. A Matlab plot of $\prod_i^r \sin(r\theta)$ (not shown) is similar in form to $\sin^r \theta$ versus θ for

even powers. Such a plot shows that the higher harmonics act like a comb (a series of Dirac delta functions) of increasing sharpness, so the area under the curve decreases with r . This quantitative spectral reduction estimate supports the measurements and conclusions of the prior thesis for multi-modal spectral elimination [58] from a time averaged return field point of view.

Spatial averaging of this *time averaged* version of a Gaussian beam illuminated target vibration modulated field at the target is best accomplished numerically. For the major part of this work Matlab scripts performed this integration for the instantaneous field and intensity calculations, the most CPU intensive task.

Even if a useful general modulation formula were available, propagation of the exitance back to an image in the detectors near the laser source using Equation 16 (merely doubling the range: $z = 2L$) is not appropriate. At the target vibrating surface the beam has spread out and after reflection per the modulation relation, Equation 22, is no longer Gaussian. For this calculation a Fresnel back propagation (numerical diffraction) of the field from the Equation 22 state at the target provides an appropriate approximate far field diffraction solution.

3.3 Stationarity: ‘Image’ SNR drives time history length

Trade study B used a structural impulse merely to ‘ring the modes’ of the structure, an alternative to input of a PSD. This method, which is similar to pendulum and impact tests that are in use in most noise and vibration labs, does not produce optical phase modulated return response as stationary as the ‘convergence’ of the FEA structural response spectra⁹ would indicate. The Fourier transforms of time history data from NASTRAN FEA results for transient implicit direct integration nonlinear contact analysis become well formed with only 50 or more time data points in it’s structural ‘steady state’ region (just past the structural transient impulse). But

⁹The FEA structural response spectra are the DFT’s of the structural direct transient time integrated (Newmark – Beta) response [8, 436], second order Newmark integration [93, 464], [52] with choice of parameters for maximum stability and minimum error for small deflection FEA that is unconditionally stable [94, 367], which comprises the historical ‘SOL 129’ in MSC/NASTRAN.

Figure 18 on page 110 shows that stationarity occurs much later. This indicates that laser vibrometry requires care with stationarity for transient Φ_e response.

Further stationarity period ($T_{stationarity}$) studies would be useful . Until $t = 60$ milliseconds the optical modulation is not as stationary for imaging return as the structural frequency response. Laser imaging stationarity does not peak in ‘image’ SNR (see page 95) until well after the structural response dies down, past their $1/e$ points. Compared to plots of $\Phi_e(t)$ and $\Phi_e(f)$ spectra, the sharpness of the modulation of the SNR indicates it may be a better candidate for classification features.

IV. Theoretical and Simulated Results

This results chapter starts with a theoretical plane wave basis for spectral reduction or elimination. Continuing with a simple but crude two DOF lumped mass model of the dynamics of typical multi – layer target skin, simple structural response calculations show modal response that both the FEA and simulated return capture; symmetrical modes are insensitive to contact stiffness changes (trade study A). This is a different mechanism of spectral reduction than those the plane wave theory presents. The chapter continues with the Matlab simulated return¹ of the modulated coherent image target. Descriptions of the physical models are in Appendix A. The FEA validation and analysis model descriptions are in Appendix B. Supporting structural analyses are in subsequent appendices.

4.1 *Theory Result: Plane Wave spectral reduction*

The integration of phase modulation from a plane wave over a one dimensional spatial deflection field generated phase modulation represents the exitance from a moderately thin beam held at both ends, oriented as shown inset into Figure 8 on page 69. The difference between this beam return and the return modulated by vibrations of a rectangular plate target (main sketch in Figure 8) is that the ‘beam’ is structurally free on the long edges (parallel to the y axis, in this case). Therefore the phase modulation is one dimensional, along the length. Calculations of the return at the detector are in two forms, slowly swept sine and multi – modal.² These calculations are for monotone excitation and small deflection assumptions respectively so that adding

¹In this work ‘return’ represents the images of the vibrating plate and non – imaging Radiant Flux, $\Phi_e(x, y; t)$ in Watts, or the returned electric field E in V/m (or Newtons/Coulomb).

²For laser vibrometry, the slowly swept sine response is a calibration metric that is not similar to the response to actual vibration due to the nonlinear nature of the system transfer function. Swept sine is one of the easiest of approximately eight FRF measurement methods that have different test analysis characteristics [4, 36]. Burst random or pseudo random loading approximately characterize the multi – modal return estimate in subsection 4.1.4. Compared to these methods sine swept signals have a higher SNR, higher SNR to peak ratio, and controlled amplitude content which burst random does not provide. The required measurement time is long and unlike burst random, sine sweeping does not remove distortion. Equations 30 through 32 show $E_{mod} \neq E_{swept}^{sine}$. Nevertheless it is such a mainstay of modal analysis that use of slowly swept sine excitation to estimate laser vibrometry results is bound to occur, if only by accident.

responses that should be negligible away from the driving frequency induces little error. An integration formula for multi-modal shows the reduction in contributions from higher ordered modes while a sine sweep excitation of the modulation provides a return result that is uniform for all modes. While these results provide insight into the spectrum of modal response, the equations also indicate that swept sine frequency response calculations based on Φ_e return are problematic for vibrometry; swept sine calculations do not properly characterize the coupled form of the received optical return. Equation 32 drives this home. However, as discussed later, sine swept results are likely to be used regardless and may serve as a calibration metric.

Multi – modal vibrometry considers the superposition of modes normally found in a structure, using an eigenvector decomposition. Multi – modal laser vibrometry is the main thrust of a spectral elimination laboratory measurement in a prior AFIT thesis [58]. That thesis showed spectral elimination when the spot size increased to a “large” spot size of diameter approximately equal to the width of the vibrating metal strip. In this work “large” spot size means that the illumination covers the entire strip – not just for this plane wave result, but for the paraxial approximation as well. The final spatial averaging integration of this multi – modal result is not carried out, but *inspection of the integrand product shows that the higher order modes have much less contribution* in a manner similar to time averaged result in Equation 23 on page 61. Small numerical integration results plotted in Figures 9 and Figure 10 shows the spectral reduction effect (medium and high order mode insensitivity) for sine swept and multi – mode systems respectively.

In the slowly swept sine form the plane wave illumination receives modulation upon reflection of the beam, vibrating in one mode only, and returns to the detector in the form of an irradiance proportional to a Bessel’s function of the first kind, order zero, *with an argument that is the same value for all vibration modes* as shown in Equation 33 where the phase modulation has already been integrated over the y dimension. This result assumes that the source only excites one mode at a time. So

Equation 32 on page 73 indicates this typical vibration FRF measurement method will not provide a proper frequency response function for the received irradiance.

4.1.1 Plane wave assumptions and preliminary details. Assume the detector and probing laser are at the same location so that \vec{r}_1 and \vec{r}_2 of Figure are vectors to object points of maximum reflected phase difference.

The general relation for return from a plate, Equation 30, does not apply to vibrating metal strips because it assumes phase modulation along the x direction for $M > 0$ modes. When considering return from a beam (strip or bar) we only have mode zero along the width. Use of sine modulation in these calculations is convenient because deflection is zero at the origin (which is also a Chladni ‘line of nodes’), which is at the bottom $y = 0$ edge in the upper right insert in Figure 8 on page 69.

Vehicle skins structural modes shapes are similar to panels held on all edges. The rectangular panel modelled for this work has a two – dimensional phase modulation, sketched in the lower pane of Figure 8 on page 69.

For plate structures with more than zero fixity on all edges, modes shapes no longer vary in just one dimension. Integration of the sinusoidal modulation (phase modulation across the target) of $\Phi_e(x, y; t)$ over two dimensions leads to non – imaging return $\Phi_e(t)$ at the detector. Use of this spatially integrated radiant flux described in Equation 45 (page 104) is preferable for fast inexpensive (non – imaging) sensor system deployment.

This section (4.1) describes the assumptions and derivation of a closed form but sine swept³ form of simple spectral reduction results in Figure 9 on page 75, as well as

³Sine sweep measurements are a typical form of FRF estimation which uses excitation with a pure tone of narrow bandwidth. This is a typically accurate method of FRF generation [26, 17], including nonlinear FRF results, and is used as a convenient alternative to random excitation [4, 36,37]. While these responses are continuous in frequency, they mostly excite the mode nearest the driving frequency (structures act differently from undamped linear oscillators). The summation of all the responses is *similar* to exciting one mode at a time. While Equations 30 through 32 indicate optical response from sine swept structures will not accurately predict the PSD ($E_{mod} \neq E_{swept}^{sine}$), optical response to sine swept structures may become a practical diagnostic as laser vibrometry progresses. There is too much sine sweep infrastructure in the test equipment industry to avoid its use.

a more formal multi – modal small deflection form of spectral reduction by inspection of an integrand (a per-integration qualitative conclusion) in Figure 10.

4.1.2 Derivation of the plane wave solutions. The BC's produce laser vibrometry Φ_e per mode that is an integer number of half cycles where there is one anti – node per half cycle in a given dimension. Each anti – node is the region between the Chladni lines of nodes.⁴ The target illuminating field density is approximately constant, but the value of a spatial vibration wavelength of integrated radiant flux decreases with the number of spatial half – wavelengths along the beam; the anti – node regions of area $(\lambda_x \times \lambda_y)$ or (width $\times \lambda_y$) become smaller for higher vibration mode frequencies. The actual deflection is a linear combination of these modes but viewing them one at a time is similar to the standard slowly swept sine FRF measurement method.

The slowly swept sine excitation result is that as long as the beam stays approximately flat (a small deflection assumption), the sum of the return from any number of these Bessel's functions remains constant. The resulting lack of vibration sensitivity theoretically verifies part of Flight Lieutenant Pepela's work, within meaningful assumptions.

The coefficient of the resulting Bessel's function solutions also remain constant for any given mode as described in Equation 27. For a particular vibration mode, the more anti – nodes there are (the higher the structural vibration frequency), the smaller is the detected energy per segment (anti – node), $\Phi_{seg} = \int_{\Delta x} \int_{\Delta y} \Phi_e(x, y) dx dy$. The solution for higher temporal frequency modes, and hence higher spatial frequency modes, has smaller coefficients of the Bessel's functions in Φ_e (Equation 27) for each segment, summed over more segments. For mode (m,n) Chladni zones of area A_{cz} within a plate of area $A_{tot} = ab$ we have $\tilde{E}_{tot} = mn \frac{A_{cz}}{A_{tot}} |\vec{E}|$ where the \tilde{E}_{tot} is the sum of the electric field from all zones. Incident field $E_{in} \equiv E_{incident}$ specifies the V/m amplitude *before* modulation. For the one dimensional mode case (beam vibration)

⁴Reference Chladni footnotes on pages 90 and 184.



Figure 7: The return off of the valleys (r_1) of an assumed specular vibrating surface will undergo a phase change related to twice the full range of vibration, four times the amplitude, compared to return from the crests (r_2).

with M half modes along the x axis (and N along y) Equation 25 provides the modulated electric field, $E_{mod} = E_{tot}$, before back propagation to the detector. For any one mode the incident field density for each of the $M \times N$ anti-nodal Chladni zones is $\tilde{E} = \frac{a}{m} \frac{b}{n} E_{in} = \frac{E_{in}}{mn}$. The phase term of Equation 25 already assumes normal incidence as detailed in Equation 28.

$$\vec{E}_{mod} \Big|_{M,N \neq 0} = \int_o^a \int_o^b \frac{\vec{k} \bullet \vec{r}}{kr} E_{in} e^{-j \frac{4\pi}{\lambda} \left(R + \sum_{m=1}^M \sum_{n=1}^N \Delta z_{m,n}^{max} \sin \frac{\pi x}{a/m} \sin \frac{\pi n}{b/n} \right)} \hat{e}_\xi dx dy \quad (25)$$

For the rest of this work, assume a particular instant in time and normalize the field at range $|\vec{r}_{ave}| = R \Rightarrow e^{-j \frac{4\pi}{\lambda} R} \approx 1$ so that only the modulation about the average range remains in the phase term, $e^{-j \frac{4\pi}{\lambda} (R + 2w_{m,n}(x,y))} \approx e^{-j \frac{4\pi}{\lambda} 2w_{m,n}(x,y)}$. The return from a rectangular plate in Equation 25 shows the phase modulation as a sum of normal modes $w_{m,n}(x,y) = \frac{1}{2} \sum_{m=1}^M \sum_{n=1}^N \Delta z_{m,n}^{max} \sin \frac{\pi x}{a/m} \sin \frac{\pi n}{b/n}$. The individual deflections $w_{m,n}^{max} = \phi_{m,n} = (\Delta z)_{m,n}^{max}/2$ are the modal participation factors (MPF's) which are related to the deflection ranges $(\Delta z)_{m,n}^{max}$. Equation 28 details the change in phase due to deflection. An alternative form of Equation 25 that hints at a simple closed form sine swept solution appears in Equation 26 which factors the modulation

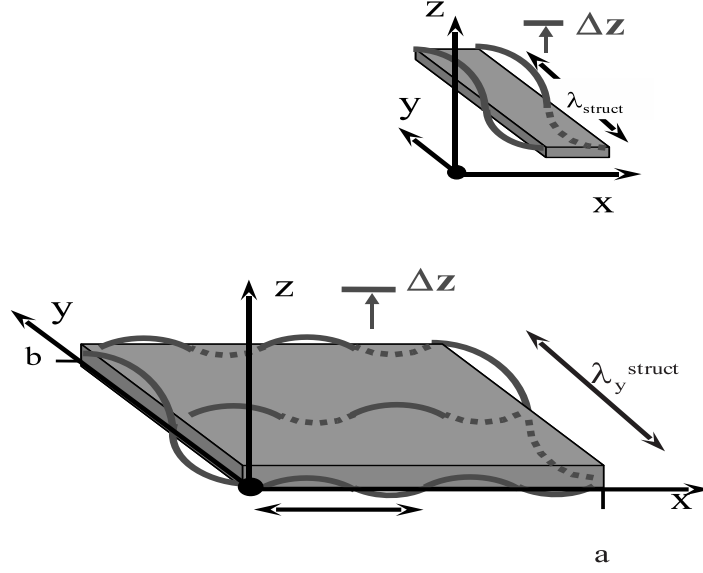


Figure 8: a) The one – dimensional result shown in the upper pane, an integration of the Bessel function of a constant (thereby becoming large compared to the oscillating argument integrations) models a cantilever or end held beam. b) Detection of variations in the two – dimensional vibration mode shapes, shown in the bottom pane, requires a detectable difference in integrated existance from the target.

per mode. To integrate into a Bessel's function for Equation 27, the product can only be over a single term. Test laboratories use sine swept measurements to assemble spectra from for monotone excitation, one frequency band at a time, as does Equation 33 for E_{swept}^{sine} .

$$\mathbf{E}_{mod} = \int_0^a \int_0^b \prod_{m=1}^M \prod_{n=1}^N E_{in} e^{-j \frac{4\pi}{\lambda} \left(\frac{1}{2} \Delta z_{i,j}^{max} \sin \frac{\pi x n}{a/m} \sin \frac{\pi n}{b/n} \right)} dx dy \quad (26)$$

In either case (sine swept or multi – mode) the wave vector ($\vec{k} = \frac{2\pi}{\lambda} \hat{e}_k$) and distance vector (\vec{r}) used in $(\Delta z)_{m,n}$ via Equation 28 are effectively parallel as shown in Figure 7, so $\vec{k} \bullet \vec{r} \cong kr$. For the remainder of these calculations arbitrarily assume a field polarized parallel to the x axis unit direction, \hat{e}_x . These are the same variables used in Equation 17 on page 58 and in the rest of that subsection 3.2.3. The **sine swept results assume a uniform modal participation** over N modes

in y (M modes in x) so that *the approximate amplitude per mode is* $w_{max}/(MN) = (\Delta \mathbf{z})_{max}/(2MN)$. Application of Equation 18 (definition of Bessel's Function) to Equation 26 provides Equation 27 which represents the return for one particular mode, $m = m_i, n = n_i$.

$$\text{For any single mode } E_i^{\frac{1}{2}\text{cycle}} = n \frac{E_{in}}{n} J_0 \left(-2 \frac{2\pi}{\lambda} \frac{\Delta z_{max}}{2MN} \right) = E_{in} J_0 \left(2\pi \frac{\Delta z_{max}}{MN\lambda} \right) \quad (27)$$

The rectangular vibrating plate with M half modes in the x direction and N half modes in y has a fundamental mode where $M = N = 1$, the main diaphragm mode which has only one half cycle along each edge. If either mode number is DC (a “Direct Current” mode with either $M = 0$ or $N = 0$) then the equation for returned E requires slight modification similar to the removal of the pertinent DC mode from consideration as shown in Equation 33 and derived in Equation 31.

To modify Equation 25 for the simple case of optical return from vibrating strips with one dimensional modes (free – free condition on opposing long sides), the number of structural modes perpendicular to the length of the strip is zero. Since we cannot merely apply $M = 0$ or $N = 0$ to Equation 26 for removal of modulation in one “dimension” of the mode shapes,⁵ a different formula is necessary. For example, the Bessel's function definition (Equation 19) produces Equation 31 whose result, Equation 33, shows a “sine swept” formula for the modulated electric field for a strip parallel to the y axis and with the short edge aligned with the x axis, where free – free unconstrained BC's are along the two long edges (the planes $x = x_1, x = x_2$). “ $M = 0$ ” defines this free – free BC. The $M = 0$ calculation of the phase modulation of the returned field excludes M and so there is no summation over that dimension

⁵Mode numbers of zero could indicate D.C. modes (Direct Current) but the spatial wavelengths of infinity that relate to these modes no longer represent an integer fraction of the plate width in Matlab (dividing by zero). All other modes ($m, n > 0$) have $\lambda_x^{str} = 2a/m$ and $\lambda_y^{str} = 2b/n$ if the divisor is positive, $\forall m, n \in \mathbb{Z}^+$. So the formula for a DC maximum mode $M = 0$ or $N = 0$ is slightly different.

(x) for return from a metal strip. Equation 33 only models optical response from sine swept vibration on an *uncoupled* system.⁶

In this uniform modal participation model the maximum mode number, N , is an indicator of a form of bandwidth that identifies the response in non – uniform discrete frequency space. The form of the modulation argument, the exponent in Equation 25, indicates what optical regime we are in: small angle, paraxial, or full calculation. \mathbf{S} is the typical Poynting vector (energy flow) of electrodynamics. The optical probe of vibrations on the assumed specular surfaces undergoes a phase change (Equation 28) of twice the deflection amplitude in wavelengths (not including the reflection phase change [21, 755 ff]) as shown in Figure 7. Optically $\Delta\phi = 2kw(x, y) = \frac{4\pi}{\lambda}w(x, y)$ is the change in phase, in radians, produced by structural variation along the plane at range $z = r \cos \theta_{incident}$. Equation 28 describes this spatial phase relation of where $r_1(x, y)$ and $r_2(x, y)$ are the distances to two points on the armor plate (HRA) in Figure 7. In the following relations choose the zero deflection shape, $r_2(x, y) = \overline{r(x, y)} = \frac{1}{T} \oint_0^T \vec{r}(x, y) dt$, as the reference amplitude for $w = 0$. For any one particular mode $\Delta z = 2w(x, y)$ is the difference in the “vertical” plate deflection field from Equation 17 on page 58 assuming $z(r_1)$ or some suitable value is a reference deflection.⁷

$$\Delta\phi_{1,2}(x, y) = 2k \bullet r \approx 2k(r_1 - r_2) \cos(\theta \approx 0) = 2\frac{2\pi}{\lambda}w(x, y) = \frac{2\pi}{\lambda}\Delta z(x, y) \quad (28)$$

This derivation requires the time modulation $\mathbb{R}[e^{j2\pi f_n t}] = \cos \omega_n t$ factor out of Equation 17 on page 58 before selection of an instant in time. Arbitrarily choose $t = 0$. The structural modes we investigated are not closely spaced enough in frequency space for the assumption to hold formally. Tabulated Pininfarina chassis frequencies [48] and Laser Doppler vehicle frequencies [54] show the discrete nature of low frequency

⁶While OEM’s avoid modal coupling, what coupling occurs produces sine swept Φ_e measurement error.

⁷Structural engineers typically use u, v, and w for deflections in the x, y, and z directions.

modes. In practice time variation does not factor out the exponent but for closely spaced modes this error is small as long as the inter – mode frequency spacing is small as seen in Equation 29.

$$\text{for } (f_j - f_i)t_{\text{integrating}} \ll 1 \quad \Rightarrow \quad e^{j2\pi f_i t} \approx e^{j2\pi f_j t} \quad (29)$$

As a comparison, start with the general rectangular plate solution of Equation 30 for $M, N \geq 1$ but *only* activate the first mode, $M = 1$, in the integration of the return from a metal strip. Using the definitions in Equations 18 and 19 on page 59 the sine swept result leaves the y modulation inside the Bessel function argument. Unless the modal distribution is uniform up to a cutoff mode, the sum requires a modal participation factor $\phi_n = w_{m=1,n}(x, y)$ defined by $\frac{\Delta z_{max}}{2} = w_{max} = \sum_{n=1}^N \phi_n \sin \frac{\pi y}{b/n}$.

$$\left| \vec{E}_{mod} \right|_{M=1} \cong \sqrt{\left| \frac{\mu_o}{\epsilon_o} \mathbf{S} \right|} = \frac{E_{in}}{\pi} \int e^{-j \frac{2\pi}{\lambda} \left[\sin \frac{\pi x}{a} \sum_{n=1}^N \phi_n \sin \frac{\pi y}{b/n} \right]} dy \quad (30)$$

The time modulation was removed by application of Equation 29 leaving the assumption that the mode shapes are chosen at the point in time where they are at maximum deflection, as is customary for modal analysis.⁸ The slowly swept sine and multi – modal estimates are instantaneous field estimates that seek to determine if the field response from modes at this amplitude point in time. If return from different modes is the same at maximum deflection for each mode then modal discrimination would be difficult while time based response methods may still detect some modal features.

4.1.3 Slow Sine Sweep spectral elimination. Restrict the area of interest to a local target region where the laser beam acts like an infinite plane wave (on a small scale). The sine swept response is the scaled sum of a complete set of single tone

⁸The mode shapes represent the modal amplitudes at different locations for the time of maximum strain energy. They are usually normalized by FEA parameters to a unit generalized stiffness or as in this work to unit generalized mass.

responses that the nearest resonance to the driving frequency tone dominates, that response of other resonances is negligible. Equation 31 is *not* merely the interchange of the integral and the product, which would be mathematically incorrect. It represents a physical linearity assumption about driving resonance domination that describes the physics of monotone FRF reconstruction; it is the *sum* of many single mode responses. The form of the $M = 0$ beam return formula in Equation 31 begs hopelessly for simplification.

$$\left| \vec{E}_{mod} \right|_{M=0} \cong E_{in} \int J_o \left[\frac{2\pi}{\lambda} \sum_{n=1}^N \phi_n \sin \frac{\pi y}{b/n} \right] dy \quad (31)$$

Application of slow sine sweep assumptions to Equation 30 provides the sine swept result in the right hand side of Equation 32.⁹ The left hand side of Equation 32 is to indicate that sine swept results cannot provide the modulated field at the detector because of the multi – modal nature of the system, especially where the modes are coupled as shown in the substantial cross – terms in the CSC in Figure 32 on page 129.

Optical response from a *sine swept* general **plate** vibration:

$$\left| E_{mod} \right|_{M=1} \neq E_{sine}^{sine}(x, y; t; f) = \frac{E_{in}}{N\pi} \sum_{n=1}^N \int_o^{b/n} \frac{ab}{\pi^2 n} J_o \left(\frac{2\pi}{\lambda} \phi_n \sin \frac{\pi y}{b/n} \right) dy \quad (32)$$

⁹Mathematically, an expectation that the Bessel's function of one phase term $2\pi J_o(\frac{2\pi}{\lambda} 2w_n) = \int_0^{\phi_n=2\pi} e^{j2w_n \cos[\phi_n(y)]} dy$ would lead to a product of Bessel's functions is incorrect. If we separate the integrand of phase factors into individual factors, $f(y) = e^{j(\phi_1+\phi_2+\dots+\phi_N)} = e^{j\phi_1} e^{j\phi_2} \dots e^{j\phi_N}$, the integrand is a product of factors. That each factor is the integrand of a Bessel's function merely tantalizes the engineer. Strict mathematicians should eschew the allure of making a product of Bessel's functions.

Optical response from a *sine swept beam* vibration:

$$\left. \vec{E}_{swept}^{sine} \right|_{M=0} \cong \sqrt{|\mu_o \mathbf{S}_{sup}|} \cong \frac{E_{in}}{ab} \sum_{n=1}^N \frac{ab}{n} n J_0 \left(\frac{-2\pi}{\lambda} \frac{\Delta z_{max}}{N} \right) = E_{in} \sum_{n=1}^N J_0 \left(\frac{2\pi}{\lambda} \phi \right) \quad (33)$$

The return from a sine swept beam in Equation 33 is a constant over the modes. For a larger uniform modal participation “bandwidth,” N , the average modal participation, $\phi = \frac{\Delta z_{max}}{N}$, decreases.¹⁰ The sine swept general plate return in Equation 32 contains a harmonic Bessel’s function argument. An expansion of this Bessel’s function in the manner of the multi – modal time averaged results in Equations 23 and 24 on page 61, further enforcing the spectral reduction conclusion that higher frequency modes produce less change in the return providing less additional target classification “power” (roughly, $P_{detection}$ [85, 89]) [73, 106]. So sine swept beam return has no variation with respect to mode, whereas sine swept plate return has a variation that decreases with increasing mode frequency. These observations support spectral elimination findings in the previous AFIT thesis [58], but only for sine swept FRF measurements.

Nevertheless, slowly swept sine FRF generation is such a large part of the modal engineer’s repertoire (and a part of expensive automated modal analysis systems) that the E_{swept}^{sine} calculation is appropriate and provides a potentially useful diagnostic metric. Modal analysis usually only uses lower frequency modes so the decrease in detection power at high frequencies is not much of a problem.

Numerically summing up the modal modulation per Equation 45 (a discrete sum of pixels versus continuous spatial integration, as detailed on page 104) the return field from plates held or simply supported on all edges has an argument in the Bessel’s function in the expression for $\Phi_e(t)$ that varies with location in y . This variation is apparent in the values represented by filled stars in Figure 9. The result from

¹⁰ $\frac{\Delta z_{max}(x,y)}{N}$ is the deflection range at a point due to the linear sum of all modes.

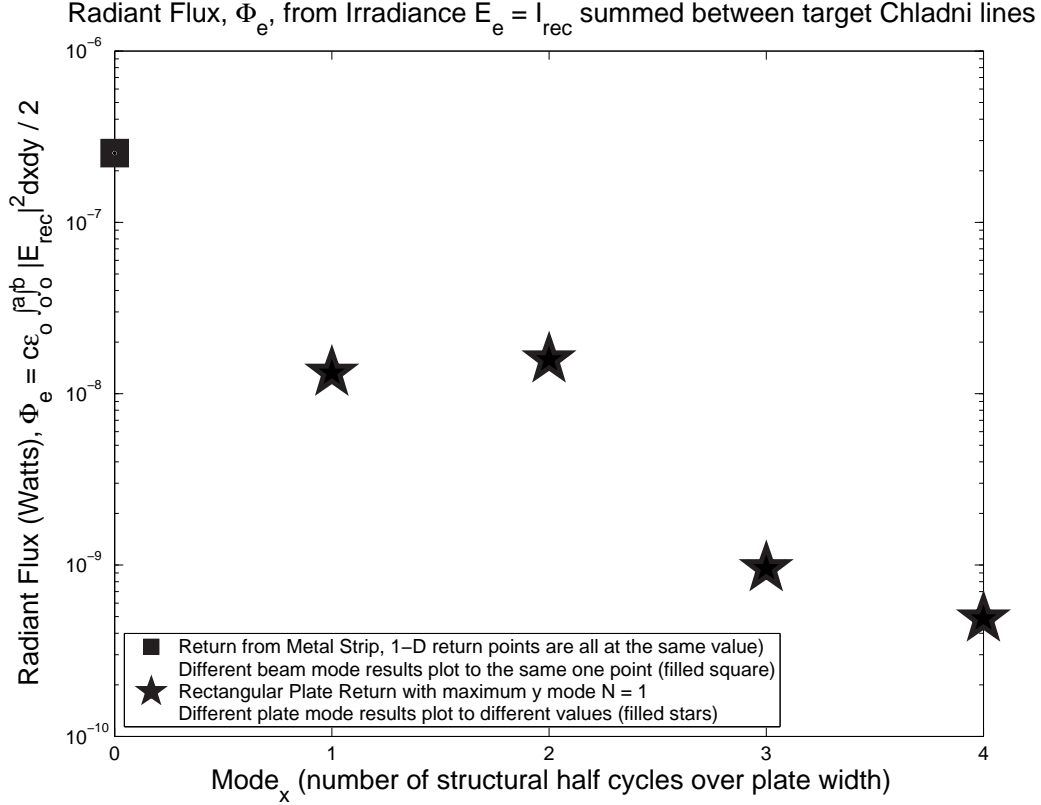


Figure 9: **Sine Swept** Plane Wave $\Phi_e(mode)$ return from two – dimensional plane wave solutions (filled stars) vary. Return from strips or bars (filled square) do not. The optical return from a superposition of 1 – D vibration modes is constant compared to the Φ_e variation from a plate for a fixed number of modes.

Equation 33 for return from a strip (beam) is the set of superposed filled squares in Figure 9. This shows that for vibrating strips, within the assumptions of this section (4.1), the sine swept modulated return remains constant over all modal variations due to the free – free BC's on both sides. The variation of the two – dimensional plane wave solutions for return from a rectangular panel (filled stars) indicates that far – field application CW will have enough variation to classify different sine swept vibration mode shapes.

A different derivation for monochromatic phase modulation in a crystal provides a similar result [91, 243 ff] because the argument of the Bessel's function is small.

4.1.4 *Multi – modal small deflection spectral reduction.* Stopping short of integrating Equation 25, *before integration created Bessel's function sine swept solutions*, an expansion of the field using the approximation for an exponential, $\mathbf{Re}[e^{j\theta}] = \cos \theta = 1 - \frac{\theta^2}{2!} + \frac{\theta^4}{4!} - \dots$, provides insight into the participation of each mode in the optical return. This approximation assumes small deflection¹¹ but does not restrict excitation, it assumes full modal response. The assumption that this return comes from a metal strip where the number of modes across the strip width is zero simplifies the return field calculations. Equation 34 follows directly from Equation 25 by use of a small deflection second order approximation of the expansion of the cosine term described above.

$$\left| E_{mod} \right|_{M=0} = \frac{E_{in}}{b} \int_0^b \left(1 - \frac{1}{2} \frac{(2\pi)^2}{\lambda^2} \left(\sum_{n=1}^N \phi_n \sin \frac{\pi y}{b/n} \right)^2 + \mathcal{O}\left(\left[\frac{2\pi^3 \Delta z}{b\lambda^2}\right]^2\right) + \dots \right) dy \quad (34)$$

The third order term in Equation 34 is equivalent to $\mathcal{O}\left(\left[\frac{N\phi}{\lambda}\right]^4\right)$ for the uniform modal participation model. Here we introduce $\phi \equiv \phi_{n_i} = \phi_{n_j} = \frac{(\Delta z)_{max}}{N}$ as the uniform modal participation factor defined by $\frac{\Delta z_{max}}{2} = w_{mx}(y) = \sum_{n=1}^N \frac{(\Delta z)_n^{max}}{2} \sin \frac{\pi y}{b/n}$.

Solving this equation explicitly, ignoring terms of $\mathcal{O}\left(\left[\frac{\Delta z}{\lambda}\right]^4\right)$ or smaller, makes use of the series solution for each term in the expansion of the square of a sum of ordered sine functions, $(\sum_p^N \psi_p)^2 = \sum_p^N \psi_p^2 + 2 \sum_{p \neq q}^N \psi_p \psi_q$. Taking the integral of the second term in Equation 34 [71, 437, #316] along the beam length y, for modes that have BC's held or simply supported at the edges, a simplification appears. The cross terms $\psi_p \psi_q$ representing $\sin \frac{\pi y}{b/p} \sin \frac{\pi y}{b/q} = \frac{1}{2} \cos \left([q - p] \pi y / b \right) - \frac{1}{2} \cos \left([q + p] \pi y / b \right)$ which shifted to the plate center, are odd functions. They integrate to zero as the formula in the tables [71, 437, #316] in Equation 35 verifies.

¹¹Equation 37 shows that this multi – mode estimate assumes very small deflections, $\Delta z_{max} \lesssim 0.57 \mu m$ for 5 % error, and $\Delta z_{max} \lesssim 0.80 \mu m$ for 10 % error, both for $N = 10$ modes on a 10 cm specimen using a $\lambda_{center} \approx 10 \mu m$ laser. For $N = 1000$ modes the minimum deflections go to 5.7 and 8.0 μm .

$$\int_0^b \sum_{p \neq q}^N \left(\sin(p\pi y/b) \sin(q\pi y/b) \right) dy = \left[\frac{\sin([p-q]\pi y/b)}{2[p-q]} - \frac{\sin([p+q]\pi y/b)}{2[p+q]} \right]_0^b = 0 \quad (35)$$

Since $y = b$ is a held edge BC, all of these cross terms cancel to produces the property that the integral of the square of these particular sums equals the sum of the squares, $\oint (\sum_1^N \sin \theta_p)^2 d\theta = \oint \sum_1^N \sin^2 \theta_p + 0$. Equation 35 provides the simplification for the expression for the multi – modal return of Equation 34. The uniform participation model allows the sum in Equation 36 to factor, resulting a single “correction” term (for the second order calculation).

$$\left| E_{mod} \right|_{M=0} \approx \int_0^b \frac{E_{in}}{b} dy \quad - \quad \frac{E_{in}}{b} \frac{4\pi^2 \phi^2}{\lambda^2} \int_0^b \sum_{n=1}^N \sin^2 \frac{\pi y}{b/n} dy \quad (36)$$

Bringing the integral inside the sum in the last term of Equation 36, the “correction” term, each summand is the same, $\int_0^\pi \sin^2 r\theta d\theta = \pi/2$ [71, 462, #629].¹² This result uses a “uniform participation model” (a uniform distribution). The highest mode number, N , is related to a cutoff frequency. N is the variable parameter that provides the estimate of vibration strain energy bandwidth in low frequency modes.

$$\left| E_{mod} \right|_{M=0} \approx E_{in} - 4\pi^2 E_{in} \frac{\phi^2}{b\lambda^2} \frac{N\pi}{2} = E_{in} \left(1 - 2\pi^3 \frac{(\Delta z_{max})^2}{Nb\lambda^2} \right) \quad (37)$$

Presuming a uniform modal participation, Equation 37 shows that to second order the deviation from a response from a flat plate with no vibrations (the first term) is inversely proportional to the cutoff mode number, N . The wider the response bandwidth, the less change to the return adding another mode makes. Physically, this insensitivity to cutoff number N (insensitivity to response with high frequencies content) is an effect of this being a one – dimensional displacement field. The 2 – D

¹²A constant coefficient of the sum for all modes ‘ r ’ forms up because a simplifying change of variables expands the limit by the same amount as the divisor, $d\xi = d\theta/2$ as $\xi(\theta = b) = 2b$.

form using Equation 34 modifies the correction term in Equation 37 via $\int_0^a \sin \frac{\pi x}{a} = 2a/\pi$ provides Equation 38 which is now a function of the beam width as expected. Using only one mode across the width, the return is inversely proportional to N . These estimates assume very small deflection, $w_{max} \ll \frac{\lambda}{4} \sqrt{\frac{Nb}{\pi^3}}$.

$$\left| E_{mod} \right|_{M=1} \approx E_{in} \left(1 - 4\pi^2 a \frac{(\Delta z_{max})^2}{Nb\lambda^2} \right) \quad (38)$$

Therefore, x dimension response restricted $M = 0$ or $M = 1$ exhibits this form of spectral reduction (insensitivity to high frequencies. However, for $M > 1$ (where, again, $N > 1$) the results are far more complicated and unlikely to provide simple monotonic results (such as the correction term proportional to $1/N$ above) since integrals of all orders and all combinations do not allow cancellation in the sum used in the transition from Equation 34 to Equation 36. This is convenient because it allows for spectral classification for perfect wide plates or more complicated structures. Equation 35 no longer represents all the cross terms in a way that factors out $\int_0^a \left(\sum_p^N \psi_p(\kappa y) \right)^2 dy$ with constant coefficients. This is a “necessary but insufficient condition” for CW return acceptance criteria (spectra, CSC’s, and MAC’s) to be adequate classifiers for actual rectangular plates. But these calculations show they appear to be poor classifiers for metal strips (beams).

A Matlab plot verifies the asymptotic nature of the response for $M = 0$ and $M = 1$ results (Equations 37 and 38) in Figure 10 on page 80 *without using any of the approximations* used to derive Equation 37. The upper pane of Figure 10 shows the deflection shape for very high mode counts becomes overly high at the edges,¹³ which is where the uniform modal participation model can break down, if we violate the very small deflection approximation, $(\Delta z)_{max} \ll \sqrt{\frac{Nb}{2\pi^3}} \lambda$. The lower pane of Figure 10 shows that including more modes makes little difference past mode 7; the return is insensitive to modes of higher frequency than mode 7. Thus, a moderate combination

¹³Actual modal participation is not uniform. A decrease in ϕ_n for higher modes would smooth the edge deformation effect in the upper pane of Figure 10.

of uniform ϕ and a modal participation cutoff at least 6 modes past the fundamental mode ($N = 7$) provides an adequate theoretical basis for a sufficient condition for the spectral elimination seen in the prior AFIT thesis¹⁴ [58, 6-1]; Each additional mode provides little change in the overall return. Therefore, the ability to distinguish one – dimensional mode shapes appears to be poor; these results predict difficulty in the use of laser vibrometry to classify return from different length beams, bars, or metal strips.

Having solved the simple system for a single mode in x ($M = 1$) using Equations 30 and 38, it appears possible that use of mathematical induction could obtain a closed form solution for M half modes in x along with these N half modes in y (the general rectangular structure). Equation 32 shows that for a sine swept system with only one mode along the short edge ($M = 1$), the CW integrated radiant flux return of Equation 30 has a dependence on all the modes. Similarly, expanding $M > 1$ past the $M = 1$ estimate, Equation 38, provides the similar mode sensitivity for multi – modal systems.

$$\Phi_e(t) = \left\langle |\vec{S}| \right\rangle = \frac{\epsilon_o c}{2} |\vec{E}_{mod}|^2 \quad (39)$$

Equation 39 provides detected radiant flux using the detected modulated field E_{mod} from these calculations or from the Matlab simulations in subsection 4.4 (page 92 ff).

4.1.5 Plane wave illumination spectral elimination. The prior half of this section showed the CW Radiant Flux received from modes above the fundamental mode of a flat beam or strip (one – dimensional deflection shapes) are weak functions of

¹⁴The prior AFIT laser vibrometry work introduced the qualitative argument that an increase in beam size covered more area that was at opposing phases; spatially integrating the phase change over a spatial cycle provides zero overall phase change as shown in empirical results [58, 4-2]. Section 9 of this thesis supports those results with sine swept and multi – modal theoretical explanations for spectral reduction.

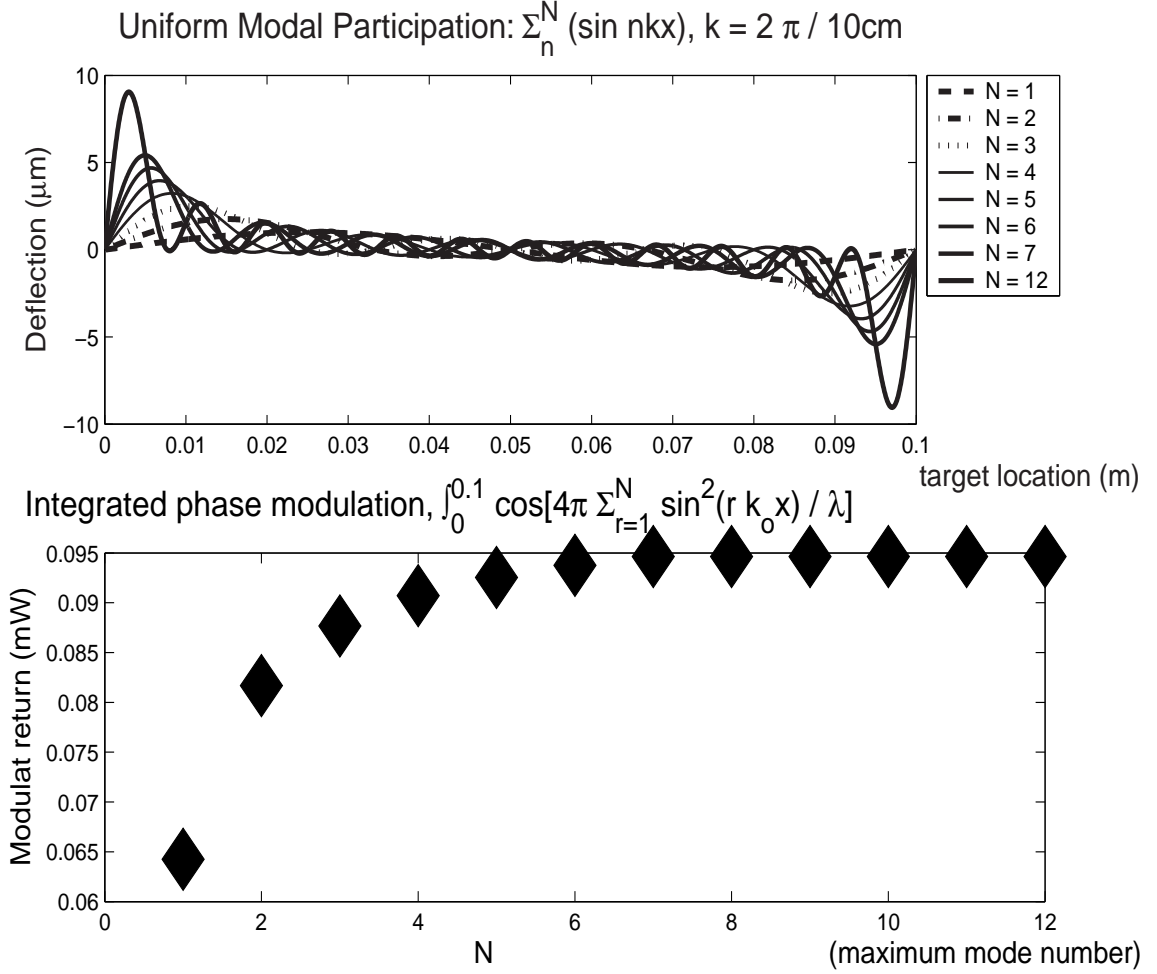


Figure 10: This full one – dimensional radiant flux result of Equation 37, without the presumption of a slowly swept sine excitation, **multi – mode** response shows modal $\Phi_e(t)$ variation decreases with N . This derivation assumes small deflection and a uniform modal participation for a set total of modes, N (the abscissa).

uniform modal participation¹⁵ response bandwidth. Sine swept second order estimates (Equation 33) are insensitive to the highest frequency mode number, N . Whereas the sine swept return from a wide plate in Equation 32 are. Second order multi – modal estimates (Equation 37) are inversely proportional to the bandwidth providing

¹⁵Modal participation in the classical sense is a linear systems parameter. Use in this context assumes that the linear system $[H(\omega_r)]_{p,q} = \psi_{pr}[j\omega - \lambda_r]_{r,r}^{-1}L_{r,q}$ [4, 44, 53] produces L vectors that may not remain constant because these modal participation vectors L_r in the matrix L do not necessarily normalized for a nonlinear system. A soliton is the extreme example where participation from different modes from different times coalesce to form a large persistent disturbance.

less classification for the addition of higher frequency modes than lower frequency modes. Multi – modal return from wide rectangular plates ($M, N > 1$) or more complicated structures are more diverse, prone to classification. These theoretical results summarized in Figures 9 and 10 for incident plane waves are similar to results seen in item 1, the laboratory laser Doppler vibrometry results [54,58], and in the simulation results (item 2 below). *Large spot size non – imaging CW return from single layer metal strips unconstrained on the two long edges have a theoretical return that is insensitive to the mode distribution.* Since return for two dimensional structures is a significant function of response modal distribution, modal classification for most moderately flat structures is at least adequate.

1. Φ_e from a flat strip / cantilever bar has spectral reduction in the lab similar to that calculated by this plane wave theory.

2. Φ_e from a plate simply supported on all edges has little spectral reduction for symmetrical modes. However, the higher anti – symmetric and un – symmetrical modes are subject to spectral reduction.

Trade study A’s results in Figures 26 through 35 show that low frequency symmetrical modes (108 Hz and a couple others in this plot) are mostly immune from spectral reduction due to a nonlinear contact dynamic effect. The second major resonance at 140 Hz in the 1 kN/mm case at the bottom is clearly related to the 180 Hz response for 15 kN/mm, without mode tracking concerns.

Table 4: Assumptions listed by Analysis Regimes

Item	Description
4.1	Atmospheric Turbulence is within the Inertial Range
4.1.1	Historical development driven
4.1.2	Domain of current laser vibrometry use
4.2	Coherent Specular target Exitance
4.2.1	Requires Propagation via diffraction
4.2.2	Detector's Φ_e image is coherent with Φ_{ref}
4.3	Transient response leads to Steady State
4.3.1	Structural impact, 3.6 ms (1.0 FWHH) duration
4.3.1.1	Deflection response follows load curve
4.3.1.1.1	Minimal integration error
4.3.1.1.2	Sufficient duration for integration
4.3.1.1.2	Steady state Normal Mode response follows
4.3.2.1	Impulse 'rings all normal modes'
4.3.2.1.1	Mode frequencies prevail in spectra
4.3.3	Energy loss
4.3.3.1	Structural damping 0.02 percent
4.3.3.2	Contact 'control law' damping
4.3.3.2.1	HRA energy deposited in hull upon lift – off

4.2 Physical and optical model assumptions

This chapter contains three main sets of numerical results that build on the theoretical result in Section 4.1. First is a set of mathematical results for closed form nonlinear analysis of simple contact systems. These provide a foundation for the FEA results including the validation normal modes analysis and the two trade studies. The last set of results is the optically detected modulated return data from the target. Each result section uses a different set of assumptions from two major categories, structural and optical.

4.2.1 Overview of the simulation assumptions. A list of assumptions for both the physical model and the optical model follows. Within these assumptions the set of analyses contain both structural and electrical engineering models of the response of this sensor system. First is a table of assumptions related to analysis followed by separate tables for structural and optical signal processing assumptions.

Table 5: Assumptions of the structural physical model

Item	Description
5.1	Small deflections and rotations
5.2	Simple Contact elements (CGAP's)
5.2.1	CGAP's remain aligned
5.2.1.1	negligible in $-$ plane shear
5.2	Simple Contact elements (CGAP's)
5.2.1	CGAP's remain aligned

As a first order assumption we assume not only that the atmospheric turbulence is in the ‘inertial’ subrange providing statistical atmospheric homogeneity and isotropy [9, 50], the first item in the assumptions listing in Table 4, but that there is no atmospheric turbulence. This work assumes the target has specular exitance that is coherent with the illuminating beam. Since the vibration field modulates the beam in a complicated manner, development of the detected field requires diffraction back to the detector where the received optical return is mixed with the properly expanded reference beam. The vibration source for the target is either random (trade study A) or has reached a sufficiently steady state after an impulse (trade study B). But the response is not entirely random, it is the modal participation factors that fluctuate randomly about a mean distribution where the structure and boundary conditions determine the mean distribution; the mean MPF distribution is not random. The work assumes negligible simulation errors, and that the excitation energizes lower frequency vibration modes. The system has customary structural damping and uses a bilinear contact stiffness at all nodes between the HRA and the hull. The mathematical development summarized in Section 4.3 indicates that some HRA vibration energy escapes into the hull at particular point locations every time the armor plate lifts off from the hull.

4.2.2 Structural assumptions. Table 5 describes structural assumptions.

4.2.3 Optical assumptions. Table 6 describes optical model assumptions.

Table 6: Assumptions of the optical simulation results

Item	Description
6.3	Gaussian cross – section illumination
6.3	Automatic reference beam gain control
6.3	Paraxial assumption
6.3	Fresnel diffraction
6.1	Stochastic FR – S and Paley – Wiener
6.1.1	historical development, current laser vibrometry use
6.2	Wiener – Khintchine [9, 30]
6.2.1.1	application on acoustic CSC provide time lags
6.2.1.2	potential to identify interior components

4.3 Results: Mathematical preliminaries

4.3.1 Simple systems that model structural contact. A major point of this thesis is that vehicle surface skins behave in a manner that avoids the spectral elimination discovered in a prior AFIT laser Doppler vibrometry thesis [58]. The saving grace of real structures are that 1) they are not as simple as flat plat cantilever beams or diaphragms used in the laboratory discussed in Chapter II (they have underlying structure complicating the response), and 2) structural response to engine idling and terrain load vibrations are not conservative, linear, time – invariant, nor uniform.

The second issue, the distribution and changes in modal (energy) participation factors (MPF's), is complicated. After some analytical work [94, 341] the FEA coding analysis community has shown transient impact response changes input PSD's to response PSD's in a manner where energy flows to low frequency modes. In the lab, the fall off of energy by mode number measured in automotive OEM laboratories is dramatic as is expected from the known nonlinear increase in generalized stiffness of the higher frequency modes. Due to this sharp roll – off, and the increase in density of modes with increasing frequency, most modal analyses only investigate responses below 400 Hz. In this section a two DOF model shows this concept with an increase in the 1 – D unsymmetrical mode frequency (which we will temporarily called ‘anti-

symmetric’ after the 2 DOF spring mass physics problem convention¹⁶) that is much different than symmetric mode frequency behavior for the same contact gap ‘closed stiffness’ value. Comparison of the ratio of frequencies of modes is an indicator of the relative stiffness ratio of an ‘effective mass’ model of those modes. The lower the modal frequency, the more energy it tends to receive, all other mechanisms and material properties being equal. Qualitatively we can see that contact surfaces (layers of skin or skin layers fastened to body frame and pillar structures) subdue unsymmetrical vibration modes (‘antisymmetric’ for the 2 DOF model). These physical systems are quite nonlinear and difficult to characterize.

This second section of the results chapter shows the mathematical foundations for single DOF (SDOF) nonlinear D.E. solutions, the stability of these solutions, the two DOF damped spring mass system eigenvalue problem complete with contact nonlinearity on the free end (modelling skin – vehicle contact). The next section describes a FEA solution related to an actual vehicle target ID structure.¹⁷ For linear systems (input x , output y) the system response any of the millions of DOF’s (in a full vehicle FE model) can be considered to follow the relationship as the SDOF system with stiffness k that has a response $G_{yy}(f)$ to an applied load $G_{xx}(f)$ [18, 125] shown in Equation 40. The damping coefficient ζ assumed common to all DOF’s modifies the resonance frequencies ($f_{damped} = f_n \sqrt{1 - \zeta^2}$). ζ should be less than 0.1. In this work it assumes the value $\zeta = 0.02$ typical for FE models of vehicles. This relationship does not consider contact nonlinearities.

$$G_{yy}^{SDOF}(f) = \frac{G_{xx}(f)/k^2}{[1 - (f/f_n)^2]^2 + [2\zeta f/f_n]^2} \quad (40)$$

¹⁶Although we have defined ‘unsymmetrical’ for 3 – D solid structures as the mode where the HRA and hull vibrate in opposition in z (at different times in different locations) this section uses the term antisymmetric as it is used in undergraduate physics classes for the sprung two mass problem as opposing Δz vibration (point contact). For 3 – D, ‘anti – symmetric’ is appropriate for a different dimension, the x,y model shape. See Figure 3 on page 31 for the symmetry naming conventions for this thesis.

¹⁷Actual military vehicle dimensions are different than those analyzed herein.

Linear multi – DOF response assumes a nearly constant input PSD $G_{xx}(f)$ for any single DOF over the frequency range $(1 - 6\zeta)f_n < f < (1 + 6\zeta)f_n$ for mode number ‘n’ [18, 126]. Application of the SDOF model over all DOF’s for linear structural response theory gives a relationship for a linear transfer function (Fourier transform of the impulse response) $H_i(f)$ where “i” is the DOF number. K_i is the generalized stiffness for that DOF. Each DOF in an linear time invariant (LTI) multi – DOF has a relationship that has the same form for the linear relationship shown in Equation 41.

$$H_i(f) = \frac{1/K_i}{1 - (f/f_n)^2 + j2\zeta f/f_n} \quad (41)$$

Equation 41 does not model nonlinear contact the FEA results will provide. The FE model stiffnesses are related to physical properties of the one by half meter inch thick Homogeneous Rolled Armor plate attached to a three inch thick hull with four 2 inch diameter A286 bolts.¹⁸

4.3.2 Single DOF Contact Nonlinear response. Appendix F Equation 88 on page 220 describes the ‘control law’ plotted in Figure 11 on page 88. The ‘control law’ shown in Figure 11 is the bilinear (nonlinear) contact stiffness model for a one gap element. Appendix F also describes how the damping DOF and frequency DOF are no longer related, issues useful in the subsection 4.4. This subsection describes the stability and application of this control law. The math follows Dr. Winthrop’s December 2004 AFIT dissertation [90]. This nonlinear contact control law for the damped oscillator is an addition to the suite of control laws Dr. Winthrop describes. Phase space (state space) plots such as Figure 12 validate its behavior. The arc-tangent function that does the switching in this simple closed form model appears in state space formulation as show below in Equation 42, which has the constants listed as Equation 43. The state space description for the single mass speed, v , and

¹⁸These dimensions define the structural physics but do not match existing systems.

acceleration, \dot{v} , shown in Equation 42 is a function of the open and closed stiffnesses, k_{open} and k_{closed} for a damping coefficient of $\zeta = \frac{d}{m}$ where m is the mass. The list of parameters in Equation 43 shows that the SDOF system models the fundamental mode of the welded panel¹⁹ system, where $f_o \approx 334$ Hz (the same value as the ‘hand’ calculation in Equation 62 and the FEA results in Figure 23b on page 115 and Table 7 on page 102).

$$\begin{aligned}\dot{x} &= v \\ \dot{v} &= -[(\omega_o^2 x(t))^{\frac{1}{2}} - \frac{1}{\pi} \tan^{-1}(rate \cdot x(t)) + \frac{k_{open}}{k_{closed}}] + \frac{d}{m} v\end{aligned}\tag{42}$$

$$\omega_o^2 = (2\pi 333.84)^2 \quad \frac{k_{open}}{k_{closed}} = 0.01 \quad \frac{d}{m} = 0.02 \quad rate = 100 \tag{43}$$

The transition to the high stiffness at $x \leq 0$ in Figure 11 is a smooth flet to model the collapse of surrounding protruding structure and imperfect contact plane. As x decreases into negative territory (deforming the structural contact surface) all the microscopic protuberances that comprise the surface roughness become compressed, and the stiffness switches rapidly to match the surrounding structure. For a “low” damping system the dimensionless damping $\mu = 0.02$ and the open to closed stiffness ratio is $k_{open}/k_{closed} = 0.01$. The plot in Figure 12 shows that the high stiffness during compression of the base is a shallow orbit, a vertically oriented orbit in the x versus \dot{x} plot. Changes in dimensionless damping change the range of the orbits during stabilization. The studies from which these plots came used the control law formulation described above and the Matlab system from Rice University [11].

A Lyapunov function analysis shows the system with the arctangent contact ‘control law’ (stiffness that switches) is asymptotically stable. The Lyapunov function turns out to be the total energy with simple damping loss. In rare cases vibration

¹⁹The term welded assumes the plate deflections at both points are the same using an infinitely stiff connection. The closed gap stiffness used in this work is more like hard rubber (see page 190) but the effect is the same.

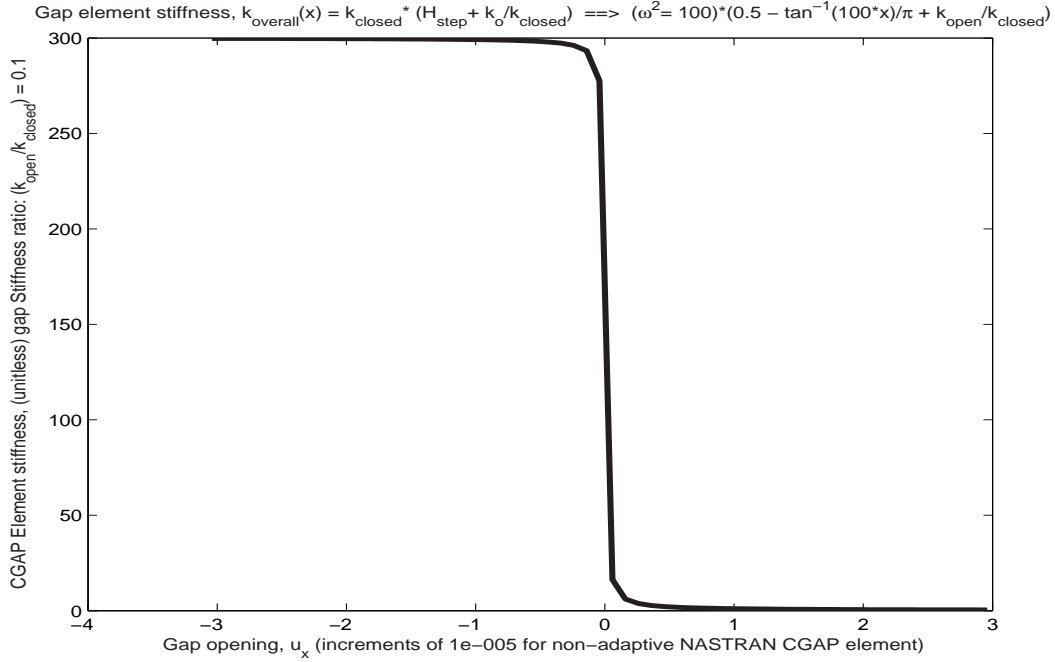


Figure 11: Using a moderately high contact “switching” rate for the argument of the arctangent function, $rate = \frac{1}{10mm}$, the open and closed contact stiffnesses matches the idealized bilinear structural contact.

energy gain to the hull matches the cycle’s damping energy losses and is in synch with plate contact. Persistent energy loss is due to structural damping, a general model for material heat losses due to bending and some fastener frictional losses. Appendix F summarizes stability and page 221 describes that the energy gain per cycle is less than the energy loss due to damping. In the case where the losses equal the gains, the system is merely stable isL (in the sense of Lyapunov).

In the event energy gain exceeds the damping loss per cycle, the mathematical model is not stable. In the realized system, such energy gains lead to component failure or at least nonlinear deflections including permanent set due to material nonlinearities that change the assumptions used in the FE model. The FE model only uses some geometric nonlinearities, large deflection and stiffness as a function of deflection, not material nonlinearities. These assumptions are considered appropriate in practice and thus are conditions for assumptions for asymptotic stability as well. Figures 14 and 17 on pages 106 and 109 show the FE model’s largest deflections in the

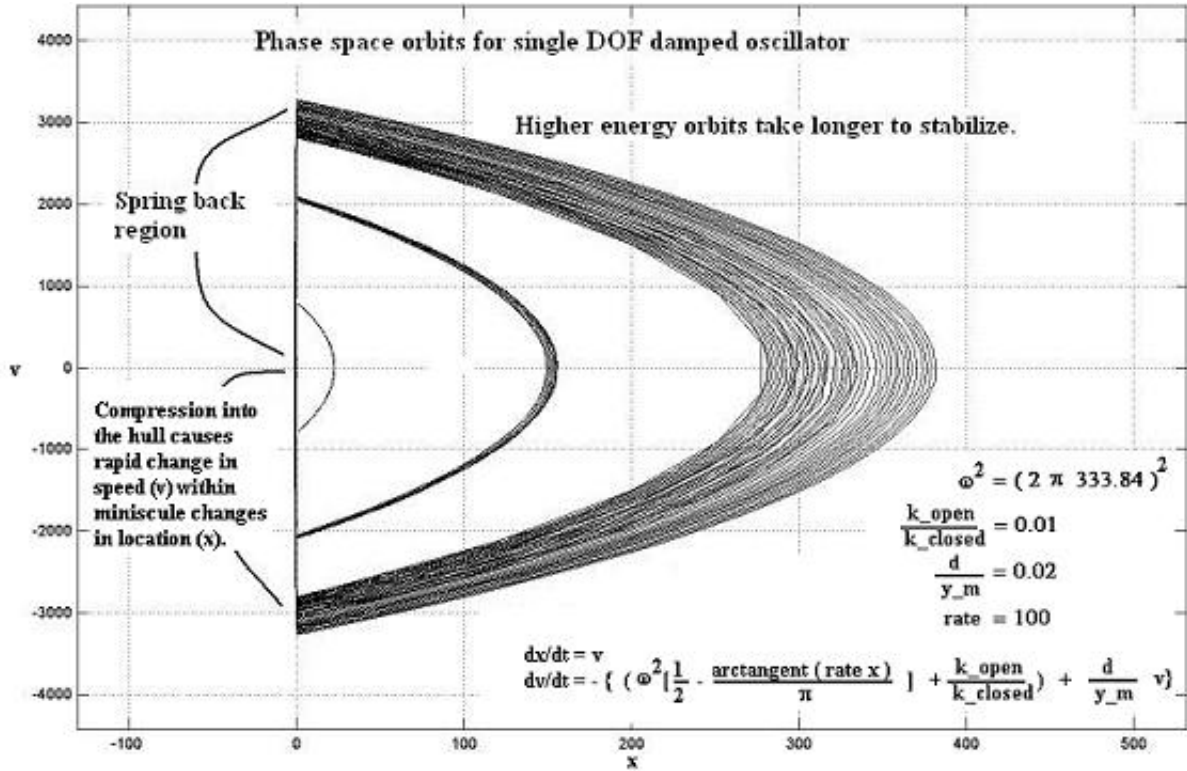


Figure 12: State space (phase space) orbits for the Single DOF damped spring mass system with contact nonlinearity using the Polking ‘pplane’ nonlinear Differential Equation solver. The arctangent based switching law appears in the \dot{v} second state equation in the title.

full three dimensional plate structure damp out with a factor of $\frac{1}{e}$ within 0.1 second for the structural vibration, thus validating the asymptotic stability assumption by FEA simulation.

Determination of the stability of the arctangent control law and general model is the basis to continue to a more pertinent multi – DOF model. The addition of one more DOF provides a relationship between contact stiffness and normal mode eigenvalues that FEA validates for many general structures with contact nonlinearity. Lagrangian formulation of the problem [81, 196 ff] provides essentially the same answer. Extended to its two DOF form, we see two solutions, symmetric and ‘anti-symmetric’ modes.²⁰

4.3.3 Two DOF system eigenvalues: Contact changes antisymmetric response.

Ideally, ‘control law’ stiffness should provide a ‘closed gap’ stiffness that is higher than the structural stiffness of the vehicle. This minimum stiffness of the ‘base’ is the resistance per millimeter deflection into the structure at a frame or stiffener. There are numerical stability consequences for having contact stiffnesses higher (and lower) than the equivalent ‘base’ stiffness, as well as validation results. Details are in Appendix F. It is customary to set physical properties, such as contact stiffness, to be uniform for a component where the structure is locally approximately uniform. The use of different closed contact or base stiffnesses can serve to model variations in armor due to hull wear, soiling, or maintenance. Development of the 2 DOF system helps show why this happens.

The FEA validates a major dynamical 2 DOF problem result: unsymmetrical modes increase in frequency for increases in contact stiffness. Investigation of these closed form simple damped sprung mass systems not only provides insight. Determination of the validity of the eigenvalue increase for anti – symmetric and un –

²⁰This ‘unsymmetrical’ mode for the 3 – D structure is the ‘anti – symmetric’ 2 DOF spring mass system of high school physics. In this work ‘antisymmetric’ means the structural half – wavelengths for a particular mode shape across the plate are even in number; most ‘antisymmetric’ spatial modes have a Chladni line down the centerlines of the plates. Nevertheless, for this section we use ‘antisymmetric’ in its classical meaning for the 2 DOF sprung mass solutions.

symmetrical modes when gap stiffness increases provides a basis for results seen in the FEA. Additionally, **this indicates that certain modes (‘symmetrical’) are better target identification features than others.** Hence the need to analyze the energy balance to validate the simple 1 and 2 DOF models.

Is the total energy a Lyapunov function? For our physical system, Appendix F shows that it is (or else the system would explode or collapse). Therefore, this model is a stable system which allows us to consider it representative of the hull – armor interaction for the case where both plates are artificially massively stiff (a ‘rigid plate model’) such that they contact everywhere at once when their centers of mass are within half the sum of their plate thicknesses. In order to prove the contrary we need to consider sources of energy gain. First consider the energy loss mechanisms.

A ‘rigid plate model’ contact ‘control law’ is considered to be an ‘elastic collision’ in the terminology of physicists.²¹ But even for an ‘elastic’ collision with no inertial consideration, energy from the HRA plate or its point mass model transfers from the ‘armor’ mass to the ‘plate’ mass upon impact.

If we consider inertia and flexibility of the plate and hull, the armor and hull will travel together for a short period of time such that it cannot be considered a complete collision in the classical billiard ball sense.²² A transfer of energy to the hull occurs upon ‘lift – off’ when the contact distance is positive. FEA simulates such energy transfer back and forth in detail. However, the mathematical one and two DOF simple contact models assume this energy never comes back to the armor plate, a practical assumption for a simple system.

Therefore, the mathematically simplified one and two DOF models have discrete energy losses from the armor plate (the HRA) into the hull which then dissipate. This

²¹This is nearly the opposite of the terminology of structural stress engineers who call an elastic system one that allows strain, one that has some measure of flexibility. Consider the contrary definition of a collision; “An inelastic collision is one in which the kinetic energy of the system of colliding bodies is not conserved.” [36, 265]

²²Billiard ball collisions have this problem too, but on such a minor level that we can consider them infinitely hard and therefore they complete the collision in negligible time.

indicates that the total energy equation is a Lyapunov function. The actual physical system, due to the flexibility of the hull, can transfer vibration strain energy from one location into a different location in the plate. But the total energy can never exceed the original energy as long as there are no exotic gain mechanisms (such as in solitons or with nuclear decay or magnetic induction). For an ordinary system of slapping, contact vibration plates on a vehicle skin the model should be asymptotically stable. We can easily show that it is stable in the sense of Lyapunov if we remove structural damping. The system is stable isL because the energy is bounded even in the bizarre case where the vibrations are tuned just right to pump all the hull strain energy into the armor plate, which is about the only way we are limited to the system only being stable isL. Otherwise we know that damping will eventually lead to an essentially zero energy state.²³

The result of this section in Figure 13 on page 105 is that the 2 DOF system is adequate to indicate that symmetrical structural modal frequencies remain constant whereas anti – symmetric and unsymmetrical modes increase in frequency with increasing contact stiffness. This is the same result that inspection of the FEA mode shapes and nonlinear FEA results in Figure 25 on page 119 provide. Identification of this feature provides a feature to distinguish between similar models of the same vehicle by sensing the change in resonance frequency of modes that are not symmetrical.

4.4 Results: Finite Element Analysis

The results of the two main trade studies include analysis of both the time splined deflection response and the optical return from the simulation of the phase modulation on the large spot size CW laser probe. Supporting background for that work includes analysis of the time history responses and normal modes analyses.

²³A boom box is not ‘Lyapunov insurance’ (does the vibration ever really go to zero?). Although there is never a real zero state, except perhaps quantum mechanically, we consider negligible energy states to be zero energy states and thus the hull – armor interaction is asymptotically stable, not merely stable isL.

A major spectral result is that for trade study A Figure 25 on page 119 shows that impulse response at 223 Hz ranges from 11% to 41% of the 108 Hz response, increasing in center frequency with gap stiffness, as Section 4.3 predicts. This inter – model feature indicates wear or structural modification while the symmetrical mode at 108 Hz stays stationary indicating the “vehicle model” which is a $(1 \times \frac{1}{2} \text{ m})$ rectangular 2 layer plate in this case. While the symmetry BC’s described in subsection B.2 on page 176 constrain fully antisymmetric modes, mode 3 displayed in Figure 23 on page 115 is antisymmetrical on the one axis and is therefore the suspect mode for the 223 Hz response. The “hand calculations” in Appendix C which match many of the modes in Table 7 on page 102 included the “large mass” in the model (details are on page 185 including the footnote citing calculation sources, resulting in Equation 59 on page 205). These matches help validate the FE model. The impulse response for trade study B in Figure 36 on page 136 is larger at 223 Hz than at 108 Hz but this appears to be due to the shape of the mode 3 response such that the impulse and the ‘large mass’ representing internal structure drives that mode more than the others, a reasonable response case.

4.4.1 Structural FEA study B : Time History Response. Since the spectra for structural impulse response does not require the averaging that random response does, the time response for a particular impulse is an adequate model of the response time history (raw un – averaged random response time histories are not). This section starts with a look at trade study B time response. FEA direct transient (MSC/NAS-TRAN’s SOL 129) response time history in Figure timeHistory on page 106 shows a “half” life ($1/e$, 37 percent) for the full model approximately between 20 and 40 ms for different parts of the model.

An estimate for an overall equivalent of this decay constant is the μ that was used in the single DOF phase space study in Figure 11 on page 88 and in the dimensionless 2 DOF simplified mathematical nonlinear contact simulation as in Equation 80 on

page 216. This is directly related to the common viscous damping coefficient,²⁴ ζ , used in Equations 40 and 41 on page 85. This dimensionless form of the DE's is the basis for Figure 13 on page 105 that shows the eigenvalue behavior for anti – symmetric (un – symmetrical) modes, the frequency increase with increasing contact stiffness.

4.4.2 FEA Time History Response: Contact Response. Figure 15 on page 107 compares deformed shape plots (left hand side) to the optical radiant flux images (right hand side). This figure shows two points in time, 1.74 milliseconds being midway through the outwardly oriented impulse directed into the top two panes and the system as it approaches steady state at 15.98 milliseconds in the lower two panes. Deformation plots on the left are from the MSC/PATRAN²⁵ FE modelling pre – and post – processing tool. These plots of the HRA upper surface only, show the un – deformed shape (flat) and the deformed shape. The deformed shape is greatly exaggerated in order to see the micron level displacements. The view alignment is along the long edge in order to align lines of nodes across the plate for a better view of the relative displacement of the hull and armor plates. So the FE model appears foreshortened in the figure. Images on the left are oriented differently than the deformed shapes. A view of the similarly organized MPEG movie derived from all the PATRAN plots shown with their sibling radiant flux (CW) images synchronized to within 20 ms, “almostSynch01.wmv,” conveys the utility of phase modulation to represent remote spectral ID.

Compare the structural response (FEA output) for fully transient sources calculated for times well into steady state (Figure 38 on page 140) to the gravity step and post gravity random responses in Figure 27 on page 124. The optically sensed CSC magnitude returns in returns for the transient (impulse) source in Figure 41 on page 143 compare similarly to the random response with and without gravity step

²⁴In actual complicated structural systems, the damping is not uniform over the entire structure but we assume constant damping here, $\zeta(x, y) = \text{constant}$.

²⁵www.mscsoftware.com

transient in Figures 32 on page 129. The latter random plot set shows a sharp strong diagonal (variances) and is not affected by the gravity step.

The bolt configuration (study B) results of direct transient response FEA provided five major results.

1) The ‘hull only’ (armor – less) structure has nearly an order of magnitude greater structural amplitude than the full HRA – hull system.²⁶

2) Structural vibration stationary appears to start within four pulse lengths after the 3.6 ms, 1.0 FWHH impulse. This is a shorter transient duration than we see in the ‘image SNR’ of the optical return by Equation 44 on page 98 in Figure 40 on page 142.

3) Figure 40 shows the behavior after 80 ms is quite a different ‘stationary behavior,’ an obvious change in the nonlinear effect of contact for minuscule deflections. Later results from analysis of the (simulated) detected radiant flux confirm that the ‘post – transient’ region before 80 ms is not really stationary as seen from the splined time history in Figure 17 on page 109 and in the optical return spatial image SNR plot for trade study B in Figure 18 on page 110. Optical stationarity requires 120 ms (more than 33 impulse widths after the applied impulse load) for this transient system, trade study B.

4) The FEA passed validation tests for this lightly damped system without much change from prior more ‘coarse’ time steps of 0.2 ms. The transient range used refined 0.01 ms steps in the final trade study B results leading to confidence that the load and time increments introduced little error.

5) Running trade study A with and without gravity compared to the fully transient trade study B shows the CSC matrices become more diagonal as the loading became more purely random, among other effects.

²⁶Since the hull – only structure was subject to the same load for 75% the mass, we expect it to respond more. An armor – less hull will have different design objectives than armored hull. So this is not a fair comparison of relative modal energies.

Inspection of the time domain response²⁷ not only shows the real dominance of the 108 Hz mode.²⁸ Most of the out – of – phase appearance of the time histories in plots of the raw data is due to the abscissa being in time step numbers rather than time value at the step. Figure 17 on page 109 shows the uniform time scale version of the time histories. In that figure what little out – of – phase appearance from the multiple plots of a central node for all the configurations in the ensembles that remains is a real phase and multi – mode vibration response effect. This behavior is partially described by the structural CSC of the spatially averaged spectra in Figure 38 on page 140 and is adequately matched by the simulated optically sensed CSC in Figure 38 on page 140.

These trade study B MSC/NASTRAN FEA result file ensembles of splined time histories plotted against time, display the transient impact (impulse) load time region as the short (3.6 ms, 1.0 FWHH) duration event it really is. The random variable is the armor attachment bolt cross – sectional area. Figure 16 shows the variable time steps on the abscissa that result in many splining operations required for the Matlab Fourier transform operator `fft` (a DFT operator). The top pane shows the response for the hull alone, without the armor surface plate to vibrate in contact against it. These strong modal responses provide a nearly discrete FRF as expected [81, 167].

The HRA – hull vibration deflection responses (the lower two panes of Figure 17) compare to the nearly comb nature of the ‘hull only’ model without the armor plate (upper pane) as if they were passed through a convolution with a time band of period T or rect function of frequency, f . This indicates a ringing in the Fourier domain, a multiplication of the ‘hull only’ system spectrum with a $\text{sinc}(Tf)$ system / filter, a set of repeated harmonics surrounding each mode’s frequency (and a low pass 300 Hz

²⁷ “FFT is a batch process. Impacts or other transient processes which occur in time frames which are short compared with the period of the analysis time block result in significant amplitude errors in terms of peak values. Therefore, a user should always view the time domain when transients are present.” [16]

²⁸ Compare the subtle 4.5 ms periodicity in Figure 17 on page 109 to the increase of the 223 Hz mode response from random response lows in Figure 25 to the impulse response case where modes coalesce near 223 HZ in Figure 37 on pages 119 and 139.

filter). In comparison to results in Section 4.3 this result is precisely what detailed solutions of the nonlinear differential equations like the Duffing equation [15] show, a set of super and sub harmonic resonances. These extra harmonics tend to move in frequency. The structural FEA industry has dealt with such resonance movement for decades. The technique to manage this movement of frequencies with design (not a necessarily nonlinear harmonic issue) goes by the name ‘mode tracking.’ The noise and vibration test community has systems of analytical gear that perform the similar function of characterization of these harmonics for nonlinear systems.²⁹

In order to save space this FE model used the non – uniform time steps, an adaptive nature of the time increment calculations in MSC/NASTRAN. The FE model mesh density had already been reduced to recover from a NASTRAN default disk space problem and special allocations was not desired. The first processing of the time response history data required for spectral analysis is to spline the data in order to allow Matlab to Fourier transform the time histories into spectra.³⁰

4.5 Simulation results: Structural and optical response

Sub – sections that follow include an analysis of responses at each location (pixel) for each load case, analysis of the time response history, and frequency response analysis for trade studies A and B.

4.5.1 Time History Response of Optical Imaging Return. For every NASTRAN time step there are at least two Matlab time steps. A movie (MPEG) comprised of these images, almostSynch.wmv is ‘almost synchronized’ because in requesting output for both all nodes, creating all the deformed shape mesh plots for the 0.1 second duration, the time increment calculation is slightly different for the same input deck (except a change in displacement output set) because the NASTRAN punch

²⁹Some of the vendors are www.bksv.com and www.vibrationresearch.com. The seismic analysis community has a set of systems to measure these nonlinear harmonics as well, from a different set of vendors except that Brüel & Kjær equipment has been the largest player in the noise and vibration industry.

³⁰The fft command requires uniform time sampling since it is essentially a DFT process.

file requests top surfaces only for the optical imaging simulations, the translations to Matlab target grid displacement variables.

From the optical return the simulation provided an ‘image SNR’ of Equation 44 related to the dynamic range of the pixels versus the average signal across all pixels (a form of noise power, S_{noise}). This integrates the pixel by pixel response, $\Phi_e(x, y; t)$, into a single metric for a particular time frame, $SNR_{img}(t)$. While SNR is not yet a detection method (ATR requires an estimate of the noise power) the changes in SNR and the spectrum of its history over time matches the structural modes well.

$$SNR_{image} = \frac{E[S_{image}(x, y) - \bar{S}_{image}(x, y)] \cdot E[S_{image}(x, y) - \bar{S}_{image}(x, y)]^*}{S_{noise}} \quad (44)$$

The spatial average of the image SNR’s from Equation 44 causes the values plotted in Figure 18 to sharply approach zero as deformed shapes approach flatness. Image SNR periodicity is more clear in SNR time histories (Figure 18 on page 110) than spectral SNR plots shown in Figure 19 in yet another example of the need to inspect the time history first [16].³¹

The more stable region after 120 ms in the “long duration” time history in Figure 18 makes it clear that the decrease from the 80 ms to 120 ms region is a transition to a stationarity. These reduced levels represent the loss of energy of the surface into the hull and into damping, and a new nonlinear contact dynamics.

In a continuation of the “look at the time history” guidelines, a manual plot of vertical lines representing two frequencies measured ‘by eye’ from the time history in Figure 18, are in Figure 19. These frequencies match the Normal Mode fundamental modes for stiff and flexible contact (eigenvalue analysis is necessarily linear) where the first two eigenvalues for both “contact stiffnesses” are approximately 108 Hz. The

³¹Periodicities of 9.3 and 4.5 ms relate to 108 and 224 Hz, the fundamental and first indicator modes. For this work the image SNR spectra of trade study A (not shown) track these two modes better than any other metric.

peaks at the first mode group at 108 Hz, near the second mode set at 220 Hz, the third at 340 Hz, and on, match the normal mode frequencies and are easy to see in the time history plots. As shown in the Normal Mode plots in Figure 23, the ‘hard contact’ eigenvalue relates to 340 Hz (the next resonance of the SNR after 224) and the ‘soft contact’ eigenvalue is related to 224 Hz. The eigenvalues, $\lambda_i = \omega^2 = 4\pi^2 f_i^2$, are proportional to the square of their related modal frequencies. Considering the NASTRAN value of 223 Hz, this is a remote sensing error of less than 0.5 % done ‘by eye’ and on the plot.

4.5.2 Normal Mode Frequencies. The Normal Modes are the eigenvalues of a structural FEA special eigenvalue Problem (SEVP) where the load is set to zero. These mode frequencies take structural damping ($\zeta = 0.02$) into account. The DFT of the time histories of the nonlinear transient FEA results (SOL 129) will necessarily be more related to the ‘open gap’ and ‘closed gap’ frequency response than that of the hull only, as the full spectral plots and even these normal mode frequency comparisons in Figure 20 on page 112 show. The normal modes are useful because the nonlinear system does excite both sets of modes; the nonlinear response is a combination of mostly the ‘open gap’ and ‘closed gap’ systems.

The fundamental mode at approximately 108 Hz shows up in all the systems. This is the symmetrical mode of the FE model, generally always the mode with the most strain energy and therefore the most deflection. The response results are a Fourier transform of a time integrated solution (SOL 129) verified by those eigenvalue solutions (SOL 103 ‘normal modes’). The 224 Hz mode 3 of the open gap system³² shows up well in the Fourier Transform of the time history FEA direct transient response (SOL 129). This result is the frequency of an armor and hull composite system where the HRA is under a vacuum of about 7 inches of mercury ($k_{open} \approx 0.5MPa$ where $P_{atm} = 0.101325$ MPa). This soft “stiffness” only serves to stabilize

³²See Table 7 on page 102 and Figures 20 and 23 on pages 112 ff.

the solver numerically.³³ This HRA – only mode appears in the transient results and their frequency spectra, as well as the 4th and 5th armor modes just above 300 Hz. The 2nd through 4th ‘closed gap’ modes are also in this region just above 300 Hz. We see these validations by comparing the eigenvalues that the eigenvectors (mode shapes) of Figures 21 through 23 represent, compared against the averaged structural deflections of Figure 36 and received optical radiant flux $\Phi_e(x, y; t)$ of Figure 37.

The phase plots for the mathematical nonlinear SDOF and 2 DOF models, such as Figure 12 on page 89 from the math in Section 4.3, show that the nonlinear structure at different points in time and space uses both eigenvector solutions. When the gaps are open, the lower frequency mode dominates (large orbit for $x > 0$) and vice versa. However, in the nonlinear FEA plate system a combination of modes is active and the contact is at different locations in space for a given instant in time. Therefore switching between modes is much more complicated. This dynamics could be characterized as a stochastic combination of open and closed contact oscillators but definition of the distribution would be a challenging task.

Analysis of the structural frequency response results shows that solutions seen in the mathematical section, Figure 13 on page 105, apply to this simple slapping plate nonlinear contact structural skin model. Plots of the averaged spectra for all six different gap contact stiffness in Figure 25 on page 119 show the unsymmetrical resonances increase in frequency with increases in closed contact stiffness. The ‘soft’ contact model (gap stiffnesses of 50 N/mm) has far more deflection taken by the HRA plate alone. The soft FE model represents the open contact vibration modes. The ‘hard’ contact model, 2,000 N/mm, represents the closed stiffness solution and couples

³³Single and double DOF closed form solutions like those described in Section 4.3 starting on page 84 can have analytical solutions. However, multi – DOF systems like this small 2900 DOF FE model can have numerical problems with convergence as all the 286 gaps are iterating towards solutions together. This mass numerical solution combined with coupling of axial and other loads at a distance providing additional interaction between elements is a modest coupling that FEA is capable of in this simple flat FE model. The FEA solution requires some stiffness. This “small” 50 N / mm value is known from experience to stabilize most full automotive FE model components at this mesh density.

more deflection into the underlying hull (hull deflection plots, not shown, were a part of FE model checks).

These eigenvector NASTRAN SOL 103 normal mode deflections in Figures 21 through 23 are normalized by effective mass for display. In the direct time integrated Newmark – Beta SOL 129 NASTRAN transient results the deflections are in microns; For modal recognition those images are also exaggerated in order to more easily identify the shape. Nearly all the transient models pumped the majority of energy into a combination of mostly first, second, and third modes, both open and closed contact. The shape the MPEG video most follows appears to be similar to the third mode. For the Fourier transform of the transient time deformation histories, this is a wide but sharp peak (cone to the top) centered approximately at 220 Hz.

Table 7 outlines the relationship between normal mode frequencies and the two major modal response frequencies for the transient nonlinear contact solution. The ‘pane’ (column 2) refers to the twin figures (Figures 21 and 23 on pages 113 ff) where the deformed shape for ‘open contact’ system modelled as a soft contact appears in the upper pane, ‘a.’ The ‘hard’ contact system (modelled as “welded” or epoxied with hard rubber, see page 190) appears in the lower pane, b. The three FE models used for the SOL 103 Normal Mode solutions were an open contact model (“soft gaps”) a model of armor welded to the hull (“hard gaps”) and a model without the armor (hull only).³⁴ There are three ‘fundamental’ modes, one for each structure, open gaps, closed gaps, and hull – only. Since the hull – only model generally assumes the same deformation shape as the hard contact case, these shapes are not shown.

Emphasized frequencies in Table 7 indicate ‘symmetrical’ mode shapes that Figure 25 on page 119 shows are not changing in frequency as the gap stiffness increases. These modes act like two masses in series vibrating in synch per Figure 44 whose results are in Figure 13 on page 105. Figure 23 a and b are symmetrical along the

³⁴Figure 22 b is almost half symmetrical with mirror symmetry along the y axis but this mode compresses into the plate along the ends (long axis is x). It is almost symmetrical as a half model symmetry along the y axis. But there is a bit of anti – symmetry in the plan view pattern parallel to y at x = 0.

Table 7: Normal modes undergoing transient excitation

Figure	Pane(U/L)	f(Hz)	Mode and Type	Comments
21 a	Soft gaps	105	1, Symmetrical	fundamental mode
21 b	Hard gaps	108	1, $\frac{1}{4}$ Sym. shape	fundamental mode
21 b	Hull only	109	Mode 1	fundamental mode
22 a	Soft gaps	127	2, 90 % Symmetrical	penetrates 2 edges
22 b	Hard gaps	306	2, $\frac{3}{8}$ Sym. + $\frac{1}{8}$ Anti	x not contained
22 b	Hull only	308	Mode 2	$\sim \frac{1}{10}$ BC constraint
23 a	Soft gaps	223	3, Sym x, Un- & anti- on y	width wise slapping
23 b	Hard gaps	344	3, Sym x, Un- & Anti- on y	” (alternating)
23 b	Hull only	380	Mode 3	$\sim \frac{1}{2}$ BC constraint

long edge, x, and both antisymmetric (plan view pattern) and unsymmetrical (about $z = 0$ surface) along the short edge, y. This indicates that slapping alternates on either edge of the short width so that the frequency of this mode will probably be higher in the actual nonlinear contact structure. The rest of the modes appear to align more easily with modes that increase in frequency with increasing gap stiffness (unsymmetrical modes).

Comments at the end of the ‘Hull only’ rows indicate the extent to which the symmetry conditions delineated in Section B.2 on page 176 constrain the indicated mode (open, closed, *or* hull). Since these are not simple one dimensional modes and the constraints are not the same on all four edges (otherwise they would not model a reasonable vehicle panel) the “desire” by the FE model to have the indicated mode shape will be modified as the time integration evolves. Therefore, the mode that would have been used in a common modal transient analysis (Solution 112)³⁵ will have been changed, if not all modes. This is another reason besides accuracy to use direct transient (SOL 129). More than likely just the indicated mode will change and this assumption is a part of the “nonlinear eigenvector” analysis in Section 4.3 on page 84.

³⁵An investigation of the Modal Complex Eigenvalue solution (SOL 110) may yield a different set of eigenvectors (mode shapes) but since the structural damping is not large they should not be different from the simple normal modes displayed in this section.

The resulting magnitude of maximum deflections was a purposeful application of a small (one g) impulse load. The “small deflection” is crucial for the simulation of optical image propagation, to avoid phase wrapping and the severe simulation consequences of wrapping combining with quadratic phase effects including aliasing and cycle skipping and their interaction due to use of a Matlab target grid. In the soft contact model (gap stiffnesses of 50 N/mm) there is far more deflection taken by the HRA plate alone. The ‘hard’ contact model, 2,000 N/mm (reference page 190), represents the closed stiffness solution and couples more deflection into the underlying hull (model check hull deflection plots not shown).

The existence of a strong 223 Hz resonance in the Fourier transform of the nonlinear contact response time histories (for the least stiff gap case) indicates that the open gap mode 3 appears to have a resonance and higher frequency contribution from 223 Hz to approximately 250 Hz (almost as strong as the 100 Hz resonance). The 250 Hz mode appears to be higher in frequency due to the partially unsymmetrical (in z) and antisymmetric (in x, y) that these two modes exhibit. Figure 25 shows the 223 Hz mode stays stationary with changes in gap stiffness indicating a symmetrical mode, while the 250 Hz nonlinear mode shifts higher. The discussion about Figure 13 on page 105 indicates the stationary nonlinear mode is a symmetrical mode and the stiffening mode (250 Hz) is an unsymmetrical mode akin to the “antisymmetric” two DOF spring mass physics problem; the clatter of the armor hitting the hull in a synchronized manner causes the nonlinear 250 Hz mode to increase in frequency for increasing gap stiffness.

4.6 Frequency Response: Optically Imaged Radiant Flux

The two types of Radiant Flux considered in this thesis are imaging, $\Phi_e(x, y; t)$, and non – imaging, $\Phi_e(sample; t)$ which has been spatially integrated over the detector by Equation 45. Figure 24 compares ‘imaging’ flux, a matrix of ensemble averaged flux values for each pixel in the 400 by 400 simulation array, to non – imaging flux,

a spatially integrated ensemble set of total flux for each sample (configuration or random load).

4.6.1 Imaging Laser Vibrometry Time Response. The spatially integrated radiant flux $\Phi_e(x_i, y_j; t)$ in time (Equation 45) is the input data for subsequent spectral response calculations. These sums of all detector pixels (x_i, y_j) per time frame t for the propagated target modulated responses necessarily have less fine structure compared to structural FEA output time histories.

$$\Phi_e(t) = \int_{-\frac{a}{2}}^{\frac{a}{2}} \int_{-\frac{b}{2}}^{\frac{b}{2}} \Phi_e(x, y; t) dx dy \cong \sum_{i=1}^M \sum_{j=1}^N \Phi_e(x_i, y_j; t) \quad (45)$$

Real λ_1 , 2 DOF nonlinear spring mass contact damped ($F=2\mu \, dx/dt$), $\mu = 0.02$ sys. Dimensionless freq. $2\pi f = \psi = 0.5$

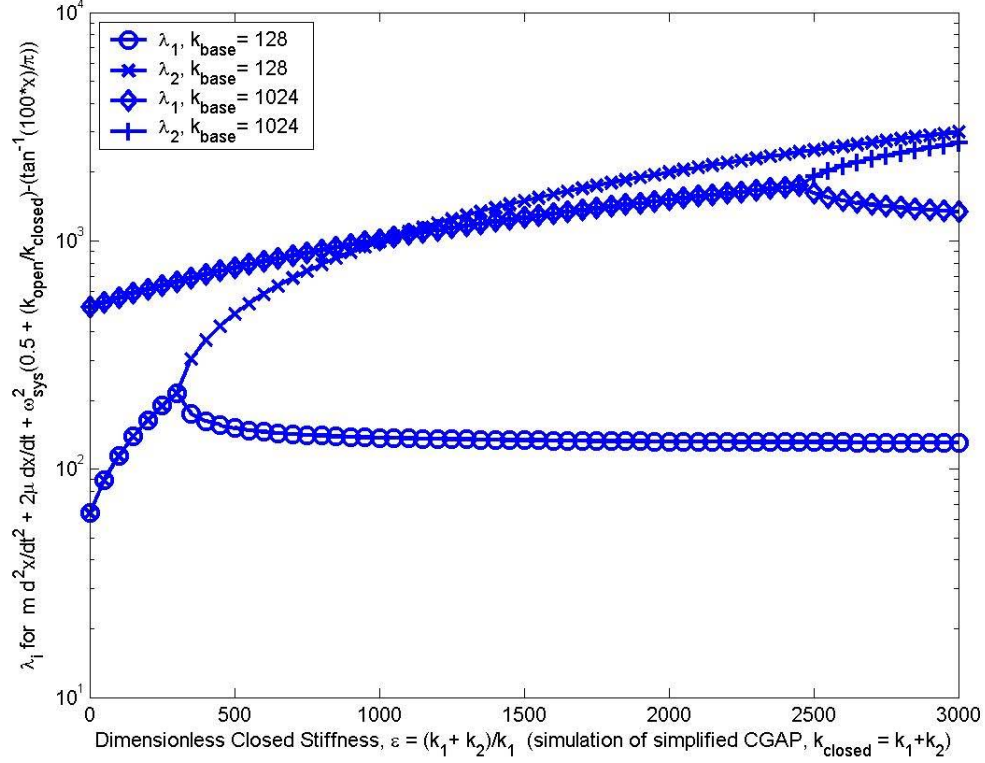


Figure 13: Real eigenvalue parts subdue antisymmetric mode: The symmetric (lower frequency) and antisymmetric (higher frequency) modes [81, 167] for this two DOF problem break out into modes of well separated energy. The arctangent based switching law appears in the label for the ordinate axis.

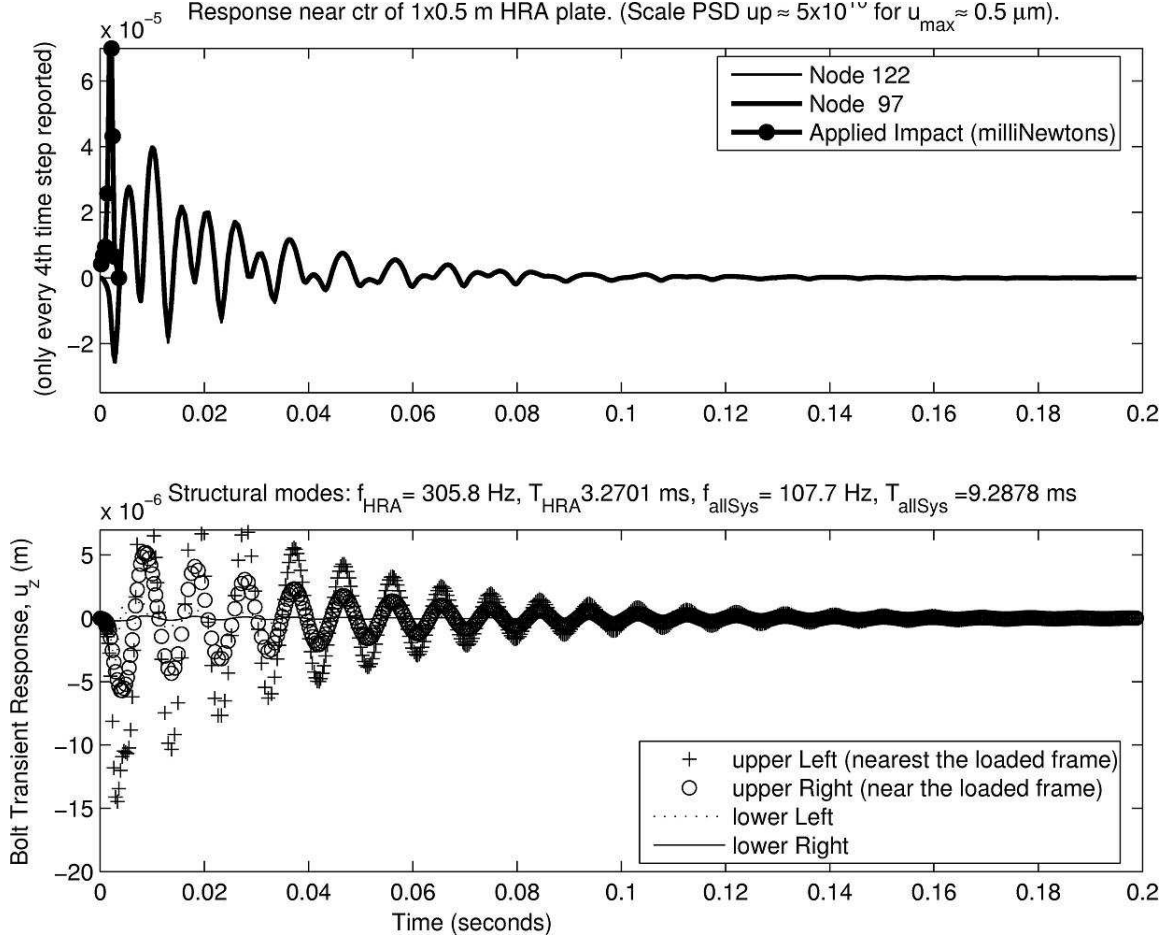


Figure 14: The 3.6 millisecond structural impulse clearly rings modes other than that corresponding to its 1.0 ms FWHH duration, 1.5 kHz (using the 3/2 rule [44]). This impulse does not excite the closest modes to its inverse half period which are the higher order modes (above mode 5) of the linear closed gap system. The damping of the plate interior decreases the response by $1/e$ within 25 milliseconds. The lower plot shows that the ‘frame’ regions of the plate, with FE Model elements that model attachments to a ‘system mass’ where the loading takes place, appears to have a larger decay constant, as expected.

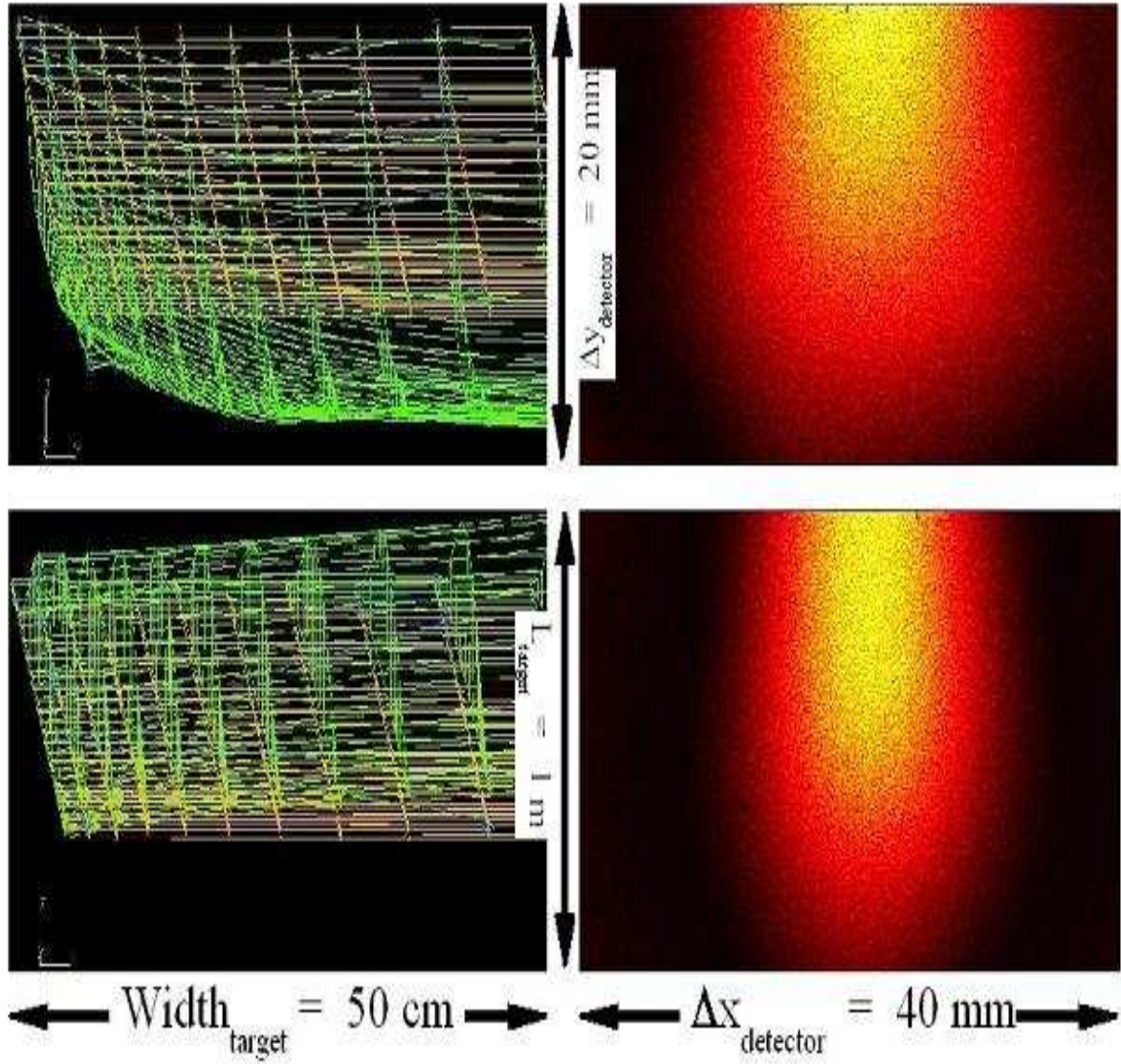


Figure 15: These typical FEA impulse deformation impulse response deformed shapes (left) and Optical Radiant Flux images (right) are for the times 1.74 ms (top panes) and 15.98 ms (lower panes). Where the target is 1 m long the image falls on the long 40 mm detector edge (foreshortened to show gap and plate deflections).

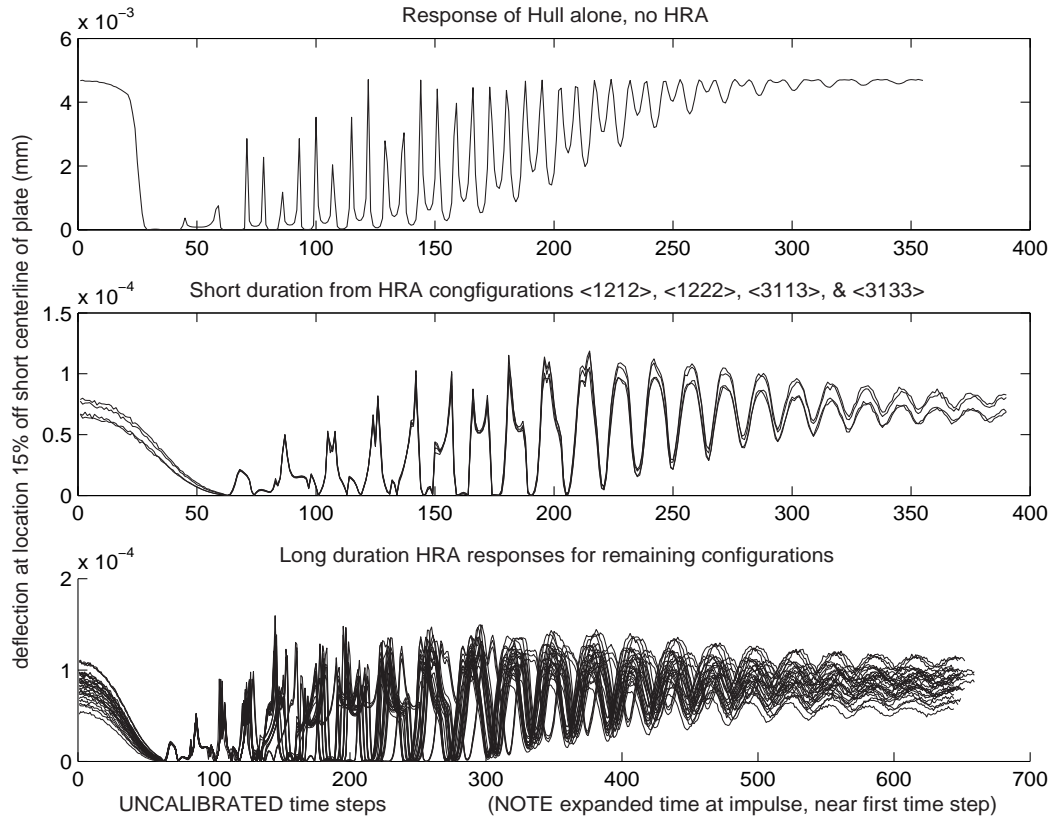


Figure 16: Trade Study B: The ensemble of un – splined time histories with the random variable being the armor attachment bolt cross – sectional area **plotted against time step** expands out the transient impact (impulse) load time region. Zero deflection is the approximate location of the maximum deformation just after the impulse.

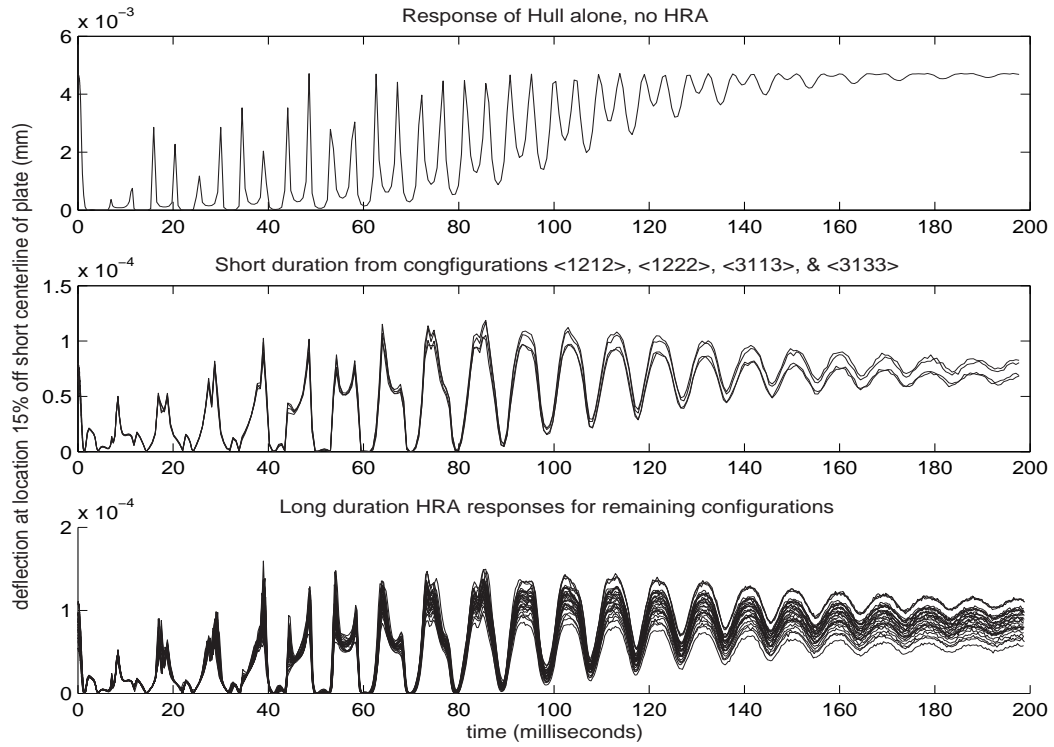


Figure 17: Trade Study B: Variation ensemble deflection ($\overline{w(x, y; t)} = \frac{(\Delta z)_{max}}{2}$) time histories, **fit to a uniform time scale**, show the major 108 and 224 Hz modes. The bottom two panes show the higher mode as a dip in the major maxima.

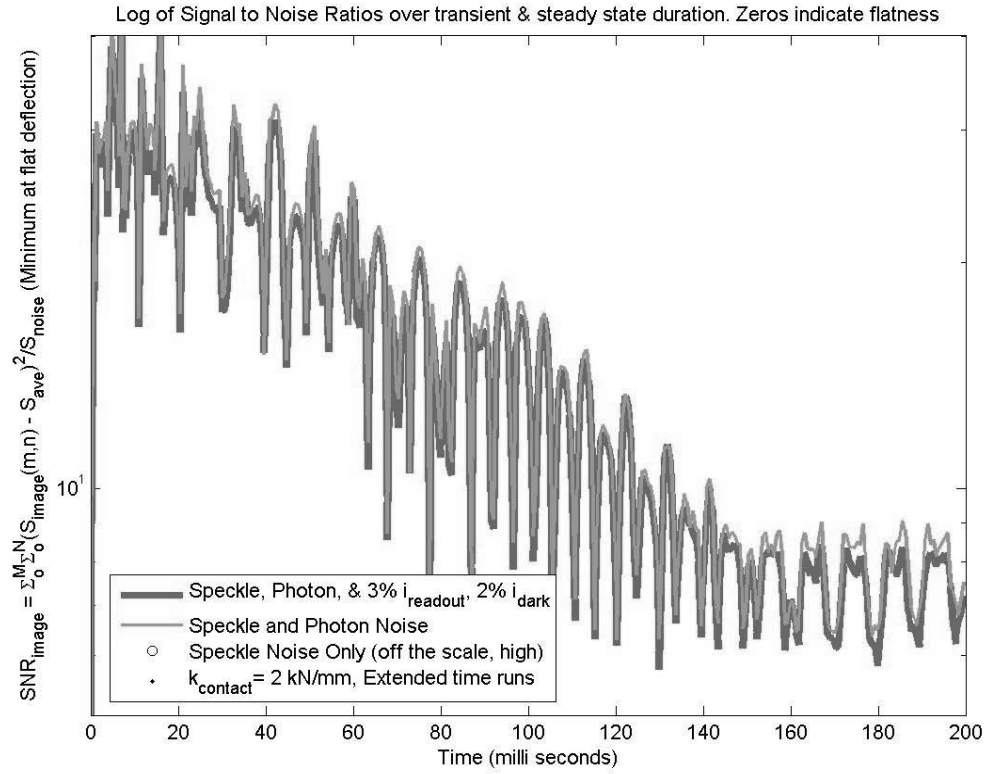


Figure 18: Trade Study B: The long time history of spatial SNR_{img} ratios show the convergence to constant values after 140 milliseconds for this 3.6 ms (1.0 FWHH) impulse, albeit at a lower level.

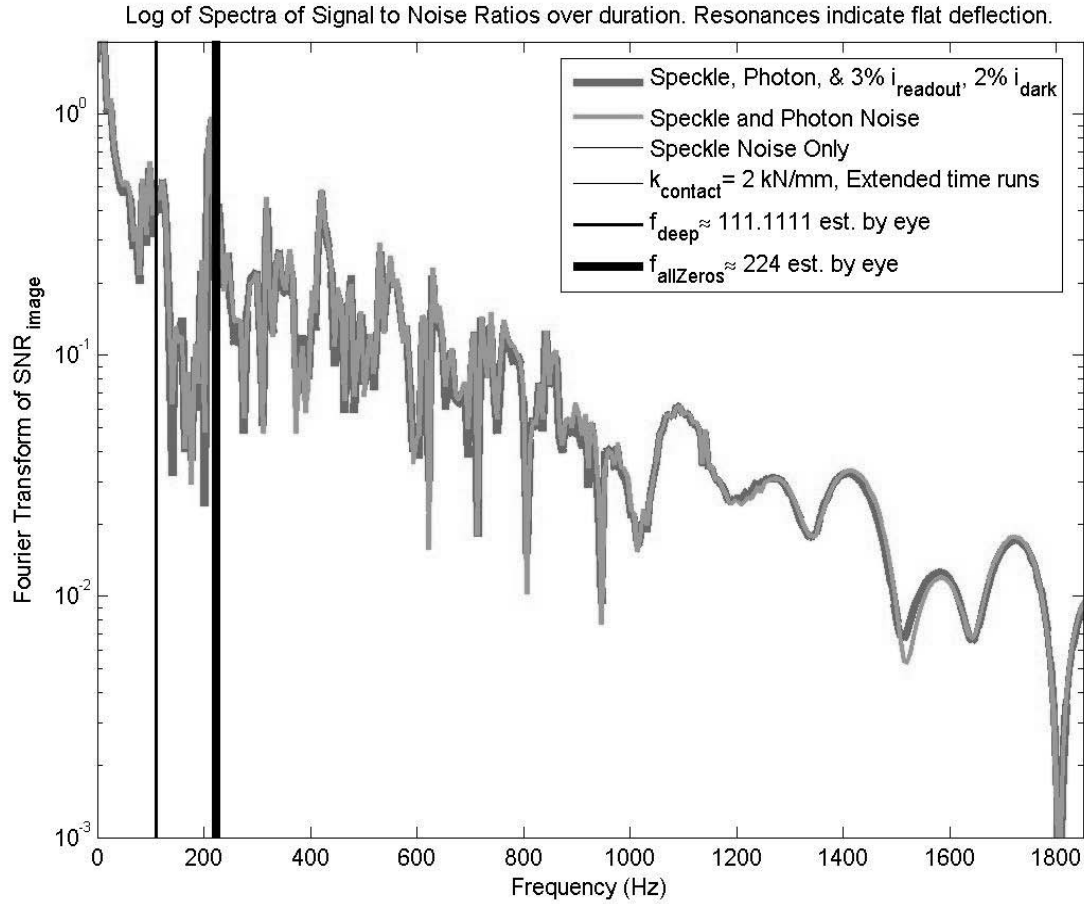


Figure 19: Trade Study B: The spectrum of spatial SNR_{image} Ratio Spectra for Long time history, a DFT of the “Image SNR” as a function of time of Figure 18, shows the 108 and 224 Hz mode groups (highlighted by vertical lines) that was apparent from the harmonic nature of the prior SNR time history plots, Figure 17 on page 109. This initial study had other noise sources before the restriction to speckle only photon limited assumptions for the rest of the work.

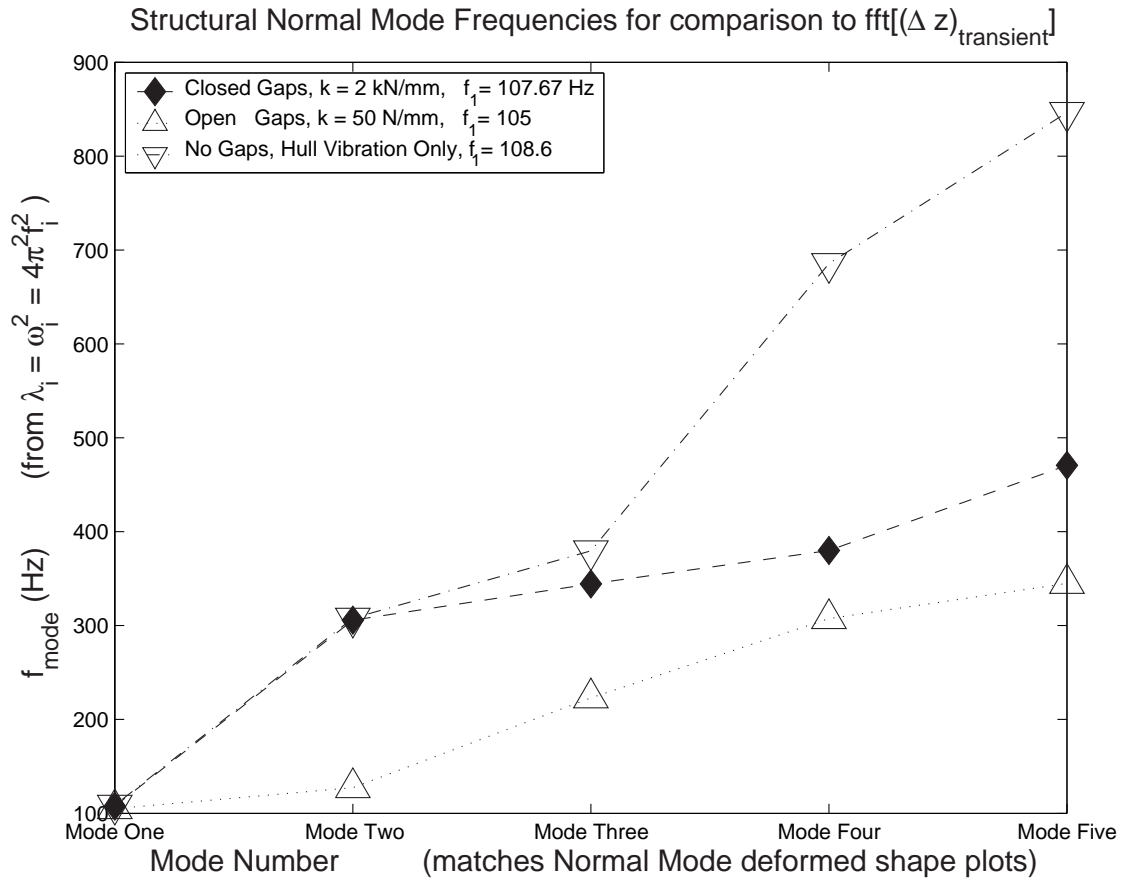


Figure 20: Structural Normal Mode Frequencies for ‘soft’, ‘hard’ and no contact – the first three mode shapes of the closed gap system nearly match those of the hull – only (no armor, laboratory plate vibration) system. Figures 21 through 23 show the mode shapes.

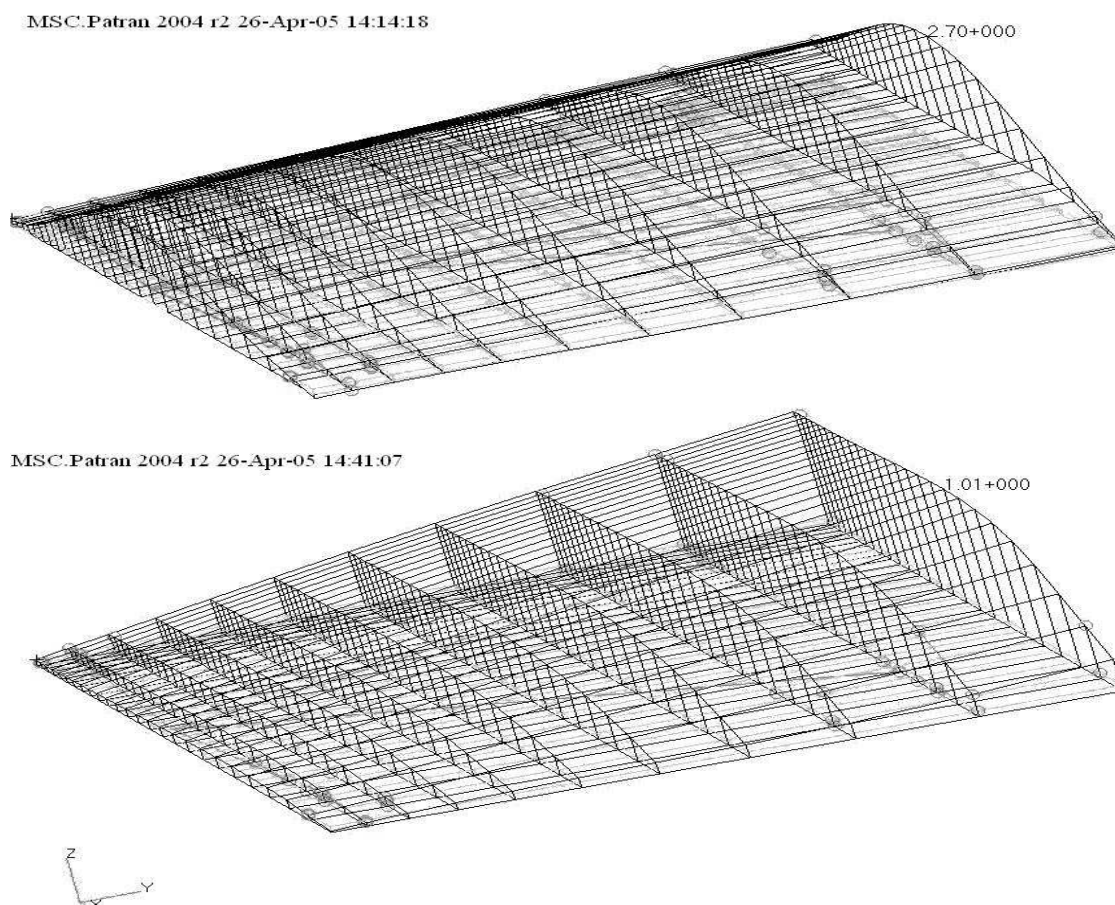


Figure 21: First (fundamental) normal mode, soft (upper) and hard (lower) contact: The fundamental frequencies are 108 Hz (lower 'hard' model), 105 Hz (upper 'soft' model), and 109 Hz for the hull only model. 'Hard' model and the 'hull – only' model mode shapes are indistinguishable.

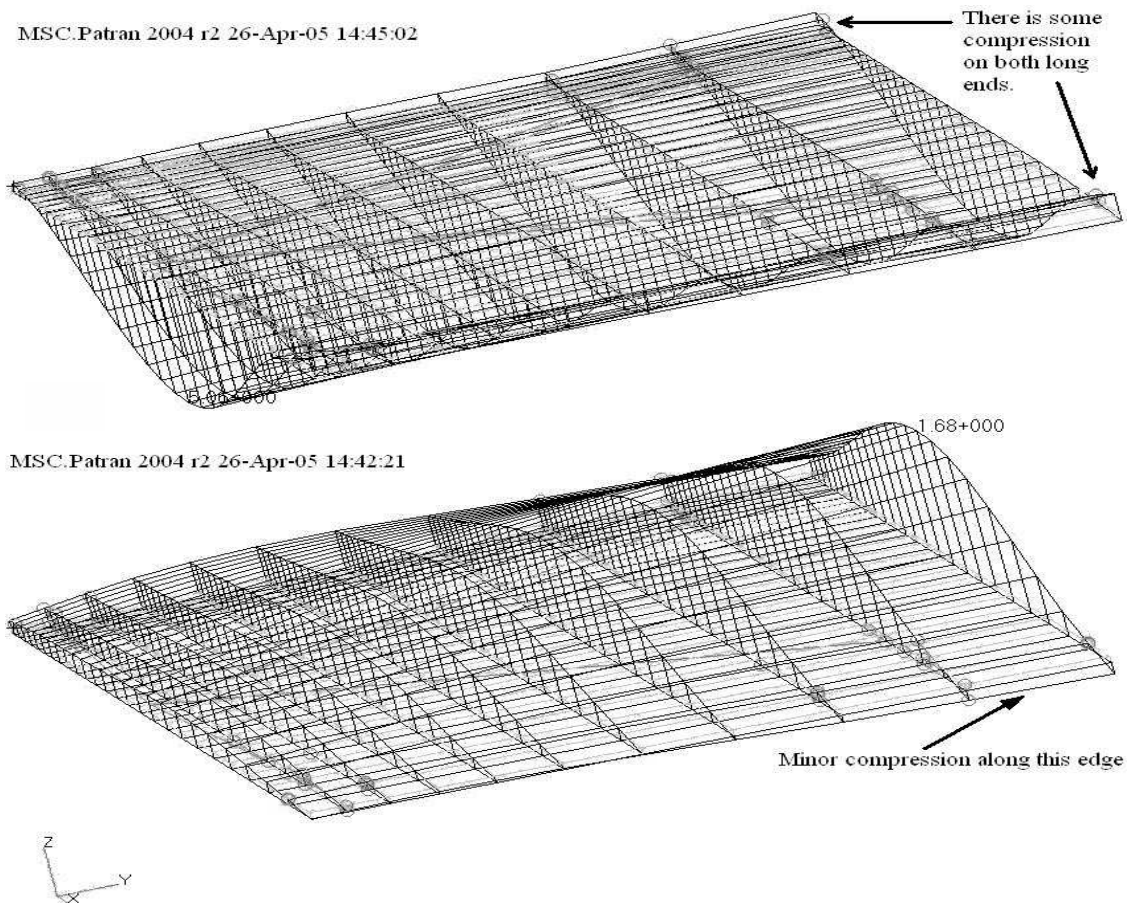


Figure 22: Second normal mode, soft (upper) and hard (lower) contact: Mode 2 frequencies are 306 Hz (lower 'hard' model), 127 Hz (upper 'soft' model), and 308 Hz for the hull only model.

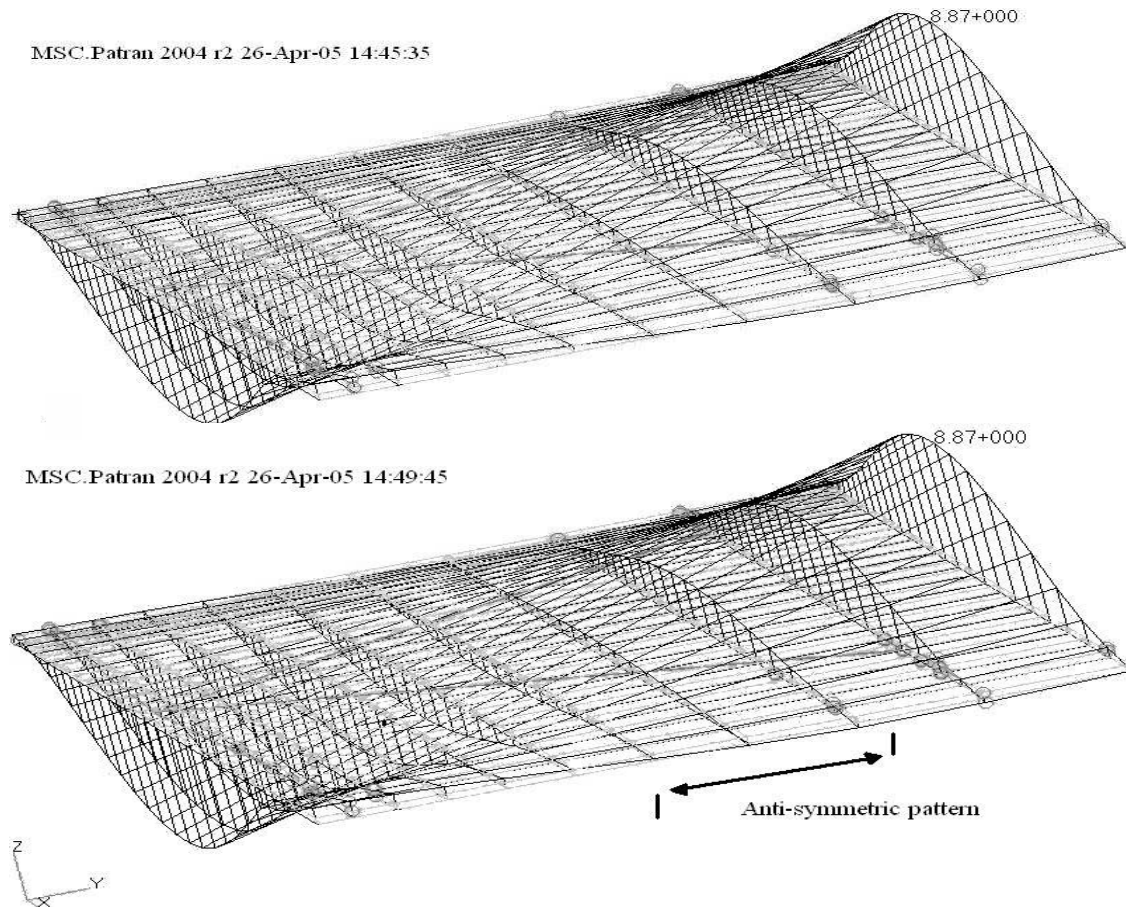


Figure 23: Major Nonlinear Mode Responding to Impulse – This third normal mode is the soft (upper) and hard (lower) contact eigenvalue / eigenvector from the SOL 103 solution sequences. Mode 3 frequencies are 344 Hz (lower ‘hard’ model), 223 Hz (upper ‘soft’ model), and 380 Hz for the hull only model.

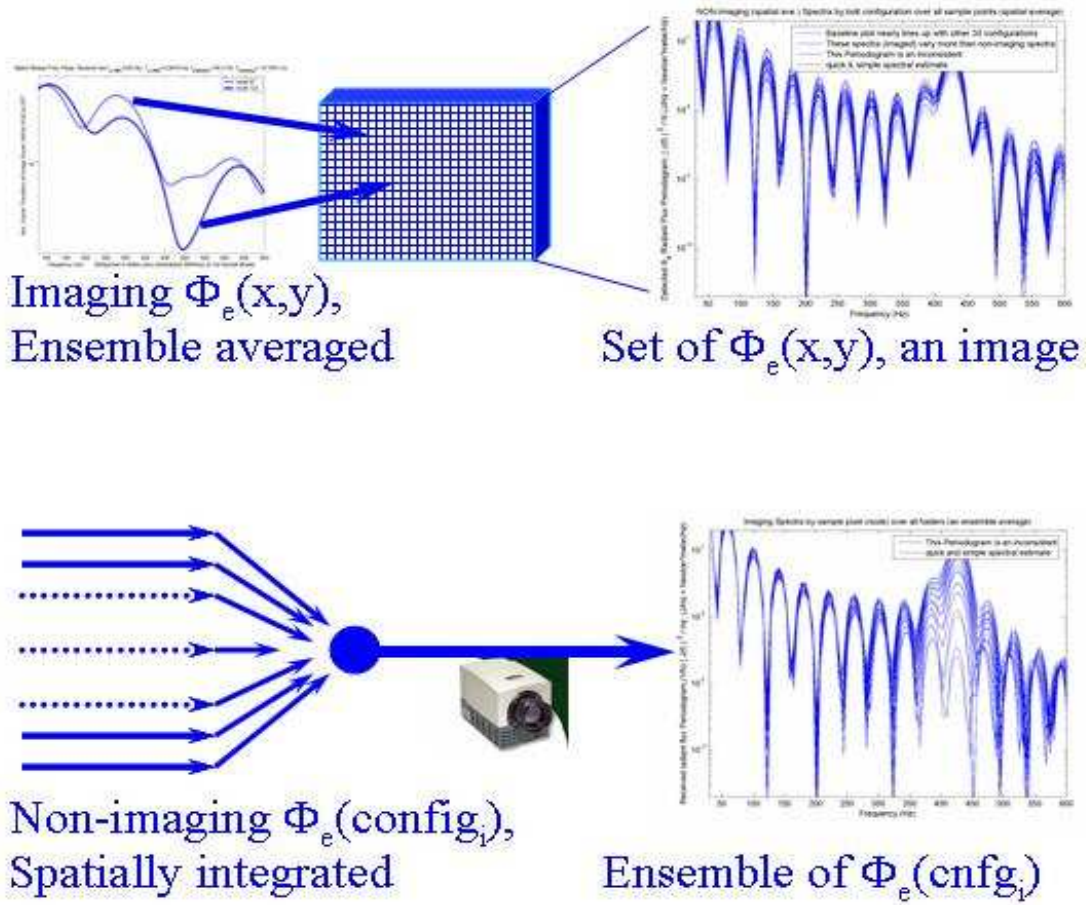


Figure 24: **Imaging** $\Phi_e(x, y; t)$ is a set of pixels, each of which has an ensemble average of responses. Non – imaging $\Phi_e(sample; t)$ is an ensemble (set of configurations or random load responses) of total flux values.

Table 8: Baseline FEA configuration

Structure	Matlab
$k_{contact} = 2 \frac{kN}{mm}$	400 × 400 target grid
stabilizing $k_{open} = 50 \frac{kN}{mm}$	range of L = 4 km
$t_{max} = 0.1$ sec duration	nominal mixing $E_{ref} \approx 1.0 * E_{return}$
A286 bolts, D = 1 inch	initial beam width 0.05 m
target is $1m \times \frac{1}{2}m$	$\lambda_{laser} = 10\mu m$
$t_{HRA} = 1$ inch	$F_o = 1km$
$t_{hull} = 3$ inches	$(\Delta z)_{max} = w_{max}$ scaled to $\frac{38}{14}\mu m$
0.4 mN max Gaussian impulse over 3.6 ms	w_{max} drives Poisson noise

4.7 Results: Trade Studies, vertices from a baseline analysis

In order to reduce the effect of the number of analyses being the product of the permutations, each permutation starts with a baseline configuration shown in Table 8. This is not a complete summary of the modelling assumptions.³⁶

4.7.1 Study A: Random Response, Contact Stiffness. Trade study A uses a set of 30 random loads. This academic design variable exercise is not indicative of the engine load, or any terrain load. The analysis results for $k_{contact} = 1$ kN/mm are similar to the baseline 2 kN/mm stiffness results, which was the model for all trade study B results. These contact stiffnesses match values used at General Motors in the 1990’s for nonlinear contact (2 kN/mm for relatively ‘fine’ meshes such as this). A comparison of contact stiffnesses to real structural values appears in subsection B.2.5 on page 190. Figure 25 (impulse) and Figure 26 (random) show the spectral response for each of the gap stiffnesses, 1kN/mm, 2, 5, 8, 10, and 15 kN/mm. Figure 25 on page 119 shows that symmetrical modes (108 Hz) remain stationary with increasing stiffness whereas un – symmetrical or anti – symmetric modes increase in modal frequency (220 Hz). Small stationary spectral spikes representing symmetrical modes are at 108 Hz (quarter panel fundamental mode), and at about 210 and 315 Hz (system and HRA fundamental modes). The unsymmetrical and antisymmetric modal spectra flatten

³⁶Physical assumptions are in Appendix A, FEA assumptions are in Appendix B, and Matlab assumptions are in the preceding Chapters and summarized at the beginning of this Chapter.

out into higher frequencies in the 220 to 300 bands as higher contact stiffness increases. While the 220 Hz mode shows a high response, the time domain plot appears to display little high response at 220 Hz except for the hull – only case. These higher frequency components are blocking off the 108 Hz sine wave response but are not a sharp 220 Hz sine wave because that ‘resonance’ is more broad, triangularly.

Before running random response for the stiffness variation study (trade study A) the impulse load for trade study B was the excitation for the plot of spectral response for each different contact stiffness value in Figure 25 on page 119. The fully random response in Figure 26 on page 121 shows a similar characteristic but not as clearly and with reduced mode 3 response. Figure 26 uses spectra with positive frequency only (one – sided) Periodograms, the Fourier transform of the cross correlation. Since the impulse load ‘rings the modes’ more cleanly than even the one – sided Periodograms, Figure 25 is the better figure to use to compare different gap stiffnesses. A copy of the $k = 2$ kN/mm random response appears in Figure 26 for comparison. Figure 26 on page 121 plots spatially averaged (non – imaging) spectra for several different gap contact stiffnesses. We see that the 220 Hz ‘nonlinear’ mode showing up after decay of the transient loaded system in trade study B (Figure 37 on page 139) is not prominent in the random response, trade study A. There is a small 210 Hz response, apparently distinct from the 223 Hz we would expect from the third soft gap normal mode (Table 7 on page 102). The large magnitude of the 210 Hz mode in Figure is a decayed transient load generated effect that appears to have merged with the 250 Hz response for the 2 kN/mm case.

The structural response spectra from the bolt load path set of data for 0.2 second duration in Figure 36 on page 136 shows that care taken to select a better time region and longer time histories for spectral analysis greatly improved the spectral resolution over the prior 0.1 second results. These impulse loaded trade study B responses are clearly more coupled to the normal modes of Table 7 on page 102 than the trade study A results. The trade study A random load results in Figure 26 on page 121 are averaged over 30 different loads. Figure 26 shows the random response is almost

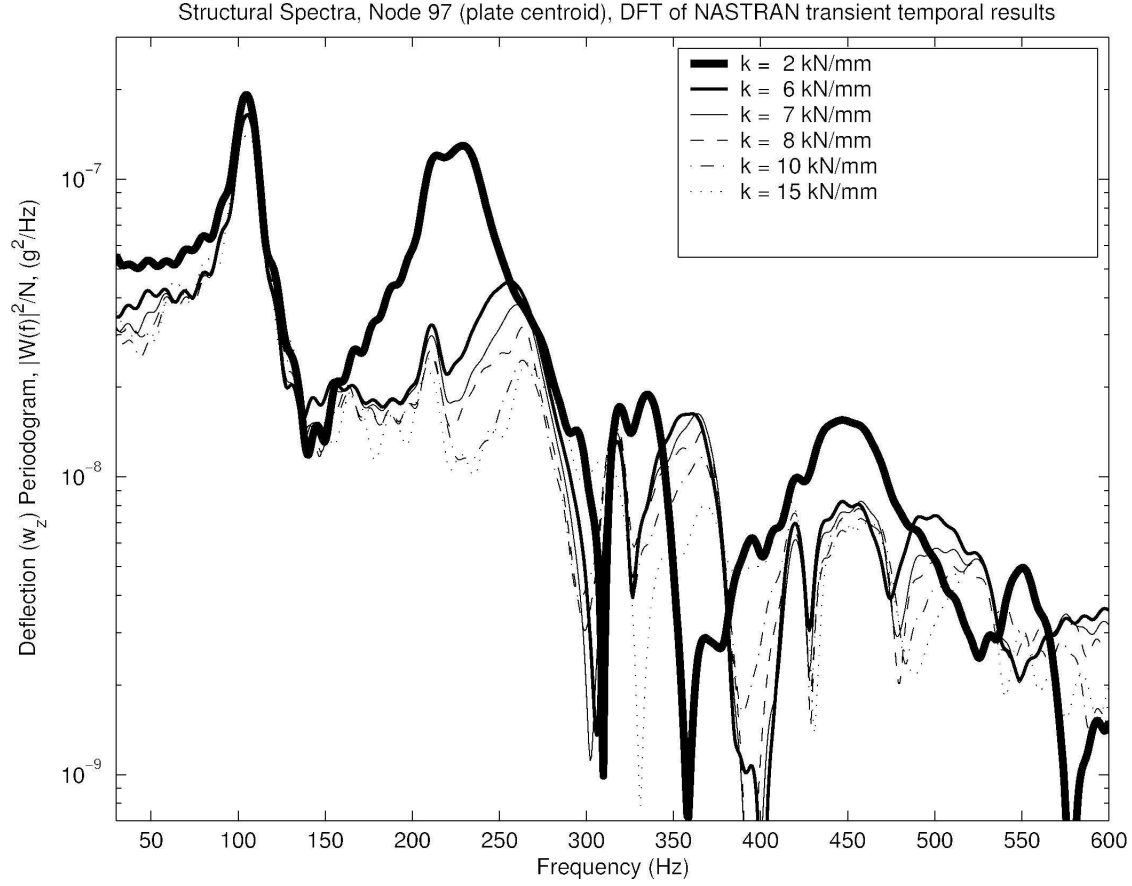


Figure 25: Trade Study A: Structural Vibration FEA Spectral Displacement Responses $FRF_w(f; k_{contact})$ (using the trade study B impulse load) for various $k_{contact}$ shows frequency stationarity of symmetrical modes (at $f = 108, 210, 315$, and 420 Hz). This set is a precursor to the random response for trade study A. This set shows that for all the resonances the response decays and moves to higher frequencies except the fundamental 108 Hz mode and a few others that appear to be component symmetrical modes. The full random response version is in Figure 26.

entirely concentrated on the fundamental 108 Hz mode; the 200 Hz mode so prominent in Figure 36 is more close to the noise and, except for the 210 to 225 Hz low response valley, is almost not visible.

While the symmetrical mode stationarity is easier to see in the impulse loaded optical return responses, Figure 26 on page 121 does show an 80 Hz mode at 1 kN /mm moving, as stiffness increased, through the 108 Hz fundamental mode that is stationary through 11 kN / mm. This non – symmetrical 80 Hz mode is related to either the large mass full system (Equation 59 on page 205) or the 4 – fold system (four of these FE models acting with the symmetries in a $(1 \times 2 \text{ m})$ plate as shown in Figure 51 on page 198). The 140 Hz mode at 1 kN / mm moves past 150 Hz for 2 kN/mm and keeps increasing after that. Identification of the 108 Hz mode for structural ID using random loading requires mode tracking effort because the unsymmetrical and antisymmetric modes move higher in frequency for higher contact stiffness, as expected.

The imaging form of the CSC in Figure 30 on page 127 has a clear plateau initiation at the fundamental mode, 108 Hz. This requires high resolution; transfer of an JPEG to eps image will not retain these features. This fundamental stationarity feature is constant over all gap stiffnesses at 1, 2, 5, 8, 11, and 15 kN/mm. The strong null at 185 Hz for this 2 kN/mm matrix is a feature that increases with increasing contact stiffness. Some orientations of the nulls (1 kN/mm and 15 kN/mm) provided a better image of the matrix than this one. These plots use 2 kN/mm because it is the baseline. Using a baseline allows avoids publication of the massive quantity of matrix images output by Matlab. Figure 28 on page 125 shows compressed view the magnitude of all the CSC matrices for trade study A for comparison. This set of six CSC matrix plots shows that the 2 kN/mm gap contact stiffness model produced the most diagonal received modulated optical $\Phi_e(t)$ CSC.

The non – imaging form of the baseline $k_{contact} = 2 \text{ kN/mm}$ structural CSC in Figure 32 on page 129 looks similar to the 15 kN/mm imaging CSC. The 108 Hz

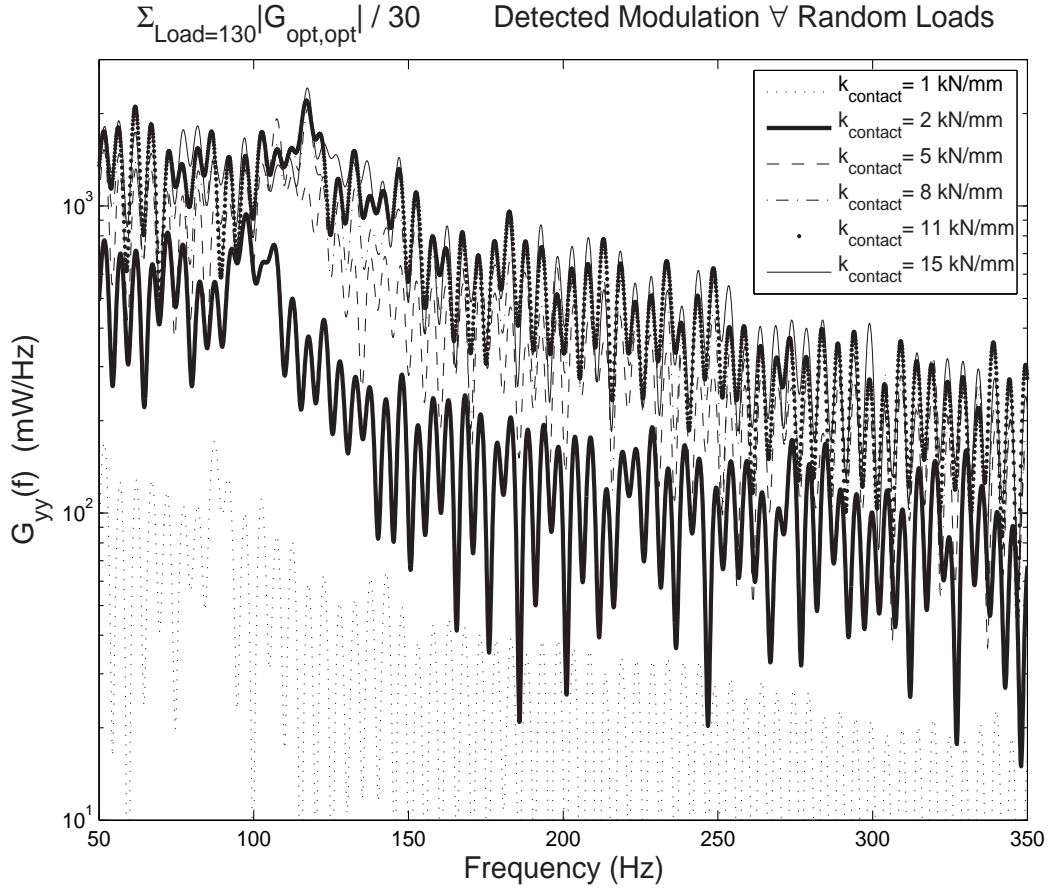


Figure 26: Trade Study A: Spatially averaged $\Phi_e(f; k_{\text{contact}})$ spectral responses correspond to the structural response upon inspection of the response band peak shapes. This data is averaged over all 30 random loads plotted for each k_{contact} .

plateau initiation is obscured by local nulls and a slight diagonalizing of the matrix. The strong nulls representing resonances of the unsymmetrical and antisymmetric modes also increase with increasing gap stiffness but are less prominent in these non – imaging CSC matrices. Figure 26 shows the mode that starts at 80 Hz tracks through the 108 Hz mode. Figure 32 gives a better sense of the effect of all six k values as this lower mode tracks past the fundamental mode. Hand calculations using Roark’s formulas [92, 717,Tbl 36, #16] result in Equation 59 on page 205 for the hull only and a result close in frequency at 83 Hz for four HRA segments acting together as the FEA symmetry conditions dictate occurs. These are the normal modes in the frequency range shown by the non – symmetrical mode in Figures 26 and 32 that tracks through the main symmetrical mode. So we see the 108 Hz mode clearly at several gap stiffnesses, especially 1 and 8 kN/mm. Looking back at the input received radiant flux spectra, $G_{yy}(f; k_{contact})$ in Figure 26 this is where the 108 Hz line is the sharpest.

Figure 32 also shows that unlike the actual structural FEA results, the CSC using a direct Fourier transform of $\Phi_e(t)$ is not sensitive to the step application of gravity in the first time step. Apparently the features removed by windowing away transient responses are not the fine structure features in the $\Phi_e(f)$ response. The right hand pane only used response well after the equilibration of the structure to the gravity load. However, Figure 27 on page 124 shows the structural CSC is markedly different with and without the delay that omits the transient due to the gravity step at $t=0$. While symmetrical modes create strong frequency – stationary responses in the spectra, these CSC’s are a different aspect of target classification strength using optical sensing of multi – layer vibrating plates.

The matrices of CSC phase also have a diagonal feature and show changes at the expected resonances but are not as useful to classification as the magnitude. The standard deviation of the CSC magnitude over the entire 400 Hz matrix ranges from 0.15 to 0.17 for the baseline gap stiffness of 2 kN/mm. Compared to the sharp resonance changes in phase associated with the imaging form of the phase of the CSC

in Figure 31, the non – imaging phase of the CSC in Figure 29 on page 126 has changes in phase at the modes that are barely resolved.

This fine structure is nearly equivalent to the fine structure of the direct optical CSC in Figure 33 on page 130. Tabulation from the Matlab scripts shows that while features in the images do ‘wrap’ color coding (dark to light), the Figure 33 plots of the phase of the structural CSC matrices barely avoid phase wrapping, $\Delta\phi_{CSC} = 2.00\pi$ across the diagonal.

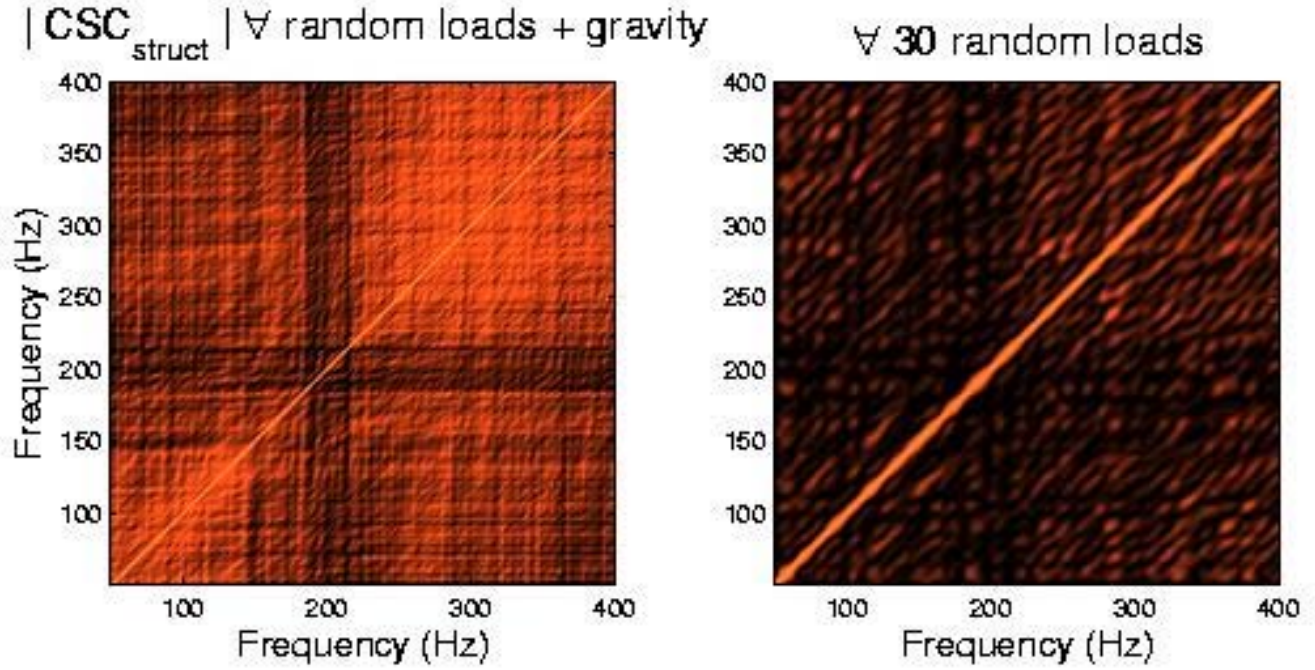


Figure 27: Trade Study A **Non-imaging** $|CSC_{structural}|$: Magnitude of the Structural Cross – Spectral Covariance (CSC) using an ensemble over 30 random loads of spatially averaged (non – imaging) response for $k_{contact} = 2$ kN/mm. The left pane uses all time steps thus including the gravity response at $t = 0$. Inclusion of some transient data strengthens fine structure (increases spectral responses at smaller frequency tolerances). The right pane uses a delay of approximately 10 ms to remove transient response, subduing fine structure. Nevertheless, the fundamental symmetrical 108 Hz and (nonlinear) non – symmetrical modes such as that near 200 Hz remain near null - valued features of the "pure" random CSC.

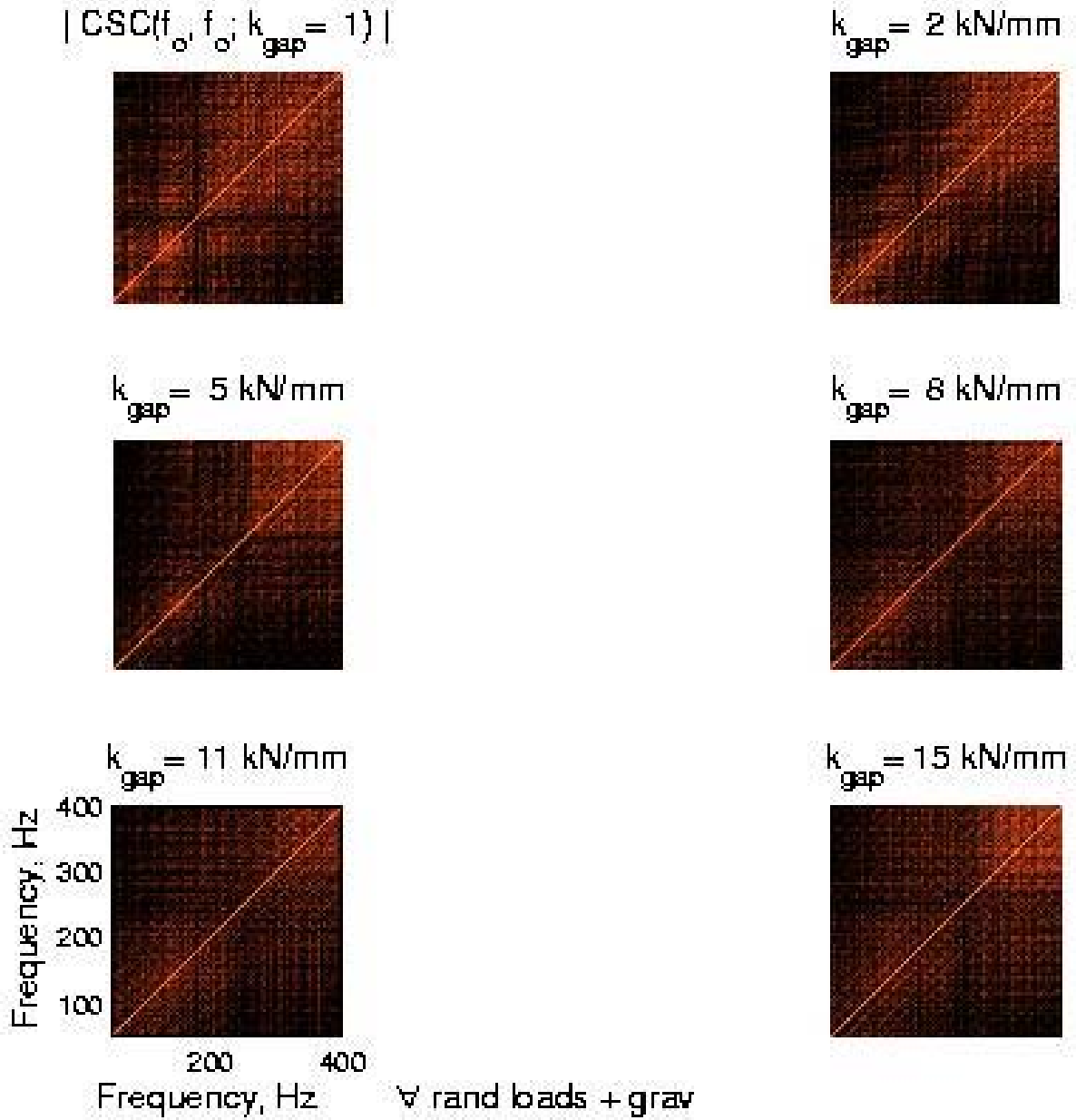


Figure 28: Trade Study A **Non-imaging** $|CSC_{optical}(f_o, f_o; k_{gap})|$: Comparison of Φ_e return CSC magnitudes across the range of contact stiffnesses from 1 through 15 kN/mm (Figure 32 shows detail for baseline $k_{contact} = 2$ kN/mm). The fundamental 108 Hz mode remains constant in frequency as the un – symmetric and anti – symmetric modes increase in frequency (including lower non – symmetrical modes passing through 108 Hz).

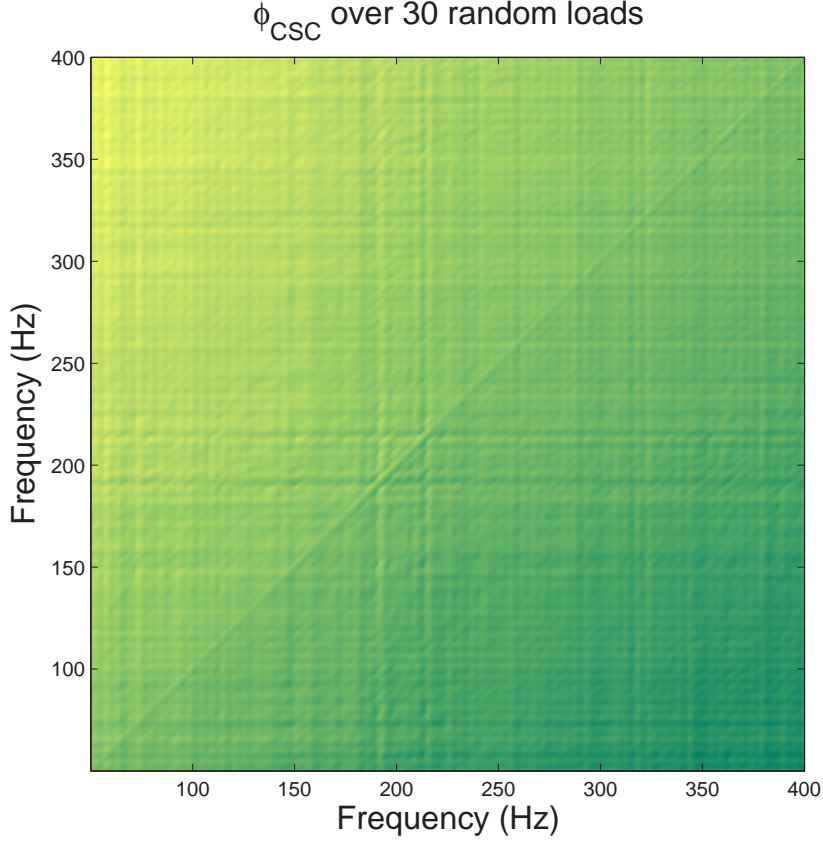


Figure 29: Trade study A **Non-imaging** $\angle CSC_{structural} = \arctangent\left(\frac{\text{Imag}(CSC)}{\text{Real}(CSC)}\right)$: Phase of the structural Cross – Spectral Covariance (CSC) using an ensemble over 30 random loads of (spatially integrated) response for $k = 2\text{kN/mm}$.

The CSC phase matrix shown in Figure 29 has the same fine structure as the CSC of the optical return in Figure 33, especially the fine structure that identifies the modes.

The dark regions of Figure 32 indicate regions of low system coherence [4, 25], [18, 54] as described in Equation 2 and the discussion on pages 17 ff for various loads [72, 16]. Plots of the structural and system coherence using one – sided spectra show high values (a couple deviations from a low mean) at the modes that are not symmetric. The coherence calculation using only the output non – imaged optical spectra comparing the square of the mean to the mean of the squares (Equation 1

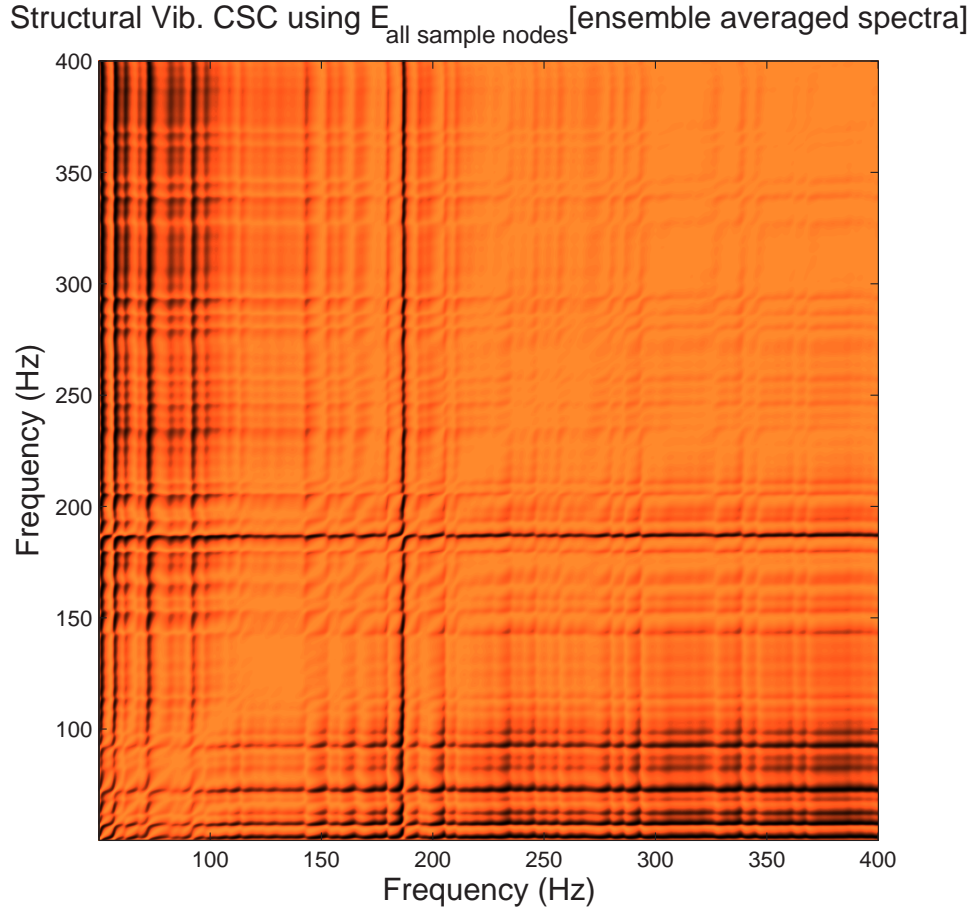


Figure 30: Trade study A **Imaging** $|CSC_{structural}|$: Magnitude of the Structural Cross – Spectral Covariance (CSC) using an ensemble over 32 locations of the ‘per pixel’ response where each location was first averaged over 30 random loads for $k = 2\text{kN/mm}$.

on page 17) shows a large increase only about the fundamental mode at 108 Hz. The extent of low (but easily measured) coherence is apparently due to the nonlinear contact between the armor and hull. However, the phase plots, from impulse loaded structures (Figure 39 on page 141), make a more direct relationship with the structural resonances that indicate their potential for spectral ID of vehicles. Figure 32 had a small initial region of gravity application impulse removed in the final result shown in Figure 32 by truncation of a small part of the beginning of the response time history.³⁷

³⁷Application of a pure random without the gravity load would have modelled a structure in space, which is not representative of ground vehicles for target ID.

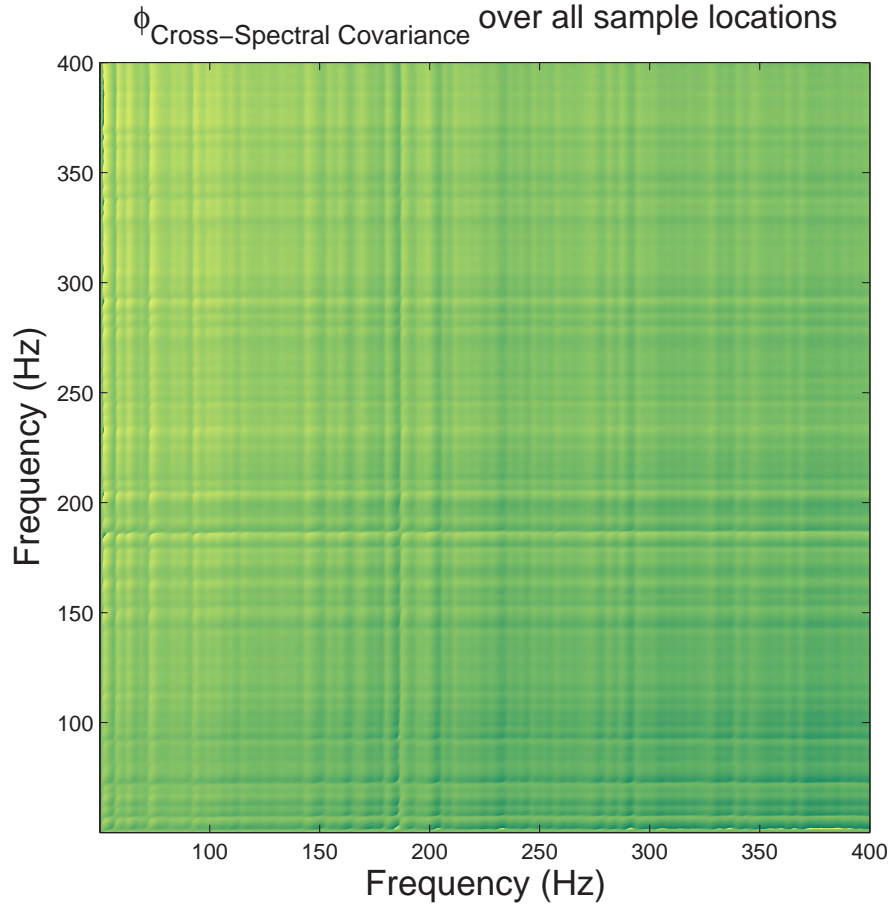


Figure 31: Trade study A **Imaging** $\angle CSC_{structural} = \arctangent\left(\frac{Im(CSC)}{Real(CSC)}\right)$: Phase of the Structural Cross – Spectral Covariance (CSC) using an ensemble average over 32 locations of the ‘per pixel’ response where each location was first averaged over 30 random loads for $k = 2\text{kN/mm}$.

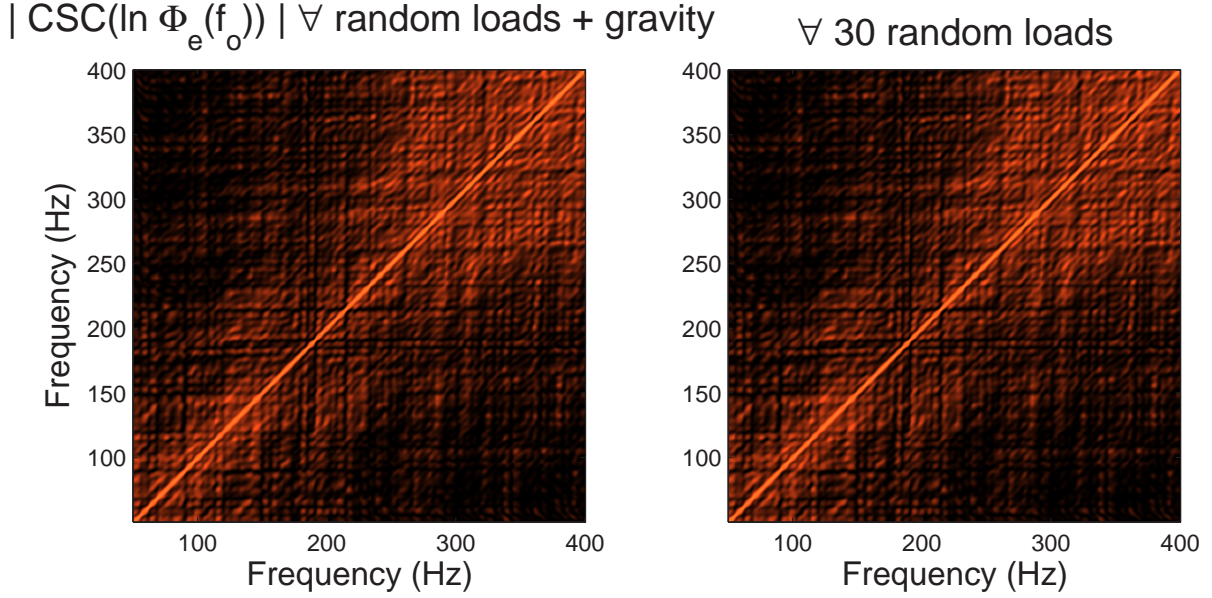


Figure 32: Trade study A $|\text{CSC}(\Phi_e)|$: Magnitude of the Cross – Spectral Covariance (CSC) of Φ_e using an ensemble over 30 random loads a) with gravity on from the start and b) after the gravity response becomes negligible (viewing the time response). Both are the **non – imaging** (spatially integrated) response for $k = 2\text{kN/mm}$. The 108 Hz symmetrical mode at 108 Hz appears as a strong null in the $k = 1 \text{ kN/mm}$ but is partially filled in this 2 kN/mm set, which indicates a potential need for mode tracking. Compare to Figures 26 and 32 where lower modes tracking up for increased k values sometimes obscure strong CSC null lines.

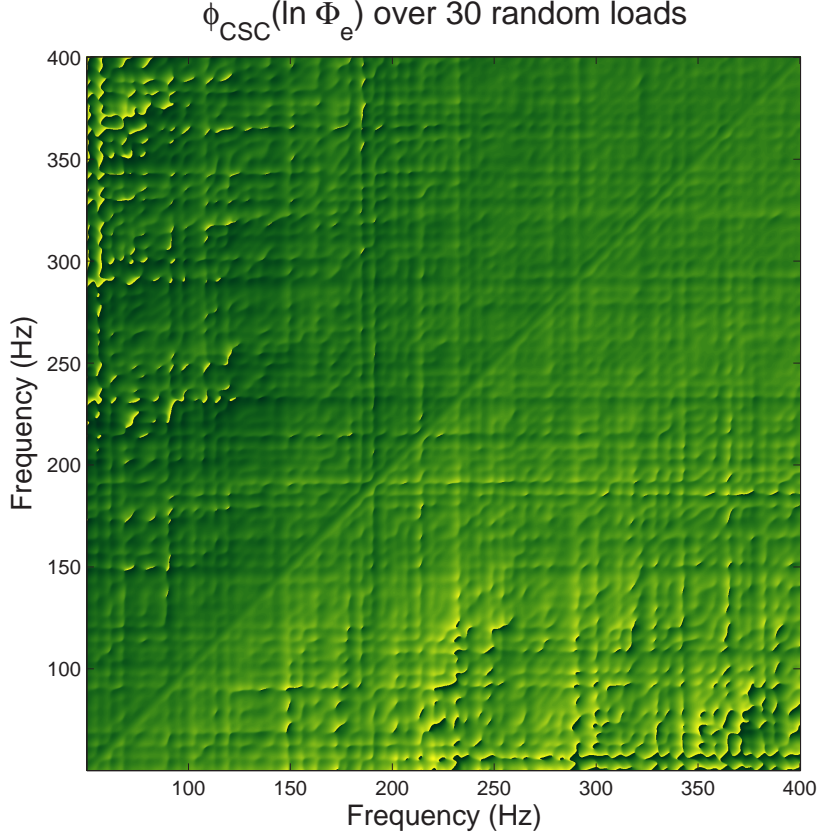


Figure 33: Direct Trade study A $\angle \text{CSC}(\Phi_e)$: Phase of the Cross – Spectral Covariance (CSC) of Φ_e using an ensemble over 30 random loads for $k = 2\text{kN/mm}$ with gravity turned on, using **non – imaging** (spatially integrated) using Fourier transform of $\Phi_e(t)$. This optical CSC based on the direct Fourier transform of $\Phi_e(t)$ is similar to the structural CSC in Figure 29, especially the fine structure that identifies the modes. Compare to the smoother optical CSC using the one – sided response $G_{\text{opt,opt}}(f)$ (Fourier transform of the cross correlation, $R_{\text{opt,opt}}(\tau)$) in Figure 29.

The phase of the CSC from direct Fourier transforms of $\Phi_e(t)$ in Figure 33 shows the resonances in fine structure that also appears in the magnitude plots, Figures 27, 28, and 30. Many of the CSC plots such as Figure 32 segment into rectangular regions between resonances due to the phase transition of a resonance in a typical academic model Bode plot (a quick nearly 2π change in phase and sign at resonance).³⁸ The antisymmetric nature of the phase of the CSC indicates antisymmetry of the imaginary part of the Fourier transform or monotonic FRF phase growth.³⁹ The gravity ‘step function’ provides a small transient. **Together with Trade Study B these three sets (impulse, gravity step, and pure random) show that the CSC becomes more diagonal as the transients are removed.**

Finally, in Figure 34 the cross – CSC comparison of the structural response to the optical response described in Equation 46 compares mean removed spectra for the optical return $S_{MR}^*(f_{opt})$ to the sensed structural vibration $S_{MR}^T(f_{str})$. These cross – CSC calculations are the direct Fourier transforms of Φ_e , not the one – sided spectra. So these matrix results contain a lot of fine structure. The horizontal and vertical features in the image of the cross – CSC matrix show that some structural frequency bands are better transmitted into optical return and some optical modulation frequencies are better suited to broadband sensing, respectively. Although the response spikes vary with gap stiffness, Figure 35 shows that these un – normalized values are far from zero and usually more close to unity. The minor differences in the CSC magnitude across all gap stiffnesses indicate that these spikes of optical response to structural response are not enough of a distortion to remove the classification capability of CW spectral ID.

³⁸Many dynamic system Bode plots show a monotonic phase growth with jumps at resonances.

³⁹The denominator of the CSC, being a normalizing product of magnitudes, is real. The numerator is the product of two complex averages, p and q. These average two different spectral bands, $S(f_u) = a + ic$ and $S(f_v) = b + id$. $p = ab+cd + i(bc-ad)$. $q = ab+cd - i(bc-ad)$. For the case $c = -d$ where $\angle y = \theta = -\angle x$ for any a,b what does this phase asymmetry indicate? Such anti-diagonal CSC matrix points have the relationship $\frac{c(a+b)}{ab+cd} = -\theta = -\frac{d(a+b)}{ab+cd}$ which fits the $c = -d$ assumption. Thus, anti – symmetric $\angle CSC$ is reasonable.

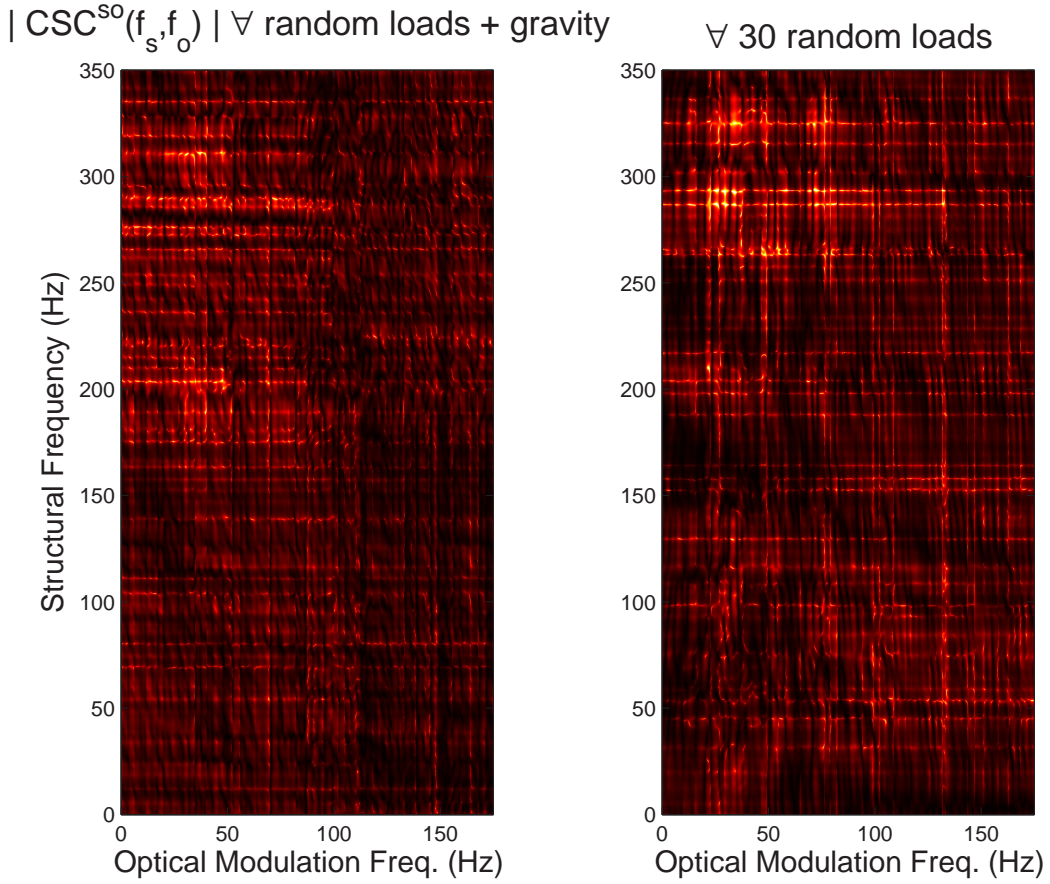


Figure 34: Trade study A magnitude of the **cross** – **CSC** ($|CSC(f_\Phi, f_{str})|$) of the structural response and sensed Φ_e using an ensemble over 30 random loads for $k = 2\text{kN/mm}$ a) with gravity and b) after gravity response is negligible, using **non** – **imaging** (spatially integrated) response.

$$CSC_{s,o}(f_{str}, f_{opt}) = \frac{E[S_{MR}^T(f_{str})S_{MR}^*(f_{opt})]}{\sqrt{E[S_{MR}^T(f_{str})S_{MR}^*(f_{str})]E[S_{MR}^T(f_{opt})S_{MR}^*(f_{opt})]}} \quad (46)$$

The phase of the cross – CSC is similar to both cases of the magnitude, full random and gravity response and the delayed response to avoid the gravity step function response. However the diagonal of the phase (the phase of the cross – cross spectral “variance”) does not loiter about unity. The range of cross – CSC magnitudes ($\overline{CSC(f_o = f_s)} = 0.997$, $\sigma_{CSC(o=s)} = 0.67$, $max[CSC(f_o = f_s)] = 51.4$) indicates that even for fully random excitation, which is more difficult to attain, spectral ID phenomenology is appropriate. The plots in Figure 34 show that modes do not track well (maintain order) and in fact cross, which is not much of a problem because the modal analysis industry routinely deals with these issues [3,4]. The important result is that the un – normalized cross - CSC values are close enough to unity to provide an adequate spectral ID for remote laser vibrometry target ID phenomenology.

Investigation of the response beyond the frequency range of Figure 35 indicates simulated spectral reduction for plate structures. Viewing higher frequencies in the optical response spectra such as in Figure 37 versus structural spectra like Figure 25 we can see this reduction is more pronounced at higher frequencies than those plotted in Figure 35. From the 108 Hz mode Figure 25 has 2 decades less response for the higher mass system whereas Figure 37 shows 3 decades of reduction for the added HRA mass. This would indicate an optical vibrometry modulation transfer function spectral reduction at frequencies not plotted. However, as shown in Figure 25 on page 25 and discussed in subsection 5.4.1 on page 157, spectral reduction is more of a modal issue than a transfer function issue.

Subsection 3.1.2 on page 52 discussed structural delays in vibration energy transmission from one part of a structure to another part which should not be present at steady state except in systems that delay bands of response by design. This delay can happen when the energy finds a structural path to follow that other frequency

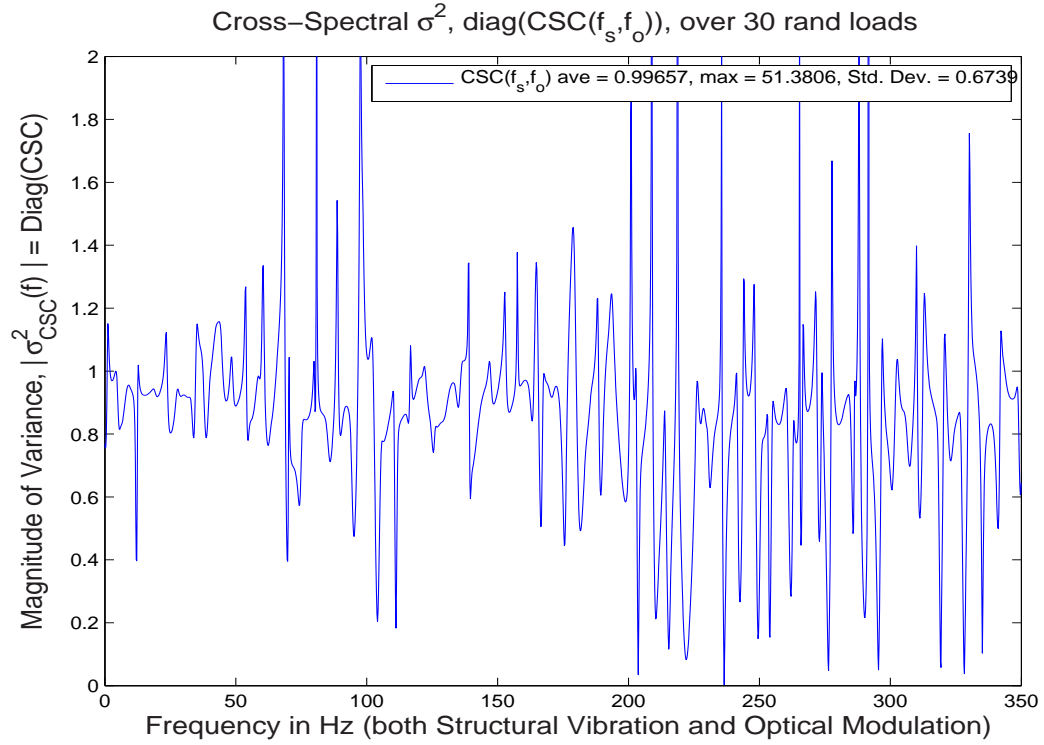


Figure 35: Trade study A magnitude of the diagonal (“variance”) of the cross – CSC ($|CSC(f_\Phi, f_{str})|$) using an ensemble over 30 random loads for $k = 2\text{kN/mm}$ a) with gravity and b) after gravity response is negligible, using **non – imaging** (spatially integrated) response. There is one plot for each gap stiffness model. The statistics are representative of all $k_{contact}$ runs; the mean is very near unity with a small standard deviation and thus most of the spectral energy is not as highly distorted as may have been imagined.

bands cannot follow. Even if the load path is the ‘long way around’ that portion of energy the bleeds through will suffer a delay that apparently shows up in the ‘ordinary coherence’ ratio described on page 53 ff, and is one reason for low values of CSC seen in Figure 32 at the fundamental frequencies like 80 and 100 Hz. The regions of high CSC in Figure 32 indicate causality. The 220 HZ band has high causality for the other modes, including 80 Hz and 108 Hz as seen in the gap stiffness studies represented by Figures 32 through 33.

A summary on page 144 (in the next subsection) provides more direct explanation of the meaning of a CSC. The simulation in that section, trade study B, uses a true ensemble by assumption of load path variations seen in reality.⁴⁰

4.7.2 Study B: Load path variation (mount vibration). In order to model the variation in optical response that would occur in a perfectly smooth atmosphere, the variation due only to the vibration of the vehicle itself, this bolt variation trade study represents minor changes in load paths in the statically indeterminate structure. This trade study uses an impulse load more applicable to that found with an engine running (even for turbine combustion) or rolling on terrain.⁴¹ While any one FE model is still statically determinant, minor changes in the structure were sufficient to model changes in the structure that would in reality include source PSD changes. This provides the static indeterminacy found in nature. These variations appear in the plots of results from the first part of this analysis task, creation of splined displacement data.

‘Shear area’ (bolt diameter) variation models static indeterminacy. The bolt cross – sectional area variation models the modest changes in load path that the statically indeterminate physical model undergoes during optical remote sensing measurements. Each spectrum in Figure 36 is slightly different due to 10 and 15 % decreases in cross – sectional areas, comprising a sufficient ensemble for a true CSC.

⁴⁰The mechanical engineering term for this variation is ‘static indeterminacy.’

⁴¹Frequency response to random loads is quite different from frequency response to sets of impulses, sinusoids and damped sinusoids which is what an engine PSD is more similar to [72, 17].

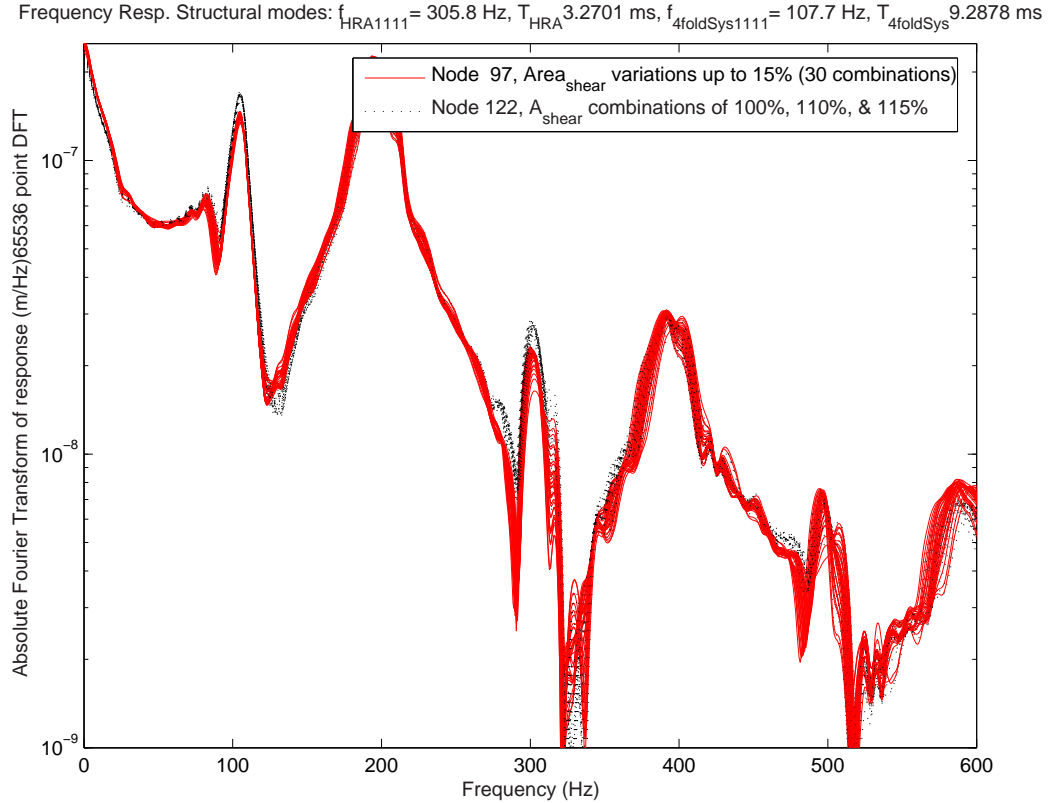


Figure 36: Trade Study B structural frequency response by variation in attachment bolt shear area: The overall structural frequency response of 27 variations in the four attachment bolts appears to be a good ensemble for use in the cross – spectral covariance analysis comparisons. Compare the 220 Hz wide response to the collection of modes trade study A identifies in Figure 25 on page 119.

This trade study varies the bolt areas by 10 and 15% to model the changes in frictional holds, which are entirely empirical, system specific, and quite random [39], [92, 657], [67, 9-159], and [68].⁴² Section 9.4.1.1 of MIL-HDBK-5H describes the reason for joint allowables being different from the shear strengths.

By use of variations in the bolt section areas for the combinations shown below, the transient response will be equivalent to that of a vehicle undergoing full vehicle strains such that the joint stiffnesses vary from nominal by at least the B – basis ($A_2 = 1.1A_o$ represents 10%) and more, $A_3 = 1.15A_o$. This work uses 15% to model the somewhat severe loads the hull is subject to compared to the usual B – basis

⁴² “9.4.1 Mechanically Fastened Joints” page 9-169 [67, 68]

design for aircraft. The four bolt arrangements of shear area appear below, giving 30 variations. This is an adequate number for a statistical ensemble (compare to Central Limit theorem guideline results). The four digits represent the location of the bolts and the numbers represent the subscripts of the areas defined above in this paragraph.

4.7.3 Bolt Area Configurations used in the Ensemble. The following 30 configurations define the 30 bolt configurations (plus one hull – only case) that contain the ensemble data for the characterization of changes in spectral response in time for the vibrating hull – HRA system. Each digit represents the areas of bolts on the 1) North East, 2) South East, 3) South West, and 4) North West corners of the HRA. A one indicates the baseline diameter (one inch). So the fifth sample, 1131, is a baseline system with one bolt that has 15% higher area (diameter of 1.15 inch) on the South West bolt, where $\langle 1131 \rangle$ represents the areas at $\langle NE, SE, SW, NW \rangle$.

1111	1112	1113	1121	1122	1131	1133	1211	1212	1221
1222	1311	1313	1331	1333	2111	2112	2121	2122	2211
2212	2221	2222	3111	3113	3131	3133	3311	3331	3333

For example, configuration $\langle 1122 \rangle$ has one inch diameter bolts on the left side of the long axis ($x < 0$) and 1.10 inch bolts on the right ($x > 0$).

A full comparison would use the joint allowable to backward engineer the effective cross – sectional area. However, material basis appears to be an adequate variation rationale. The relationship between shear stiffness and shear area,⁴³ $G \propto A$, shows that B – basis design will ordinarily consider there to be 10% variations in cross – sectional area.

⁴³These variations in section area affect the shear stiffness, $G = \gamma/\tau$ [74, 33], per $\tau_{max} = b \frac{V}{A}$ where $b = [1.5$ (square cross – section), 1.33 (circular section), 2 (hollow pipe), or 1 (structural webs)] where ‘b’ is the cross – sectional shape parameter [74, 52]. So the shear stiffness is directly proportional to the cross – sectional area. It turns out that calculation of the effective area from joint allowables shows a huge difference in cross – sectional area.

The NASTRAN transient analysis runs have adaptive time steps. Three of these runs finished within 350 to 400 time steps, nearly half the tight $650 \pm \text{ten}$ time steps of the other 27 configurations. Since the spline of those runs would incur more error than the 27 ‘long’ runs, trade study B only uses 27 configurations in the final analyses.

4.7.4 Imaging versus Non – imaging CSC calculations. There are two ways to average all the spectra $\Gamma(x, y; \omega_{time}; configuration; t)$ which is in this case a set of $400 \times 400 \times 27$ spectral tensors using different time domain segment windows. Using the ensemble average of all the image based spectra for each bolt configuration, the spectral tensor $\Gamma(x, y; \omega_{time}; configuration; t)$, we arrive at an average image of spectra $\Gamma_{img}(x, y; \omega_{time})$. This represents the imaging average spectrum $\Gamma_{imgAve}(\omega_t)$ where the argument $\omega_t = 2\pi f$ and f is the temporal frequency. For trade study B the average of the response at one pixel is the ensemble average for 27 bolt A_{shear} configurations (and the hull – only case) at that pixel. For each bolt configuration there are 24 spectra representing a spatial sample of the $400^2 = 160,000$ sample points / pixels. This ΔA_{shear} ensemble average excludes the hull – only.

Using, $\Gamma_{img}(x, y; \omega_{time}; configurations)$, the original tensor of spectral response for each sample pixel with which to take an average over all the pixels, we get a set of non – imaging radiant flux spectrum scalars, $\Gamma_{configuration}(\omega_t)$, representing all the bolt configurations, with the argument $\omega_t = 2\pi f$ where f is the temporal frequency. The average of the response for any bolt configuration is the spatial average over all sample pixels of the image.

The Cross – Spectra Covariance (CSC) plots give us an indication of the correlation between different bands of frequency. These calculations using Equation 47 on page 144 described on page 52 ff are a direct function of the spectra. The input radiant flux spectra in Figure 37 on page 139 are remote sensing estimates of the actual (simulated) structural spectra shown in Figure 36 on page 136. The structural CSC in Figures 38 and 39 shows dependence of response at one frequency band to an-

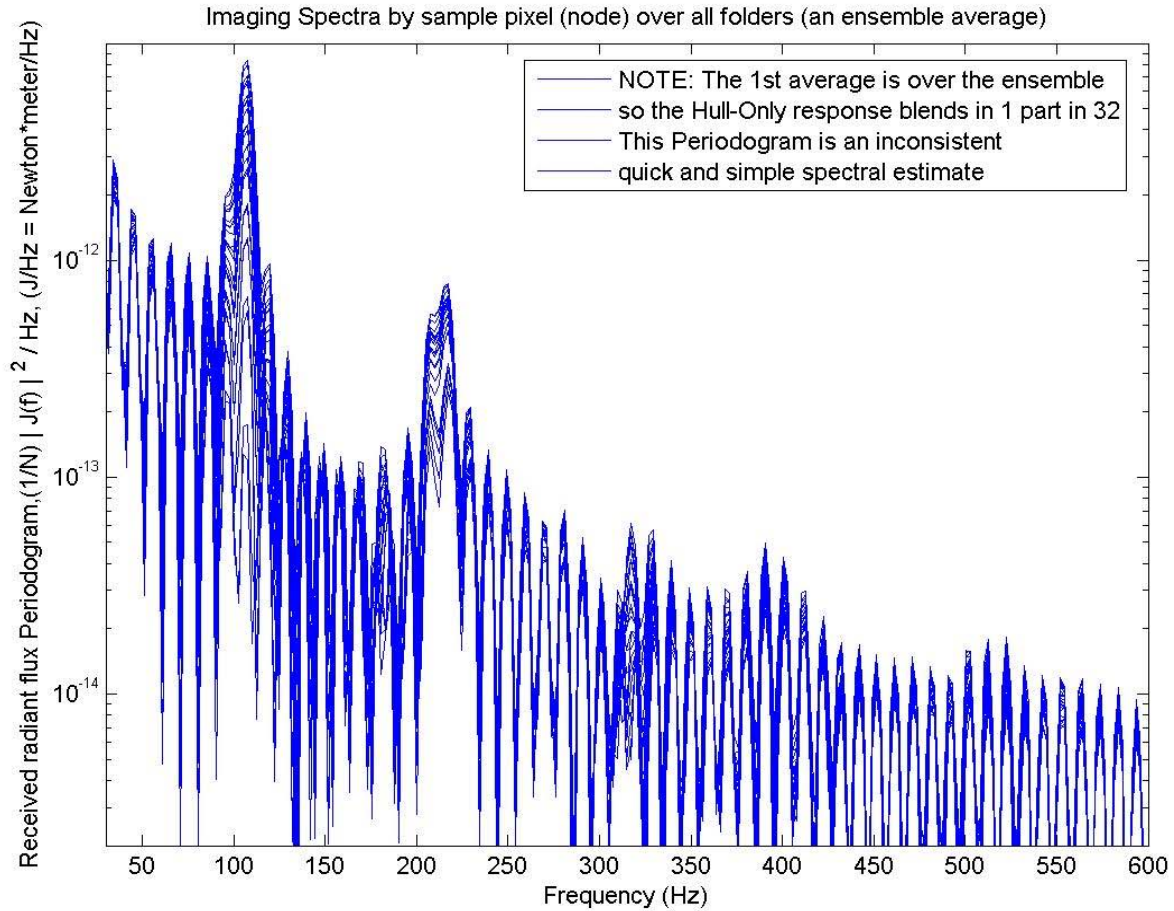


Figure 37: Trade Study B: This ensemble average of the 64k point DFT for each sample pixel (an imaging Laser Vibrometer simulation) – Radiant flux frequency responses averaged over all the bolt configurations < 1111 > through < 3333 > for each pixel have roughly the same overall response. Only results for the 24 sample nodes (pixels, or sample points) appear in the plot.

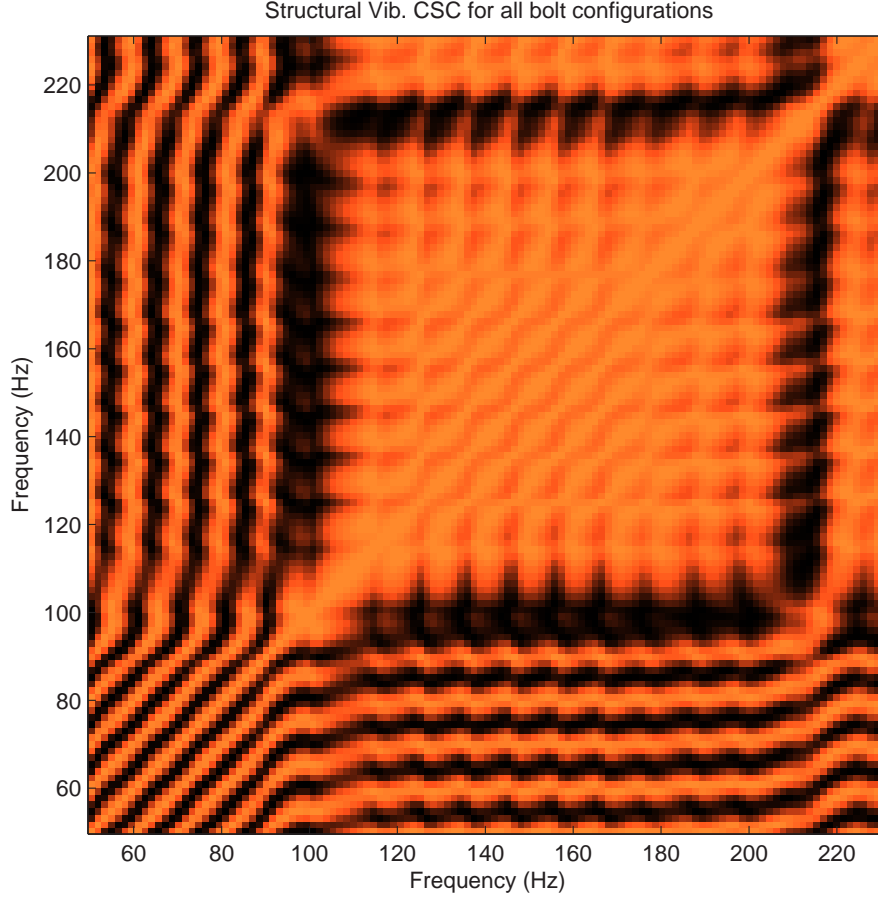


Figure 38: Magnitude of the **non – imaging** (spatially integrated) Structural CSC

other frequency band for physical systems with high (above 50%) structural vibration coherence.

The spectral magnitude and phase shown in Figure 38 and 39 do match the structural eigenvalues for the fundamental mode and mode 3. Compared to the gap stiffness variation (trade study A), this trade study B data is closer to a true⁴⁴ Cross – Spectral Covariance analysis. The other CSC’s in trade study A use spectra from different point locations and from different random loads for the gap stiffness variation study. This CSC in Figure 38 uses different simulated instantiations of measurements of the same structure, a true measurement ensemble. The image shows where there is

⁴⁴The ensemble averages should be over the variation seen in physical reality which is the static indeterminacy trade study B models.

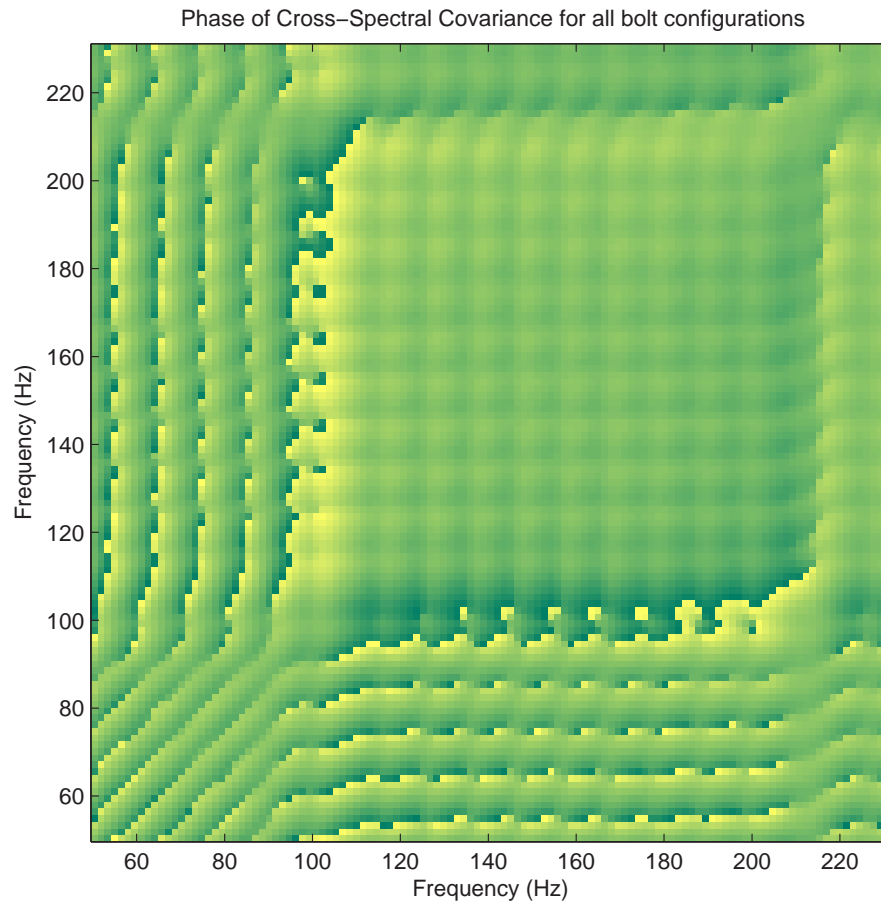


Figure 39: Trade Study B Phase of the **non – imaging** (spatially integrated) Structural CSC

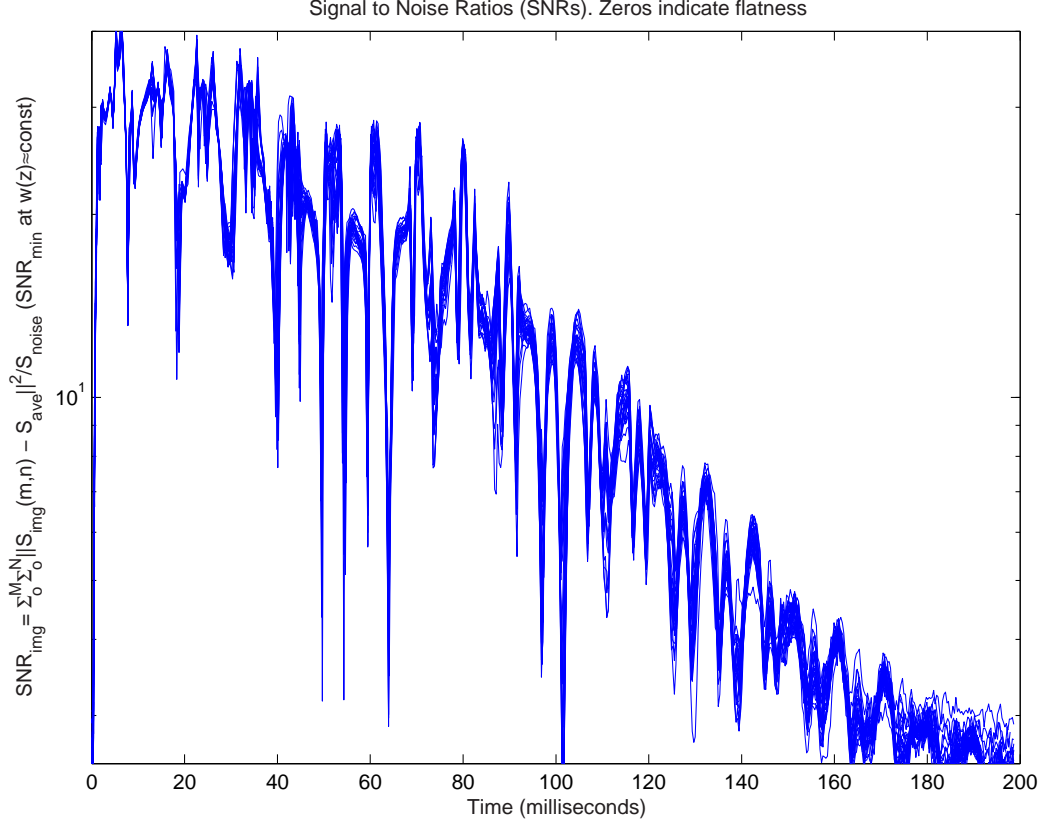


Figure 40: The Signal to Noise Ratio (SNR) for all bolt configurations plotted over time. There is a long post – transient period (post 3.6 ms) that is still not stationary. The region after 100 ms is becoming stationary but exhibits a steep 1/f decay.

a gain in one frequency band correlated with energy in another band as well as where bands of vibration strain energy are independent (uncorrelated) usually due to low, near zero structural coherence.

The optical CSC magnitude features from Figure 41 show up the structural spectra used in the structural CSC in Figure 38. This CSC simulates 27 different measurement instantiations of the same structure, which comprise a true ensemble using static indeterminacy due to moderate forced load path variations in the 27 FE models. A rectangle of apparent structural coherence appears in Figure 41. This appears on the diagonal between 95 Hz and 230 Hz of the optically sensed CSC simulation (using Equation 47) in Figure 41. The plateau of covariance attains its ‘full height’ at the region where the structural CSC is in mid – ramp up to a similar rectan-

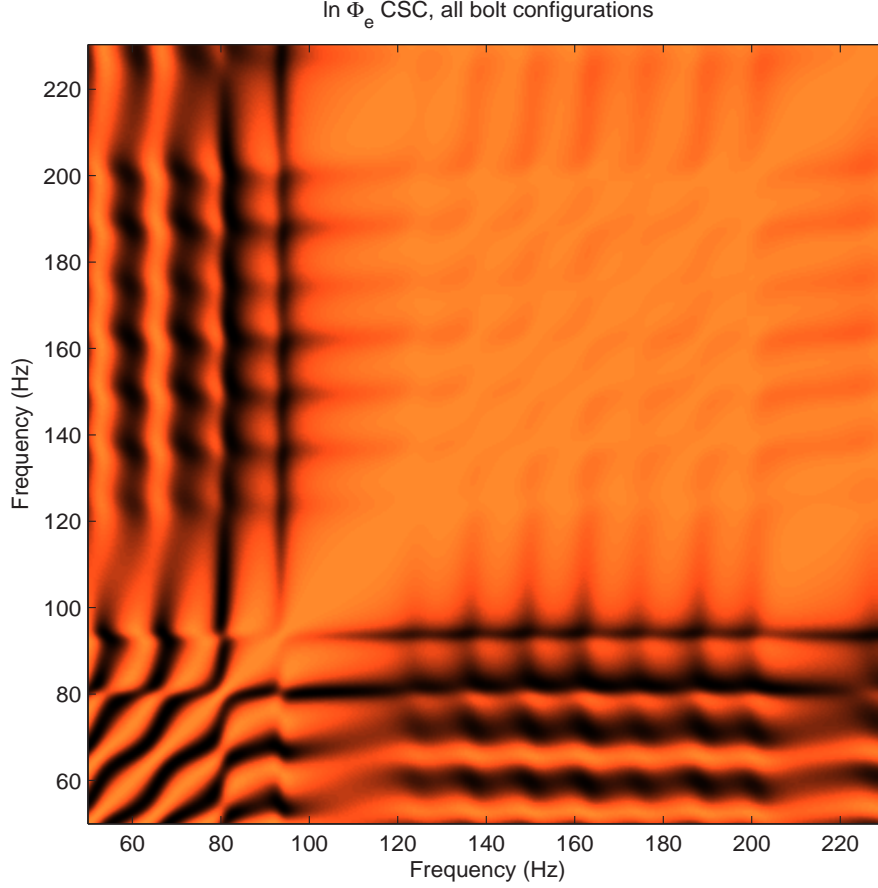


Figure 41: Magnitude of the **non – imaging** (spatially integrated) Optical CSC

gle; the optical CSC appears to overstate this sensed structural coherence frequency band limit by approximately 10 %. A comparison of this image to the phase image in Figure 42 shows that only in this 100 to 200 Hz rectangle of structural coherence is there no phase wrapping. *This region the CSC in Figures 41 and 42 identifies is the region between the fundamental mode and the next highest mode at 224 Hz.* Note that after the main symmetrical mode (108 Hz) in Figure 38 the phase variation remains within 2π through the first main anti – symmetric mode (200 Hz). Here Equation 47 is equivalent to Equation 8 on page 50 where the generic mean removed spectral response $F(u)$ is specifically the optical PSD, $\Phi_{MR}(f_k)$. The same discussion on page 50 about CSC measurement of phase relationships between different frequency bands of the same spectral response applies here.

$$CSC(f_u, f_v) = \frac{E[\Phi_{MR}^T(f_u)\Phi_{MR}^*(f_v)]}{\sqrt{E[\Phi_{MR}^T(f_u)\Phi_{MR}^*(f_u)]E[\Phi_{MR}^T(f_v)\Phi_{MR}^*(f_v)]}} \quad (47)$$

The optical CSC in Figure 41 shows a maximum at the edges of the apparent rectangle of structural coherence. Since this refinement of frequency resolution followed a trend of block diagonal covariance formation, the actual system may be more uniform over this rectangle.⁴⁵

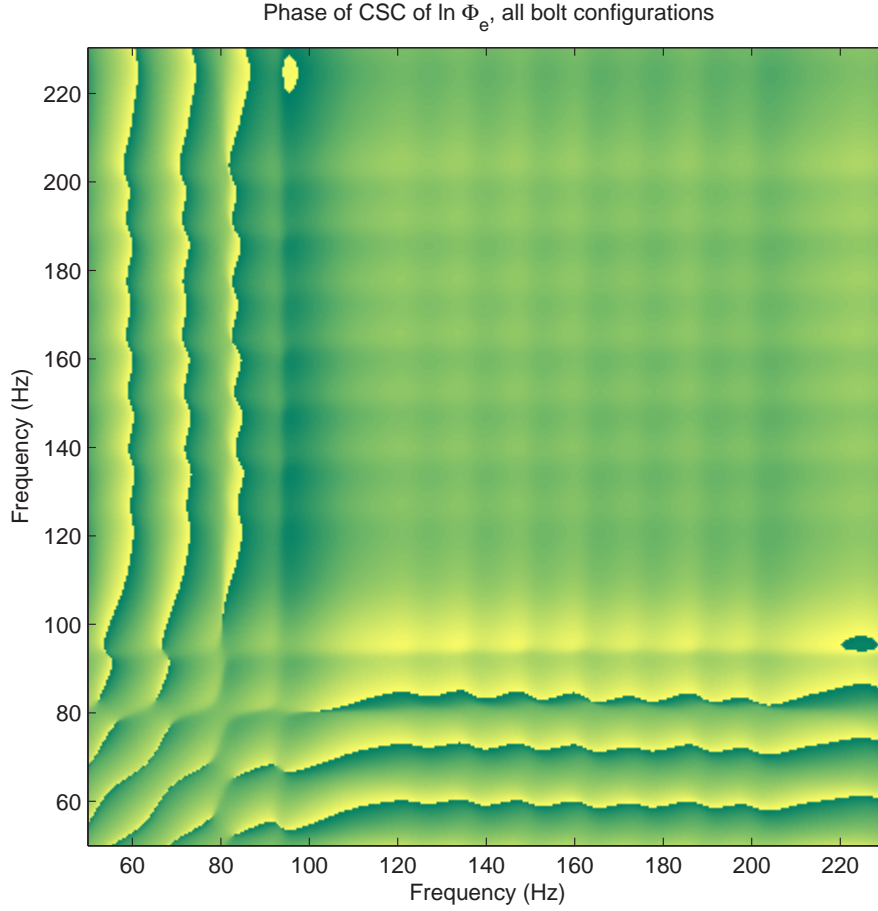


Figure 42: Phase of the **non – imaging** (spatially integrated) Optical CSC – Phase of the sensed CSC using the Radiant Flux frequency responses of the ensemble of bolt configurations.

⁴⁵Using more advanced estimates of the spectrum including Welch averaging or ARMA or other parametric models is out of the scope of this work.

Plotting a horizontal or vertical slice between the main modes (108 and 235 Hz) through Figure 38 shows a “hill” of maximum CSC gain in the 100 to 170 Hz range. 108 Hz is the fundamental frequency of the main symmetrical normal mode, the first ‘breathing’ mode. The diagonal is precisely unity at all frequencies.

V. Conclusions: target & spectral ID, industrial use

The final output data is comprised of two studies.

Trade Study A: Variation in contact gap closed stiffness

Trade Study B: Variation in bolt cross – section area

There are four major results from these studies, and subsequent insight into both the structural nonlinear contact layer problem and the cross – spectral covariance (CSC). These results listed below support the hypothesis that optical CW sensing of vibration is adequate to allow for spectral ID sufficient to classify vehicle models.

1. **The structural system transfer function is nonlinear:** Even for this simple rectangular plate model, vibration strain energy transfers to low frequency modes. This is perhaps more easy to see in the time history plots. Spectral responses and nonlinear time histories show nonlinear response for the impulse of 3.6 milliseconds duration, with effective width of 1.0 ms,¹ Stead state after impact retains a mode combination response about 220 Hz that is approximately 2 % larger than the fundamental response at 108 Hz (Figure 36 on page 136) but is entirely missing from the averaged random response spectra (Figure 26 on page 121). A discussion on page 120 describes the nonlinearity and collection of modes at 220 Hz. Comparison of the nearly flat input spectrum² to the output spectra for various similar models from trade study A in Figure 25 on page 119 shows response that is clearly nonlinear and with a concentration of strain energy to low modes. Following the convention of modal analysis engineers [16] to avoid reliance on spectral results,³ a view of time histories such as Figure 17 on page 109 shows a 2 mode form of nonlinearity in the structural transfer function. The “higher” mode has a lower response; it manifests as

¹The pulse of acceleration is defined over 3.6 ms with a full width at half height (FWHH) of 1.0 ms, centered on 2.0 ms with a standard deviation of $\sigma_{pulse} == 0.5164$ ms. Using 3/2 sinc PSD guidelines [44] the effective bandwidth of this pulse is approximately $1.5 / 0.001 \text{ sec} = 1.5 \text{ kHz}$, well above our region of interest.

²The flatness of the input spectra is understood for random loads and is displayed in Figure 53 on 199 for the sharp Gaussian impulse.

³See subsection 4.4.2 on page 94 and on page 95 after (5) [16].

a divot in the 93 ms (108 Hz) time history peaks.⁴ The movement of strain energy towards the lower mode discussed on page 154 in section 5.3 uses this insight gained from time histories as well. In all cases the strain energy moved monotonically to low frequencies, as linear damping theory (page 163 ff) [94, 340, 341].

2. Plane wave calculation shows a mechanism of spectral elimination:

Assumption of a plane wave coherent illumination and equipartitioned modes in a metal strip target provides a “swept sine” return response⁵ for each mode that is constant. Section 4.1 and Figure 9 on page 75 show that return from the superposition of modes is a constant of the system. A small deflection multi – modal calculation provides similar results in Figure 10 on page 80 using Equation 37 on page 77 without the monotone excitation assumption. These calculations more closely validate a prior AFIT thesis [58]. This indicates that to second order CW return from thin strips (bars or beams) produces no detectable CW phase modulation distortion. Since most structures are not strips, CW classification methods are not adversely effected by this type of spectral elimination / reduction.

3. Spectral reduction for non – symmetrical structural modes:

The FEA results produce dynamic response to random loads (trade study A with gap stiffness changes) and transient loads (trade study B with statically indeterminate load paths) which excite the normal modes of the structure. Structural changes in structure modelled in trade study A have no discernable effect on symmetrical modes while the anti – symmetric and un – symmetrical modes (Figure 3 and subsection 2.2.7 on page 30 define these non – symmetrical modes) have decreased response and increasing center frequency for increases in gap stiffness (Figure 25 on page 119). Discussion in

⁴The splined data on a log scale in Figure 17 on page 109 also shows this effect. This energy transfer includes the triangular 210 Hz mode resonance whose peak is high but whose base is broad. Additional inspection of Figure 25 shows that the high 210 Hz response whose effect in the time history is subdued by high nearby response bands, is an effect seen mostly in the 2 kN / mm closed stiffness response spectrum (not the time history, reference page 154). See the discussion and footnote on page 96.

⁵Equation 25 on page 68 shows why industry standard sine swept (monotone excitation) FRF measurements are qualitatively different from detected response. Yet sine sweep methods provide a potential calibration tool for laser vibrometry.

subsection 5.4.1 on page 157 considers the spectral results. This spectral reduction is a modal effect more than a transfer function effect. Future physical tests should show a ‘spectral reduction’ in all modes except the lowest frequency fundamental modes for the structure and each significant component. Another indicator of the difference between symmetrical mode response (such as the 108 Hz mode) and non – symmetrical modes appears in the next conclusion item number 4. The CSC matrix features are sharp at symmetrical modes. **A classifier based on symmetrical modes should experience improved performance over one that tries to match all modes or a wide PSD band.** This result supports the lab results that showed modes above the fundamental mode for a simple beam were susceptible to spectral elimination [58, 6-1].

4. **Detected $\Phi_e(t)$ is an adequate system classifier:** This is the main result, the objective of this thesis. The Cross – Spectral Covariance (CSC) matrices and resulting image display of same show that, especially for the more practical trade study B method, the optical return radiant flux images produce nearly the same phase relationships between the most relevant vibration energy bandwidths. Trade study B CSC matrices had broad bandwidth features apparently due to the fully transient nature of the source (although data retrieval started far after the detection system achieved steady state). However, trade study A results showed much more fine structure related to minor resonance features.

The trade study A (random response) CSC phase non – imaging plots is Figures 27 and 29 on pages 124 and 126.⁶ The ‘imaging’ form of the CSC phase matrices in Figures 30 and 31 on pages 127 and 128 on page 128 is more detailed and orderly as expected. The trade study B optical CSC phase matrix in Figure 42 on page 144 appears to be a good non – imaging indicator of the frequency location of structural symmetrical modes. This CSC matrix is the simulation of the remotely sensed structural CSC in Figure 39 on page 141.

⁶The non – imaging optical phase CSC matrices such as in Figure 33 on page 130 assist identification of the symmetrical structural modes in their fine structure showing the stationary 108 Hz and the moving (versus $k_{contact}$) 180 Hz lines; they indicate a necessary but insufficient condition for a resonance ID.

The trade study B time history of $\Phi_e(t)$ in 17 on page 109 shows that single layer surfaces (upper pane) have less symmetrical mode response than the multi – layer skin (lower pane). The nonlinearities discussed in item 1 on page 146 assist in target ID. This classification improvement for multi – layer skin may be more universal than it appears, which is the reason for the nonlinear oscillator derivation in Section 4.3 on pages 84 ff.

The trade study B CSC classification results were sufficiently adequate for spectral ID such that the more detailed and graphically “busy” imaging forms of the CSC are not included. This work emphasizes the utility of non-imaging results. However, trade study A phase CSC’s for imaging versus non – imaging comparison are Figures 29 versus 31 respectively. The magnitudes of the imaging versus non – imaging CSC’s, Figures 32 and 30 have a much more stark difference. Apparently the magnitude of the CSC has much more covariance when there was a history of transient behavior even though the magnitude of the CSC (Figure 38) for trade study B only used steady state response history long after the deflection transient died out. The prior version of the “image” SNR plot in Figure 18 on page 110 led to a new sequence of FEA results to remove an apparent lack of optical return stationarity long after the structural system would be considered to be in “steady state” after the transient. This indicates that the optical CSC magnitude is sensitive to time lags in the structure that are not apparent (below the noise) in structural data.

The phase modulation at the target is a function of the mode shapes in the linear superposition of modes that modify the incoming laser irradiance. A discussion of the relative importance of this spatial effect due to Equation 22 on page 60 versus overall frequency response appears at the end of section 5.3 on page 155. These radiant flux results comprise a detailed CW study compared to the WPAFB study [64] and the NATO study [54]. Yet those studies provided adequate clustering of vehicle spectral ‘fingerprints’ [43]. Therefore, since this method provides refined spectral ID, the simple sigmoid or other more common classifiers such as Karhunen – Louve should

have more than adequate target classification capability using structural modes as a classification feature.

A review of some of the discussions on structural coherence such as those in section 2.1.1 through page 17 may be helpful in understanding the structural effects indicated by the CSC plots.

5.1 Considerations for Target ID

The “Local Ergodicity” result for the final trade study show in item number 2 above, helps validate the results of the contact gap stiffness study. ‘Local ergodicity’ indicates that spatially averaged CSC are insensitive to physical system variations produced by the bolt configuration ensemble average and the physical effect it models, the variation in frictional hold during laser data acquisition.

The pseudo – ensembles of trade study B (modelling static indeterminacy) and the trade study A contact stiffness variations provided classification features in CSC matrices (plotted as images) showing their generic responsivity to design variables.

a) Imaging CSC’s are more sensitive to environmental variation than non – imaging CSC’s. But non – imaging CSC’s range of sensitivity is adequate for target ID.

b) Nulls in CSC’s representing **symmetrical modes are insensitive** to frictional hold and contact surface variations.

c) Nulls in CSC’s representing **un – symmetrical modes are sensitive** to frictional hold and contact surface variations.

d) Time window averaged CSC might be sensitive to small design parameter changes (requires more work).

e) For steady state response after transient excitation,⁷ square regions of structural coherence show up as near unity cross – spectral covariance shown from the

⁷Data acquisition started after 100 ms, well after 30 pulse widths from the transient 1.0 ms FWHH pulse, approximately five times the duration of the structural approach to sufficient steady

spectral DFT of the FEA time history results compare appropriately with the optical Φ_e CSC rectangular regions. These regions form along the unity CSC diagonal (the variances are all unity). *The CSC's identify the symmetrical fundamental mode as the start of the first block diagonal region of apparent structural coherence.*

Trade Study A results in Figures 34 on page 132 showed that the cross terms in the CSC decreased as transients were removed from the data. Steady state from a transient is insufficient to diagonalize the CSC,⁸ the physical model must be like a structure in space (no gravity) undergoing a pure random load.

Figures 38 and 41 on pages 140 and 143 are trade study B “transient” structural and optical return CSC's respectively. Regions of low CSC are areas where the spectrum is independent of the other corresponding frequency. Regions where the CSC is unity are where response at one frequency has full covariance with response at another. For the cross – CSC only, abscissa and ordinate being different spectra, the small regions where $CSC_{s,o} > 1$ (Figure 35 on page 134) are regions where the response has a gain with respect to the response at the other frequency, the one appears to drive the former. This effect appears in the cross – CSC of trade study A that uses structural and optical spectra (Figure 34 and the more useful Figure 35 on page 134), but not in typical “auto – CSC's” which use an ensemble of the same spectrum, FEA or optical, for both arguments.

5.2 Considerations for Spectral Estimation

The results show that the optical integrated radiant flux return is more prone to require refinement, high spectral resolution, than the structural response. Improvement of the resulting spectra should improve target ID based on CSC using these

state and twice the approach to small deflection steady state. Compare Figure 17 to 18 on pages 109 and 110.

⁸The random structural CSC of trade study A in Figure 27 and its related optical return CSC in Figure 32 have concentrated covariance near the diagonal, a nearly band diagonal matrix indicating a strong drop in covariance outside of a bandwidth that increased in center frequency along the diagonal.

spectra. Nevertheless, the current system already provides spectral features that are improvements over prior studies [54, 64] that are already adequate classifiers [43].

Using these spectra or better spectral estimates of the PSD will still require some understanding of the nonlinear system transfer function whose covariance appears in a ‘cross – CSC’ shown in Figure 34 on page 132. Although this is a matrix of response, a view of its diagonal in Figure 35 on page 134 gives an understanding of the behavior of the log of the CW coherent response to this vibrating plate. The mean value of the transfer function $H_{str,opt}(F)$ over the frequency range 50 to 350 Hz was 1.0012 with a standard deviation of 0.086. There was a spike to 88.4 in the 15 kN/mm case but that set only had a standard deviation of 0.796 (1.26 σ over σ_{ave}). The mean standard deviation of $H_{str,opt}(F)$ was $\sigma_{ave} = 0.684$ with a standard deviation of $\sigma(\sigma_{Hso}) = 0.0892$. Therefore the non – imaging optical detection system simulated response is adequate to convey enough of the spectral content of the target to the detector for spectral ID. Actual Receiver Operating Characteristic (ROC) curves, left for later study, will require more data.

5.3 *Considerations for Structural Design*

This thesis fills a gap in structural analysis of vibration response for plates in contact. There are some torsional clutch studies such as Tae – Chung Kim’s dissertation for Ohio State U. (OSU), Daimler Chrysler, and Ford [41]. Most of this work at OEM’s like GM was preferably kept as trade secret. Studies in the industry appear to center on signal processing methods like use of a harmonic balance method (HBM) for the clutch issues. The torsional clutch problem is concerned with smooth application of a moderately constant torsional power, whereas in the plate vibration model lift – off is not a problem, it is a part of a remote sensing solution.

This thesis extends the torsional solution with the one and two DOF close form contact models of Section 4.3 by use of a smooth arctangent function rather than the bi – linear and tri – linear segmented contact stiffnesses used in the torsional HBM dissertation. Combined with the methods in Major Winthrop’s dissertation [90]

this leads to easy phase space (state space) plots, determination of the stability and stabilizability of the solutions, and a set of nonlinear “eigenvalues” for the two DOF problem that characterize the behavior seen in the FEA results.

FEA results more accurately represent the contact nonlinear frequency response than the closed form solutions because the time history derives from direct transient time integration analyses from NASTRAN (SOL 129) of the 3 – D structure. Matlab calculated Fourier transforms estimate the nonlinear frequency response. The resultant spectra are used in CSC calculations to measure the phase relationships between frequency bands for an ensemble representing laser measurements of a structure undergoing variations for trade studies A and B, moderate load and load path variations due to the static indeterminacy of non – truss structures like the target vehicles in question.

While the HBM is an internal OSU code that seeks to determine sub – and super – harmonics of a nearly determinate structure (the powertrain), nonlinear effects produced by translating nonlinear contact NASTRAN time histories into Matlab appear to be less prone to modelling error that would generate false or unduly high harmonics.

The results show that *Vibration Strain Energy transfers to the lower frequency modes*. 1) A major mechanism driving strain energy to low frequencies is high structural stiffness at high vibration modes. The full simple contact nonlinear time history analysis is a proof of the test engineer’s credo that vehicle systems drive vibration strain energy to the lower components in the system through many mechanisms. The ‘input PSD’ of the 3.6 millisecond Gaussian impulse is very broad (Figure 53 on page 199) but the response concentrates below 240 Hz. First, the ‘hull – only’ spectra show this happens without nonlinearity since the higher frequency modes have substantially smaller deflections.⁹ As the discussion for item 1 on page 146 indicates, the

⁹Higher frequency modes have much higher generalized stiffness calculated by NASTRAN SOL 103 Normal Mode eigenvalue analyses used to characterize the modes prior to the SOL 129 transient analyses.

concentration to lower frequencies is even more pronounced for the nonlinear contact model. 2) Additionally, the change in contact nonlinearity in trade study A drove some modes higher in frequency (‘anti – symmetric’ and ‘un – symmetrical’ modes) while symmetrical modes remain at approximately the same frequency. The result is a further shift in strain energy to the low frequency modes “avoiding” the increased stiffness. Tae – Chung Kim’s OSU torsional study did not include energy drains that would contribute to this mechanism, but it does show that the powertrain is another component that adds nonlinearity to the system model.

Closed form relations describing damping mechanisms that shift energy to lower frequencies in linear systems (see Zienkiewicz’ proof in subsection A.2.1 on page 163).

It is mostly the nonlinearity of the surface contact that drove high frequency energy to low frequencies on average. The energy shift in these FEA results validated the calculations shown in the Mathematical section 4.3.3 of the results Chapter IV. Figure 13 on page 105 forecast an increase in ‘antisymmetric’ (‘un – symmetrical’) modes. Results of trade study A validate the ‘anti – symmetric’ mode effect for this multi – plate system. Anti – symmetrical modes decrease in response for increases in contact stiffness as shown in Figure 25 on page 119, while their center frequencies increase as described on page 120. Figure 26 on page 121 shows detected radiant flux does indicate this effect.

Why would a variational energy techniques¹⁰ show such an energy shift? Partly because even the “simple” Melosh, Zienkiewicz, and Clough plate formulation used higher order DE’s [7].¹¹ Element formulation reflects a simplified form of the underlying structural dynamical equations. Even the plane stress (modelling thin sheet

¹⁰Variational techniques such as the Hellinger – Reissner principle are a clean method to develop finite element formulations defining the relationships between all the element DOF’s [50, 55]. These methods minimize the potential energy of the element to calculate these terms. The terms comprise the ‘element formulation’ some of which is a part of the fairly quick ‘assembly’ activity during execution of FEA on a computer.

¹¹This ‘MZO’ element was a step along the path to “modern,” simple, “linear” quadrilateral elements [50, 5] up from the constant strain Turner triangle element [84] (using even higher order DE’s).

metal) elements have deflections that are at least combinations of second order derivatives. The basic stress and strain relations are elliptical DE's. Thus, the transfer of structural stress in statics is not a linear process. Truss structures do have less of these effects, hence their popularity in certain forms of construction. Hence, for ordinary plate structures undergoing dynamical loading, physical properties unrelated to the shape commonly undergo nonlinear effects that transfer energy in frequency space.

We can see this energy shift effect directly as a reduction in the 4.5 ms period of the upper (hull – only) after adding the HRA contact and mass (lower pane) in the time histories (Figure 17 on page 109) for the bolt configuration study, trade study B. Laser interferometry is not limited by small displacement, it thrives on displacement that is a fraction of a wavelength (less than a micron). So the lighter hull – only response has no classification advantage due to higher deflection. The 4.5 millisecond period (224 Hz) harmonic response in the ‘hull – only’ is nearly 80% of the symmetrical mode 9.3 ms harmonic. So while symmetrical modes (e.g.: the 9.3 ms 108 Hz mode) attract more strain energy than other modes on average, some un – symmetrical and anti – symmetric modes (200 – 235 Hz) can coalesce a concentrated *spectral* response exceeding even the fundamental symmetrical mode.

The HRA – hull combinations have more mass and their deflections in the lower part of Figure 17 on page 109 are on the order of a micron (maximum). The 220 Hz harmonic only has about 20 % of the *deflection* response compared to the deflection at 108 Hz. This ratio is not apparent in the spectra (see subsection 4.4.2 on page 94 and after item (5) on page 95 [16]). Higher frequencies are transforming the shape of these 108 Hz sine wave responses. The hull – only plot has smooth 108 Hz sine waves but multi – layer contact structures systems (HRA – hull) have wide 108 Hz (9.3 ms) spikes squared by higher frequency components (4.5 ms and others).

The use of bolt stiffness configuration variations (trade study B) is a non – standard method used to obtain an ensemble of microscopic changes to model static indeterminacy. As alluded to in the listing of the four major results of this thesis

on page 146, the optical integrated radiant flux frequency response (non – imaging) is not explicitly matched to the frequency response of the out – of – plane vibration deflection of the target. There is a modulation phase summation effect that causes the sensing system to prefer some mode shapes over others (low frequency long spatial wavelength modes for the most part).

For both trade studies the optically sensed mixed optical (log radiant flux) frequency response as a direct comparison to the structural frequency response was adequate. The same comparison in Trade Study B for optical versus structural CSC shows remarkable similarity in the location and nature of the phase relationships between energy at different frequency bands, namely the 108 Hz and 224 Hz modes. Compare the structural CSC in Figure 38 on page 140 to the radiant flux CSC in Figure 41 on page 143.

5.4 Considerations for Industrial Laser Vibrometry

Numerous areas of this work indicate capabilities to remotely sense contact surface spectra. While vehicle skin is the focus of this thesis, any nonlinear system where the future phase modulation is a sharp nonlinear function (like contact) of the past phase modulation uses essentially the same mechanism described herein. This could apply to systems with an index of refraction as a nonlinear function of some rapid reversible chemical reaction.

The results along the way toward pure random response characterization in subsection 4.7.1 on page 127 showed the CSC provides an indication of the amount of transient source energy in even when systems are well within conventional ‘steady state’ domains. Compare the off diagonal cross term value for 1) trade study B which has a step gravity application and an impulse, Figure 38 on page 140, to trade study A where 2) the only “transient” is the step function that “turns on” gravity in Figure 32 on page 129, and finally 3) to the removal of gravity, the more purely random response CSC shown in Figure 32 on page 129. **As the system moves to a more**

pure random response the CSC diagonalizes, the cross terms become small compared to those in the diagonal bandwidth.

5.4.1 CW laser covariance vibrometry. This work analyzed continuous wave irradiance (CW), which is less dependent on stability in the physical base¹² for the laser than for DPLM / Moving Target Indicator / TDOA methods [42] and also less sensitive to phase averaging (spatial elimination or reduction) of higher ordered structural modes discussed in Section 4.1 and 4.7. Section 4.7 discusses the difference between remote sensing of symmetrical versus other (higher frequency) modes. Viewing higher frequencies in the optical response spectra such as in Figure 37 versus structural spectra like Figure 25 we can see more pronounced reduction at higher frequencies than those plotted in Figure 35. From the 108 Hz mode Figure 25 has 2 decades less response for the higher mass system whereas Figure 37 shows 3 decades of reduction for the added HRA mass. These plots and the discussion on page 133 shows simulated spectral reduction for plate structures. *This spectral reduction is more of a modal effect than an effect of the optical sensing transfer function.* Figure 25 on page 119 shows that the system mode at 108 Hz and some component modes at 210, 315, and 420 Hz maintain approximately constant in response and center frequency for changes in the structure (gap stiffness). However, modes that are not symmetrical (un – symmetrical and anti – symmetric) near 260, 360, 450, 510, and 550 Hz decrease in response as their center frequencies increase. These modes are non – symmetrical compared to the modes with emphasized frequencies in Table 7 on page 102 (the table of linear normal modes frequencies for the structure). The transfer function is nonlinear but the modes are sensed in their proper frequency location. However, the optical response for symmetrical modes exceeds the non – symmetrical mode response by a wide enough margin to reduce the response of higher frequency structural modes. *Therefore, this full 3 – D spectral reduction is primarily a modal effect.*

¹²For a system where the variation in mount deflection is less than the integrated deflection distance, $\delta u_{mnt} < \Delta t_o \frac{\delta v_{mnt}}{2\pi}$, the dwell phase time corrupts MTI spectral ID phase modulation more than CW ID ($\Delta \Delta \phi_{MTI} > \phi_{coherent} \quad \forall v_{instant} > 2\pi v_{mean}$) [42].

For trade study A the random response at 224 Hz is 11% to 41% of the 108 Hz response, increasing in frequency as it wanes in response with increasing gap stiffness. The impulse response is larger for trade study B at 224 Hz than at 108 Hz due to a coalescence of non – symmetrical modes.

The underlying spectra and even the random load generated CSC’s (trade study A) in Figure 32 on page 129 more strongly respond to the 108 Hz main system symmetrical mode than other modes. The 220 Hz response seen in the impulse loaded trade study B in Figure 41 on page 143 is mild in comparison to the 220 Hz down – step feature in Figure 32. However, the structure of the 100 to 200 Hz rectangle of apparent structural coherence is becoming evident in the random response (Figure 32) and becomes more clear in with the impulse load (Figure 41). This comparison reveals that optical sensing of transient response, although in a mechanical “steady state” having decayed to less than the normal mode response, contains cross – spectral phase information that is a function of the structural normal modes. The subdued transient features provide a CSC that has strong system classification features related to these spectral phase relationships.

The FEA shows that most of the energy is in the lowest and lower order (fundamental) component modes (item 1 on page 146). This distribution drives up required minimum integration times. Development of the plane wave Φ_e response Equations 25 through 27 on page 68 ff show a mechanism for spectral reduction like that found in the laser Doppler measurements [58]. This theory provides an extension of the theory behind DPLM sensing since each pulse is a coherent detection before the COTS systems determine speed from the time between pulses.

5.4.2 Non – stationarity of nonlinear dynamics. Not only are structural plate contact systems nonlinear (in a geometric sense) but they have a stationarity issue as well. Results in Chapter IV show what appears as a stationary response with some “high” frequency modes (300 – 550 Hz) modulating the time domain response (Figure 17 on page 109) with a dominant 108 Hz mode. This appears to be the

reason the 224 Hz response is so prominent (Figure 25) even though the time response clearly shows 108 Hz is dominant in Figure 17. The band at 224 Hz (and other non – symmetrical modes) is “squaring” the 108 Hz sine wave in time.

A lack of stationarity, the response being not quite in steady state, appears in the short duration Periodograms of $\Phi_e(t)$ and the image SNR¹³ calculations over time, the result of otherwise apparently sufficient 0.1 second duration data and analysis. The rationale for attempting to run these runs out to 0.2 sec was the appearance of a change in integrated radiant flux and the SNR fluctuations¹⁴ at the detector near the end of the 0.1 second duration that appeared to ‘level off’ compared to the response during the 20 to 80 ms time frame. The 0.2 second ‘long runs’ have response after 0.12 sec that is much more ‘smooth’ and the SNR fluctuations tapered off asymptotically in that time region as well. Image SNR plots averaged over the random loads for trade study A provided the best feature so far for both the 108 Hz symmetrical mode and showed the main (170 to 220 Hz) moving non – symmetrical mode with equal prominence.

5.5 Concluding Remarks

CW is an adequate spectral ID phenomenology for target classification. During this work a theoretical reason for spectral reduction became evident. These simulations provided evidence to support spectral reduction. one motivation is that CW phase modulation remote spectral ID is less sensitive to mounting vibration than dual pulse vibrometry. The structural model matched closed form results indicating only symmetrical modes avoid both an increase in modal frequency for increases in gap stiffness and spectral reduction. This modal symmetry behavior provides one dis-

¹³Equation 44 on page 98 describes the ‘image’ SNR.

¹⁴The spatial image SNR calculation of Equation 44 on page 98 is sensitive to the flatness of the deflection, $w(x,y)$, the uniformity of the phase modulation. SNR is low for low deflection gradients and high for sharply bent shapes due to its spatial nature. This SNR is easy to calculate since we have introduced our own noise and know its power, S_{noise} . The average optical return power of all the pixels, $\overline{image(x,y)}$, causes the numerator to go to zero for a flat (spatially constant) deflection;

$$SNR = \frac{E[S_{image}(x,y) - \overline{S_{image}(x,y)}] \cdot E[S_{image}(x,y) - \overline{S_{image}(x,y)}]^*}{S_{noise}} .$$

criminator within vehicle models (non – symmetrical modes) and another for model to model classification (symmetrical modes).

Appendix A. Physical Vibration model

The physical model is an abstraction, a starting point between the physical world and the mathematical models of closed form analysis and numerical models such as those used in Finite Element Analysis (FEA). At this point in the conception of the simulation the assumptions of exactly uniform material density, Young's Modulus, and other physical properties remain, which is an optimistic model.

A.1 Structural Loading

Trade study A uses a random load set generated in Matlab read into 30 contact nonlinear transient NASTRAN (SOL 129) FEA runs. The response from the random load cases requires averaging to estimate the structural modal resonances. Trade Study B uses a structural impact to 'ring all the modes' which the results show works well; the impact response spectra clearly show modal response related to the FEA normal modes (SOL 103) without the spectral averaging required for trade study A. Definitions for 'impulse' and 'impact' vary, but the Mechanical Engineering community generally defines impacts to be sharper than impulses.

The results of this work show energy transfer from high frequency energy (sharp impulse) to the fundamental mode near a low 108 Hz. For trade study B, the low frequency energy part of the engine power spectral density or density function (PSD or PDF) is due to these impact or impulse events. That the structural PSD spectrum changes due to impact is seen even in 'linear impact theory' where deflections and stresses are approximately double the static equivalent values [40, 239].

There is an MSC Conference Paper that gives us some insight into this discrete nature. In an analysis using LMS systems Brughmans, Lembregts, and Furini [48] provides a table of frequencies for the major modes of a Pininfarina test chassis system that correlate sufficiently to known vehicle structural modes. Their study calculated modal acceptance / assurance criteria (MAC) numbers [2, 3] related to correlation between FEA and test [4], damping ratios for the lower modes, and indicated lower damping at higher modes (but not uniformly decreasing damping). The modes started

with the sequence 39.3, 45.0, 50.4, 77.1, 81.0, 89.0, . . . past 160 Hz without coalescence of modes. These frequencies indicate a typical stiff chassis structure.

In most domestic sedans care is taken to design separation structural mode frequencies (“resonances”) away from suspension modes usually found around 15 to 28 Hz. Usually the design can shift mode frequencies above the suspension values to avoid coupling. However, there are designs where modes below the suspension frequencies are unavoidable.¹ These lower frequency modes are nearly discrete well separated spikes in spectral energy density (Joules / Hz) but have small finite bandwidths. That the vibration energy resides in these low energy modes is the reason so many hundreds of millions of dollars are spent world wide on such analysis. All vehicle OEM’s model these ‘Normal Modes’ below 300 Hz in their FE models which are on file for each model. Use of these proprietary FE models and their resulting modal frequency definitions, the normal modes of each structure, is the most effective way to prove their vehicles meet many Federal vehicle safety standards. This is one reason OEM’s store this data, which could be of use for laser spectral ID.

The FEA for trade study B used to generate vibrating surface deflection data for the phase modulation of the sensor laser uses an artificial (purposefully applied) impact load to ring the modes. These geometric nonlinear modes gathered from direct transient time integration with MSC/NASTRAN’s Newmark – Beta solution sequence (SOL 129)² are the response to wide band excitation, nearly a white noise response.

The use of impacts (short duration impulses) without signal processing windows to energize the structure for analysis of structural normal modes is a common practice in the vibration industry as described in “Golden Nugget” number 12 [16]:

¹For example, in convertible sedans, the main free – free cantilever mode is usually approximately in the low 20’s – even with high rocker panel sections meant to stiffen the vehicle against this one particular mode (the reason you need to step higher up to exit such low riding vehicles).

²Original theory: [52], NASTRAN theory: [46] page 8.3-1, implementation in NASTRAN: [46] 9.1-4 (This is the page with the resonance testing quote.)

“When performing resonance test, do not use the Hanning or any similar windows, unless the impact and response signals are delayed to move them to the center of the time block. Since the response is maximum after the impact, these data must be moved away from the edge of the time block where it would be destroyed or severely attenuated by the weighting factor. Use of a uniform window does not require a delay, because it does not attenuate the signal at the beginning or end of the time block.” [16]

A.2 *Structural Nonlinearities*

This physical model assumes a linear superposition of vibration modes and an assumption of a linear optical model (no air turbulence). However, some ordinarily assumed linear effects for dynamic response are assumed nonlinear at the outset. A treatment of how fixity changes the modes and therefore the sensed optical radiant flux is in subsection B.2.3 on page 187, including nonlinear examples that compare to the contact nonlinearity of the FE model for this work. These complications require care in following the load deflection curve and in control of the nonlinear solution per time step and over time. Subsection B.2.6 on page 192 discusses load increments, iterations, and other aspects of following the millions of DOF’s load deflection “curve” of ordinary vehicle FE models in greater detail.

A.2.1 Zienkiewicz’ closed form energy transfer proof. Vehicle structures of all types have complicated nonlinear load paths that dump energy into low frequency structural modes. The engines have non – negligible vibration spectral energy down at these “fundamental” and near fundamental mode³ frequencies even without the nonlinear effects. Damping helps drive the energy into the lowest modes. Zienkiewicz showed [94, 340, 341] this energy transfer using only viscous damping to form a ratio of damping to its critical value,⁴ $c_i = 2\omega_i c'_i$ as shown below. \mathbf{K} is the stiffness matrix, \mathbf{M} the mass matrix, \mathbf{C} the damping matrix in the general DE that Zienkiewicz uses, $\mathbf{M}\ddot{\mathbf{a}} + \mathbf{C}\dot{\mathbf{a}} + \mathbf{K}\mathbf{a} + \mathbf{f} = \mathbf{0}$, a forced vibration problem.

³The ‘fundamental’ mode is the one at the lowest frequency.

⁴Critically damped systems remove all oscillation from the system.

“ . . . we have indicated that the damping matrix is often assumed as $\mathbf{C} = \alpha\mathbf{M} + \beta\mathbf{M}$. Indeed a form of this type is necessary for the use of modal decomposition, although other generalizations are possible [references given in the book]. From the definition of c'_i , the critical damping ratio [described above], we see that this can now be written as

$$c'_i = \frac{1}{2\omega_i} \bar{\mathbf{a}}_i^T (\alpha\mathbf{M} + \beta\mathbf{M}) \bar{\mathbf{a}}_i = \frac{1}{2\omega_i} (\alpha + \beta\omega_i^2)$$

Thus if the coefficient β is of larger importance, as is the case with most structural damping, c'_i grows with ω_i and at high frequency an over – damped condition will arise. This is indeed fortunate as, in general, an infinite number of high frequencies exist which are not modelled by any finite element discretizations.” [94, 340, 341]

A.3 Modal Analysis

While many types of nonlinearities have little effect in typical laser vibrometry of vehicle systems, enough nonlinearities remain that a discussion and list of them is appropriate. A start on such a list appears in Table 9 on page 173. This appendix first discusses a set of linear assumptions. The next part is devoted to structural nonlinearities. Then the discussion flows into the nonlinearities and nuances that are required to describe vibrating structures considered for target ID. The one and two DOF simplified differential equation models assume a structural energy flow similar to that shown in Figure 43.

A.3.1 Field nonlinearities, in general. As discussed in subsection A.3.3, the vibration PSD resulting at the surface is different from the input motor PSD and is especially concentrated on low frequency modal energies including most of all the fundamental modes of the various components and the full vehicle fundamental mode. Section 4.3 on page 84 analyzed closed form damped nonlinear contact one and two DOF models using recent methods from an AFIT dissertation [90]. At some locations in the vehicle many ordinary vehicle loads are ‘large loads’ for the local structure. This generates local nonlinear response. Nonlinear effects are often thought of in terms of field disturbances in the realm of electrodynamics and acoustic analysis. Geomet-

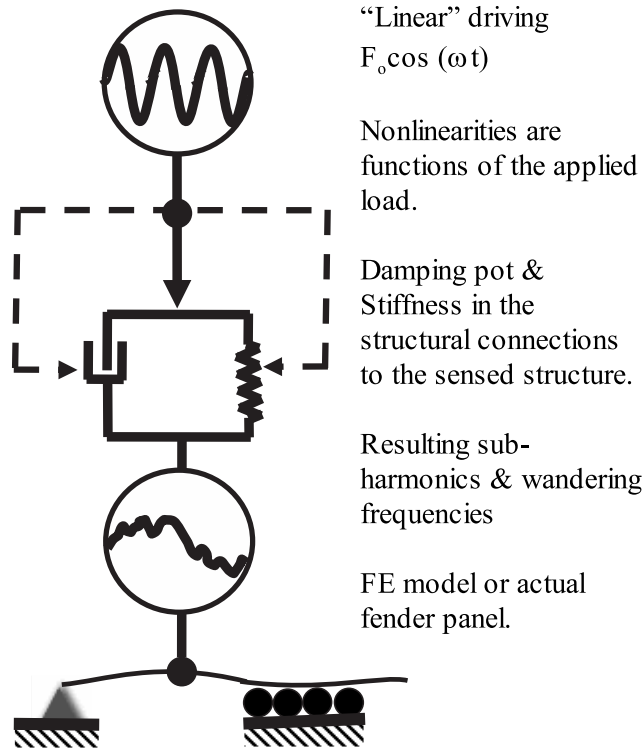


Figure 43: The motor PSD feeds vibration energy into the full vehicle including many subcomponents with nonlinear response.

ric nonlinear structural field issues are not the major nonlinearities causing modal participation at frequencies far lower than source noise and vibration (engine vibration). Nevertheless, some issues observed in field disturbances do apply in a minor way. Classical texts on electrodynamics, hydrodynamics, seismology, and acoustics will often initially investigate the linearity of vibration in transverse versus compression waves. Additionally there is a consideration of nonlinearity as an evanescence of the vibration energy, a loss term. Pierce [61, Ch. 11] considers the nonlinear effects of shock waves and then considers effects caused by a “small nonlinear perturbation” such as radiation pressure.

Acoustic radiation is a substantial part of the vibration modes in the outer surface skin. Acoustical energy emanates from piston type air compression due to vibrating surfaces and the structure absorbs this energy in a manner similar to that

generated.⁵ This ‘linear piston theory’ energy generation and absorption is a strong function of the ‘panel’ geometry. The interaction directly from the engine (a fairly hard panel) causing engine compartment acoustical modes impinging on the hood will directly cause hood panel modes from acoustical absorption, subject to radiation pressure nonlinearities.

Considering vibration alone (ignoring acoustics), assumptions of Simple Harmonic Oscillation used in Figure 43 are lower order assumptions where strain energy density is assumed to be low enough not only for linear elasticity assumptions (lack of permanent set) but also for an interesting point from Lord Rayleigh; There is no such thing as a real sine / cosine wave in reality (a crudely paraphrased summary). After deriving the differential equations (DE’s) for Newton’s theory for isothermal compressive – vacuum (“condensation – rarefaction”) vibration, he provides the DE in this second order form [80, Vol 2,33].

$$\left(\frac{dy}{dx}\right)^2 \frac{d^2y}{dt^2} = \frac{dp}{d\rho} \frac{d^2y}{dx^2}$$

Lord Rayleigh then comments on the ability of simple harmonic motion SHM to maintain shape in nature.⁶

A.3.2 Driving mass structure definition. The physical model of the two DOF model considered in this work would ordinarily be an ‘isolator problem’ but

⁵Statistical Energy Analysis software documents this well. It is the mechanical impedance and other properties of the panels that determine both the radiation and absorption of acoustic energy.

⁶“Since the relation between the pressure and the density of actual gases is not that expressed in [$p = \text{constant} - \frac{u_o^2 \rho_o^2}{\rho}$], we conclude that a self – maintaining stationary aerial [acoustic] wave is an impossibility, whatever may be the velocity u_o of the general current, or in other words that a wave cannot be propagated relatively to the undisturbed parts of the gas without undergoing an alteration of type. Nevertheless when the changes of density concerned are small, [$p = \text{constant} - \frac{u_o^2 \rho_o^2}{\rho}$] may be satisfied approximately; and we can see from [$\frac{dp}{d\rho} = u_o^2 \frac{\rho_o^2}{\rho^2}$] that the velocity of stream necessary to keep the wave stationary is given by [$u_o = \sqrt{\frac{dp}{d\rho}}$] which is the same as the velocity of the wave estimated relatively to the fluid.” [80, vol. 2, p. 33]

since we fix the base to ground in this study, the system is a ‘suppression problem.’ Except here we do not try to suppress vibration, but measure it.

The ‘large mass’ representing interior components attached to the hull and the remainder of the entire vehicle is attached through a ‘frame’ member to the hull as shown in Figure 48 on page 185. The mass matrix for this lumped mass, and interim masses similarly lumped at single nodes, the bolts representing fastener doublers and washers, uses three identical diagonal (scalar mass) entries and six properly scaled mass moment of inertia terms for a sparse 6 x 6 mass matrix (6 DOF’s by 6 DOF’s).

In the FE model for this system, the ‘spring’ representing the base system stiffness (k_{base}) has a stiffness of 1.57×10^8 Newtons per mm. With the system mass of 0.5×10^5 Mega grams⁷ (giving a mass moment of inertia of $24.5 \times 10^{10} Mg \cdot mm^2$) this gives a low angular speed, and subsequent vibration frequency of 8.9 Hz as shown in Equation 48. This is the eigenvalue for the mode of the full system mass acting against the albeit weak ‘spring’ attaching both the FE plate model and the system large mass to ground. Only the out of plane (z) direction is active for the current system large mass. Rotational inertia due to the vehicle system is not significant for this work.

$$\omega_{base}^2 = \frac{1.57 \times 10^8 \frac{N}{mm}}{0.5 \times 10^5 Mg} = 56.04^2 \frac{Mg \cdot \frac{mm}{s^2}}{mm \cdot Mg} = 2\pi(8.9)^2 s^{-2} \quad (48)$$

This low (DC – like) 8.9 Hz mode is below the substantial 1/f noise below 50 Hz. It is the plate structural resonances that have most of the vibration energy at the surface. So the ‘large mass’ accomplished its mission.

In the nonlinear model the normal modes excited include ‘open’ and ‘closed’ stiffness modes and hybrid modes where the energy of the mode changed due to

⁷A Newton is a $kg \frac{m}{sec^2} = Megagram \frac{mm}{sec^2}$. The later mm form is used for consistent units in the FEA. A Newton of force is 0.138 ‘poundal’ in inch-lbm-sec units, or in the more common pound force units, $4.448222 N = 1 lbf$, $1 N = 0.224809 lbf$. The automotive industry has been using metric units exclusively since the 1980’s except that tools at that time were mostly still in English units. Although automobile designs have been in only metric units for over two decades, the Aerospace industry is still today using mostly ‘English’ units.

moment arms during contact of one region of the plate when another is in ‘lift – off’ condition. Normal Modes of the FE model with all edges ‘simply supported’ show up close to their resonance peaks in the Fourier transforms of the steady state post impact time regions of the direct transient nonlinear contact time history FEA results. While “nonlinear eigenvalues” are merely proposed here, these ‘hybrid’ resonance modes are clearly related to the ‘open’ and ‘closed’ stiffness normal modes.

In trade study A we track the variation in these modes, the resonances calculated from SOL 129 direct transient results, with respect to changes in a structural design parameter (the gap stiffness k). These ‘hybrid’ resonance modes vary in a manner dependent on the mechanics of the structural nonlinearities. Simulation of contact occurs when a large increase in stiffness from a moderate k_{open} value to the stiff $k_{closed} = k_{open} + k_{contact}$, occurs. k_{closed} is meant to represent the surface compression, the contact of two rough surfaces. The effects of the contact are not as straightforward as it would seem.

A.3.3 Wandering modes of nonlinear structures. Table 9 on page 173 listing the pertinent loading mechanisms affecting and effected by nonlinearities helps characterize the source of vehicle surface vibrations. Structural nonlinear effects have many forms including material, geometric,⁸ large deflection, large strain, follower forces, joint friction (structural damping), nonlinear damping, and active or semi – active control. Much funding for studies into the latter come from the ubiquitous new motor mounts with internal hydraulics, orifices, and check valves.

In a typical vehicle, impact type loads from piston engine reciprocating components and turbine combustion travel through many nonlinear systems before showing up as vibrations on the surface. Some energy from these modes distributes due to the spread of the response curves as a result of damping.

⁸Geometric nonlinearities include arc length member shortening versus first order perpendicular deflection where the length in the un – deformed direction is only affected by axial loads and thus incorrectly increases. A ‘linear’ cantilever stretches more than a nonlinear cantilever due primarily to the geometric assumption of using $\sin \theta \approx \theta$. Contact is another geometric nonlinearity.

Viewing the engine PSD load (or PDF) as separate impulse events provides additional insight. “Linear” impact loading (non – explosive, e.g.: spring loading into jounce) will drive the structural response at about twice the static deflection thereby approaching many (small load related) nonlinearities more closely than static analysis would imply. Separately, consider impact: “Whether the loading should be considered as *quasi – static* or impact loading is often judged by comparing the time of application of the load, or *rise time*, with the longest natural period of the structure (approximately that wavelength due to the lowest frequency in the FEA results).” [25, 526, Ch. 15]. There are many such static, quasi – linear, and full impact loads in typical commercial structures and other vehicles. These impulses and impacts lead to a transfer of energy to lower frequencies.

After the vibration PSD’s decrease in energy and grow in bandwidth due to the effect of nonlinear stiffness and damping from the motor mounts and other internal hardware, the propagating vibration energy encounters thin sheet metal parts and nonlinear stiffness material fasteners. These parts contribute structural damping resulting from the true structural nature of fasteners. Additional nonlinearities come from subharmonics and non – stationary resonance frequency values of these structural components. Structural damping is akin to a stiffness approximately $\frac{\pi}{4}$ out of phase with the structural deflections of any given mode. These results act as a linear superposition of all the resultant structural damping for all the structural modes in proportion to the modal participation of the vibration (strain) energy of the structure in steady state.

Due to the cost of supporting engineering staff to analyze full vehicles, the domain of much analysis in the discipline, the majority of the technical reports in this field are proprietary and closely held. With thousands of engineers on duty at the Milford Proving Grounds and other sites within GM, the multi – million dollar cost of determination of the “ride and comfort” criteria like the nonlinear transfer function for engine noise transmission into cabin and panel acoustics drives this information to remain in proprietary status.

One public study apparently provided for analysis of Nissan vehicles [83] has some charts showing clear differences in the nonlinear (test data) versus linear (FEA) results. While these results are for road vibration, the transfer function through the suspension is not unlike the transfer function from engine noise into and out of the suspension on the way to the vehicle surface skin.⁹ Experience has shown that useful nonlinear mappings are not cost effective for many engineering purposes, even for vehicles undergoing incremental changes. This ineffectiveness of full nonlinear mapping is due in part to some of the issues of ergodicity and the size of the solution space. For this reason **the industry just looks at the modal excitation and tabulate the frequencies of the lowest modes**, a technique that appears to work well for the number of vehicles in production today.

A.3.4 Damping Distributes the Driving PSD. The frequent near instantaneous impact level loads from turbines (combustion and components) or piston engine reciprocating components travel through many nonlinear systems before showing up as vibrations on the surface of the vehicle. These systems also have damping. The PSD of the engine rarely appears on the skin in the same form as the source,¹⁰ except perhaps on parts of an engine hood of typical commercial vehicles (but that is primarily an acoustic transmission). The PSD of the target plate in our study has a mild driving load at low frequency structural modes due to damping and a larger effect due to nonlinearities discussed previously.

⁹It should be noted the plots displayed in the presentation showed far more difference between linear and nonlinear analysis (5 dB difference) than the charts in the published paper. Some of the results presented at the conference were not approved for final publication. This work provides overall mapping from the linear response of analyses like FEA and test into a better estimate of the actual nonlinear full vehicle system response.

¹⁰Response to engine PSD's will undergo distortion. If classification beyond differentiating between turbine and reciprocating engines is necessary, this is a problem. Except for direct load paths this distortion usually renders the response unsuitable for spectral ID of vehicle model types. For example, OEM's work to remove engine noise from the cabin starting with motor mounts which necessarily distort the transferred PSD. Using Acoustic Boundary Element Analysis in the early 1990's Walker Automotive in Michigan made the exhaust system of the Corvette so quiet that customers complained until they backed off the improvements. Military vehicle manufacturers work hard to remove this particular type of noise radiation. This thesis suggests the use of normal modes for target ID, which has been proven to work [43, 54].

Motor mounts have nonlinear stiffness and include intentional nonlinear damping. Although damping will excite more modes than allowing a theoretically high oscillator quality¹¹ lightly damped engine PSD to drive the structure, the trade – off in mount design uses viscous fluids and viscoelastic materials in mounts to remove energy by other dissipation mechanisms. DE’s for check valve – orifice systems has mass terms that are not constant. Motor mounts also isolate vibration using energy transfer into heat. Originally this isolation was similar to RC circuit tuning but they now accomplish active, semi – active, and semi – passive control through various nonlinear means. Equations 49 and 50, which are Equations 1-33a and 1-33b in the referenced text, describe the strain rate ($\frac{\partial \epsilon}{\partial t}$) effects of nonlinear viscoelastic equivalent to Young’s Modulus, E , on the stress, σ . Unlike the usual use in structural engineering (t = thickness) here ‘ t ’ is time.

“Linear viscoelastic materials are those for which the hereditary relations above [the usual stress and strain relations] are expressed in terms of linear superposition integrals, which, for infinitesimal strains, take the forms

$$\sigma_{ij}(t) = \epsilon_{kl}(0^+)E_{ijkl}(t) + \int_0^t E_{ijkl}(t - \tau) \frac{\partial \epsilon_{kl}}{\partial \tau} d\tau \quad (49)$$

$$\sigma_{ij}(t) \equiv E_{ijkl}(0^+)\epsilon_{kl}(t) + \int_0^t \epsilon_{kl}(t - \tau) \frac{\partial E_{ijkl}}{\partial \tau} d\tau \quad (50)$$

. . . thus the materials are assumed to have purely elastic volumetric change. The definition of a Poisson’s ratio is somewhat ambiguous in viscoelasticity.” [13, 6 ff]

The effect of the relaxation tensor, $E_{ijkl}(t)$, and on the stress, σ_{ij} , is nonlinear in a hysteresis manner, although at any point in time “the materials are assumed to have purely elastic volumetric change.” This is just another form of linearity (purely elastic change) in a system that is clearly nonlinear in time as the usual extension of this theoretical development into the Creep Compliance Tensor shows. Creep is a

¹¹Off resonance response increases with damping, γ . $Q_{SDOF} = \frac{\sqrt{\omega_o^2 - \gamma^2}}{2\gamma} \approx \frac{1}{\gamma}$ (light damping [81, 75])

nonlinear material effect. But at certain points in time, the response of a viscoelastic material such as those used in motor mounts may appear to be locally linear in time and space. These nonlinearities all effect the vibration responses seen at the vehicle skin surfaces.

A.4 Nonlinearities Summary

Full system FE models can include the damping mechanisms described earlier and other more sophisticated damping models. The combination of the structural damping and contact nonlinearly excited low frequency modes. Proof and test data showing this effect in general are implied by the basic texts [6,17,18,25,46]. Additionally, other nonlinear effects transport more vibrational strain energy into the lower frequency modes.

It is precisely these lower frequency structural surface vibration modes that are under investigation in order to identify the model and vehicle type of the structure. The combinations of their FE model eigenvalues (frequencies) and FE model eigenvectors (mode shapes) are the characteristic matrices, Eigenvalues $\mathbf{\Lambda}_i$ and Eigenvectors \mathbf{U}_i , that together form the solution. $\mathbf{\Lambda}^{model}$ is a bandwidth = 1 diagonal matrix where each diagonal term is an eigenvalue $\lambda_i = 4\pi^2(f_i^{model})^2$ for that particular vehicle model. Eigenvalues $\mathbf{\Lambda}^{(A)}$ represent the modal frequencies, $f_i^{(A)}$, for a particular model A. Similarly, the Eigenvector matrices \mathbf{U}_i^{model} composed of eigenvectors \vec{u}_i^T for each object class (model and type). These $\mathbf{\Lambda}_i$ and \mathbf{U}_i for engine and structure number ‘i’ are substantially different for slight model changes of the same vehicle type. *These are the structural features we seek to detect.*

One last form of nonlinearity, the only one that this thesis will analyze in detail, is contact nonlinearity. This is a physically geometric nonlinearity. The stress – strain curve is bilinear with the vertex at the ‘contact’ location. However, in a typical vehicle FE model there are millions of DOF’s so a 2 – Dimensional bilinear model is a bit simplistic and does not include solution conditioning parameters.

Table 9: Nonlinearities Affecting FEA – CW

Type	Description
Geometric	Large Deflection
Geometric	Thin sheet thickness
Geometric	Follower Forces
Geometric	Contact
Material	Hardening Materials / springs / motor mounts
Structural Joints	‘short time’ variations: Structural Damping
Structural Joints	‘short time:’ Fastener clamp – up
Structural Joints	‘short time:’ Joint allowables
Structural Joints	‘long time:’ Creep, fretting fatigue, wear, & spalling
Acoustic	Small parts low frequency noise generation inefficiency
Optical	$\tau(\lambda_o)$
Remote Sensing	Mode shape effects on pixel SNR
Signal Processing	Phase wrapping, aliasing, and cycle jumps
Signal Processing	Optical modal participation and ‘image SNR’ $\sum_{modes}^{all} \Phi_k^{opt} \Psi_k^{opt} = \int_{t=0}^{t_{int}} \Phi_e dt, \quad \Phi_e(t) = \int \int \Phi_e(x, y; t) dx dy$

A.4.1 Nonlinearities affecting FEA and CW results. Appendix C discusses a closed form solution that shows resonant frequency movement in time and the subharmonic generation due to use of a control law for unsupervised contact like that found between a vehicle sheet skin and stiffeners in the region between fasteners (bolts, rivets, or spot welds, which all have different fixity). Most commercially available vehicle FE models will not have the substantial work of contact definition in the FE model for the full system partly because “it is only the modes that matter” (matching PSD’s is unnecessary for target ID since a few of the first modal frequencies adequately classify any vehicle make and model). The structural nonlinear characteristics can, in principle, be tabulated by geometry and fixity, which varies for fastener type.

Table 9 lists two sets of nonlinearities, structural and optical. The first set of nonlinearities are ‘geometric’ because the effect on the DE is in the geometric matrices that define the order of the static solution (Green’s strain tensor), the fit of basic thin shell theory, the orientation of a load during deformation, and switching of point to point contact (actually a material bi – linearity). Material nonlinearities are in effect

in actual physical structures and they also transfer vibration energy in a nonlinear way (to lower frequencies). These nonlinearities are also active in long term system change. Finally the radiation of surface vibration into sound and subsequent re – absorption with multi – path combination and non – uniform mechanical impedances is a highly nonlinear process even if it is the easiest way to sense engine PSD from the skin. This phenomenology (engine spectral ID) is a physical entity that is under attack at all OEM design centers and has already become obsolete for the 2005 Prius whose running gasoline engine was several decades lower in noise power level than the other 200 vehicles in a collection at WPAFB in 2006 [64] using AETC sensing technology.

A.4.2 Why use Bolt Area Variations for an Ensemble? There are two rationales for using bolt cross – sectional variation for trade study B. The first one, use of MIL–HDBK–5H statistical variation guidelines for strength considerations, is an indirect model for static indeterminacy variations. However, it is statistical and those values are roughly the variation in strength of materials. While the MIL–HDBK–5H A and B basis variations are not specifically the joint strength variations, they model the strength variations available for the bolt shanks and envelope the static load paths available before frictional considerations. The more straightforward rationale is the concept of joint allowables. The former rationale is a more simple number to follow and follows the spirit of some aircraft design methods in using a set of tabular constant conservative values (less variation in application). The latter rationale of an effective joint allowable cross – sectional area follows the physics of the problem more closely. In using joint allowables that are conservative for strength calculations we expanded the variation considerations beyond those the structure will experience in common application. Since we seek to characterize the structure as it appears to the remote sensing system, *the use of both rationales envelope the selection of a 10 to 15 % variation in bolt cross-sectional area.*

In considering the mechanisms by which several tests of a structure would produce different samples of return for an ensemble required for the statistical cross – spectral covariance (CSC) methods, the issue arose that running the FEA over and over again gives the exact same answer, not an ensemble of measurements that the Electrical (and Optical) Engineering community is used to in many of their experiments. What is the physical mechanism that changes the load paths ever so slightly such that our statistics of phase relationships in space and time become useful? This proposal is that the variation seen in reality is a combination of frictional hold variation and the static indeterminacy of the 4 bolt system. So this trade study varies the bolt areas by 10 and 15% to model the changes in frictional holds, which are entirely empirical, systems specific, and quite random [39], [92, 657], [67, 9-159] and [68].¹² Section 9.4.1.1 of MIL-HDBK-5H describes the reason for joint allowables being different from the shear strengths.

¹²“9.4.1 Mechanically Fastened Joints” page 9-169

Appendix B. Finite Element Model

This appendix discusses the Finite Element Modelling details and the structural engineering effects related to choices for the FE model.

B.1 FE modelling for surface displacement and speed output

The FE model generates the surface displacements and out – of – plane speeds that represent a typical armored vehicle. This choice of a vehicle is merely more simple to start with than a pickup truck or other commercial vehicle due to issues with multi – layer body – in – white manufacturing (see the body – in – white footnote on page 7). The M1A1 – like panel modelled for this work also has conveniently simple flat surfaces with only two layers, the hull and the HRA which is bolted to the outside of the hull to provide ablative and other impact protection. However, the dimensions are arbitrary and do not reflect any design for an actual tank.

B.2 Physical Model

The model of the HRA plate connection is similar to actual use. The goal is to form a physical model of a vehicle component that acts the way the HRA would, without having to use an existing design. The overall characteristics of the physical model are as follows. The one inch (1) Homogenous Rolled Armor (HRA) is bolted onto a hull. Rotations are released at joints. Hull edges have both symmetric and antisymmetric boundary conditions (BC's) per Figure 45. Therefore, the FE model behaves like a segment of a larger structure framed on the sides. The gravity load is at 45 degrees to the surface normal. The applied Gaussian (in time) impulse/impact has duration 3.6 milliseconds (1.0 FWHH). The impulse acts into a frame in the hull interior then into the bolt pattern. The bolt pattern is sufficiently interior to edges (St. Venant's theorem) to avoid high stress or displacement concentrations. Equation

51 shows the material data including the HRA Bulk Modulus (B) gathered from Natl. U. of Singapore data [75].¹

$$\begin{aligned} B &= \frac{E}{3(1-2\nu)} = 1.70 \times 10^5 MPa & \rho &= 7.85 \times 10^3 \frac{Kg}{m^3} \\ G &= 8.70 \times 10^4 MPa & S_y &= 1,320 MPa \end{aligned} \quad (51)$$

B.2.1 Symmetric Boundary Conditions. These boundary condition (BC) symmetries are unrelated to the mode shape symmetries defined in subsection 2.2.7 on page 30. Apart from the need constrain the model, symmetry is useful to model a larger structure with a smaller one to keep from reaching memory limits. The symmetry techniques in this model may be unconventional in the public literature but most are used routinely at OEM's. Ordinarily anti – symmetry is used to model a case where the loads on the opposing planes of symmetry are opposite of their mirror images. A more common use is the linear combination of symmetric and unsymmetric “subcases” where the BC's change from one subcase to the other and the results are added together to form the un – symmetrically loaded result set. An example of this is ordinary full aircraft one gear landing with no spin – up. The symmetry BC's in Figures 45, 46, and 50 are easy to visualize. There is no displacement allowed through the plane of symmetry and the structures have guided fixity along that plane; no moments are allowed to rotate the structure out of plane except for torques allowed to rotationally deform the structure about the symmetry normal.

In this case the two antisymmetric edges each model the connection of a frame to the hull. The intersection is allowed to deflect perpendicular to the bulkhead (in the plane of the hull) but not along the intersection, inboard, or outboard. While an actual hull and bulkhead joint will have some of this “forbidden” deflection, it is negligible enough that from the point of view of the hull only, a welded bulkhead – hull joint behaves similar to the antisymmetric boundary condition in the FEA. While rotation about the normal and translation in plane are not allowed, the major

¹Current found at http://staff.science.nus.edu.sg/sciloee/srp_2003/sci_paper/dsta/research_paper/neo_wei_siong.pdf (underscores omitted).

bulkhead – hull displacement effects of out of plane rotations and displacement of the joint – intersection in and out of the symmetry plane (the plane at zero load before deflection) are active. The only draw – back to this arrangement, convenient for modelling a bulk – head joint, is that it also models moments at the joint due to an oppositely placed load on the ‘large mass’ (Figure 47 on page 184) mirrored onto the outboard on the opposite side (Figure 50 on page 197) of the antisymmetric boundary. The exterior gravity loads are similarly oppositely directed. However, a consideration of how loads transfer through the bulkhead and into the plate shows this BC can be reasonable. Due to their remote location from the main FE model quarter panel segment Saint Venant’s theorem applies but we do not need to apply it. In the physical model this structure undergoes loads in all directions, from many different locations, from many different types of auxiliary loads. The turret running rail ring opposite the business end will actually have an upward vertical shear load. It is reasonable that a full vehicle would undergo loading complicated enough that there would be a critical load case such as the one these BC’s model.

The symmetric conditions that cut the panel into four model boundaries assumes a turret – like exterior hardware insert into the skin in a very crude way (on both symmetric BC edges, which is different from an actual turret). This model is meant to represent modes similar to those on the tank (or other armored vehicle) but not to the extent that the geometry is representative. This is a “general estimate” of how an armored vehicle would respond. Boundary Conditions can have drastic effects on the solutions. For example, the symmetric conditions exclude ‘antisymmetric’ mode shapes across their boundaries. Therefore, we know that a mode or set of modes between 108 and 220 Hz is constrained thereby making the solution more stiff than it would be without this quarter panel symmetry. It is customary in the industry to use symmetry when the lower frequency modes are the only modes of interest and the exclusion of modes that are antisymmetric about the planes of symmetry does not substantially increase the stiffness of the structure. For the structure as assumed,

there is some attachment on the exterior between the armor plates that effectively provides a guided condition at the symmetry lines, so these spectra are valid.

The antisymmetric BC's approximately model boundaries of a large panel and the symmetric BC's segment that panel into quarters, two symmetric edges interior to the panel on each segment. Figure 45 shows each panel has deflection results that are mirror images of its neighbors on the symmetric (not antisymmetric) edges. The results for the FE model are only for the segment modelled but combined with knowledge of the symmetry, Figure 46 shows they become a set of results for the entire system of where the symmetric kernel is only a portion of the FE model.

In David Smallwood's article on analysis versus test [77] he notes the typical problem of limited, sparse data that represents little of what is perceived to be product behavior when the product passes tests. "We typically test in one axis at a time although we know that the use environment excites all axes at the same time. We do very little testing with combined environments." The offset in the large mass model of the connection to system source to the hull armor interface is an attempt to avoid lining up to a particular coordinate axis of linear symmetry, which would provoke similar problems.

Vibrating surfaces of vehicles have characteristic "Normal Modes" that are a useful identification feature to distinguish models and vehicle types from each other [43, 54, 83]. Convertibles typically have the lowest fundamental mode frequencies, f_o , of nearly any common vehicle due to the low positive maneuver bending stiffness. The values of f_o for these vehicles are often below the suspension mode frequencies² in the initial design stages. A major goal in commercial vehicle structural design is to maintain mode separation to reduce the transfer of strain energy from mode to mode (see Section A.3 on page 164). Coupling between modes can lead to more problems than the common transfer of vibration energy down to lower frequency modes – some resonances may become problematically high. Mass 'dampers' absorb

²Suspension frequencies are often roughly in the 20 to 30 Hz range.

energy at certain modes.³ Some modes are stiffened to move the frequency response peaks to more desired values.⁴ It is the normal modes that designers work to change, not a continuous PSD.

Armored target vehicles will usually have a fairly flat panel which at some point in time faces a direction that is nearly in line with part of an airborne sensor's field of view (FOV). The modes for the un – reinforced rectangular panel are a superposition of vibration modes that are sinusoidal in space and time as shown in the FEA results (Figures 21 and 23 through on pages 113ff) and basic structural references [92, 717, #16].

B.2.2 Physical Model for the FE model. The physical model of the structural component used for the FE model begins with work on an overly lumped mass model. The idealized structure (physical model) is an assumed perfectly manufactured $1m \times \frac{1}{2}m$, 3 inch thick armor plate on an inch thick armored vehicle hull. Figure 50 sketches the overall system. Figure 44 describes The geometric nonlinear contact at each node.

The FE model is composed of plates meshed with linear quadrilateral elements that span 11×26 nodes per plate. These plates represent the one inch thick HRA plate and an assumed three inch thick hull. Between the two plates at each of the 286 nodes is a contact element, an MSC/NASTRAN CGAP element without any adaptive or other exotic options. Figure 44 shows a physical representation for the gap element. Any node on the armor plate will be aligned exactly above the node at the centerline of the hull shell elements two inches below. All such gap element node pairs have maximum shear in the x or y directions that are approximately 0.15 % of the z displacement values as can be seen in all of the FEA output *.pch (PUNCH files). So most of the transverse deflections are negligible. Therefore, rather than

³Mass “dampers” were used, for example, in some 1987 GM front wheel drive sedan exhaust systems to subdue acoustical – structural resonance modes.

⁴Convertible Corvettes had very high rockers (and / or high center consoles) to stiffen the fundamental mode by creating deep beam webs on both sides of the vehicles, thereby increasing a very low f_o . The general concept of moving modes by detailed design such as changes in the body mounts uses calculation of the modal ‘mobilities’ of the model.

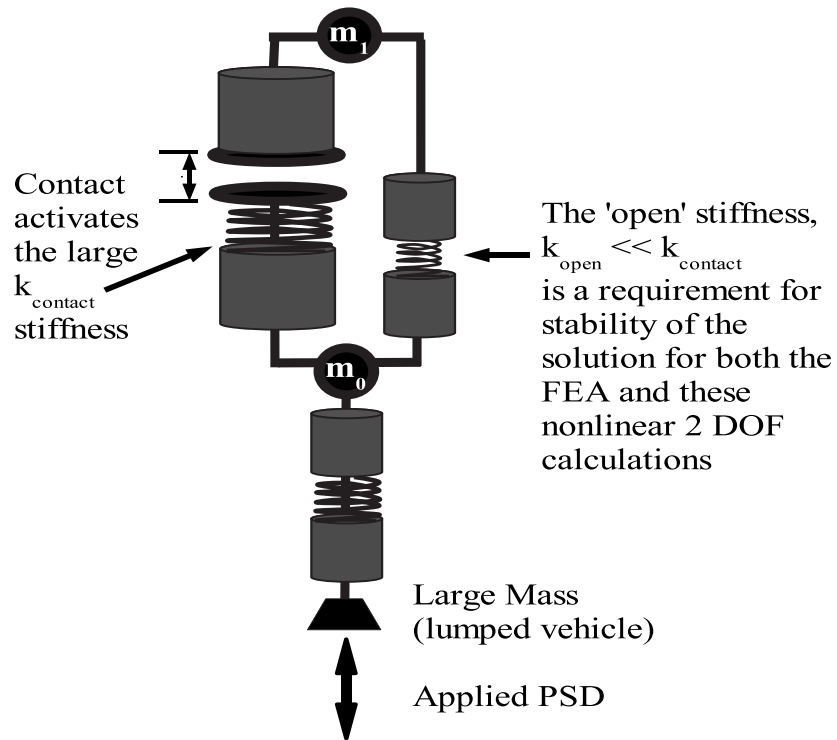


Figure 44: Two DOF over – simplified physical model for contact: The closed stiffness is the combination $k_{\text{closed}} = k_{\text{open}} + k_{\text{contact}}$.

use MSC/NASTRAN slidelines, HKS/ABAQUS plate centroid technologies, or other techniques, simple gaps without friction are sufficient to model the contact. The number of DOF's is approximately $5 \times 2 \times 286 \approx 3,000$ which is the same number of modes a modal FEA could generate if automatic truncation to the lower frequency modes did not occur. Compared to the usual vehicle system models that number in the millions of DOF's, this is a small model.

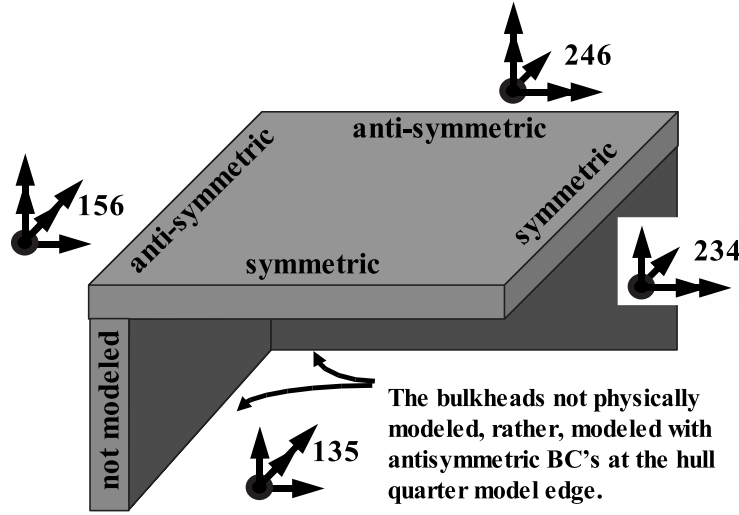


Figure 45: The FE model represents a quarter of a skin panel (upper surface) where each quarter has its own $1m \times \frac{1}{2}m$ armor plate. There are bulkheads on two adjoining edges of the model, and the other two edges are 'free' except that their nearly guided edges model the other side of the plane of mirror symmetry. Arrows represent allowed DOF's

The mirror symmetric BC's described in Figure 46 on page 183 model an extension of the plate through the plane of symmetry in a mirror symmetric pattern. The 'far' end of the beam of width 'a' and length 'b' is where the mirror symmetry condition would be applied, to all nodes on that $x = b/2$ location (parallel to the $y - z$ plane). Single arrows represent translation. Double arrows represent rotation. The antisymmetric conditions are more difficult to explain and often confounding to try to understand.

In an antisymmetric BC the rotation about the symmetry plane normal is constrained (double arrows parallel to x), as are translations in the plane of anti - sym-

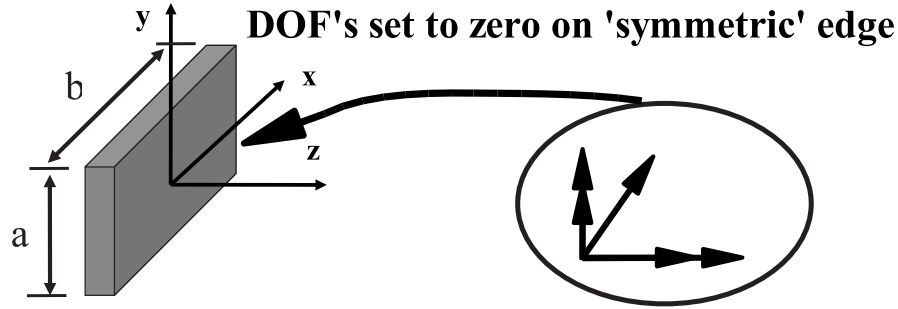


Figure 46: The set of arrows on the right that looks like a coordinate system describe constrained DOF Boundary Conditions for a mirror symmetry on the $x = b/2$ edge of this beam of length ‘ b ’ and width ‘ a .’ This condition models a system on both sides of the ‘mirror plane’ because the deflections, stresses and other result fields are the same on the ‘other side’ in a mirror symmetric pattern. So a symmetric mirror BC models an “extended” plate through the plane of symmetry. DOF’s set to zero are x translation and rotation about y and z .

metry (single arrows parallel to y and z). These BC’s are meant to model loading and constraints that are reflected through the mirror (seen on the ‘far’ side) opposite to those on the ‘near’ side. *But a side benefit of these BC’s are that they model the equivalent of an edge that terminates on a bulkhead.* Most bulkheads are shear panels that attach to the skin panel through a stiffener necessary for shear flow connectivity. Bulkheads and their frames resist the out of plane translation of the skin panel at levels orders of magnitude greater in stiffness than their stiffness against skin panel slippage normal to the bulkhead. That ‘slippage’ direction is precisely the ‘through the anti – symmetry plane’ DOF that is released for antisymmetric BC’s. Additionally, antisymmetric BC’s allow moments that rotate through the anti – symmetry plane, which is another two DOF’s that the bulkheads do not have much stiffness to react against. Therefore, antisymmetric BC’s are used in this FE model to approximately represent the bulkheads described in the physical model sketch in Figure 45.

The large mass connection in Figure 47 could be a mount (frame, storage, engine, turret reaction, ordinance recoil) or a road wheel torsion rod connection. This spring – mass frequency (8.9 Hz) is below all frequencies of interest. The mass is off of the long

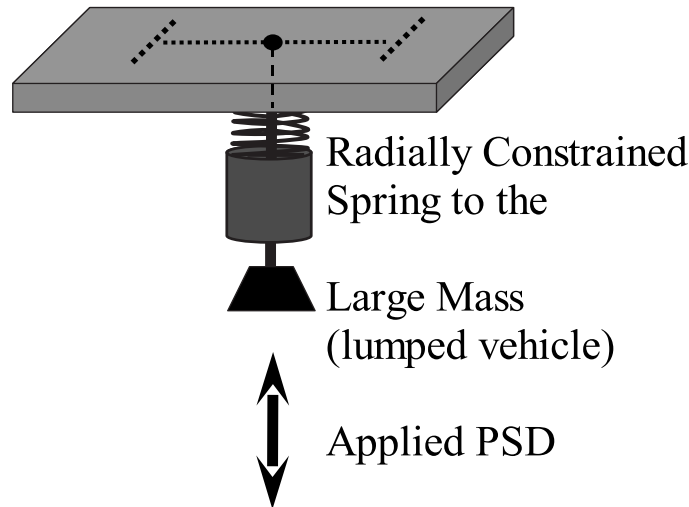


Figure 47: The large mass whose loading represents the load path from the rest of the vehicle.

axis centroid to avoid accidental symmetries (see buckling perfection on page 194 and ‘test axis’ discussion on page 179), causing a small moment on the panel. The frame locations are inboard of the HRA attachment bolt locations and their ‘doubler’ type stiffeners. The location of the system mass / load to hull panel ‘frame’ stiffener being inboard of the armor bolt attachment plate doublers could cause discernable shear for large loads. While it is an Aerospace Engineering travesty to terminate a stiffener in the panel before hitting an edge frame or stiffener, these short frames model the non – aircraft nature of the target vehicles and the initiative of their occupants to attach structures to the interior that might transfer loads to the hull. This frame is allowed to breath in the membrane directions (x and y) and, in a mathematical sense, to provide no extensional stiffness to the hull shell elements. Therefore, the ‘large mass’ system models a generic method to load the plates directly that could include acoustic loads from an engine, terrain loads, or ordinance.

The rectangular structure shown in Figure 48 creates mode shapes that are straightforward to analyze, their Chladni line locations⁵ follow Cartesian alignment.

⁵Chladni lines of nodes are the zero displacement locations for a particular mode. “Doctor Young and the brothers Weber appear to have had the idea of superposition as capable of giving rise to

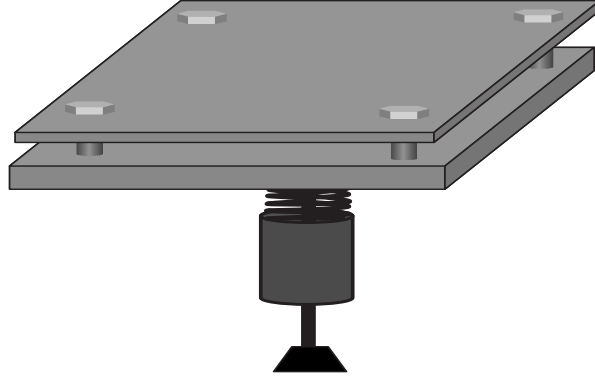


Figure 48: For this ‘generic contact model’ the Homogeneous Rolled Armor attaches to the hull with four bolts assumed to have a shank diameter of one inch. The FE model assumes armor has no initial gap opening but is shown gapped here for clarity.

One half wavelength across each dimension, a single antinode overall, is the mode shape of the fundamental mode. The fundamental frequency for the normal modes analysis (SOL 103) of the HRA plate alone, 331.7 Hz, was within one percent of the 334 Hz MathCad results (via Roark’s formulas, reference [92], page 717, Art. 15.4, Table 36, #16). As a check on the system model, this fundamental mode results in a frequency of 287.15 Hz⁶ compares favorably with the MathCad vibration frequency analysis result of 334.3 Hz, at 16% lower than the Simply Supported calculation based on empirical formulas and tables.⁷

A lower 80 Hz frequency mode seen in the FEA in Figures 26 37 on pages 121 139 (more easily seen in the former random response) matches the calculation result in Equation 59 on page 205 added inertia from the ‘large mass’ of 500 kg acting through 405 kg mass of the hull that is attached to the HRA outer plate through the four bolts that are inboard of the simply supported (SS) Edge Boundary Conditions.

new varieties of vibration, but it is to Sir Charles Wheatstone [89] that we owe the first systematic application of it to the explanation of Chladni’s figures.” [80, Vol 1, p 377]

⁶This MSC/NASTRAN result validates the transient nonlinear model, for which no ‘hand calculation’ is possible. A slightly stiffer model produced a fundamental frequency of 291.15 Hz giving an error of 15%.

⁷Material properties of the HRA plate were from a prior page at <http://staff.science.nus.edu.sg/scilooe>. For bolts, MIL-HDBK-5 A286, and hardware, AISI 4335V Material Spec. AMS 6435, MIL-HDBK-5 / AR-MMPDS01 table 2.3.1.0(f2) p 2-23. For the calculation formulas, reference [92], page 717, Art. 15.4, Table 36, #16, Rectangular Flat Plate, definition of D on page 714 (all edges simply supported).

The frequency of the full 4 – fold hull – only system (not shown), that this FE model is only a quarter of, is also just below 80 Hz. The HRA plate acting as a component should show up as the lowest component frequency, as was the case. The hull, modelled with Roark’s formulas has a fundamental frequency of about 1 kHz. These SS BC’s correlate the model with ‘hand’ calculations from Roark’s formulas for stiffness [92, 469] applied to vibration frequency solutions. Since there were Roark formulas that apply for this SS case and a simple modification of the FE model emulates them, the fundamental frequency for the SS HRA was a good validation case.

The gravity load applied at the inception does not change the vibration modes but does show up in the effects of the downward acceleration 3.6 millisecond impulse, 1.0 ms FWHH.⁸ The applied load in the direct transient impact load models hitting a curb and thus the initial effect is a sharp depression of the system in a negative z direction followed by equilibrium back above the un – deformed plate centerline.⁹

The FEA deformation results represent only that region of the full panel that the FE model represents, the solid curves that pass through the ellipse in Figure 51. These solid curves are the fundamental deformation mode displacements that the FEA provides using this FE model, the first normal mode displayed in Figure 21. The dashed lines are the implied deformation shape for that mode, the shapes NASTRAN does not give but are understood from the mirror symmetry of the two inboard edges. This deflection field models symmetric segments of the deformation of the entire panel with four separately attached HRA plates, in the shape of a cross in plan view (Figure 50). The symmetric BC’s do exclude higher frequency modes that are not symmetric across the boundary, assumed to have small modal participation in the model. While the deformation is expected to be oppositely oriented on the other side of the antisymmetric planes of symmetry, those deformations are not considered

⁸This full width at half height (FWHH) relates to a standard deviation of 0.52 ms (page 190).

⁹This spring – through effect appears in FEA deflection results in the motion picture MPEG file almostSynch01.wmv, created from 90 deformed shape JPEG images produced using MSC/PATRAN.

to be important to the considerations for remote sensing of the outer skin of target vehicles because adjoining panels are usually at a large angle to the original. Since those panels are not usually broadside to the detector and thus outside the FOV, this FE model is appropriate for modelling the vibration modulated optical radiant flux return of a “generic” vehicle.

B.2.3 Fixity. The BC concept of fixity affects the linearity of the signal processing transfer function for the full vehicle signal processing model. Consider the fixity of bolted, spot welded, and riveted joints in a commercial or military vehicle. For structural stress analysis of bolted or riveted structures “. . . , it is customary to disregard the frictional resistance of the joint. The capacity of a joint is thought of in terms of its ultimate capacity after frictional resistance between the plates is “broken.” ” [62, 502] For vibrating vehicle surface skin it is precisely this unknowable frictional connection (BC’s for local stress analysis) that causes fixity to be fractional rather than fixed / clamped, $c = 0$, or free, $c = 1$. SS indicates the location is fixed but rotations are free. This unknowable frictional force is a part of the structural damping (estimated at $\zeta = 0.002$) often thought of as internal material damping.¹⁰

B.2.4 FE Model Element Summary. Subsection B.2.2 describes the use of CQUAD4 and CGAP NASTRAN elements. The plan view in Figure 52, the FE model of the HRA – hull system, shows the frames as linear one dimensional elements between the shell elements. This figure also shows the RBAR elements used in the system of application and distribution of the loads. The RBAR definitions allow extension (breathing) where practical. The CONM large mass only acts vertically against the solitary CELAS2 element that connects it to the inner frame in Figure 47.

¹⁰Structural damping is an imaginary stiffness (approximately π out of phase with any harmonic displacement) necessary for the proper function of semi – monocoque fuselage and wing box beam structures. “If all the connections in an aircraft were welded rather than riveted, aircraft would vibrate to pieces.” [6].

In order to get the Fourier transform using the Matlab `fft` command (a DFT) of these time histories, the time step increment must be uniform. The time histories are of different lengths due to the adaptive nature of the default ‘METHOD’ for the ‘TSTEPNL’ is ‘ADAPT’ [66, 1030 ff] which tells the NASTRAN program to calculate the optimum time increment. Since a refined model ran out of default system memory this disk space, caution is necessary even for this small model. Note 10 of the MSC/NASTRAN Nonlinear Handbook [66, 1033] indicates that the bi – section process¹¹ “. . . is activated when divergence occurs. . .” MSC/NASTRAN SOL 129 is the direct transient solution sequence (group of subroutines) that performs Newmark – Beta integration.¹² “Since the automatic time step adjustment is based on the mode of response and not the loading pattern, . . .” NASTRAN indirectly determines when the current response requires time step refinement using the effects of a short duration impulse, sharply changing load, or high frequency content PSD, and adjusts the time increment accordingly. The nonlinear handbook suggesting to use an ADJUST feature to have the time steps ready to refine in an area of load application. However, use of ADAPT worked without ADJUST even though the 3.6 ms (1.0 ms FWHH) impulse duration is 11 % of the 9.3 ms period for the fundamental 108 Hz mode. Apparently “. . . loading much shorter than the . . .” fundamental mode applies to impacts shorter than 1/3 the fundamental period.

Finite element aspect ratios vary uniformly from 0.8106 at the origin to 91.875 (ordinarily considered thin) at the opposing corner. Along the antisymmetric x – axis “bottom” edge of the model this aspect ratio increases from 0.8106 to 3.2379. Along the symmetric y – axis “left” side of the model this aspect ratio increases from 0.8106 to the maximum 91.875 but with little stress gradient across the short width. This is a simple model with the usual example model qualities of lack of curvature, nice symmetry, rectangular mesh, and it has a flat orientation parallel to

¹¹Bi – section reduces the time increment below that defined on the TSTEPNL ‘card,’ but only for that nonlinear solution increment. The next time step starts with the default.

¹²Original theory: [52], NASTRAN theory: [46] page 8.3-1, implementation in NASTRAN: [46] 9.1-4 (This is the page of the following quote.)

the basic coordinate system $x - y$ plane thus avoiding the great annual K6ROT versus AUTOSPC SNORM debate. This FE model is well within all standard FE modelling guidelines (including NAFEMS).

Therefore, the only static structural element complexity in the FE model is the RBAR system that distributes load to a ‘frame’ section of two strips that model attachments interior to the hull that transmit load to the hull. These could represent equipment mounts, drivetrain mounts, or internal impact points in the structure such as where empty shells hit the hull upon expulsion. Not meant to model an actual structure, this load application ‘frame’ set is a way to get PSD energy into the hull for excitation of the HRA.

Rather than use an actual PSD, for reasons explained in Section 3.3, the structure experiences random excitation (trade study A) and what in reality would be akin to a pendulum impact (trade study B). In crashworthiness testing, an inexpensive alternative to full vehicle impacts is to drop a heavy pendulum into the side of the vehicle to test the structural integrity against side impact. This is just an outboard impulse on the ‘frame’ member’s interior to the panel, a force in time increasing and decreasing to zero in the approximate shape of a Gaussian function of time.

The impact / impulse load drives the need choose a transient NASTRAN ‘solution sequence’. This model’s only nonlinearity is geometric nonlinear. Assumptions included in the NASTRAN model are that strain is small and that the structural properties other than the gap elements between the plate and the hull are linear.

The (rather small) impulse load is Gaussian in time with the maximum load, 0.0828 N, occurring at 2 milliseconds. Trapezoidal integration gives an impulse, $J = 8.6683 \times 10^{-5} * 5000.0 = 0.4334$ Newton seconds where 8.6683×10^{-5} is the integration under the Gaussian temporal profile of the TABLED1 NASTRAN time profile entry. The DAREA ‘card’ contains a load factor of 5 kilo Newtons which

NASTRAN multiplies against this dynamic load.¹³ This resulting small 0.097 pound second load is a useful value to produce small deflections that require little adjustment for the optical propagation model where for numerical convenience we keep the deflection below the optical wavelength (as described in Chapter 2.3, page 42).

This pulse FWHH from Figure 53 on page 199 was approximately 11 % of the 9.3 period related to the first fundamental mode¹⁴ (108 Hz). The full width at half height is 1.0 ms (FWHH). Digital signal processing (DSP) guidelines would indicate a frequency response function (FRF) to 3/2 of the first sinc zero, or 1,500 Hz. But the Gaussian shape tightens up the PSD so that most of the energy is within 1.0 kHz. A much more sharp impulse is desired, yet not usually physically feasible with typical test lab equipment. Any sharper and local permanent set will absorb much of the energy (material nonlinearities) arise. So the impulse size used for the FEA is appropriate.

For this work the Matlab scripts only read in the NASTRAN out – of – plane displacements ($w = \Delta z/2$) results. A view of the ASCII punch output files shows the in – plane shear displacements are at least three orders of magnitude lower than z deflections, validating this zero shear assumption.

B.2.5 Contact Gap Element Validation. Using the 11×26 node FE model mesh, baseline gap element contact (2 kN/mm) at each of these 286 nodes provides an overall stiffness of approximately 5.7 MegaN/mm per square meter. The axial stiffness is $K = EA/L$ with $L = (1'' + 3'')/2 = 50.8$ mm, $A = 5 \times 10^5 mm^2$ (element edges range from 18.4 to 73.5 mm, 0.72 to 2.9 inches), and $E_{HRA} = 65,188$ MPa. We seek a low stiffness that is softer than the surface treatment (paint or zinc coating, and dirt) and a contact stiffness k_{closed} much higher than the surface treatment, or

¹³The combination of DAREA and TABLED1 ‘cards’ provides the maximum load of 0.0828 N. Integrated in time the ‘action’ is nearly one Newton millisecond due to the Gaussian formulation, except for truncation, which changes the step integrated value to 0.62 N – ms.

¹⁴The SOL 103 diagnostic runs (the normal mode analyses) used the Lanczos eigenvalue decomposition method in MSC/NASTRAN specified to select the first (lowest) 10 ‘normal modes.’ Figures 21 through 23 display some of the eigenvectors from the SOL 103 results.

perhaps higher than the plate material stiffness. A rough estimate gives a high contact gap stiffness of 5,522 MPa and a low open stiffness of 0.47 MPa (using $k_{open} = 50 \text{ N} / \text{mm}$).

The open stiffness is high enough that it models a vacuum of 7 inches of mercury ($P_{atm} = 0.101325 \text{ MPa}$) whereas the closed stiffness models a set of plates with a hard rubber interface. Considering different surface treatments and the non – uniform nature of soil that can enter the gap, such stiffnesses are reasonable. The intent of this k_{open} is merely to stabilize the numerical solution, as is the common practice in industry.

Trade study A investigated stiffness variations, comparing the spectra at two centrally located positions for six different contact stiffnesses: 1, 2, 5, 8, 10, and 15 kN/mm. Figure 26 shows the response for all the different gap stiffnesses. This plot compares symmetrical and non – symmetrical mode response providing a large range for model ID (symmetrical modes) and surface wear or modifications (non - symmetrical modes).

The effect of response for lower open stiffness (lift – off) is barely apparent in the ‘movie’ made for this project from the MSC/PATRAN deformed shape plots and the Matlab simulation images shown side by side in the almostSynch01.wmv MPEG as described in subsection 4.4.2 on page 94. The open stiffness effect on the dynamics was negligible. An open stiffnesses set to zero is the proper model for a pure contact but would tend to cause instability in the solution. So the “open” stiffness, k_{open} , is a stiffness known to stabilize the solution. A variation of 40:1 is a good measure of the nature of the nonlinear response as the two DOF closed form model described in Section 4.3 on page 84. The correlation of resonance peaks in the Fourier transforms of the transient response to the normal mode frequencies validates the idea of using response to modes for target ID, as is customary in the modal analysis industry. These ($k_{open} \approx 50 \frac{\text{N}}{\text{mm}}$, $k_{contact} \approx 2 \frac{\text{kN}}{\text{mm}}$) stiffnesses for contact are common in the automotive component industry. Lower open stiffnesses would

improve model accuracy at the expense of divergence of the solution. Considering the bi – sections seen in the ‘short duration’ model, these parameters were not far from such a convergence issue, so the $k_{open} \approx 50 \frac{N}{mm}$ choice was a proper balance.

B.2.6 Contact nonlinear: static (per time step) solution. In static nonlinear FEA one of the considerations driving load increment choice and the choice of Newton’s method (over the more computationally efficient Newton – Raphson iteration method), is to ensure that every DOF in this 2900 DOF model follows its load deflection curve. For the moment we ignore time increment integration error, which has been made small. Transient solutions sequences perform a static nonlinear solution for each time step. Selection of “kiter” = 1 in the nlparm “card,” activates the old Newton’s method, which enforces decomposition of the system matrices at every (static) iteration within a particular time step.¹⁵

B.2.7 Transient Model Validation. Separate hull – only FE models to compare to hand calculations in Appendix C used the same FE models with SS BC’s. These SS spectral results inferred from the time domain data also plotted in Figure 54 appear to be too coarse (not enough time samples) however there is a clear local maximum at 0.004 and 0.008 seconds. This is just a test case to further validate the model with simply supported BC’s that have a theoretical solution found using Roark’s formulas [92, 717] provided in Appendix C. A sub – fundamental ‘mode’ is the major the response centered at 0.008 s with a period of approximately 0.012 sec

¹⁵The popular and sometimes default Newton – Raphson uses the initially calculated inverse system matrix to calculate the first n estimated iterations where the new deflection is input to calculate the next iterations’ deflection estimate. At this point there is no ‘integration’ error added to the system. For complicated multi minimum stress strain curves, the kind that describe creation of Lüder’s bands [25] in nonlinear permanent material deformation (set), keeping the same “slope” (the 2900×2900 size $[K]^{-1}$ matrix is the “stiffness slope” the DECOMP subroutine generates) to solve for the new deflection in subsequent iterations will cause us to miss correct solutions. The extreme example of a Lüder’s band stress strain curve is extremely multi – valued (the nearly harmonic bands) on the stress axis which causes a constant K solution to miss the mark as we skip around the actual solution where the load equals the stiffness times the deflection, $P_i = \vec{k}_i^t \vec{u} \Leftrightarrow u_i = [\vec{k}_i^t]^{-1} \vec{P}$. So we avoid these problems by choosing the old Newton’s method over the time efficient Newton – Raphson methods.

duration (83 Hz). This mode appears to corresponds the the large mass load application and the full 4 – fold symmetry 1×2 m assembly of four HRA elements. The high frequency mode that appears to be excited, with maximum response at 0.004 sec for period of duration 0.003 sec (333 Hz), is a short term higher frequency mode. This is compares to the 334 Hz fundamental mode for Simply Supported Normal Modes analysis (SOL 103) and the hand calculation of one HRA segment in Equation 62 on page 205.

The 0.1 second duration run with the time increment specification of 0.2 ms (a suggested Δt to the adaptive process) had a more complicated time step increment history (Figure 55) than the refined time step longer duration run (Figure 56) for trade study B.¹⁶ Trade study B's $k_{contact} = 2$ kN/mm time step history appears identical to that for another refined time extended duration gap stiffness FEA, $k_{contact} = 1$ kN/mm. The random load sets for trade study A changed so frequently that NASTRAN remained in the small time increment region for those 30 runs for each of the 6 gap element stiffnesses.

The 2 kN/mm stiffness baseline choice models a more normal contact stiffness. The range in stiffness and mesh density bias model paint or zinc treatment variation along the surface.¹⁷ But this thesis outputs displacement only for the upper surface (that part that can be remotely sensed) so the dynamics of the inter – plate contact are only indirectly important and thus not a focus of the thesis. The intent is to introduce

¹⁶The manual processes of matching times and comparison to other ‘configurations’ such as, in this case, different quantities of gap contact stiffness for the same quantity of noise simulation (photon limited) was time consuming. While the issue of system administrative control over the NASTRAN computer determines alternatives to deal with the size of the output files, it would be advantageous to work the data processing issue from the FEA results side and live with massive NASTRAN output (and the long read times in Matlab these files would generate). However, this work was already near the NASTRAN default system limit, so disk space caution is appropriate.

¹⁷The area per gap ranges from from 0.042 to 0.824 cc which produced negligible lack of symmetry in the deformed shapes. The bias in mesh density creates a gap stiffness bias that models a bias on the inter – plate contact surface as is commonly found in machinery where a film on one side cants the un – deformed contact crevice. Higher contact stiffnesses model surfaces of increasing cleanliness and then increasing polish.

mild non – symmetry to avoid problems encountered with formerly accepted methods (purported correlation to test)¹⁸ and to ensure the model reflects reality.

B.3 Frequency Response: Vibrating Plate Contact Response

The previous section described ‘Normal Mode’ eigenvectors (mode shapes) from NASTRAN SOL 103 runs, transient loading that “rings” these modes, and many FEA parameters. This work uses several random and impulse loaded versions of the FE models.

B.3.1 Fourier Transforms of Direct Transient Time Histories. The plate interior spectra in Figure 37 on page 139 show four resonance peaks near the frequencies for the first five ‘hard’ and ‘soft contact’ eigenvectors using the full 0.2 second simulation duration. The thick lines represent the response of the frame members attached to the hull which only indirectly have a load path through the four bolts outboard of these hull frame stiffeners. They transfer a load in from a large mass that receives the impact loading to represent transmission of vibration energy from a mount or road – wheel torsion bar base in the hull. The effect of the large mass after impact subdues the third modal shape’s frequency, which is ‘antisymmetric’ along the short edge of the plate, open to both sides being a half spatial wavelength long but with the node in the center. The other dimension is centered as expected. Contact has driven this mode’s frequency higher (from 223 Hz to 330 Hz) for ‘soft’ to ‘hard’ contact, and the frames (the connections to the system mass) apparently resist this mode as well.

Detailed plots (not displayed) of the long time Fourier transform of the time history frequency response summarized in Figure 37 on page 139 are of sufficient spectral resolution to allow us to see relationships between spectra at different nodes

¹⁸For example, cylinder buckling is under – estimated by perfectly cylindrical flawless FE models – the kind typically produced quickly from CAD models in order to approve a drawing in record time. To be anywhere near reality the modeler must remember to introduce some random surface variation in order to bring the buckling load down to reality. Also see page 179 for a testing example by Smallwood.

(locations). This excludes the resonance at the 108 Hz fundamental resonances, where some plate interior nodal spectra have nearly null response (seen in the wide spread of some spectral lines at 108 Hz). In other regions the nodes at the frames have an inflection (vanishing second derivative with respect to frequency) and vice versa at a frame zero for node 3051 where the plate and other frame have a linear segment of frequency response. These effects (not shown) are at 160 Hz (in the detail) and 230 Hz. Based on the knowledge of gap stiffness response we can say that the former appears to be a nonlinear contact stiffened form of the eigenvector for normal mode 2. The latter is slightly higher than the mode 4 open contact frequency seen in Table 7 on page 102.

B.3.2 Trade Study B, ensemble ΔA_{shear} . This consideration appears down the thread of logic in MIL-HDBK-5H section “8.1.2.1 Protruding – Head Solid Rivet Joints” where “For convenience, ‘unit’ sheet bearing strengths for rivets, based on a bearing stress of 100 ksi and nominal hole diameters, are given in Table 8.1.2.1(a).” But Table 8.1.2.1(b), based on (a), shows the ‘strength correction factors’ for these values to range somewhat uniformly from 91% to 100% for increasing sheet thickness for single shear rivets up to 3/8”. The double shear rivets suffer a correction factor down to 52% for the thin sheet allowed for the respective rivets (0.063” for 3/8” rivets, page 8-13). So variations of strength in excess of 10% are common for compound lap joints.

Using Table 8.1.2.1(c) “Static Joint Strength of Protruding Head A – 286 Solid Rivets on A – 286 Alloy Sheet . . . ” as a guideline, the effective area to give the joint allowable strength of a 3/16” fastener in 0.16” sheet is only 25 % of the original area. So a variation of 15% is conservative. S_{ut} , S_{eff} (strength) are in psi.¹⁹ Areas (A) are in inches squared.

¹⁹<http://www.grantadesign.com/MILpdfs/MIL5-H/MIL5H-8-1-2.pdf> ‘ksi’ = kilo pounds/ in^2

$$\begin{aligned}
S_{ut} &= 90ksi, & S_{eff} &= \frac{2,543}{A_1} = 22,189 \text{ psi} \\
A_{eff} &= A_1 \frac{2,543}{A_1} \frac{1}{90,000psi} = 0.0283 \text{ in}^2 \\
(A_{ratio}^{effective})_{joint} &= \frac{A_{eff}}{A_1} = 0.2465 \quad (dimensionless)
\end{aligned} \tag{52}$$

The non – armor (hull – only) case is not the baseline of trade study variations. Comparison between the ‘hull – only’ response in Figure 17 (upper trace) on page 109 show the utility of the nonlinear vibration effect of contact vibration removal of ‘unsymmetrical’ modes that are prone to cause spectral reduction. The higher frequency oscillations in the upper (higher magnitude) deflection response for the lighter ‘hull – only’ case are clearly subdued in all the 27 bolt configurations plotted together on the same plot (which have lower defection due to the extra mass and the nonlinear contact).²⁰ The total strain energy of the HRA – hull assembly is equivalent to the hull – only case because, while the hull – armor models have only $\frac{0.4Mg}{10.3Mg} = 0.96\% \approx 1\%$ more mass than the hull – only model (due to the large mass at load application), they have $4''/3'' = 33\%$ more plate mass at the vibration location. The dynamic effect of the ‘large’ 10 Mg system mass to the modes of interest is negligible. Only the effect of the top surface is in the plots, the hull for the hull – only case and only the armor for the 27 HRA – hull bolt configuration variation FE models.

²⁰This is another example the way that nonlinear components remove high frequency strain energy in favor of lower frequency modes.

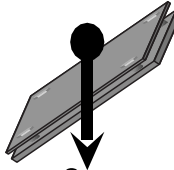
$$\begin{aligned} & \text{Gravity at } 45^\circ \\ & \Sigma_i (m_i g) = \\ & \Sigma_i(m_i) * 9.8 \text{ m/s}^2 \end{aligned}$$


Figure 49: The gravity load, applied at 45 degrees to the z axis, models the HRA – hull interface as a side panel that is oriented at a 45 degree angle to nominal ground surface.

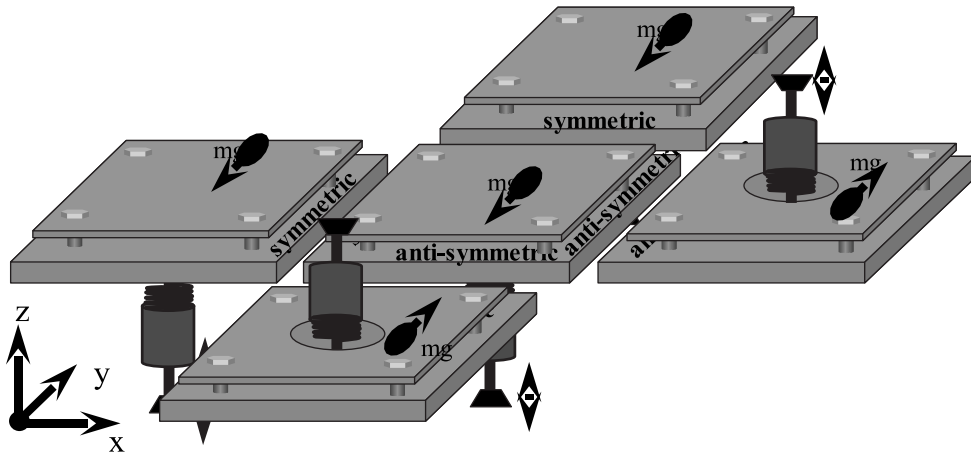


Figure 50: Symmetric BC's on two adjoining edges model a quarter of a panel four times the size of the $1m \times \frac{1}{2}m$ FE model. Antisymmetric loads outside the kernel model external hardware (see turret discussion page 177 ff).

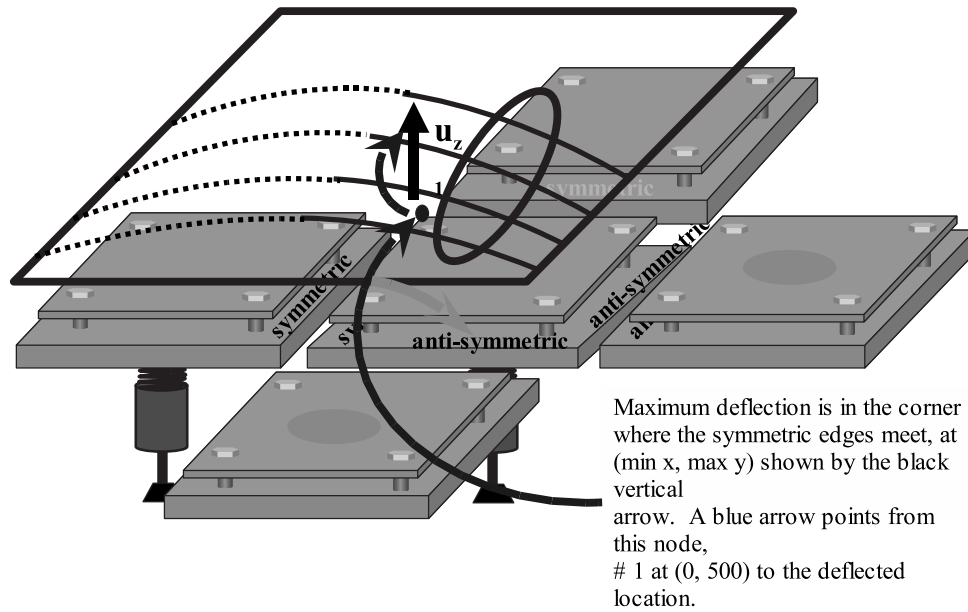


Figure 51: Solid curves represent the Quarter Model's portion of the full deformation shape.

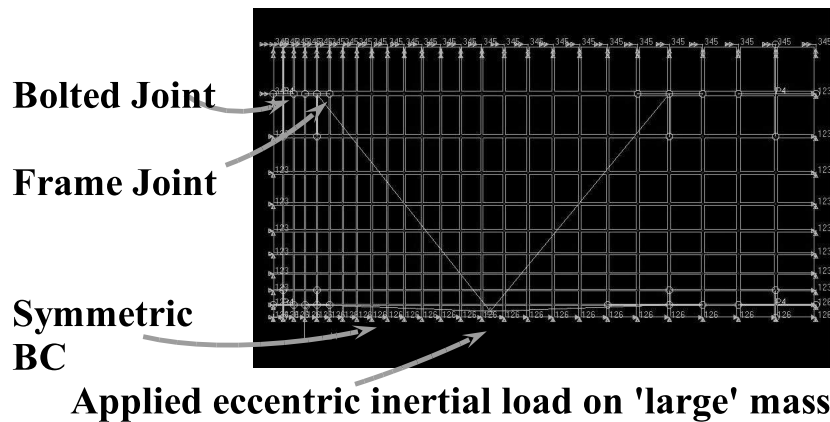


Figure 52: Plan view of the FE model, constraints, and loads: The shell elements are slightly shrunk for ease of viewing. The line between the shell element edge lines indicates a bar or in this case rigid rod.

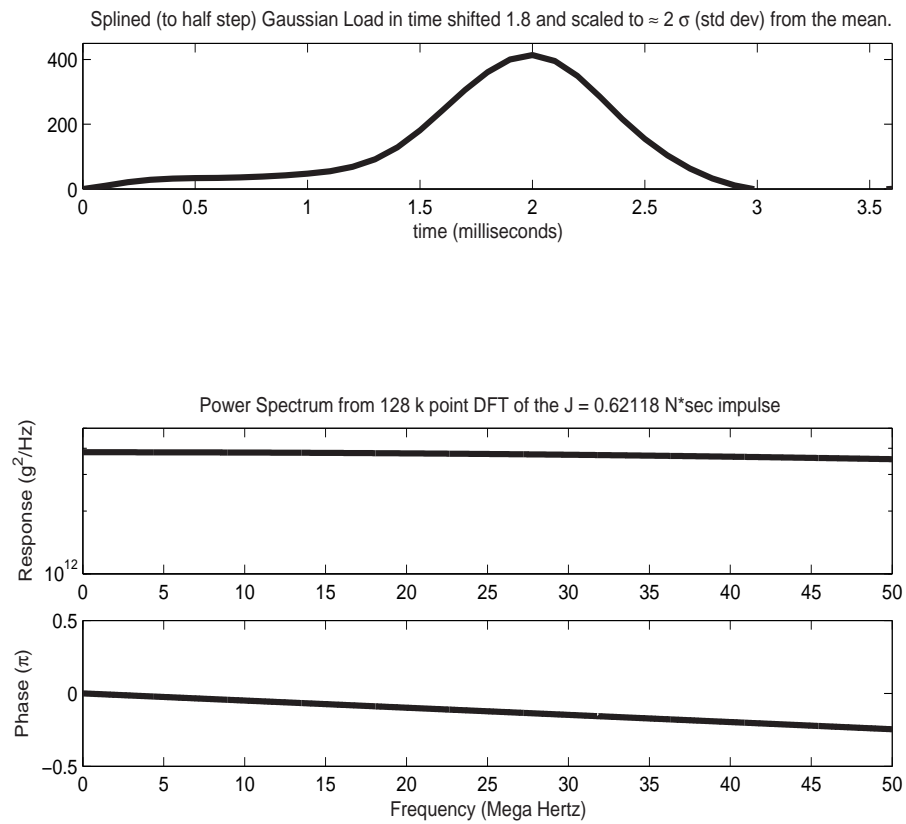


Figure 53: The sharp impulse does ‘ring all the modes’ except at very high frequencies.

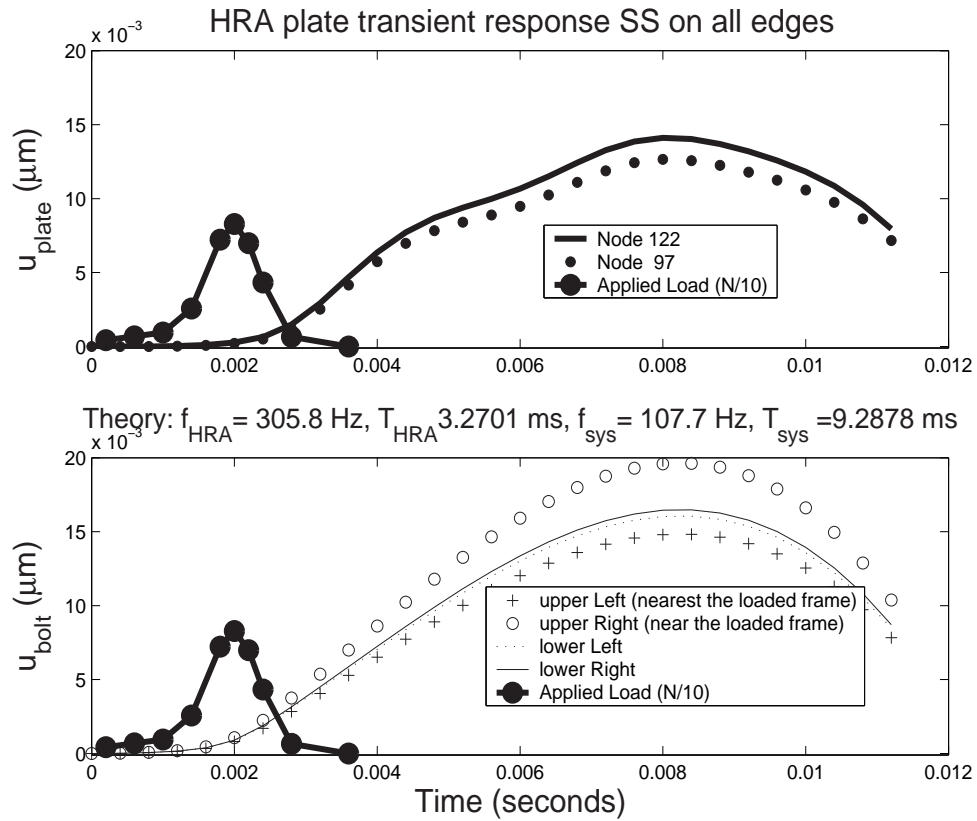


Figure 54: Direct Transient Structural FEA with SS BC's: The plots for time integration with Simply Supported BC's have simpler response to the impulse load than the impulse response. It equilibrates more efficiently and has the same Simply Supported BC case modal frequencies that the normal modes (SOL 103) analysis with SS BC's provided.

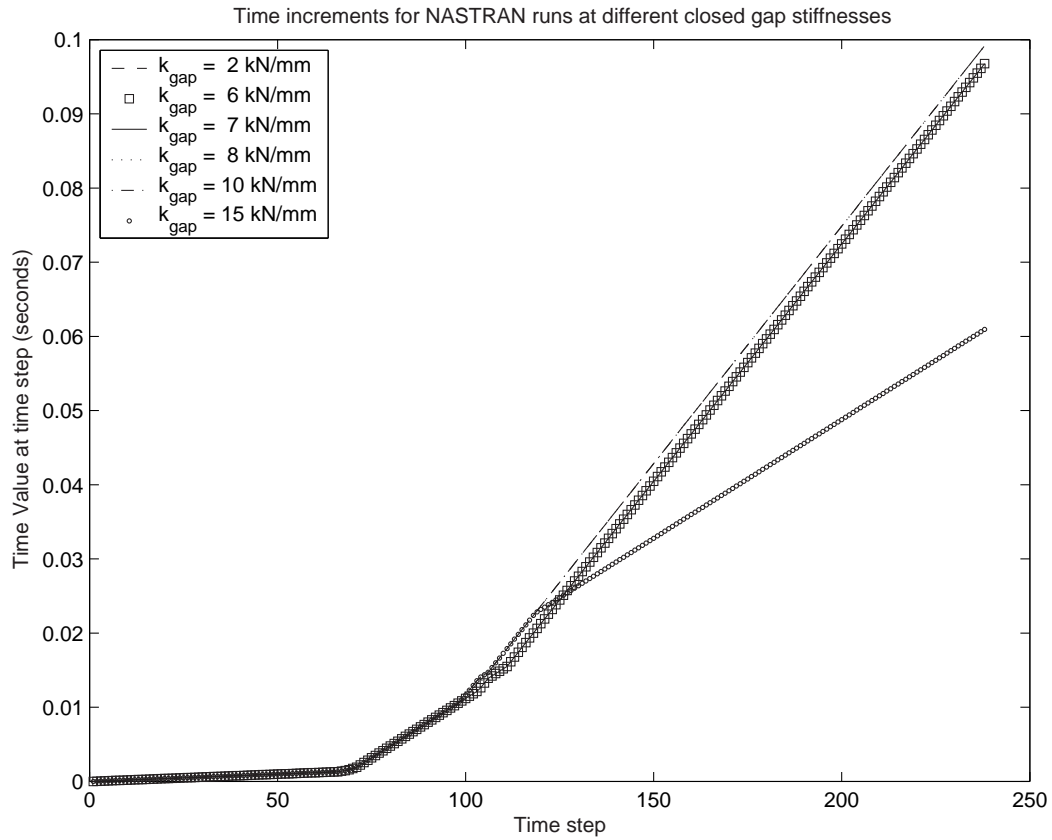


Figure 55: This “shorter duration” run specified the TSPTENL TINC time increment specification, which NASTRAN assumes as a mere suggestion, as 0.2 milliseconds. The high gap stiffness solution required finer time steps for this short duration analysis.

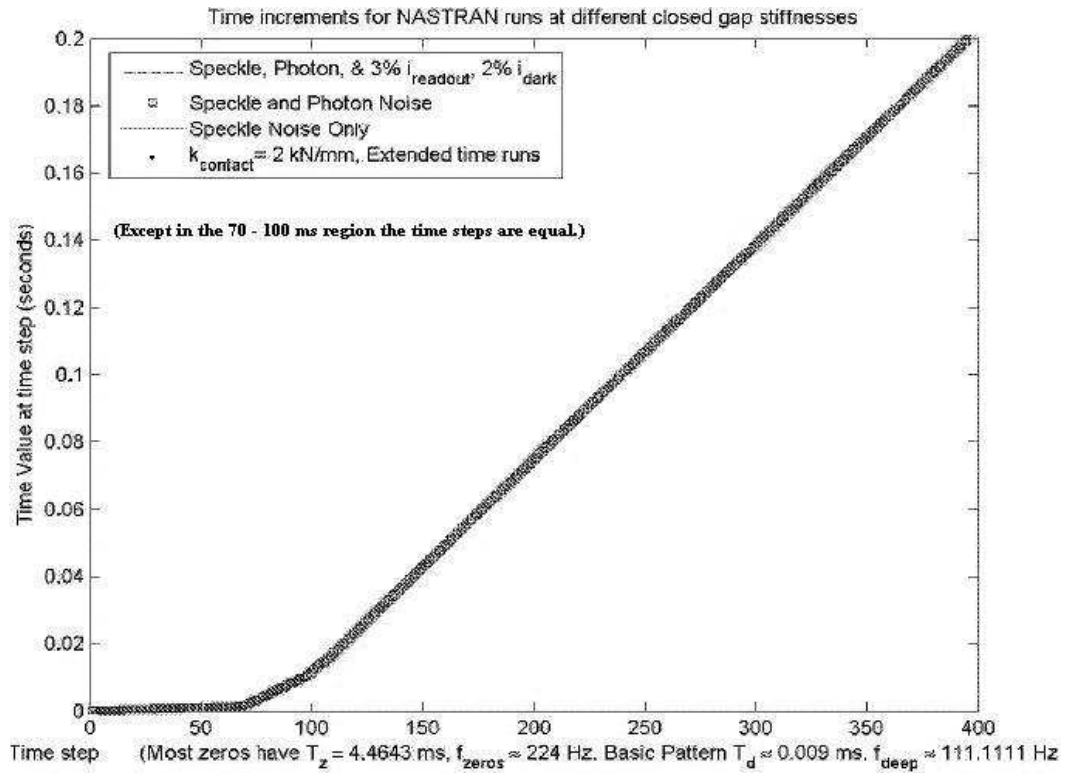


Figure 56: This “longer duration” run specified the TSPTENL TINC time increment specification, which NASTRAN assumes as a mere suggestion, as 10 microseconds. All cases have nearly the same time step sequence.

Appendix C. MathCad Vibration Frequency and Deflection Estimates

This copy of the graphical text and equation output from a MathCad file provides the estimated frequencies for armor and hull of various thicknesses. Since MathCad allows for placement of text and equations and their results anywhere on the page, the Aerospace engineering field developed ‘stress report’ formats which the MathCad file conforms to. The LaTeX copy provided in this Chapter attempts to follow that format.

C.1 Closed form plate frequency calculations

MathCad unit translation equations such as for Mega Pascals (MPa) and Mega grams (Mg) are omitted.

C.1.1 Input Parameters. Overall dimensions, physical, and material properties:

$$\begin{aligned}
 a_1 &= \frac{1}{2}m & \nu &= 0.33 \\
 b_1 &= 1m & B_a &= 1.7 \times 10^5 MPa & t &= 4'' \Rightarrow \text{welded armor} \\
 t_a &= 4 \cdot 25.4mm & S_{y_a} &= 1320MPa & \rho_a &= 7.85 \times 10^{-9} \frac{Mg}{mm^3} \\
 E_a &= B_a [3(1 - 2\nu)] & E_a &= 2.515 \times 10^4 ksi & E_a &= 1.734 \times 10^5 MPa \\
 G_a &= \frac{E_a}{2(1+\nu)} & G_a &= 6.519 \times 10^4 MPa & E_a &= 1.734 \times 10^5 \frac{Newton}{mm^2}
 \end{aligned} \tag{53}$$

Using the weight load only:

$$M_{\text{plane A}} = \rho_a a_1 b_1 t_a \tag{54}$$

Including the ‘large mass’ ($10^4 kg$) without the 0.1 Mg armor:

$$M_{plate} = M_{plate} + 10Mg = 10.399Mg \tag{55}$$

$$\begin{aligned}
w_{\text{per unit area}} &= \frac{M_{\text{plate}g}}{a_1 b_1} = 29.561 \text{psi} &= 0.204 \text{MPa} \\
G_{\text{given}} &= 8.7 \times 10^4 \text{MPa} & \nu_{\text{given}} = \frac{E_a}{2G_{\text{given}}} &= -3.448 \times 10^{-3} \\
\text{unreasonable } \nu_g &\Rightarrow E_{\text{given}} = 1(1 + \nu)G_{\text{given}} &= 2.314 \times 10^5 \text{MPa} \\
B_{\text{from E}} &= \frac{E_{\text{given}}}{3(1-2\nu)} &= 2.369 \times 10^5 \text{MPa}
\end{aligned} \tag{56}$$

C.1.2 Modal frequencies, HRA welded to hull ($t=4''$). Empirical constants for modal effects are in Table 36, # 16, page 717 of Roark's formulas [92] for $K_{(m,n)}$ where (m,n) are the modes in (x,y). These three constants, **K**, are from the table insert for (m,n) = (1,1), (1,2) and 2,1), and (1,3) and (3,1), respectively. Definition D is on page 714. The HRA – hull vibration system includes the system ‘large’ mass.

$$\begin{aligned}
K_{\text{modes}} &= \begin{pmatrix} \frac{11.5+13.4}{2} \\ \frac{24.1+16.2}{2} \\ \frac{41.9+24.1}{2} \end{pmatrix} = \begin{pmatrix} 12.450 \\ 20.150 \\ 33.000 \end{pmatrix} \\
D_{\text{table}} &= \frac{E_{\text{given}} t_a^3}{12(1-\nu^2)} = 2.270 \times 10^7 \text{Joules} \\
\mathbf{f_a} &= \frac{K_{\text{modes}}}{2\pi} \sqrt{\frac{D_{\text{table}g}}{w_{\text{perunitarea}} a_1^4}} = \begin{pmatrix} \mathbf{261.84} \\ \mathbf{423.78} \\ \mathbf{694.02} \end{pmatrix} \text{Hz} & \frac{1}{\mathbf{f_{a1}}} = \mathbf{2.360 \times 10^{-3} \text{sec}}
\end{aligned} \tag{57}$$

C.1.3 Normal mode frequencies, Hull-only ($t = 3''$). The hull vibration system includes the system ‘large’ mass.

$$t = 3 \cdot 25.4 \text{mm} \quad M_{\text{plate}} = 11.196 \text{Mg} \quad w_{\text{per unit area}} = 0.055 \text{MPa} \tag{58}$$

$$\mathbf{f_a} == \begin{pmatrix} \mathbf{81.95} \\ \mathbf{132.63} \\ \mathbf{217.22} \end{pmatrix} Hz \quad (59)$$

$$\frac{1}{\mathbf{f_{a1}}} = \mathbf{7.540 \times 10^{-3}sec} \quad (60)$$

C.1.4 Normal mode frequencies, HRA – only ($t=1''$). The HRA (armor – only) model *excludes* the system ‘large’ mass.

$$t = 1 \cdot 25.4mm \quad M_{plate} = 0.100Mg \quad w_{\text{per unit area}} = 1.954MPa \quad (61)$$

$$\mathbf{f_a} == \begin{pmatrix} \mathbf{334.27} \\ \mathbf{541.00} \\ \mathbf{886.01} \end{pmatrix} Hz \quad (62)$$

$$\frac{1}{\mathbf{f_{a1}}} = \mathbf{1.848 \times 10^{-3}sec} \quad (63)$$

Appendix D. Closed form nonlinear contact response, Single DOF

This section displays a copy of the MathCad output for the closed form solution to the damped single DOF (SDOF) oscillator meant to represent a lumped mass model of the HRA – hull vibration. The mechanics are based on the nonlinear solutions in Dr. Major Winthrop’s dissertation with a simplification of the “control law” (shown in Appendix E) that models simple contact. $x(t)$ is Dr. Winthrop’s Equation 3.14 [90].

D.1 Single DOF (SDOF) calculations

The SDOF calculations shown below, with suitable simplifications and assumptions, are used in Appendix E for the two DOF solution. This SDOF description of the effect of contact stiffness (bi – linear stiffness nonlinearity) on a solution composed of symmetric and antisymmetric one dimensional modes applies to the FE model for the tank hull and armor in a severely lumped mass model manner. The derivatives here act on the dimensionless system using all variables as nonlinear. After starting with a restricted case we can bring them in one at a time to refine the calculation. Appendix E has a comparison of the dimensioned and dimensionless DE’s for 2 DOF.

$$x(t) = (\dot{a}(t)t + a_o(t))e^{-(\dot{\mu}(t)+\mu_o)t} \cos \left[(\dot{\psi}(t)t + \psi_o)t + (\dot{\beta}(t)t + \beta_o) \right] \cong a \cos(\psi t + \beta) \quad (64)$$

$$\dot{x}(t) = \frac{d}{dt} \left[(\dot{a}(t)t + a_o)e^{-(\dot{\mu}(t)t+\mu_o(t))t} \cos \left[(\dot{\psi}(t)t + \psi_o(t))t + (\dot{\beta}(t)t + \beta_o(t)) \right] \right] \quad (65)$$

Even the first derivative is a bit complicated. The output from MathCad allows factoring in several ways. Collecting on $\cos \phi$ and then on $\sin \phi$, Equation 66 provides for a somewhat compact expression of the speed.

The “undamped” speed is $\frac{\dot{x}(t)}{\exp[-(\dot{\mu}t + \mu_o)t]} =$

$$(2\dot{a}\dot{\mu}t^2 + (2a_o\dot{\mu} + \dot{a}\mu_o)t + a_o\mu_o - \dot{a}) \cos\left(\dot{\psi}t^2 + (\psi_o + \dot{\beta})t + \beta_o\right) - \left((2\dot{a}\dot{\psi}t^2 + (2a_o\dot{\psi} + \dot{a}\psi_o + \dot{a}\dot{\beta})t + a_o\psi_o - a_o\dot{\beta}) \sin\left(\dot{\psi}t^2 + (\psi_o + \dot{\beta})t + \beta_o\right)\right) \quad (66)$$

With some more assumptions restricting the nonlinearity of the solution, the acceleration is also collected on $\cos \phi$ and then $\sin \phi$ in Equation 67 for the simplified expression.

$$\ddot{x} = (-\dot{a}\psi_o t + [\dot{a}\mu_o - a_o\psi_o^2]) \cos(\psi_o t + \beta_o) - (\dot{a}\mu_o\psi_o t + a_o\mu_o\psi_o) \sin(\psi_o t + \beta_o) \quad (67)$$

$\forall \quad \dot{\mu} = 0, \quad \dot{\beta} = 0, \quad \& \quad \dot{\psi} = 0$

The first order nonlinear solution in Equation 67 uses a constant amplitude ‘a.’ While not explicitly a function of time, it has a constant time rate of change, \dot{a} . A further order of nonlinearity to allow the amplitude change rate to be a function of time would follow in priority the use of $\dot{\psi}$, a dimensionless frequency rate of change. Further refinement is left for future model refinement. The end result of these calculations, after more work in Appendices E and F, is the “nonlinear” eigenvalue behavior in Figure 13 on page 105 which shows that symmetrical modes are the only ones not affected by stiffness change.

Appendix E. Closed form MathCad 2 DOF nonlinear contact

This section displays a copy of the MathCad output for the closed form solution to the damped two DOF (SDOF) oscillator meant to represent a severely lumped mass model of the HRA-hull vibration. These dynamical equations are an extension of the SDOF relations developed in Appendix D based on the nonlinear solutions in Dr. Major Winthrop's dissertation with selection of a "control law" that models simple contact. 'r' is the rate that defines the sharpness of the contact. x(t) is Dr. Winthrop's Equation 3.14 [90].

E.1 Two DOF DE's and solutions

Equation 68 is a dimensioned form of the two DOF damped oscillator DE.

$$\begin{pmatrix} P_1(t) \\ 0 \end{pmatrix} = \begin{pmatrix} m_1 & 0 \\ 0 & m_2 \end{pmatrix} \frac{d^2}{dt^2} \begin{pmatrix} \xi_1 \\ \xi_2 \end{pmatrix} + \begin{pmatrix} d_1 & 0 \\ 0 & d_2 \end{pmatrix} \frac{d}{dt} \begin{pmatrix} \xi_1 \\ \xi_2 \end{pmatrix} + \left[\begin{pmatrix} 1 & 1 \\ 1 & 1 \end{pmatrix} + \begin{pmatrix} \epsilon_1 & 0 \\ 0 & \epsilon_2 \end{pmatrix} \left(\frac{1}{2} - \frac{1}{\pi} \begin{pmatrix} \arctan(r\xi_1) & 0 \\ 0 & 0 \end{pmatrix} \right) \right] \begin{pmatrix} k_1 & -k_1 \\ -k_1 & k_1 + k_2 \end{pmatrix} \begin{pmatrix} \xi_1 \\ \xi_2 \end{pmatrix} \quad (68)$$

'k' will be the dimensionless stiffness ratio for the second oscillator, $k = \frac{k_1 + k_2}{k_1}$ which is the stiffness of the base of the system. ξ indicates the dimensioned form of location in the x direction. 'x' will be the dimensionless form. The dimensioned "control law" for structural contact for this two DOF problem is the $u(\xi)$ of Equation 69.

$$u(\vec{\xi}) = \left[\frac{1}{2} - \frac{1}{\pi} \begin{pmatrix} \arctan(rate\xi_1) & 0 \\ 0 & \arctan(r\xi_2) \end{pmatrix} \right] \quad (69)$$

The DE in Equation 70 takes a dimensionless form following the method of Dr. Major Winthrop [90]. $\vec{x} = [x_1 \ x_2]^T$ is the dimensionless location of the two masses.

$$\begin{pmatrix} 1 & 0 \\ 0 & 1 \end{pmatrix} \ddot{\vec{x}} + 2 \begin{pmatrix} \mu_1 & 0 \\ 0 & \mu_2 \end{pmatrix} \dot{\vec{x}} + \begin{pmatrix} 1 + \epsilon_1 u(x_1) & -1 \\ -1 & k \end{pmatrix} \vec{x} = \begin{pmatrix} F_{applied}(t) \\ 0 \end{pmatrix} \quad (70)$$

Continuing with the method and assumptions outlined in the Winthrop dissertation assume a straightforward solution. Equation 71 shows all the variables that vary with time. Subsequent assumptions listed in Equation 72 will compare keeping some of these variables constant to making the two DOF components equal.

$$x_i = a_i(t) e^{\mu_i(t)t} \cos(\psi_i(t)t + \beta_i(t)) \quad (71)$$

Substituting the assumed solutions from Equation 71 into Equation 70 results in a Special Eigenvalue Problem (SEVP) for the entire system. The (dimensionless) system frequencies ψ_i are functions of the individual frequencies $f = \omega/2\pi$ from $\omega_i^2 = \frac{k_i}{m_i} - 2\zeta_i^2$ (where $\zeta_i = \frac{d_i}{2m_i}$). In order to assist in making the solutions tractable, exclusion of some forms of time variation and non-uniformity of variables is appropriate. The first step is to restrict variation in the amplitude, damping, and phase, and to remove the driving load. Equation 72 lists these assumptions of linearities and uniformity that restrict us to a ‘first order’ nonlinearity, a time variation of the dimensionless frequency, ψ .

$$\begin{aligned} a_1(t) &= a_2(t) = \text{constant} = a && \text{Constant ‘a’ cancels out of the DE.} \\ \mu_1(t) &= \mu_2(t) = \text{constant} = \mu && \text{Uniform } \mu \text{ is for simplicity.} \\ \beta_1(t) &= \beta_2(t) = \text{constant} = \beta && \text{But uniform phase is realistic.} \\ F_{applied}(t) &= 0 && \text{Solve for free vibration first.} \end{aligned} \quad (72)$$

Using a new variable phase $\phi = \psi t + \beta$ to simplify the DE, we start with a definition of the speed (Equation 73) and acceleration (Equation 74).

$$\dot{x} = -\left[a\mu e^{-\mu t} \cos \phi + a\mu e^{-\mu t} \sin \phi\right] \quad (73)$$

$$\ddot{x} = a(\mu^2 - \psi^2)e^{-\mu t} \cos \phi + a(\mu\psi + \mu\psi)e^{-\mu t} \sin \phi \quad (74)$$

The resulting DE in Equation 75 starts to take a form (Equation 76) that can change into the SEVP form easily solved by eigenvalue extraction methods. We move representation of the derivatives into the coefficients of the vectors so that the vectors $\vec{x} = [x_1 \ x_2]^T$ factor out. Here we carry the different μ and ψ until the formal solution (subsequent “nonlinear” eigenvalues and eigenvectors). While the only actual ‘nonlinear’ modes are those produced by the FEA, those indicated with the ensuing math and descriptions provide insight into the dynamics.

$$\begin{aligned} & \begin{pmatrix} (\mu_1^2 - \psi_1^2) + 2\mu_1\psi_1 \arctan \phi_1 & 0 \\ 0 & (\mu_2^2 - \psi_2^2) + 2\mu_2\psi_2 \arctan \phi_2 \end{pmatrix} \begin{pmatrix} x_1 \\ x_2 \end{pmatrix} + \\ & \begin{pmatrix} 2\mu_1 \begin{bmatrix} -\mu_1 - \psi_1 \arctan \phi_1 \end{bmatrix} & 0 \\ 0 & 2\mu_2 \begin{bmatrix} -\mu_2 - \psi_2 \arctan \phi_2 \end{bmatrix} \end{pmatrix} \begin{pmatrix} x_1 \\ x_2 \end{pmatrix} + \quad (75) \\ & + \begin{pmatrix} 1 + \epsilon_1 u(x_1) & -1 \\ -1 & k \end{pmatrix} \begin{pmatrix} x_1 \\ x_2 \end{pmatrix} = \begin{pmatrix} 0 \\ 0 \end{pmatrix} \end{aligned}$$

Equation 75 is of the SEVP form shown in Equation 76. $\epsilon \equiv \epsilon_1 = k_{closed}/k_{open}$.

$$\begin{pmatrix} A_{1,1} & A_{1,2} \\ A_{2,1} & A_{2,2} \end{pmatrix} \begin{pmatrix} x_1 \\ x_2 \end{pmatrix} = \begin{pmatrix} 0 \\ 0 \end{pmatrix} \quad (76)$$

Equation 77 shows the form of the system matrix A for submission to an eigen-solver. Some of the terms in $A_{1,1}$ and $A_{2,2}$ were kind enough to cancel.

$$\mathbf{A} = \begin{pmatrix} A_{1,1} & A_{1,2} \\ A_{2,1} & A_{2,2} \end{pmatrix} = \begin{pmatrix} -\mu_1^2 - \psi_1^2 + 1 + \epsilon u(x_1) & -1 \\ -1 & -\mu_2^2 - \psi_2^2 + k \end{pmatrix} \quad (77)$$

Calculation of the determinant of \mathbf{A} with MathCad provides solutions to the characteristic polynomial of the system after using an assumption that the contact is active. So there are two sets of solutions: free classical vibration, and the vibration solution where the parts are welded together (modelled as “welded” or epoxied with hard rubber in the FE model, see page 190). The latter reduces to the former for $u = 0$. Therefore, the “welded” solution gives an indication of the dynamics by investigating the behavior of variations in u from zero to one; the switching determines the actual frequencies. Clearly these frequencies have a cyclic variation, one value for open gap and another for closed. But as the nonlinear FEA results show, both systems are active on average and energy flows into and out of both ‘open gap’ and ‘closed gap’ modes when averaged over many cycles according to the ‘control law’ for the contact, $u(x)$. The contact gap system is a time composite system with dynamics that are still susceptible to useful analysis with modal analysis techniques. Indeed, the noise and vibration industry developed these techniques with nonlinearities such as contact in mind [2–4, 26, 72].

The eigenvalues in Equation 78 are therefore a dual set for zero and nonzero control law values, $u(x)$. In the dimensionless system, the non-contact state has unity stiffness in DOF 1 and stiffness of k for DOF 2. But DOF 1 adds to the stiffness when in contact so that DOF stiffness becomes $1 + \epsilon$. The derivation of the “eigenvalues” of Equation 78 came from the Mathematica results discussed in Appendix F, Equation 82 on page 217.

$$\begin{pmatrix} \lambda_1 \\ \lambda_2 \end{pmatrix} = \frac{1}{2} \begin{pmatrix} (1 + \epsilon + k) - [2(\mu^2 + \psi^2)] - \sqrt{5 - 2\epsilon + \epsilon^2 + 2k - 2\epsilon k - k^2} \\ (1 + \epsilon + k) - [2(\mu^2 + \psi^2)] + \sqrt{5 - 2\epsilon + \epsilon^2 + 2k - 2\epsilon k - k^2} \end{pmatrix} \quad (78)$$

For subsequent nonlinear calculations we assume $u = 1$ so that contact is active. Assume $\epsilon > k$ (dimensionless) and $\epsilon_1 > k_2 = k_{base}$ (dimensioned) for stability.

The results of this Appendix are used in Appendix F in a copy of the Mathematica results for a “nonlinear” eigenvalue relation for the two DOF problem. Specifically, the related eigenvectors from Equation 83 used in a symmetric response $\Phi_{symm} = (\Phi^T + \Phi)/2$ calculation [22, 360 ff] provide a set of eigenvalues from $\Phi^t \Lambda \Phi$ that match, thus providing a necessary check on these results.

Appendix F. Closed form 2 DOF nonlinear contact eigenvalues

Application of the SDOF model over all DOF's for linear structural response theory gives a relationship for a linear transfer function (Fourier transform of the impulse response) where “ i ” is the DOF number. K_i is the generalized stiffness for that DOF. Each DOF in an LTI multi – DOF system has a relationship that has the same form as shown in Equation 41 on page 86. For the ensuing 2 DOF system, the results of Appendices D, E, and the 2 DOF extension of the SDOF theory are formulated for entry into Mathematica. This Appendix shows the reformulation and the Mathematica results.

The FE model used the simple ‘non – adaptive’ MacNeal – Schwendler NAS-TRAN CGAP element. This work assumes the closed stiffness is the sum of the two stiffness functions (an algebraic definition difference that does not change the results). The contour plot in Figure 57 shows that a ‘base’ stiffnesses, k_{base} (vehicle structural stiffness inboard of the armor or skin) higher than approximately 2.4ϵ that will provide imaginary parts to the eigenvalues. Positive and negative real parts will cause growth or decay in the phase or state space ‘orbits’ (Figure 12 on page 89). Due to nonlinearity, that change is not monotonic; for example, the response could be oscillatory, growing and decaying every other half cycle.

F.1 Damped 2 DOF sprung mass system Eigenvalue solutions

Repeated roots in Figure 13 on page 105 indicate the symmetric and antisymmetric modes have the same frequency but that there are real and imaginary parts to the eigenvalues [81, 171]. This indicates that there is a growth in energy for one mode and a decay in the other. Over time energy will move from the higher energy antisymmetric mode to the lower frequency symmetric mode.

However, this low base stiffness situation (repeated roots) merely indicates that the stiffness of the base is so low that the close and far masses (a one – dimensional lumped mass model for the hull and armor) vibrate as if in free space. Either they start with negligible relative motion and both vibrate away from and towards the

base (the trivial solution for low base stiffness) where the center of mass is oscillating according to the small base stiffness ($f_{CG}^2 = \frac{k_{base}}{4\pi^2[m_{hull}+m_{HRA}]}$), or they vibrate apart and together with their center of mass remaining stationary. Investigation of these closed form simple damped sprung mass systems not only provides insight. Determination of the validity of the eigenvalue increase for anti – symmetric (and unsymmetrical) modes when gap stiffness increases provides a basis for results seen in the FEA. Additionally, **this indicates that certain modes (‘symmetrical’) are better target identification features than others.** Hence the need to analyze the energy balance to validate the simple 1 and 2 DOF models.

F.1.1 Stiffnesses for stable systems. This Mathematica eigenvalue analysis of the MathCad system matrices in Appendix E for a two DOF damped spring mass system, springs and masses in series, shows the effect of contact stiffness on the eigenvalues. This effect results in a change in the energy balance between modes, a change in the modal participation factors (MPF’s). The eigenvalue results from the MathCad calculation are at the end of Appendix E. Assignment of $k_{contact} > k_{base}$ ensures an appropriate base and contact stiffness. The contour plot in Figure 57 on page 215 of the base stiffness versus the switching law (contact dimensionless stiffness) indicates the domain where the eigenvalues are real. The Matlab script used to plot this surface uses the formula $Z = (5 + (2X) + (X^{\odot 2}) - (2Y) - (2X \odot Y) - (Y^{\odot 2}))$, the quantity under the radical in the eigenvalues in Equation 82. Here $a^{\odot 2}$ is the element by element square of an array ‘a’ where the Matlab script uses “ $\wedge 2$ ” and $a \odot b$ is the element by element multiplication of matrices a and b using the Matlab “ \odot ” operator. Therefore, an element of the radical in Equation 82 would be $z_{i,j} = 5 + 2x + x_{i,j}^2 - 2y_{i,j} - 2x_{i,j}y_{i,j} - y_{i,j}^2$. Each element in the resulting Z matrix is a “stiffness.” Epsilon ϵ is the ratio of the contact stiffness to the small open (stabilizing) stiffness. Appendix E contains descriptions of these calculations.

F.1.2 Dimensionless formulation. The Mathematica results for this DE (Equation 81) in Equations 82 and 83 on page 217 shows the ‘special’ eigenvalue

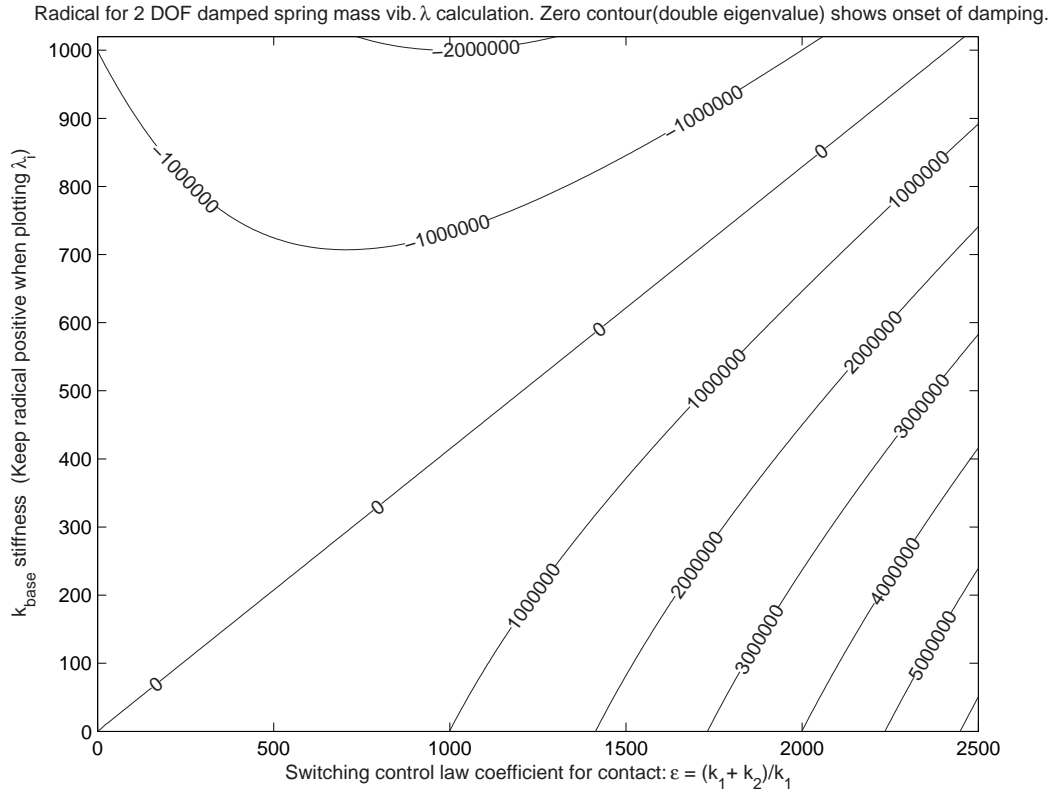


Figure 57: In the space where the radical used in calculations of the eigenvalues is zero, the two DOF damped contact nonlinear simple spring mass system eigenvalues are in transition between real and complex values. The abscissa is the ‘closed gap stiffness’ switched on by the ‘control law’ in the gap element.

problem (EVP) system matrix $[A_1]$, the eigenvalues, and eigenvectors for the simplified nonlinear contact system. The system matrix A_1 provides the special EVP (SEVP) where $[A_1]\vec{\Lambda}_i = zero$ for each eigenvector $\vec{\Lambda}_i$ in the matrix of (two) eigenvectors $\mathbf{\Lambda}$. Appendix E describes the composition of this matrix from the three terms in the dynamical D.E. but we can see that the system matrix is $[A]$ from $[A_1] = |[A] - \lambda[I]|$. The simplifications include that the damping is uniform for both the base and contact stiffness line elements; damping from the fixed base to the concentrated point mass modelling the hull is the same coefficient of the speed as the damping for the relative motion of the armor versus the hull. The stiffnesses in the lower right part of Figure 57 are stable. The more severe assumption, that dimensionless frequency $\psi_1 = \psi_2$ (setting the natural frequency of both the hull and the armor to be the same). While this is a strong assumption, it was understood that the FEA will give proper simulation results for all modes. Also, with this statement, we are saying that the particular solution is the same for both DOF's which is not actually the case except for purely symmetric and antisymmetric modes. However, we know that physically symmetric and antisymmetric modes, specifically these two modes alone, comprise the complete set of time solutions in Equation 79 for the undamped SEVP considered. So the assumption $\psi_1 = \psi_2$ gets validation from the physical dynamics of a two DOF undamped system. Damping will add a complication to this system but to first order assume both masses have the same particular order of solution set in time.

$$x(t) = \frac{\overline{x_{max}}}{L^*} \left(\text{nonlinear terms} \right) e^{j\psi t + \phi_o} = a(t) e^{-\mu_i t} \cos(\phi_i t + \beta(t)) \quad (79)$$

$$[A_1] = \begin{pmatrix} -\mu^2 - \psi^2 + 1 + \epsilon & -1 \\ -1 & -\mu^2 - \psi^2 + 1 + k_{open} \end{pmatrix} \quad (80)$$

The dimensionless frequencies, ψ , just happened to be in this system matrix in the same form as an eigenvalue in the form $A_1 = |[A] - \psi^2[I]|$.

This form where $\psi_1^2 = \psi_2^2 = \lambda_i$ are the eigenvalues only applies to the assumptions of equal damping and frequency for the two masses. Usually there is a superposition of both symmetric and antisymmetric modes at the same time so the hull – HRA subsystem will resonate at both $\psi_1 = \sqrt{\lambda_1}$ and $\psi_2 = \sqrt{\lambda_2}$ in a linear combination of modes. Each of the two Λ_i modes will have both ψ_1 and ψ_2 active for that one mode. Therefore, the energy applicable to both ψ_1 and ψ_2 for λ_1 is the same. This energy will generally be different from that for both ψ_1 and ψ_2 for λ_2 . The FEA eigenvalues (the values of the diagonal NASTRAN Λ matrix) are related to their eigenvectors \vec{u}_i^T , as plotted in Figures 21 on page 113 through Figure 23. The square roots of the eigenvalues, the FEA modal frequencies, are summarized in Table 7 on page 102 and Figure 20 on page 112. Those frequencies and plots of \vec{u}_i^T represent eigenvalues λ_i within Λ and eigenvectors Γ_i within Σ described in this Appendix (for this simple 2 DOF problem). As discussed above, the similar frequency argument makes physical sense. Yet the similar damping assumption does not have a physical rationale but is necessary to keep this calculation simple enough for the extra ψ terms to cancel.

$$A_1 = \begin{pmatrix} 1 + \epsilon - \mu^2 - \psi^2 & -1 \\ -1 & k - \mu^2 - \psi^2 \end{pmatrix} \quad (81)$$

The eigenvalues in a matrix form are $\Lambda = \begin{pmatrix} \lambda_1 & 0 \\ 0 & \lambda_2 \end{pmatrix}$ but it is more convenient to display them in the vector form in Equation 82.

$$\begin{pmatrix} \lambda_1 \\ \lambda_2 \end{pmatrix} = \frac{1}{2} \begin{pmatrix} 1 + \epsilon + k - \sqrt{5 - 2\epsilon + \epsilon^2 + 2k - 2\epsilon k - k^2} - 2\mu^2 - 2\psi^2 \\ 1 + \epsilon + k + \sqrt{5 - 2\epsilon + \epsilon^2 + 2k - 2\epsilon k - k^2} - 2\mu^2 - 2\psi^2 \end{pmatrix} \quad (82)$$

$$\Sigma = \begin{pmatrix} u_1 & v_1 \\ u_2 & v_2 \end{pmatrix} = \frac{1}{2} \begin{pmatrix} -1 - \epsilon + k + \sqrt{5 + 2\epsilon - \epsilon^2 - 2k - 2\epsilon k + k^2} & 1 \\ -1 - \epsilon + k - \sqrt{5 + 2\epsilon - \epsilon^2 - 2k - 2\epsilon k + k^2} & 1 \end{pmatrix}^T \quad (83)$$

Eigenvectors in Equation 83 are one dimensional 2 DOF mode shapes.

F.1.3 Analysis of the 2 DOF SEVP DE. Mathematica shows the eigenvalues $\lambda_i = \omega_i^2$ for each column Γ of the eigenvector matrix (Σ) . Σ appears on the last two output ‘lines.’ Equation 84 represents a component fixity extreme, the low frequency DC limit.

$$\vec{\lambda}_{\psi=0} = \frac{1}{2} \begin{pmatrix} 1 + \epsilon + k - 2\mu^2 - \sqrt{5 + 2\epsilon + \epsilon^2 - 2k - \epsilon k - 2k^2} \\ 1 + \epsilon + k - 2\mu^2 + \sqrt{5 + 2\epsilon + \epsilon^2 - 2k - \epsilon k - 2k^2} \end{pmatrix} \quad (84)$$

The radical in this first order correction to the linear eigenvalues is only a function of stiffnesses. Compared to prior Mathematica results, the component frequency was set to zero, $\psi = 0$, to analyze the dimensionless frequency in the square root of the eigenvalue. **This is only valid for $\mu_1 = \mu_2$ and $\psi_1 = \psi_2$ as described earlier.** Otherwise more nonlinear terms remain and the system is not susceptible to SEVP solution for modes in Equation 85.

$$\Sigma^T = \begin{pmatrix} \vec{\Gamma}_1 & \vec{\Gamma}_2 \end{pmatrix}^T = \begin{pmatrix} -1 - \epsilon + k + \sqrt{5 + 2\epsilon + \epsilon^2 - 2k - \epsilon k - 2k^2} & 1 \\ -1 - \epsilon + k - \sqrt{5 + 2\epsilon + \epsilon^2 - 2k - \epsilon k - 2k^2} & 1 \end{pmatrix} \quad (85)$$

F.1.4 Synthesis of the 2 DOF SEVP DE. The synthesis equation for these Mathematica analysis results is Equation 87 below. First we can synthesize the ‘system’ matrix to which these eigenvectors belong. This first subsection is merely a convenient explanation of how these eigenvalues came to be. The kernel of the SEVP

is $A_1 = |[A] - \lambda[I]|$. Using the fact that ψ^2 is the dimensionless frequency, the approximate system matrix A is available from the terms of $[A_1]$. This is only approximate because of the many combinations of nonlinear and approximately linear variables (like this ‘linear’ ψ) selected in Dr. Major Winthrop’s dissertation [90] and used in the “Mathematical Preliminaries” in section 4.3 on page 84 of this work. Taking the matrix $[A_1]$ we can add a diagonal of $\lambda_i[I] = \psi_i^2[I]$ to extract A from $A_1 = |[A] - \lambda[I]|$.

$$[A] = \begin{pmatrix} 1 + -\mu^2 + \epsilon & -1 \\ -1 & 1 - \mu^2 + k_{open} \end{pmatrix} \quad (86)$$

Equation 86 is essentially a 2 DOF system with springs of stiffnesses k and ϵ and uniform damping of the same magnitude for both DOF’s. The eigenvectors and eigenvalues are most easily recognized in relation to this standard EVP. This equation also contains the assumption ($\lambda_i = \psi^2 \quad \forall i$) described above.

$$\begin{pmatrix} 1 + -\mu^2 + \epsilon & -1 \\ -1 & 1 - \mu^2 + k_{open} \end{pmatrix} \times \vec{\Gamma}_i = \lambda_i \times \vec{\Gamma}_i \quad i \in [1, 2] \quad (87)$$

F.1.5 Physical nonlinear 2 DOF solution Synthesis. Extrapolating the derivation of the eigenvalue solution back to the initial structural D.E. we can use Equation 87 and the expressions derived above, the solutions in Equations 84 through 85 to the SEVP.

For clarification and to bring us back to the full nonlinear D.E. with the proviso that the eigenvalues for each DOF are the same for each mode as described above on page 218 and 216, the full nonlinear D.E. with separate damping appears in Equation 89. Except here we use the physical argument on page 216 leading to Equation 79 to maintain the frequencies equal. Therefore, the frequency subscript represents the same subscript as that for the eigenvector, rather than matching the damping as done for Appendix E.

The control law, $u(x_1)$ of Equation 88 plotted in Figure 11 on page 88 is the nonlinear stiffness. Based on the relative displacement, $\xi_1 = L^*x_1$, the switch occurs between the hull lumped point mass and the HRA plate lumped point mass.

$$u(\xi_1) = \frac{1}{2} - \arctangent(rate \cdot \xi_1) \quad (88)$$

Harmonic argument $\phi_k = \psi_k t + \beta(t) \approx \psi_k t$ relates to the eigenvector whose temporal dynamics it describes for both DOF's, the hull and HRA point masses.

$$\begin{aligned} & \begin{pmatrix} ((\mu_1^2 + \psi_k^2) + (2\mu_1\psi_k \tan(\phi_k))) & 0 \\ 0 & ((\mu_2^2 + \psi_k^2) + (2\mu_2\psi_k \tan(\phi_k))) \end{pmatrix} \times \begin{pmatrix} \Lambda_1 \\ \Lambda_2 \end{pmatrix}_k + \\ & \begin{pmatrix} 2\mu_1(-\mu_1 - \psi_k \tan(\phi_k)) & 0 \\ 0 & 2\mu_2(-\mu_2 - \psi_k \tan(\phi_k)) \end{pmatrix} \times \begin{pmatrix} \Lambda_1 \\ \Lambda_2 \end{pmatrix}_k + \\ & \begin{pmatrix} 1 + \epsilon u(x_1) & -1 \\ -1 & k_{open} \end{pmatrix} \times \begin{pmatrix} \Lambda_1 \\ \Lambda_2 \end{pmatrix}_k = \begin{pmatrix} 0 \\ 0 \end{pmatrix} \end{aligned} \quad (89)$$

Equation 89 provides an iid estimate of the dynamics modelled as N independent identically distributed oscillators. Since ‘oscillators’ for each DOF in a FE model and in continuous media (reality) are not independent nor of a random distribution in a structure, this relationship merely guides independent behavior that quickly effects other DOF's. More importantly, the “nonlinear” eigenvalue behavior in Figure 13 on page 105 shows the un – symmetrical modes are the only ones unaffected by stiffness change (item 3, FEA results, on page 148).

F.1.6 Energy balance, Lyapunov function. For our physical system the Lyapunov function is the total energy (or else it would explode or collapse). This model is a stable system which allows us to consider it representative of the hull – armor interaction for the case where both plates are artificially massively stiff (the ‘rigid plate model’) such that they contact everywhere at once when their centers of

mass are within half the sum of their plate thicknesses. In order to prove the contrary we considered sources of energy gain in Section 4.3 on page 84.

Table 4 at the beginning of Section 4.3 shows the full system forced vibration system does continually add energy. In this case we rely on the unlikelihood that a coincidence of vibration modes would increase the plate energy to be more than the initial energy for an instant in time; use the ‘No Tsunami Assumption’ for total energy. With this baseline we can assume that the driven oscillator is stable isL, but not asymptotically stable (unless driven through some molasses).

F.1.7 One DOF Lyapunov Function: Solution envelope. A search for a Lyapunov function restriction to the single DOF problem is a start. Even for this restricted function, formulation of the Lyapunov function from the total energy function remains formidable.

Using the non – dimensional location and speed calculations in Major Winthrop’s dissertation, [90], for the control shown in the previous arctangent control law plot, Figure 11 on page 88, the problem with using only two time scales is tractable, but clear. The time spent where the armor point mass model is in contact and compressing the hull point mass model requires expansion and an energy loss mechanism is required for lift – off. The FEA takes care of this issue with nonlinear contact elements.

Much mathematical analysis remains. Future activity could provide a full energy function, not from the energy derivation used for this work, but using kinematics and dynamics for the small 2 DOF problem. The main result of this one and two DOF damped nonlinear contact kinematics modelling section is the knowledge that un – symmetrical modes (that are the equivalent for classic ‘anti – symmetric’ modes of spring physics) increase in frequency whereas symmetrical modes do not, as shown in Figure 13 on page 105. This result appears in the multi – DOF FEA results as shown in Figures 21 through 23 and summarized in Figure 20.

Bibliography

1. Abramowitz, Milton and Irene A. Stegun. *Handbook of Mathematical Functions*. National Bureau of Standards, U. S. Government Printing Office, Washington D. C. 20402, 1964.
2. Allemang, R. J. *Investigation of Some Multiple Input/Output Frequency Response Function Experimental Modal Analysis Techniques*. Ph.D. thesis, The University of Cincinnati, Structural Dynamics Research Lab., Mech., Ind., and Nuclear Eng., U. of Cincinnati, OH 45221 – 0072, 1980.
3. Allemang, R. J. “The Modal Assurance Criterion Twenty Years of Use and Abuse”. *Sound and Vibration*, 37(9):8–17, Aug 2003.
4. Allemang, Randall J. *Chapter 21, Modal Analysis and Testing*. McGraw – Hill, New York, 4th edition, 1996. Cyril M. Harris, editor, Shock and Vibration Handbook.
5. Allemang, Randall J. and David L. Brown. “Chapter 16, Experimental Modal Analysis”. Albert S. Kobayashi (U. of Washington ME Dept. Seattle) (editor), *Laser Speckle and Related Phenomena*. Prentice – Hall, Inc. for the Society for Experimental Mechanics, Inc., Englewood Cliffs, New Jersey 07632, 1987.
6. Anderson, William. AERO 511 Dynamic and Nonlinear Analysis Class handout Sold by Kinkos, U of Michigan, Ann Arbor, Jul 1989.
7. Anderson, William. AERO 510 Linear Static and Normal Modes Class handout Sold by Kinkos, U of Michigan, Ann Arbor, Jul 1989.
8. Anderson, William. AERO 511 text Sold by Kinkos, CD from billa@umich.edu, U of Michigan, Ann Arbor, Jan 1993.
9. Andrews, Larry C. and Ronald L. Phillips. *Laser Beam Propagation through Random Media*. SPIE Optical Engineering Press, New York, 1998.
10. Arfken, George. *Mathematical Methods for Physicists*. Academic Press, Inc., Orlando, FL, 32887, 2nd edition, 1985.
11. Arnold, David and John C. Polking. *Ordinary Differential Equations using MATLAB*. Prentice Hall, ISBN 0-13-011381-6, PO Box 1892, Houston, TX 77251, 2nd edition, 1999.
12. Arsenault, H. H. and G. April. “Properties of speckle integrated with a finite aperture and logarithmically transformed”. *Journal of the Optical Society of America*, 66(11):1160–1163, Nov 1976.
13. Atluri, Satyi N. and Albert S. Kobayashi. “Chapter 1, Mechanical Responses of Materials”. Albert S. Kobayashi (editor), *Standard Handbook for Mechanical*

- Engineers*. Prentice – Hall Inc. (for the Society for Experimental Mechanics), Englewood Cliffs, NJ 07632, 1987.
14. Avallone, Eugene A. and Theodore Baumeister III. *Standard Handbook for Mechanical Engineers*. McGraw – Hill Book Company, Inc., New York, ninth edition, 1987.
 15. Baker, William. “EENG 605 Nonlinear Differential Equations”, April 2004. An A.F.I.T, Mathematics course.
 16. Baxter, Nelson L. “Nuggest of Gold”. *Sound and Vibration*, 5–6, June 1998. (contributing editor).
 17. Bendat, Julius S. *Nonlinear System Techniques and Applications*. Wiley – Interscience, John Wiley & Sons, New York, 1998.
 18. Bendat, Julius S. and Allan G. Piersol. *Engineering Applications of Correlation and Spectral Analysis*. Wiley – Interscience, John Wiley & Sons, Inc., New York, 1993.
 19. Binning, Gerd, Heinrich Rohrer, Ch. Geber, and E. Weibelall. “Surface Studies by Scanning Tunneling Microscopy”. *Physical Review Letters*, 49:57, Jul 1982.
 20. de Boer, Johannes F., Barry Cense, B. Hyle Park, Mark C. Pierce, Guillermo J. Tearney, and Brett E. Bouma. “Improved signal – to – noise ratio in spectral – domain compared with time – domain optical coherence tomography”. *Optics Letters*, 28(21):2067–2069, Nov 2003.
 21. Born, Max and Emil Wolf. *Principles of optics; Electromagnetic theory of propagation interference and diffraction of light*. Cambridge U. Press, The Edinburgh Building, Cambridge, CB2 2RU, UK, seventh (expanded) edition, 1999.
 22. Brogan, William L. *Modern Control Theory*. Prentice Hall, Upper Saddle River, NJ 07458, third edition, 1991.
 23. C. Y. Shih, R. J. Allemang, Y. G. Tsuei and D. L. Brown. “Complex Mode Indication Function and its Applications to Spatial Domain Parameter Estimation”. *IMAC VII*, Jan 1989.
 24. Cain, Professor Stephen. Matlab scripts sizAperture.m and prop2detect.m, 2004.
 25. Collins, Jack A. *Failure of Materials in Mechanical Design*. John Wiley & Sons, Inc., 605 Third Avenue, New York, NY 10158 – 0012, second edition, 1954.
 26. Curtis, Allen J. and Steven D. Lust. *Chapter 20, Concepts in Vibration Data Analysis*. McGraw – Hill, New York, 4th edition, 1996. Cyril M. Harris, editor, Shock and Vibration Handbook.
 27. Dereniak, Eustace L. and G. D. Boreman. *Infrared Detectors and Systems*. John Wiley & Sons, Inc., New York, 1996.

28. Dierking, Matthew, Robert Muse, Lawrence Barnes, Michael Seal, and E Armstrong. *AFRL Vibrometry Assessment Outline*. Contract AFRL-SN-WP-TR-2003-XXXX, USAF/AFRL/SN Combat Identification Technology Branch, 3109 P Street, Building 622, WPAFB, OH 45433 – 7700, Dec 2003.
29. Friedan, B. Roy. *Probability, Statistical Optics, and Data Testing*. Springer – Verlag, Berlin, 3rd edition, 2001.
30. G.Halvorsen, W. and J. S. Bendat. “Noise Source Identification Using Coherent Output Power Spectra”. *Sound and Vibration*, 15–24, Aug 1975.
31. Giglia, Dennis C. and Mark D. Pritt. *Two – Dimensional Phase Unwrapping*. John Wiley & Sons, Inc., New York, 1998.
32. Goodman, Joseph W. *Introduction to Fourier Optics*. McGraw – Hill Book Company, San Fransisco, 1968.
33. Goodman, Joseph W. *Statistical Optics*. Wiley – Interscience Publications, John Wiley & Sons, Inc., New York, 1985.
34. Gutjahr, A. and Charles R. Holmes. *Estimates of the Minimum Dimensions of Charged Cloud Volumes that Produce Lightening*. Contract ADA051954, New Mexico Institute of Mining and TEchnology, Socorro, NM 87801, Charles B. Moore, P O Box 1333, Socorro, NM 87801, Oct 1978.
35. Gutjahr, Allan J. and Charles R. Holmes. *Cross Spectral Analysis of Acoustic Signals*. Contract ADA051954, Office of Naval Research, 800 N. Quincy Street, Arlington, Virginia, 22217, Mar 1978.
36. Halliday, David, Robert Resnick, and Jearl Walker. *Fundamentals of Physics, Extended version*. John Wiley & Sons, Inc., New York, 1993.
37. Holmes, Charles R. *Low Frequency Sound Generation from Thunderstorms*. Contract ADA051954, New Mexico Institute of Mining and TEchnology, Socorro, NM 87801, Charles B. Moore, P O Box 1333, Socorro, NM 87801, Oct 1987.
38. Jain, Anil K. *Fundamentals of Digital Image Processing*. Prentice – Hall Inc., a Pearson Education Co., Upper Saddle River, NJ 07458, 1989.
39. Juvinall, Robert C. *Engineering Considerations of Stress, Strain, and Strength*. McGraw – Hill, New York, 1967.
40. Juvinall, Robert C. and Kurt M. Marshek. *Fundamentals of Machine Component Design*. John Wiley & Sons, Inc., New York, 1991.
41. Kim, Tae Chung. *Analysis of clearance non – linearities and vibro – impacts in torsional systems*. Ph.D. thesis, The Ohio State University, ME Dept., Columbus, Ohio, Dec 2003.
42. Kobold, Michael C. “Laser and Acoustic Exploitation Concept for Unconventional Target Covariance”. *Proceedings of the 2005 STAR Conference*. USAF/AFRL/SN, WPAFB, Ohio, 2005.

43. Kobold, Michael C. “videst.m based on NATO data in the 2003 Swedish dissertation the Andreas Olsson”. Unclassified Matlab ROC code used to propose laser vibrometry to DARPA, videst.m, Dec 2005.
44. LaMeres, Brock. Agilent Technologies Techonline Internet technical report, Oct 2004.
45. Lee, M. H., J. F. Holmes, and J. R. Kerr. “Statistics of speckle propagation through the turbulent atmosphere”. *Journal of the Optical Society of America*, 66(11):1164–1172, Nov 1976.
46. Lee, Sang H. *MSC/NASTRAN Handbook for Nonlinear Analysis (based on Versions 65, 66, & 67)*. MacNeal – Schwendler Corporation, Costa Mesa, CA, 1992.
47. Lowenthal, S. and H. H. Arsenault. “Image formation for coherent diffuse objects: statistical properties”. *Journal of the Optical Society of America*, 60:1478, Nov 1970.
48. ir M. Brughmans, ir R. Lembrechts, and ir F. Furini. “Development of a Nonlinear Frequency Response Program for Simulating Vehicle Ride Comfort”. *Proceedings of the 1995 MSC World Users Conference*. MacNeal – Schwendler Corporation, www.mscsoftware.com, Costa Mesa, CA, 1995. Paper 5.
49. Mach, Von E. and P. Salcher. “Photographisch Fixirung der durch Projectile in der Luft eingeleiteten Vorgänge”. *Sitzungsber. der Wiener Akademie mathem. – naturw.*, C1. XCV(Bd. II Abath.):764–780, Aug 1889.
50. MacNeal, Richard H. *Finite elements: their design and performance*. Marcel Dekker, Inc., 270 Madison Avenue, NY, NY 10016, 1994.
51. Moore, Charles B. Personal Correspondence, P O Box 1333, Socorro, NM 87801, Feb 2005.
52. Newmark, N. M. “A method for computing numerically integrated stiffness matrices”. *Eng. Mech. Div. ASCE*, 85:67–94, 1959.
53. Oberg, Erick, Franklin D. Jones, Holbrook L. Horton, , and Henry H. Ryffel. *Machinery’s Handbook*. Industrial Press, 200 Madison Avenue, NY, NY 10016 – 4078, 24th edition, 1992.
54. Olsson, Andreas. *Target Recognition by vibrometry with a coherent laser radar*. Examensarbete, Linköpings University, Institutionen för Systemteknik, 581 83 LINKÖPING, 04 2003. Wwww.ep.liu.se/exjobb/isy/2003/3050.
55. Oppenheim, Alan V. and Ronald W. Shafer. *Digital Signal Processing*. Prentice – Hall, Inc., Englewood Cliffs, NJ, 1975.
56. Parker, Sybil P. (editor). *McGraw – Hill Concise Encyclopedia of Science and Technology*. McGraw – Hill Book Company, Inc., New York, 1984.

57. Pascual, Rodrigo, roberto Schalchli, and Mario Razeto. "Damping Identification using a robust FRF – based model updating technique". *XXI International Modal Analysis Conference*. IMAX, Kissimmee, FL, 2003. Rpascual@ing.uchile.cl.
58. Pepela, Mgoya. *Effect of multi – mode vibration on signature estimation using a laser vibration sensor*. Master's thesis, Air Force Institute of Technology ENY, Wright Patterson AFB OH 45433 – 7321, December 2003. AFITGEENP03-02.
59. Phillips, Allyn W., Randall J. Allemang, and William A. Fladung. "The Complex Mode Indicator Function (CMIF) as a Parameter Estimation Method". *International Modal Analysis Conference*, pp. 705–710. SAE, Santa Barbara, CA, 1998.
60. Phillips, Allyn W., Randall J. Allemang, and Andrew T. Tucker. "A new excitation method: Combining Burst Random Excitation with Cyclic Averaging". *International Modal Analysis Conference*, pp. 891–899. SAE, Santa Barbara, CA, 1998.
61. Pierce, Allan D. *Acoustics (1994 Edition)*. American Institute of Physics, Acoustical Society of America, 500 Sunnyside Boulevard, Woodbury, NY 11797, 1991.
62. Popov, Egor P. *Engineering Mechanics of Solids*. Prentice – Hall Inc. (for the Society for Experimental Mechanics), Englewood Cliffs, NJ 07632, second edition, 1998.
63. Powell, R. L. and K. A. Stetson. "Interferometric Vibration Analysis by Wavefront Reconstruction". *Journal of the Optical Society of America*, 55:1593, 1965.
64. Priddy, Kevin and Rob Williams. Building 38 Three – Dimensional Lidar dimensioning and acoustic data collection for various vehicles, Jan 2006.
65. Randall, Robert. *Chapter 14, Spectrum Analyzers and their use*. McGraw – Hill, New York, 4th edition, 1996. Cyril M. Harris, editor, Shock and Vibration Handbook.
66. Raymond, Michael and Mark Miller. *MSC/NASTRAN Nonlinear Handbook V69*. MacNeal – Schwendler Corporation, www.mssoftware.com, Costa Mesa and 815 Colorado Boulevard Los Angeles, CA 90041 – 1777, 1996.
67. Rice, Richard C., Jana J. Jackson, John Bakuckas, and Steven Thompson. *MIL–HDBK–5H, Metallic Materials and Elements for Aerospace Vehicle Structures*. Contract 1560-0187, FSC 1560, DoD, Army, Navy, Air Force, and FAA, MIL–HDBK–5 Coordinating, AFRL/MLSC, 2179 Twelfth St. Rm. 122, WPAFB, OH, 45433 – 7718, Dec 1998. DOT/FAA/AR-MMPDS-01.
68. Rice, Richard C., Jana J. Jackson, John Bakuckas, and Steven Thompson. *Metallic Materials Properties Development and Standardization (MMPDS)*. Contract F33615-97-C-5647, Office of Aviation Research, www.tc.faa.gov/its/worldpac/techrpt/ar-mmpds-01, Natl. Tech. Info. Service, Virginia, 22161, Dec 2002. DOT/FAA/AR-MMPDS-01.

69. Roark, Raymond J. *Formulas for Stress and Strain*. McGraw – Hill Book Company, Inc., New York, third edition, 1954.
70. Roggemann, Michael C. and Byron Welsh. *Imaging through turbulence*. CRC Press, Boca Raton, Florida, 1996.
71. Rubin, Sheldon. *CRC Standard Mathematical Tables*. The Chemical Rubber Co., 18901 Cranwood Parkway, Cleveland, Ohio 44128, 21st edition, 1973.
72. Rubin, Sheldon. *Chapter 23, Concepts in Shock Data Analysis*. McGraw – Hill, New York, 4th edition, 1996. Cyril M. Harris, editor, Shock and Vibration Handbook.
73. Scharf, Louis L. *Statistical Signal Processing*. Addison – Wesley Publishing Company, Inc., Reading, MA, 1991.
74. Shigley, Joseph Edward and Charles R. Mischke. *Mechanical Engineering Design*. McGraw – Hill, New York, 1989.
75. Siong, Neo Wei and Dinesh Raghavan. *Numerical Simulation for Optimizing Penetration of Segmented Projectiles*. Web published pdf <http://staff.science.nus.edu.sg/>, National University of Singapore, University Hall, Lee Kong Chian Wing, #UHL0301, 21 Lower Kent Ridge Road, Singapore 119077, 2003.
76. Sitton, Grant (editor). *MSC/NASTRAN Basic Dynamic Analysis User's Guide*. MacNeal – Schwendler Corporation, www.mssoftware.com, Costa Mesa and 815 Colorado Boulevard Los Angeles, CA 90041 – 1777, 1993.
77. Smallwood, David O. “The correct balance between analysis and test”. *Sound and Vibration*, 6–7, Mar 2000.
78. Stetson, Karl A. “Chapter 10, Optical Heterodyning”. U. of Washington Seattle Albert S. Kobayashi, ME Dept. (editor), *Standard Handbook for Mechanical Engineers*. Prentice – Hall Inc. (for the Society for Experimental Mechanics), Englewood Cliffs, NJ 07632, 1987.
79. von Storch, Hans, Thomas Bruns, Irene Fischer Bruns, and Klaus Hasselmann. “Principal Oscillation Pattern Analysis of the 30 – to 60 – Day Oscillation in General Circulation Model Equatorial Troposphere”. *Journal of Geophysical Research*, 93D(D9):11022–11035, Sep 1988.
80. Strutt, John William. *The Theory of Sound*. Dover Publications, NY, Printed by General Publishing Co. Ltd., 30 Lesmill Road, Don Mills, Toronto, Ontario, second revised edition, 1945. (the Baron Rayleigh Sc.D. F.R.S.).
81. Thomson, William Tyrrell. *Theory of Vibration With Applications*. Prentice Hall, Englewood Cliffs, NJ 07632, 1988.
82. Töpler. “Optische Studien nach der Methode der Schlierenbeobachtung”. *Annal. Physik*, CXXXI:33, 180, 1867.

83. TsuTsui, Keiichiro, Ray Nogami, and John L. Bretl. "Development of a Nonlinear Frequency Response Program for Simulating Vehicle Ride Comfort". *Proceedings of the 1995 MSC World Users Conference*, paper 37. MacNeal – Schwendler Corporation, www.mssoftware.com, Costa Mesa, CA, 1995.
84. Turner, M. J., R. W. Clough, H. C. Martin, and L. J. Topp. "Stiffness and Deflection Analysis of Complex Structures". *Journal of Aeronautical Science*, 23:803–823, 1956.
85. vanTrees, Harry L. *Part I: Detection, Estimation, and Modulation Theory*. John Wiley & Sons, Inc., New York, 1968.
86. vanTrees, Harry L. *Optimum Array Processing, Part IV: Detection, Estimation, and Modulation Theory*. Wiley – Interscience, a John Wiley & Sons, Inc. Publication, New York, 2002.
87. Vold, Håvard, Jan Leuridan, and Herman Van der Auwerær. "The Analysis of Nonstationary Dynamic Signals". *Sound and Vibration*, 14–26, Aug 1994.
88. Wangness, Roald K. *Electromagnetic Fields*. John Wiley & Sons, Inc., New York, 2nd edition, 1986.
89. Wheatstone, Sir Charles and communicated by Michael Faraday (Esq. D.C.L. F.R.S.). "On the Figures Obtained by Strewing Sand on Vibrating Surfaces, Commonly Called Acoustic Figures". *Philosophical Transactions of the Royal Society of London*, (XXV):593–633, Mar 1833.
90. Winthrop, Michael F. *Engineering Tools for Variable Stiffness Vibration Suppression and Isolation*. Ph.D. thesis, Air Force Institute of Technology ENY, Wright Patterson AFB OH 45433 – 7321, Dec 2004. AFITDSENY04-9.
91. Yariv, Amnon and Poci Yeh. *Optical Waves in Crystals, Propagation and Control of Laser Radiation*. Wiley – Interscience, a John Wiley & Sons, Inc. Publication, New York, 2003.
92. Young, Warren C. *Roark's Formulas for Stress and Strain*. McGraw – Hill Book Company, Inc., New York, sixth edition, 1989.
93. Zienkiewicz, Olgierd Cecil and R L Taylor. *The Finite Element Method, Volume 1; Basic Formulation and Linear Problems*. McGraw – Hill Book Company, London, 4th edition, 1991.
94. Zienkiewicz, Olgierd Cecil and R L Taylor. *The Finite Element Method, Volume 2; Solid and Fluid Mechanics Dynamics and Nonlinearity*. McGraw – Hill Book Company, London, fourth edition, 1991.

Index

The index is conceptual and does not designate every occurrence of a keyword. Page numbers in bold represent concept definition or introduction.

anti – symmetric, *see* 147, 214
anti – symmetrical, *see* 30, 147
automated target recognition, *see* 1, 23

coherent imaging, *see* 40
contact vibration, *see* 173
cross – spectral covariance, *see* 49

finite element analysis, *see* 176

independent, identically distributed, *see* 220
inter – pulse period, *see* 36

nonlinear analysis, *see* 163

probability of false alarm, *see* 4
pulse repetition interval, *see* 36
pulse repetition rate, *see* 36

recognition, *see* 1, 23

spectral elimination, *see* 61
spectral reduction, *see* 61, *see* 147
static indeterminacy, *see* 135
symmetrical, *see* 30, 147

target identification, *see* 4

unsymmetrical, *see* 30, 147

REPORT DOCUMENTATION PAGE

Form Approved
OMB No. 0704-0188

The public reporting burden for this collection of information is estimated to average 1 hour per response, including the time for reviewing instructions, searching existing data sources, gathering and maintaining the data needed, and completing and reviewing the collection of information. Send comments regarding this burden estimate or any other aspect of this collection of information, including suggestions for reducing this burden to Department of Defense, Washington Headquarters Services, Directorate for Information Operations and Reports (0704-0188), 1215 Jefferson Davis Highway, Suite 1204, Arlington, VA 22202-4302. Respondents should be aware that notwithstanding any other provision of law, no person shall be subject to any penalty for failing to comply with a collection of information if it does not display a currently valid OMB control number. **PLEASE DO NOT RETURN YOUR FORM TO THE ABOVE ADDRESS.**

1. REPORT DATE (DD-MM-YYYY) 14-09-2006		2. REPORT TYPE Master's Thesis		3. DATES COVERED (From — To) June 2004 — Sep 2006	
4. TITLE AND SUBTITLE Laser Covariance Vibrometry for Unsymmetrical Mode Detection				5a. CONTRACT NUMBER	
				5b. GRANT NUMBER	
				5c. PROGRAM ELEMENT NUMBER	
6. AUTHOR(S) Michael C. Kobold, GD - AIS contractor to AFRL/SNAT				5d. PROJECT NUMBER	
				5e. TASK NUMBER	
				5f. WORK UNIT NUMBER	
7. PERFORMING ORGANIZATION NAME(S) AND ADDRESS(ES) Air Force Institute of Technology / ENG Professor Stephen Cain, Advisor, Stephen.Cain@afit.edu Graduate School of Engineering and Management 2950 Hobson Way WPAFB, OH 45433-7129				8. PERFORMING ORGANIZATION REPORT NUMBER AFIT/GE/ENG/06-61	
9. SPONSORING / MONITORING AGENCY NAME(S) AND ADDRESS(ES) AFMC/AFRL/SNAT, Dr. Robert Williams, Lead Eng, (937)212-4051 2241 Avionics Circle, Building 620 Rm 3D037 Wright Patterson AFB, OH 45433-7321 AFRL/SNJM, Dr. Matthew Dierking, Branch Chief, laser vibrometry contact General Dynamics - AIS (A. Zembower, D. Gross, M. Axtell, & D. Doty) (937)253-4770, 5200 Springfield Pike, Suite 200 Dayton, OH 45431-1289				10. SPONSOR/MONITOR'S ACRONYM(S)	
				11. SPONSOR/MONITOR'S REPORT NUMBER(S)	
12. DISTRIBUTION / AVAILABILITY STATEMENT Approved for public release; distribution is unlimited.					
13. SUPPLEMENTARY NOTES					
14. ABSTRACT Simulated cross – spectral covariance (CSC) from optical return from simulated surface vibration indicates CW phase modulation may be an appropriate phenomenology for adequate classification of vehicles by structural mode. The nonlinear structural to optical relationship is close to unity, avoiding nulls and high values; optical return contains sufficient spectral ID information necessary for data clustering. The FE model has contact between the homogeneous rolled armor and vehicle hull, a simple multi - layer skin model typical of most vehicles. Most of the high frequency energy moved to lower frequencies. This nonlinearity segments contact vibration modes into two classes: symmetrical modes that do not vary with minor structural changes, and those that do. The fundamental mode symmetry created features that were insensitive to slight structural load path changes. Structural aging simulation affected spectral and CSC fine structure generated by non-symmetrical modes. Structural vibration spectral analysis related to the nonlinear contact uses methods from Maj Winthrop's December 2004 AFIT PhD dissertation. Analysis of the propagated optical field confirms the spectral reduction results of Fl Lt Pepela's December 2003 AFIT thesis.					
15. SUBJECT TERMS cross – spectral covariance, target ID & classification, recognition, ATR, coherent imaging, optical coherent tomograph, coherent scattering tomography, FEA, static indeterminacy, nonlinear analysis, contact vibration, spectral elimination, spectral reduction					
16. SECURITY CLASSIFICATION OF:			17. LIMITATION OF ABSTRACT UU	18. NUMBER OF PAGES 221	19a. NAME OF RESPONSIBLE PERSON Professor Stephen Cain, AFIT/ENG
a. REPORT U	b. ABSTRACT U	c. THIS PAGE U			19b. TELEPHONE NUMBER (include area code) (937) 255-3636 x 4716